FINAL TECHNICAL REPORT
VOLUME I

HOLOMEM

OPTICAL MASS MEMORY INVESTIGATIONS

CONTRACT NUMBER NAS8-30564

JUNE 1977

FOR

GEORGE C. MARSHALL SPACE FLIGHT CENTER
NATIONAL AERONAUTICS AND SPACE ADMINISTRATION
MARSHALL SPACE FLIGHT CENTER, ALABAMA 35812

BY

ELECTRO-OPTICS DEPARTMENT

HARRIS
COMMUNICATIONS AND INFORMATION HANDLING
HARRIS CORPORATION Electronic Systems Division
P.O. Box 37, Melbourne, Florida 32901 305/727-4000

89678

FINAL TECHNICAL REPORT
VOLUME I

HOLOMEM

OPTICAL MASS MEMORY INVESTIGATIONS

CONTRACT NUMBER NAS8-30564

JUNE 1977

FOR

GEORGE C. MARSHALL SPACE FLIGHT CENTER

NATIONAL AERONAUTICS AND SPACE ADMINISTRATION

MARSHALL SPACE FLIGHT CENTER, ALABAMA 38512

BY

ELECTRO-OPTICS DEPARTMENT

TABLE OF CONTENTS

TABLE OF CONTENTS (Continued)

TABLE OF CONTENTS (Continued)

TABLE OF CONTENTS (Continued)

LIST OF TABLES

LIST OF TABLES (Continued)

LIST OF ILLUSTRATIONS

LIST OF ILLUSTRATIONS (Continued)

LIST OF ILLUSTRATIONS (Continued)

LIST OF ILLUSTRATIONS (Continued)

LIST OF ILLUSTRATIONS (Continued)

LIST OF ILLUSTRATIONS (Continued)

LIST OF ILLUSTRATIONS (Continued)

SUMMARY

This final technical report summarizes research and design activities in support of the development of a 10^{12}-bit holographic read/write optical mass memory (HOLOMEM) with some moving parts for space applications.

The NASA Optical Mass Memory Investigations Program has as one goal the evolution of a dynamic, space-qualified optical mass memory. To ensure maximum reliability and to minimize operational impacts on the host vehicle, the optical mass memory was to have no moving parts. As light can be modulated and deflected with inertialess electro-optic or acousto-optic devices, a block-oriented read/write memory of this type appeared feasible if the incoherent superposition of holograms could be achieved in a reusable volume phase recording medium. Research and component development advanced the state of the art of page composers, photodetector arrays, beam deflectors, modulators and media transports. However, a suitable read/write volume phase medium was not identified and problem areas related to the storage and retrieval of large blocks of data in a fixed format memory were discovered.

In view of current technology limitations, the decision was made to expand the scope of the investigation to include memory concepts that incorporated some moving parts. By adapting and expanding technology developed on previous program phases, a breadboard holographic recorder/reproducer was constructed that demonstrated the feasibility of this approach by recording and reading out one-dimensional microholograms of digital data blocks at a 1 Mb/sec rate. In parallel with this activity, an in-depth study of read/write photoplastic recording media on flexible substrates (for both fiche and tape-oriented memory concepts) was performed.

The report consists of four sections. Section I is a general introduction, which includes a summary of key accomplishments and the principal conclusions of the study. Section II is a comprehensive analysis of alternative HOLOMEM system concepts. Section III is a discussion of important design and trade-off considerations related to the fabrication, test, and evaluation of a breadboard holographic recorder/reproducer. Finally, Section IV is a summary of experimental data generated to define the holographic recording performance of two quasi-commercial photoplastic recording films.

FOREWORD

This report was prepared by the Electro-Optics Department of the Electronic Systems Division of Harris Corporation. It documents technical effort on the HOLOMEM phase of NASA Contract NAS8-30564, entitled "Optical Mass Memory Investigations", between 1 July 1974 and 14 May 1976. Mr. G. A. Bailey, Marshall Space Flight Center, was the project engineer and COTR.

The principal investigator and program manager was Dr. H. N. Roberts. Project engineers were B. R. Reddersen and Dr. R. G. Zech. Task leaders were Lynda M. Ralston and M. W. Shareck. Important experimental contributions were made by D. G. Lipscomb.

Contributors to this report are Dr. T. R. Bader, L. M. Ralston, B. R. Reddersen, Dr. H. N. Roberts, M. W. Shareck, D. N. Wied, and Dr. R. G. Zech. Dr. Zech is the technical editor, and is responsible for the content and format of the report.

Technical direction and research and development personnel were provided by the Optical Processing and Storage Section (Dr. H. N. Roberts, Section Head). Program monitoring was the responsibility of the Program/Systems Management Section (R. H. Nelson, Section Head). The Electro-Optics Department is under the general direction of Dr. Anthony Vander Lugt.

The publication date of this report is June 1977.

ACKNOWLEDGEMENTS

We are pleased to acknowledge the cooperation, advice and insight provided by the following individuals:

- Mr. G. A. Bailey and Mr. E. J. Reinbolt,
  NASA Marshall Space Flight Center
  Huntsville, AL
- Dr. Johan Dirks,
  Scott Graphic Incorporated
  Holyoke, MA
- Dr. Johannes Munder and Dr. Roland Morow
  Kalle, AG
  Weisbaden, West Germany
- Mr. F. E. Dailey, Jr.
  Image Technology and Application
  Wilbraham, MA

SECTION I

INTRODUCTION AND BACKGROUND

SECTION I

INTRODUCTION AND BACKGROUND

This final technical report documents analysis, design and experimental activities directed toward the goal of developing a 10^{12} bit read/write holographic optical mass memory with some moving parts. Section II provides an in-depth treatment of several HOLOMEM systems concepts. Section III presents analysis, trade-offs, and experimental data for key breadboard components and the results obtained with an experimental HOLOMEM breadboard. Finally, Section IV summarizes characterization and systems experiments aimed at the development of a systems-qualified photoplastic recording film.

1.1 BACKGROUND

In the late 1960's NASA identified the need for a high capacity (10^{12} bit) read/write mass memory for earth-orbit space applications. The functions of the mass memory were to be twofold: short term storage of perishable data and on-line data processing. A primary application was preprocessing of and feature extraction from ERTS (now LANDSAT) satellite data. Other feasible applications included Skylab, support for deep space probes, data processing for orbiting large-aperture space telescopes, and the then developing concept of Space Shuttle.

The construction, delivery and operation in a space-type environment of a mass memory is extremely challenging. Volume, weight and power consumption are greatly constrained. The mass memory must withstand the multi-G forces developed during launch, large temperature extremes and the anomalies of operation in hard vacuum. As the mass memory is unattended and generally inaccessible for repair or maintenance, reliability and operational considerations are foremost. To minimize the chance of component failure, there should be no moving parts. When all these factors are considered together the formidable nature of the problem is evident.

At the time, it was clear that no existing commercialized technology could provide the desired mass memory system. Magnetic tape, disk, or drum computers, for example, were simply too large and inefficient to be packaged into a space-qualified 10^{12} bit mass memory. With the current development of semiconductor, bubble, and ion implantation memories, this is no longer as true; however, there is no clear evidence that these approaches can be implemented on a practical basis to achieve the 10^{12} bit capacity. The only alternative to a magnetic mass memory was an optical mass memory.

A multi-year development program for the design, engineering and packaging of a 10^{12} bit read/write space-qualified optical mass memory with no moving parts was initiated by Harris Corporation in 1969 with NASA support. Laser holography was selected as the baseline storage and retrieval technology. A volume phase recording medium was specified to obtain maximum diffraction efficiency and to allow the multiplexing, in depth, of a large number of holograms in the same recording area. To satisfy the no moving parts constraint, a block-oriented random-access format was chosen for the holographic recorder/reproducer subsystem of the optical mass memory. To maximize information packing density, Fourier-transform holograms were to be used to store digital data.

The block-oriented random-access memory (BORAM) approach is elegant. Aside from several electronic control and data processing subsystems, a BORAM system consists only of a N x N block data composer (a device for converting electrial information into optical information), reference and signal beam deflectors, a M x M hologram array, a number of high quality infinite conjugate lenses, a N X N photodetector array (to convert optical information back into electrical information), a multi-wavelength (tunable) laser, and a read/write recording material. Conceptually, the development of a BORAM system should have been straightforward.

In late 1972, after performing a thorough basic concept study and developing several key components to the state of the art level, a 0.4 Mb read/write breadboard optical memory with no moving parts was delivered to NASA/MSFC. Principal system components were argon and helium-neon lasers, a block data composer, a read/write

recording material, a photodetector array, and the electronics required to drive, synchronize and control these components. The helium-neon laser was used in both the read and write modes; the argon laser was used only in the read mode. An acousto-optic beam deflector (AOBD) deflected the reference and signal beams to any hologram location; this provided the random access capability. A block data composer, operating at micro-second switching speeds and capable of handling a read-in data rate of 1 Mb/s, supplied the interface between the input data and the memory. A photoplastic storage material was developed to simulate the read/write requirement of the memory. At the output end of the memory, a photodetector array converted the optical data back to electrical data. The memory could operate in two modes; an erasable mode having a capacity of 0.4 Mb and a permanent mode having a capacity of 10 Mb. Data input and output functions were accomplished with a block data composer and photodetector array. The block data composer (constructed of PLZT, a ferroelectric ceramic) transduced time sequential blocks of electrical data into a 2-dimensional spatial array. This array modulated the recording laser beam, which was directed to the hologram recording plane where it was mixed with the reference beam to form an analog Fourier transform hologram. For readout, a hologram was addressed by the reference beam alone; this reconstructed the image of a stored data block onto the photodetector array. Finally, a computer and various programs to control it were implemented to permit the simulation of dynamic memory operation. Although many orders of magnitude away from the 10^{12} bit capacity goal, this BORAM HOLOMEM system demonstrated in large measure the feasibility of the concept.

1.2 CONCEPT TRANSITION

Further research and development effort revealed various fundamental problem areas. Chief among them was the unavailability of a write/read/erase volume phase recording material that was simultaneously capable of high recording speed, sensitive to helium-neon and/or argon laser light, stable, reusable at least 500 times and self-processing. Photoplastic recording media simulate these requirements but they are planar, rather than volume, phase materials. To this date, no light-sensitive system, or principle upon which to base one,

has been identified. Another major problem was related to the scale of the block data composer and the photodetector array. For small arrays (N~10) reliable block data composers and photodetector arrays with uniform performance that met system specifications could be acquired; however, for large arrays (N~100 to 1,000), state of the art technology could not provide the required block data composers or photodetector array. The optics were another severe test. The Fourier transform/ imaging lenses were required to yield wide-angle, flat-field, distortion-free imaging of the block data composer onto the photodetector array and, in addition, to be of large aperture. The inefficiency of space-qualified lasers and the bulk of auxiliary computers needed for control and monitoring were other negative impacts. Overall, the prospects for the near-term implementation of a 10^{12} bit spaceborne optical mass memory with no moving parts were not good in view of these considerations.

(Documentation of research and development work on the 10^{12} bit optical mass memory can be found in References 1 through 5 of Section 2. The detailed analysis and experimental data presented there provide further background relevant to our discussion up to this point.)

The probability of a successful system implementation increases dramatically if some moving parts are allowed. Constraints on the recording material, block data composer, photodetector array and optics are greatly reduced. The moving parts need only be those required for scanning and descanning holograms and transport of the recording material, which can now be on a flexible substrate. On this basis, the original BORAM concept remains a candidate approach, and other approaches became feasible. The technical effort reported in the remaining sections of this report explores these possibilities.

1.3 THE BOTTOM LINE

Important accomplishments of the HOLOMEM study were

- A detailed analysis and trade-off study of alternative system configurations for a 10^{12} bit/read/write optical mass memory with some moving parts.
- The design, fabrication, and testing of key system components: scan-descan subsystem; 128 element acousto-optic page composer; photo-detector array; and floppy disc recording medium transport
- The complete and successful end-to-end operation of a holographic recorder/reproducer that demonstrated the feasibility of a FORAM-type HOLOMEM
- A thorough experimental characterization of several read/write photo-plastic recording media with special emphasis on: diffraction efficiency; signal-to-noise ratio; number of read/write cycles; construction; and problems related to charging and development.
- The design, fabrication, and testing of a tape transport system for inline charging, exposing, and heat developing holograms dynamically recorded on photoplastic recording media.

The conclusions to be derived from the HOLOMEM study are:

- A holographic optical mass memory with some moving parts is feasible for space applications. However, significant improvements in efficiency and reliability are required of key systems components, such as the laser and the recording medium. Weight, volume, and power consumption must be further reduced.
- The performance of read/write recording media remains a problem area. Although photoplastic recording films closely simulate storage material performance for a read/write optical mass memory, performance

consistency and recyclability remain key problem areas. This effort demonstrated the feasibility of holographic recording on a read/write photoplastic system coated on a flexible substrate. However, further research and development are required to improve the overall performance of photoplastic recording films.

- The most promising approach to the implementation of a space-qualified optical mass memory is FORAM. The reasons are: best performance potential in terms of access time and storage density; the availability of most key system components; a higher probability of developing and consistently acquiring read/write recording media in a fiche format; and lowest overall risk. Independent research and development activities parallel and subsequent to this effort reinforce this conclusion.

SECTION II

HOLOMEM SYSTEM DESIGN CONCEPTS AND CONSIDERATIONS

SECTION II

HOLOMEM SYSTEM DESIGN CONCEPTS AND CONSIDERATIONS

A 10^{10} to 10^{12} bit read/write holographic memory with no moving parts is feasible only with a suitable thick phase storage media in which holograms can be spatially multiplexed with wavelength or angle discrimination during readout. A suitable thick phase material does not exist at present, and the probability that one with adequate sensitivity will be developed in the next few years is not high.

Photoplastic recording films are the best presently available recording media for read/write holographic memories. Since photoplastic recording films are inherently thin phase media with no real prospects for aerial multiplexing (volume storage), the maximum data packing densities are not much greater than 10^6 bits/cm^2. Thus, 10^{10} to 10^{12} bit memories require 10^4 to 10^6 cm^2 of useful recording area.

Systems which can access such a large data storage area without moving parts are not currently feasible. A number of alternative system approaches which involve certain mechanical translation devices offer the potential for reaching the 10^{10} to 10^{12} bit memory capacity goal with reusable photoplastic recording films as the storage material; conventional recording materials can also be used in these systems for testing and for certain applications. Four types of random-access HOLOMEM systems can be implemented at this time; they are:

1. Block-oriented with two-dimensional input and output data arrays (similar to the presently configured NASA 10^{12} bit feasibility system);
2. Tape-oriented with one-dimensional input and output data arrays (similar to the Wideband Recorder/Reproducer developed by Harris Corporation for RADC);

3. Disc-oriented with one-dimensional input and output arrays (similar to tape systems, but capable of faster random access);

4. Fiche-oriented with one-dimensional input and output data arrays (similar to tape systems).

The present status and future potential of each of these HOLOMEM system types are reviewed in this section; quantitative design examples are discussed to provide comparative data. A number of high capacity magnetic tape and disc systems are available; certain features of these systems are compared to the holographic memory systems.

Thin phase or amplitude holographic recording materials, other than photoplastic recording films which have read/write capabilities, can also be considered for the systems described here. However, other read/write recording materials are not specifically considered in the following discussions because they are, in general, quite impractical. We will indicate how such systems can be tested with photographic films. It is conceivable that the systems described here could be used with photographic films in certain applications for which off-line development is feasible.

A major goal is to design all systems with a minimum of moving parts, especially rapidly rotating components and high inertia loads operated in a reversible stop-and-go mode. Such a goal may be incompatible with requirements for rapid random access to each hologram in the memory, or even to each hologram in fairly large blocks of the full memory. The trade-offs between simple mechanical designs and rapid random access of data are therefore important ones.

The systems under consideration are intended for use on board a spacecraft. The specific environmental constraints have not been described. However, it is understood that all components of the memory must be qualified for the high acceleration associated with orbital insertion. Furthermore, the overall system must lend itself to compactness (size and weight), low power consumption, high reliability, and long lifetime. The effects

of the various memory translation mechanisms on the spacecraft dynamics must be considered. Low acceleration and low inertia are desirable features of the memory mechanics.

Key performance parameters to consider for all system types are unit (or block) capacity, total capacity, record/readout rates, and random access times (within each unit and unit-to-unit). Important considerations for the system configuration are volume, weight, power consumption, and special utility requirements (such as water or cryogenic fluids).

2.1 BLOCK-ORIENTED RANDOM-ACCESS MEMORY (BORAM)

The BORAM system design considerations have been fully documented in reports previously submitted to NASA by Harris Corporation [1-4] and in a published paper.[5] The discussion here draws on the notation and derivations presented in Reference 5. In Table 2-1 the important parameters are listed and defined. Table 2-2 summarizes key relationships.

A BORAM system of the type depicted in Figure 2-1 has a block capacity given by Q^2. That is, the amount of data in a block is the amount of data which can be randomly accessed by the components shown in Figure 2-1. Other blocks (other hologram arrays, HA's) can be mechanically translated into and out of the system. The full capacity of such a memory is

$$Q_T = N_B Q^2 \tag{2.1}$$

where N_B is the number of similar HA's that can be positioned at the record/readout station.

TABLE 2-1

BORAM PARAMETERS AND TYPICAL UNITS

Page Composer (Square)	
Number of elements in each dimension:	N
Length of each side of each element (mm):	d
Center spacings between adjacent elements (mm):	cd
Length of a diagonal (approximate for large N) (mm):	$\sqrt{2}\,Ncd$
Aperture ratio:	R_P
Hologram Array (Square)	
Number of storage locations in each dimension:	$\bar{N}$
Length of each side of each location (mm):	$\bar{d}$
Center spacings between adjacent locations (mm):	$\bar{cd}$
Length of a diagonal (approximate for large $\bar{N}$) (mm):	$\sqrt{2}\,\bar{N}\bar{cd}$
Aperture ratio:	R_H
Capacity per dimension (bits):	Q
Maximum capacity per dimension (bits):	Q_{max}
Linear packing density within each hologram (bits/cm):	ρ
Linear packing density for $Q = Q_{max}$:	ρ_{max}
Transform Lenses	
Aperture ratio (inverse of f-number):	R
Aperture ratio for $Q = Q_{max}$:	R_{max}
Power (inverse of focal length) (mm^{-1}):	K
Focal length (mm):	f
Magnification from PC to PDA:	M
Laser	
Wavelength (nm):	λ
Output power for readout (mW):	P_o
Output power for recording (mW):	P_i
Duty factor for readout:	α
Duty factor for recording:	$1-\beta$
Other Parameters	
Average readout rate (Mb/s):	ν_o
Average readin rate (Mb/s):	ν_i
Photodetector sensitivity (Joule/bit):	S
Hologram diffraction efficiency:	η_h
Transmissivity of the system optics from the laser to the beamsplitter:	η_o
Transmissivity of reference/readout path:	η_r
Transmissivity of signal path:	η_s
Fraction of power in the full Gaussian beam profile used for system illumination:	η_g
Ratio of reference beam intensity to signal beam intensity at the HA:	Z
Sensitivity of the recording material ($Joule/cm^2$):	E_o
Time interval to read a page of data:	τ_o
Time interval to record a page of data:	τ_i

TABLE 2-2

BORAM KEY DESIGN RELATIONSHIPS

$$R_p = \sqrt{2}\ NcdK$$

$$R_H = \sqrt{2}\ \bar{N}\bar{c}\bar{d}K$$

$$R = R_p + R_H \left|\frac{M}{M-1}\right|$$

$$R_{max} = 2\sqrt{2}\ NcdK$$

$$Q = (R - \sqrt{2}\ NcdK)\frac{N}{\sqrt{2}\ \bar{N}\bar{c}\bar{d}K}\left|\frac{M}{1-M}\right|$$

$$Q_{max} = \frac{R^2\left|\frac{M}{M-1}\right|}{8\,cd\,\bar{c}\bar{d}K^2} = \frac{R^2\left|\frac{M}{M-1}\right|}{16\,\bar{c}\,\lambda K}$$

$$\bar{d} = \frac{2\lambda}{cdK}$$

$$\rho = \frac{N}{\bar{d}} = \frac{NcdK}{2\lambda}$$

$$\rho_{max} = \frac{R_{max}}{4\sqrt{2}\,\lambda}$$

$$\tau_c = \frac{N^2}{\nu_o}$$

$$\tau_i = \frac{N^2}{\nu_i}$$

$$P_o = \frac{S\nu_o}{\alpha\eta_h\eta_o\eta_r\eta_g}$$

$$P_i = \frac{E_o\,\nu_i\,(\eta_s Z + \eta_r)}{(1+Z)\,\eta_r\eta_s\eta_o\eta_g\,(1-\beta)\rho^2}$$

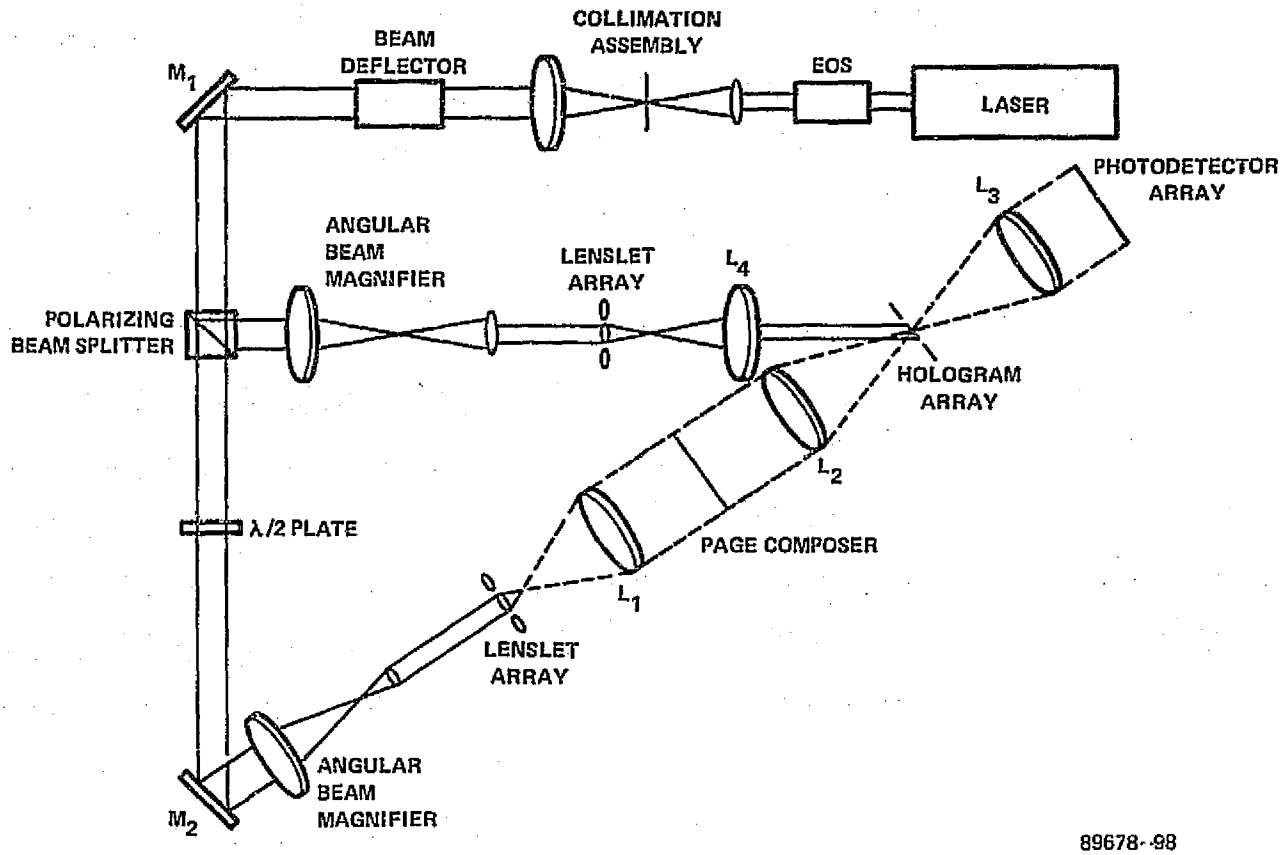

FIGURE 2-1. BASIC CONFIGURATION OF A BLOCK-ORIENTED RANDOM-ACCESS MEMORY (BORAM)

2.1.1 Status of Key BORAM Components

2.1.1.1 Page Composer (PC)

A 32 x 32 element PC of PLZT with cd = 0.254 mm and d = 0.127 mm was fabricated. This PC has been available for testing in a NASA feasibility system since early 1974. Plans to design and fabricate a 128 x 128 element PC of PLZT (with identical cd and d) were advanced as part of the goals of a past program effort (Contract NAS 8-26672). Certain PLZT material properties, however, must improve before such PC's will become practical. In particular, the electro-optic characteristics from point-to-point in any selected slice must be more uniform and batch-to-batch repeatability must be improved.

Instantaneous data loading rates up to 1.0 Mb/s are feasible with a 128 x 128 element PC of PLZT. This rate can be increased only by increasing the number of elements in each row with row-at-a-time readin.

A particular appeal of PLZT is that a PC will function for a reasonable range of incident angles (such as $\pm 10^{o}$) in both dimensions. Signal beam deflection can be used to steer the beam to the various HA positions. Deflection angles are constrained to much smaller angles with many other electro-optic and acousto-optic PC approaches, although deflection in one dimension is allowed with acousto-optic PC's.

The fact that a fully operational PLZT PC has not been demonstrated after several years of research and development must be considered in assessing the potential of the BOROM system approaches. Any BORAM system will require such a two-dimensional, multielement PC.

2.1.1.2 Photodetector Array (PDA)

A 32 x 32 element PDA with cd = 0.254 mm has been installed in a NASA feasibility breadboard. The recent advances in this technology indicate that a satisfactory

128 x 128 element PDA can be fabricated in the near future. Alternative approaches, including charge-coupled device technology, are rapidly emerging and should be considered in assessing BORAM system potential. Readout rates in the 1 to 10 Mb/s range are feasible.

2.1.1.3 Hologram Array(HA)

A 5 x 5 position HA with corona charging of a photoplastic recording film is presently in use in a NASA feasibility breadboard. A 10 x 4 position array with parallel plane charging was installed in 1974. Difficulties related to heating only one pad at a time must be overcome in the fabrication of larger arrays.

Sensitivities of photplastics in present HA's are about 75 $\mu J/cm^2$, which is comparable to Kodak 649-F high resolution film. Lifetime is a function of several parameters, including type of thermoplastic, sensitizer concentration, exposure to oxygen (ozone) during the charging and heating cycles, and erase pulse power. Packing densities of 2×10^6 bits/cm^2 are achieved at 13.5 dB SNR with sensitization for 75 $\mu J/cm^2$ exposures. With corona charging, practical charge-expose-develop-erase cycle times are about 5 seconds. With parallel plane charging, cycle times are shorter, but the long I^2R heating for erasing still dominates. Cycle times in the 10 to 100 ms range are considered feasible with parallel plane charging and heating for erasure by a pulsed infrared laser beam (possibly CO_2 or Nd: YAG).

The size of each data block with a 20 x 20 HA and a 128 x 128 PC is $Q^2 = 6.6 \times 10^6$ bits.

2.1.1.4 Lenses for Signal Transformation and Imaging

The lenses presently in the NASA feasibility breadboard which form a Fourier transform of the PC at each HA position and subsequently image the PC onto the PDA are inadequate for a full data block. Bit shifting at the PDA is excessive for bits in the PC farthest from the optical axis when positions near the edges of the HA are used. By either limiting the PC aperture or using only the innermost group of positions in the HA, it is possible to use existing lenses for system experiments.

Designs have been completed for lenses which will perform acceptably for block sizes of 6.6×10^6 bits and 2.5×10^7 bits. (1) The design of lenses for a 10^8 bit block size has been considered. (1) While it is possible to design and fabricate such lenses, the lens apertures are in the 140 to 325 mm range with separations between the PC and PDA of from 0.85 meter to 2.0 meters. At present, we conclude that even if all other system components function ideally, the maximum block size will be constrained to less than 10^8 bits by the design of such lenses.

2.1.1.5 Hologram Random Accessing

The X-Y AOBD presently in use in the feasibility system permits random access to any of at least 20 x 20 positions in the HA. Random access times are 4 μs, less for reduced resolution operation. The measured overall optical efficiency of the AOBD is 25 percent at 488.0 nm and 35 percent at 647.1 nm. The full useful bandwidth of each of the two orthogonal cells is 40 MHz. The deflected reference beam must be at least triple-Rayleigh resolved to provide adequate control of the amount of light which illuminates adjacent holograms.

A key performance feature of the AOBD is the stability of the deflected beam position during hologram exposure and during readout. To prevent fringe smearing during exposures, the frequency of the drive signals must not vary by more than 0.1

percent. To guarantee that reconstructed bits do not wander too far from the center of each corresponding photodetector during readout, the frequency stability must also be 0.1 percent. Such a stability requirement is met for each of the two cells in the present system by controlling voltages to VCO's that are thermally stabilized. A modifiable look-up table in the computer is used to record the appropriate voltages which correspond to each position to be accessed.

Both digital and analog controlled oscillators can be built which are stable to 0.01 percent over the required bandwidths; considerable thermal stabilization is essential for open-loop operation. If suitable error signals can be generated, improved stabilization is possible in a closed-loop mode. One possible way to produce an error signal would be to include a photodetector at each HA position. With closed-loop frequency stabilization, other factors which affect the position of the deflected beam (such as thermal gradients or air turbulence in the light transmission paths) could also be compensated.

2.1.1.6 Laser

The NASA feasibility breadboard includes a CRL Model 52 argon laser optimized for single axial mode operation at 514.5 nm. This CW laser is capable of providing over 400 mW with a TEM_{oo} transverse mode structure (a Gaussian beam profile). Exposure control is provided by an electro-optic modulator, which operates in conjunction with a Glan-air prism beam splitter and a half-wave plate to establish the required reference-to-signal beam intensity ratio at the HA.

With a PDA which requires 5 to 10 x 10^{-12} joule/element for positive detection, we find that the required laser output power is in the 20 to 200 mW range for practical optical efficiencies, hologram diffraction efficiencies of $\approx$ 0.01, and for a 10^6 bit/sec output data rate with a 50 percent duty on the laser output (α = 0.5).

For a photoplastic sensitivity of 75 $\mu J/cm^2$, a 10^6 bits/cm^2 packing density, and an exposure time of 8 ms, we find that the required laser output power is in the 40 to 400 mW range, depending on optical efficiencies and on the fraction η_g of the Gaussian beam profile used for illuminating the PC in the signal path and the HA in the reference path. The 8 ms exposure time will permit 10^6 bit/second average record rates with a 50 percent duty ($\beta = 0.5$).

The present CRL Model 52 argon laser operates at an overall power efficiency of $\eta_L = 3.7 \times 10^{-5}$ and requires $P_L = 11$ kW of three-phase power plus cooling water (2.5 gallons/minute at a maximum inlet temperature of 40° C). It is conceivable that an argon laser which supplies sufficient power for recording and readout at 10^6 bits/sec and requires less than 1 kW of prime power could be built for a BORAM system.

It is also conceivable that a helium-neon laser ($\lambda = 632.8$ nm) could be used. The system parameters would have to be modified accordingly; see Table 2-2. A commercial Spectra-Physics Model 125A laser supplies over 50 mW with a maximum of 450 watts of prime power ($\eta_L \geq 10^{-4}$); it does not require forced air or water for cooling.

2.1.2 Potential of the BORAM Approach

An assessment of the risks involved in developing the key components of a 10^7 bit/block BORAM system is presented in Table 2-3. The component parameters given in Table 2-3 were calculated with the equations in Table 2-2 and Reference 5 by selecting,

$$Q = Q_{max}$$

$$R = 0.4$$

$$N = 128$$

TABLE 2-3

KEY BORAM COMPONENTS AND DEVELOPMENT RISKS
FOR A 10^7 BIT BLOCK SIZE

Component Parameters		Risk
Hologram Array		
$\overline{N} \times \overline{N} = 25 \times 25$		
$\overline{c}$	$= 1.5$	Moderate
$\overline{d}$	$= 0.93$ mm	
$\rho 2$	$= 1.9 \times 10^6$ b/cm^2	
$\overline{Ncd}$	$= 34.9$ mm	
Page Composer/Photodetector Array		
$N \times N = 128 \times 128$		
c	$= 1.5$	High/Moderate
d	$= 0.18$ mm	
Ncd	$= 34.6$ mm	
Transform Lenses		
M	$= -\infty$	
R	$= 0.4$	
f	$= 244$ mm	Low
D	$= 97.6$ mm	
λ	$= 514.5$ nm	

TABLE 2-3

KEY BORAM COMPONENTS AND DEVELOPMENT RISKS FOR A 10^7 BIT BLOCK SIZE (CONTINUED)

Component Parameters		Risk
Acousto-Optic Beam Deflector		
$\overline{N} \times \overline{N} = 25 \times 25$		
τ_{bd}	= 5 μs (random access time)	Low
B	≤20 MHz (bandwidth)	
η_{bd}	≥0.5 (diffraction efficiency)	
Laser		
λ	= 514.5 nm (argon)	
P_o	= 66 mW	
	$\alpha = 0.5$, $S = 10^{-11}$ Joule/detector,	
	$\nu_o = 10^6$ b/s, $\eta_h = 0.01$, $\eta_o \eta_r \eta_g = 0.03$	
P_i	= 20 mW	
	$\beta = 0.5$, $E_o = 75\,\mu J/cm^2$,	Low
	$\nu_i = 10^6$ b/s, $\eta_s = 0.01$,	
	$\eta_o \eta_r \eta_g = 0.03$, $Z = 10$, $\eta_r = 0.75$	
η_L	≤10^{-4} (overall efficiency)	
P_L	≥660 Watts (input power)	

NOTE: A helium-neon laser ($\lambda = 632.8$ nm) could be used; such a laser can be 2 to 4 times more efficient.

$M = -\infty$

$\lambda = 514.5$ nm

Other parameters assumed for the laser power calculations are noted in Table 2-3. Note that the packing density in each hologram is $\rho^2 = 1.9 \times 10^6$ bits/cm^2 and that the assumed input and output data rates are $\nu_i = \nu_o = 10^6$ b/s. By setting $Q = Q_{max}$, we also guarantee that the overall size of the PC and the HA are the same; both are about 49 mm x 49 mm. It is assumed that a matched pair of transform lenses is used between the PC and the PDA to achieve unity magnification between these planes; the overall PDA size is also 49 mm x 49 mm.

2.1.2.1 Page and Block Access Times

The AOBD is designed for a 5 μs random page access time within each block. Block-to-block access times will depend on how the memory is organized. At one extreme, each block might be inserted by the user into the BORAM. A modification of this approach would be to position several similar HA's on a disc which could be inserted by the user. Step-wise access times to any HA on the disc would be of the order of one second. Many discs, each with several HA's on them, could then be available to the user for inserting into the memory. Mechanical means for automatically accessing and loading individual HA's or HA-disc's into the memory can also be designed. Unit access times of 10 to 30 seconds would be typical.

For an average data transfer rate of 10^6 b/s into and out of the memory, the cycle time for each page is $\tau_i = \tau_o = N^2/\nu_i = 16.4$ ms. A random page access time of ten percent of this interval would not severely compromise net data transfer rates, especially if instantaneous transfer rates could be increased by a similar percentage, and if page rather than word access is employed. The 5 μs random access time to pages in a block provided by the AOBD in the 10^7 bit/block BORAM can only be justified if word

access is essential. Alternative beam deflection approaches which can randomly access pages in 1 to 2 ms can be considered if word access is not required. Galvanometer driven mirrors are candidates. A key point to note is that random access times of several microseconds are not essential to achieve average data transfer rates of 10^6 b/s if full pages are read after each access.

2.1.2.2 Component Development Risks

The highest risk component is the PC. A significant risk factor must also be assigned to the HA and to the PDA.

The key problems with PC development which lead to an assignment of high risk (see Table 2-3) were discussed in the previous section.

The risks with the HA are largely related to uniformly developing and erasing the $\overline{N} \times \overline{N}$ storage pads. Either a complex heating electrode structure is required, or new techniques must be developed to heat the pads with a deflectable pulsed infrared laser beam. A photoplastic-substrate combination which absorbs sufficient infrared radiation for heating while transmitting a high percentage of the readout light must be developed. The photoplastic layers are typically 1 to 2 μm thick. The preparation of a 1 to 2 μm photoplastic layer on a suitable substrate which absorbs strongly in the near infrared (say, at the 10.6 microns wavelength from a CO_2 laser), which has a good recording sensitivity in the visible (say at 514.5 nm), and which exhibits a reasonable net diffraction efficiency during readout involves considerable development and at least moderate risk.

One important parameter of the PDA is element center spacings. Spacings on the order of 0.20 to 0.25 mm are desirable in the PC to achieve a high packing density. With unity magnification from the PC to the PDA, such center spacings are required in the PDA. With the PDA design approach used for the present 32 x 32

element unit, such center spacings are achievable. With other technologies - in particular, CCD technology - such a requirement will be difficult to meet. Magnifications other than unity from PC to PDA may be required with such alternative approaches. The moderate risk factor assigned to the PDA in Table 2-3 takes into consideration that a 128 x 128 element PDA with 0.20 to 0.25 mm centers has not yet been built, and accounts for the fact that little emphasis in the new technologies has been placed on applications of this type (digital image sensing).

2.1.2.3 10^8 Bit/Block Design

A memory system with 10^8 bits/block requires considerably more development and design activity on the HA and the transform lenses, and it requires a higher resolution beam deflector. The element dimensions for the PC and the PDA will be larger. The laser requirements will not change much, if at all.

We briefly consider a 10^8 bit/block design which begins with the same assumptions given at the beginning of Paragraph 2.1.2. The results of these calculations are presented in Table 2-4. The HA size increases to 79 x 79 hologram positions, but the size per position is unchanged. This increase leads to a high risk factor, rather than moderate. The element sizes for the PC and the PDA increase to 0.568 mm with 0.852 mm centers. This increase will make the fabrication more difficult because larger plates of PLZT are required. However, the larger elements are easier to form and edge effects are less of a problem, if adequate large area uniformity can be achieved.

The larger transform lens will clearly be more difficult to fabricate. The clear aperture must be 309 mm, or over 12 inches. The overall space-bandwidth product must be close to 5×10^8 resolution elements to accommodate the 10^8 double-Rayleigh resolved bits plus guard bands and the $\sqrt{2}$ factor for the PC diagonal. The high risk

TABLE 2-4

KEY BORAM COMPONENTS AND DEVELOPMENT RISKS FOR A 10^8 BIT BLOCK SIZE

Component		Risk
Hologram Array		
$\overline{N} \times \overline{N} = 79 \times 79$		
$\overline{c}$	$= 1.5$	High
$\overline{d}$	$= 0.93$ mm	
ρ^2	$= 1.9 \times 10^6$ b/cm^2	
$\overline{Ncd}$	$= 110$ mm	
Page Composer/Photodetector Array		
$N \times N = 128 \times 128$		
c	$= 1.5$	High/Moderate
d	$= 0.568$ mm	
Ncd	$= 109$ mm	
Transform Lenses		
M	$= -\infty$	
R	$= 0.4$	
f	$= 772$ mm	High
D	$= 309$ mm	
λ	$= 514.5$ nm	
Acousto-Optic Beam Deflector		
$\overline{N} \times \overline{N} = 79 \times 79$		
τ_{bd}	$= 5$ µs	Low
B	≤ 64 MHz	
η_{bd}	$= 0.5$	

89678-71

factor assigned to this component reflects these rather severe performance and fabrication requirements.

The AOBD must access 79 x 79 positions. This requirement is still well within the present state of the art and is not considered too risky.

The major differences between the designs for the 10^7 and 10^8 bit/block BORAMS are the larger HA and transform lenses. If all technical problems associated with the HA, the PC, and the PDA could be overcome, the design and fabrication of the transform lenses would limit the capacity of a BORAM block to less than 10^8 bits.

2.1.2.4 Volume and Weight Requirements

Each block of 10^7 to 10^8 bits could consist of a multilayered structure containing glass, the active coatings (including the photoplastic), and a mounting structure which holds the plates in the proper arrangement. For a 10^7 bit block size, typical dimensions of the HA block using glass substrates are:

$$V_7 = 45 \text{ mm} \times 45 \text{ mm} \times 10 \text{ mm}$$

$$V_7 = 20.25 \times 10^3 \text{ mm}^3 = 20.25 \times 10^{-6} \text{ m}^3.$$

A minimum volume which contains 10^5 such blocks for a 10^{12} bit memory would be

$$V_{12} = 10^5 V_7 = 2.025 \text{ m}^3 = 71.5 \text{ ft}^3.$$

The overall system volume would be in the 150 to 200 ft^3 range, including the controller, all electronics, and the block accessing mechanism.

Suppose that each block consists of two glass plates each 42 mm x 42 mm x 1.5 mm, plus aluminum mounting hardware to about 10 mm x 2 mm x (4 x 45 mm). The density of glass is 2600 kg/m^3 and of aluminum is 2700 kg/m^3. Using these figures, we

find that each block would weigh

$$W_7 = 0.0295 \text{ kg}.$$

All 10^5 blocks of this type would weigh,

$$W_{12} = 2950 \text{ kg} = 6490 \text{ pounds}.$$

A complete 10^{12} bit system of this type would weigh from 9,000 to 12,000 pounds.

The weight and volume parameters estimated above are for a system which permits each element in the HA to be individually developed and erased while in place in the BORAM. Suppose that a system could be configured such that development and erasure could take place at a position remote from the read/write station. Further suppose that the data can be recorded on a photoplastic which is deposited on a flexible substate such as acetate, which has a density of 1300 kg/m^3. Assume that 2 x 4 = 8 blocks of 10^7 bits are on a 100 mm x 150 mm x 0.175 mm chip of acetate. The total volume of memory material is then

$$V'_{12} = 0.0328 \text{ m}^3 = 1.16 \text{ ft}^3,$$

and the weight of 10^{12} bits stored on 12,500 such chips is,

$$W'_{12} = 43 \text{ kg} = 95 \text{ pounds}.$$

A total memory system of this type would occupy a total volume in the 120 to 160 ft^3 range, and it would probably weigh from 2,500 to 4,000 pounds.

The volume and weight figures for the 10^8 bit/block BORAM will not differ significantly from the numbers given above. The basic optical system, particularly the lens apertures and focal lengths, is larger and will weigh a few hundred pounds more.

2.1.2.5 Power Consumption

An important item in estimating the total memory power requirements is the laser. As noted earlier (see Table 2-3), it is possible that a special argon-ion laser can be designed which requires under 1,000 watts, assuming a 128 x 128 element PDA and PC, 10^6 bits/cm^2 packing density, 10^6 b/s average transfer rates, 75 μJ/cm^2 photoplastic sensitivity, and 5×10^{-12} Joule/detector PDA sensitivity. Such a laser would be adequate for any block size as long as the parameters cited above are not altered. The possibility of using a more efficient helium-neon laser must also be considered.

Other key power consuming elements will be the motors which move blocks in and out of the read station and the electronics (possible including a small computer) which control and drive the system components. Part of the memory system power budget may have to be allocated to the pumps which provide cooling water for the laser (if water is needed) and to the heat transfer system which removes heat from this water.

Overall power requirements for a 10^{12} bit BORAM system are estimated to be in the 3,000 to 6,000 watt range.

2.1.3 Technology Development

The above considerations outline certain technological activities which must be pursued in order to develop a BORAM system with a block size of 10^7 to 10^8 bits and mechanical means for inserting 10^4 to 10^5 blocks into the record/readout position (the HA position in Figure 1). In particular, fabrication procedures for larger HA's must be improved, or else new techniques for heating the pads must be developed. The material uniformity and device fabrication difficulties with PLZT for the PC must be overcome.

If a block size close to 10^8 bits is required, the design and fabrication of the transform lenses will demand special attention. A 128 x 128 element PDA with

appropriate element center spacings, sensitivities, and overall readout rates must be developed in parallel with the PC and HA development activities.

For a power-limited spacecraft environment, a maximum efficiency laser is clearly important. The specifications for a laser which meets all of the requirements of a BORAM system must be defined, and a laser which meets these specifications should be developed. Strong emphasis should be placed on efficiency and on minimizing utility requirements (water or air). Semiconductor laser technology is advancing steadily. The overall efficiencies of such lasers can approach 10 percent at 900 nm and are still near 1 percent at visible wavelengths (particularly near 600 nm). However, certain key problems still must be overcome before these devices can be considered for any read/write holographic memory system. In particular, the coherence of such lasers is inadequate for these systems. Coherence lengths are typically less than 0.1 mm, and divergence angles are 2 to 20 degrees and asymmetric. Furthermore, the energy per pulse available from a single laser diode is typically only a few tens of microjoules, which is about 10 times lower than required for the BORAM approaches. For certain of the tape-oriented approaches, this much energy might be enough. Considerable improvement will be required in such performance parameters before laser diodes can be considered for these systems.

Mechanisms for block access require further development. One or two promising approaches could be breadboarded and tested. In particular, a technique which uses X or X-Y slide translators merits attention. Such an accessing technique could be incorporated into an existing feasibility breadboard for testing.

2.2 TAPE-ORIENTED RANDOM-ACCESS MEMORY (TORAM)

A system for recording wideband data in the form of one-dimensional holograms on 35 mm roll film has been developed for the Air Force (RADC) at Harris Corporation.[6-9] An Exploratory Development Model of such a system capable of

recording data at 600 Mb/s and also reproducing it at 600 Mb/s has been constructed.[6] Many of the Wideband Recorder/Reproducer System concepts can be adapted to the NASA Holographic Memory (HOLOMEM) system requirements.

The read/write material with this system approach would be in the form of a flexible tape which has an appropriate photoplastic coating. Considerable development will be required to perfect such a read/write storage material (see Section IV). In the interim, conventional photographic films could be used to perform sytem tests. A tape transport system will translate the tape (or film) through the record station. The tape may be spooled on reels or in special cassettes. As shown in the discussion which follows, the amount of data per tape will be much larger than 10^8 bits for reasonable tape lengths. A key trade-off is random access time to any position on a tape versus tape length. The design of the tape transport must be considered in making this trade-off.

2.2.1 Basic System Configuration

The basic design for a TORAM system is shown in Figure 2-2. The film drive assembly shown would be designed as a photoplastic tape transport which could also be adapted for photographic film.

In Figure 2-3, more detail of the basic configuration is shown; the beam-forming optics for the signal and reference beams are not shown for sake of clarity. Lenses L_9 and L_{10} in Figure 2-3 are the transform lenses. The beam deflector (spinner, galvanometer mirror, or other devices) is not shown in Figure 2-3; it would be near plane P8 where an image of the PC and the reference beam source is formed. The film or tape is translated upward in the Top View. The anamorphic optical system forms a Fourier transform of the PC in the plane of the Top View and an image of the PC in the Side View at the film. This arrangement is required to maintain a high packing density (narrow holograms) in the across-track dimension. The spatial invariance property is

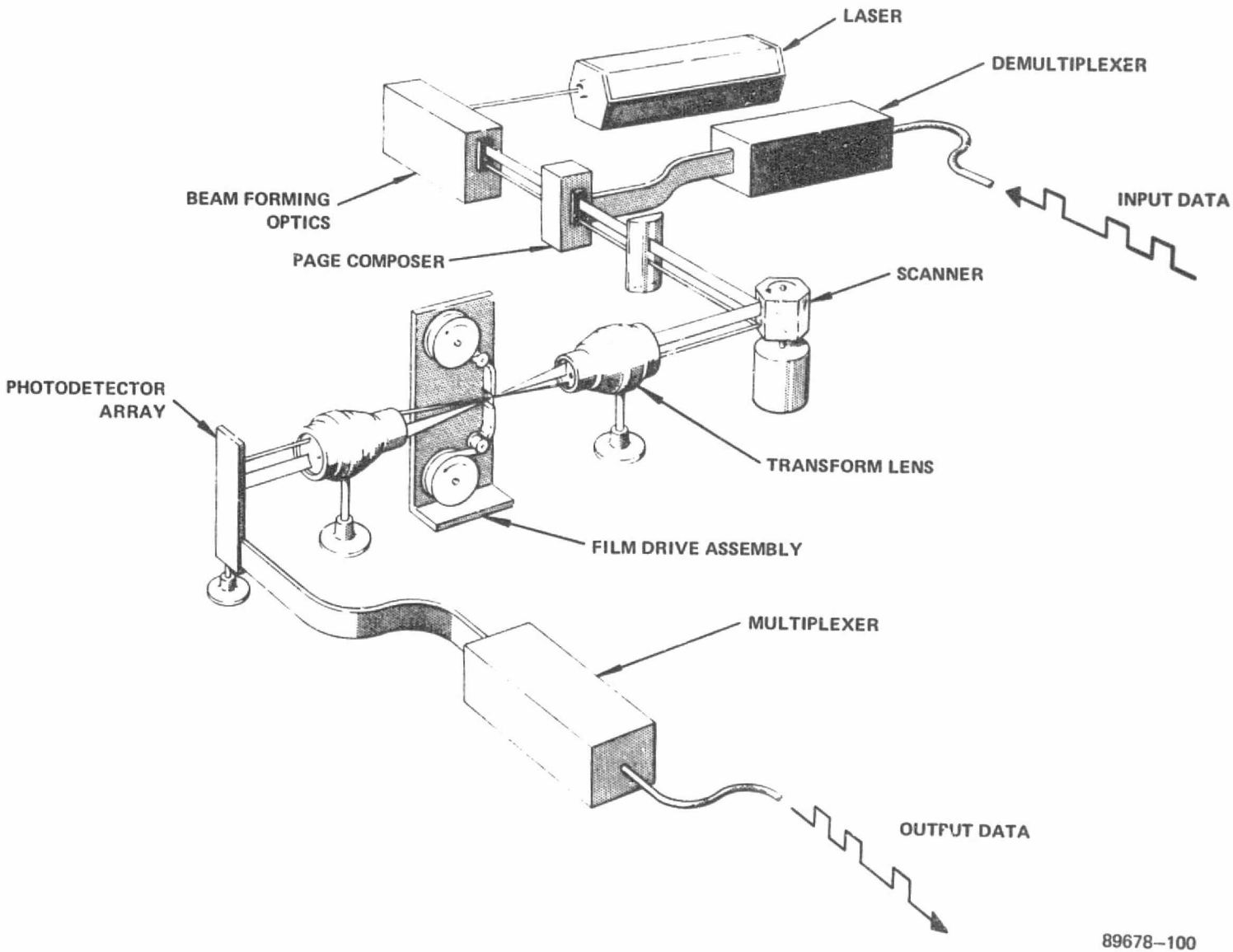

FIGURE 2-2. BASIC CONFIGURATION OF A TAPE-ORIENTED RANDOM-ACCESS MEMORY (TORAM)

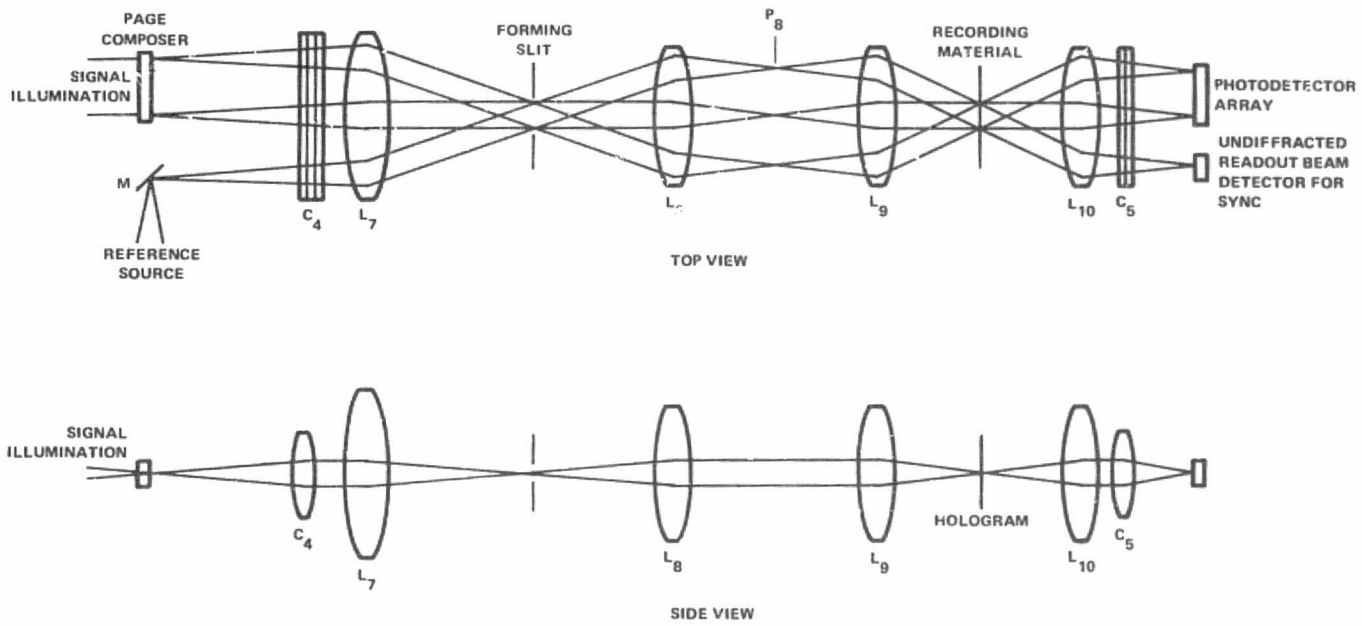

FIGURE 2-3. DETAILS OF THE ONE-DIMENSIONAL HOLOGRAM RECORD/READOUT OPTICS (THE SCANNER IS OMITTED FOR CLARITY)

still effective along the data at the PDA. Means for precisely synchronizing the sampling of the PDA with film and spinner motion can be implemented to guarantee that the correct hologram is being reconstructed onto the PDA at any instant during a readout cycle. One approach which has been used to maintain this synchronization is indicated in Figure 2-3. The undiffracted light during readout is sampled by a single photodetector near the PDA. This signal is at a minimum when the readout beam fully overlaps a hologram and reaches a maximum when it is centered between adjacent holograms.

Most of the equations listed in Table 2-2 for the BORAM approach can either be used directly or modified slightly and used for the TORAM approach. The applicable parameters defined in Table 2-1 can also be used here. The packing density in the dimension parallel to the data is given by

$$\rho_x = \frac{Ncd'K}{2\lambda} = \frac{R_x}{2\lambda} \tag{2.2}$$

where d' is the size of an input bit in the image of the PC at the input to the transform lens and R_x is the focal power of the transform lenses in this dimension. In the other dimension,

$$\rho_y = \frac{1}{\delta_y} \tag{2.3}$$

where δ_y is the center spacing between holograms; a δ_y of 15 μ is typical. Therefore, the two-dimensional packing density is,

$$\rho^2 = \rho_x \rho_y = \frac{Ncd'}{2\lambda\delta_y f} \tag{2.4}$$

where we used K = 1/f. The film velocity is given by,

$$V_f = \frac{\nu}{W_f \rho^2} \tag{2.5}$$

where W_f is the active film width (the portion which contains data) and ν is the readin or readout rate. We can also write,

$$W_f \doteq M \delta_y \tag{2.6}$$

where M is the number of holograms per track across the film width; M $\approx$ 1500 for a 35 mm film format. A number of design relationships for the spinner are summarized in Table 2-1 of Reference 6.

2.2.2 Data Distribution

The tape transport permits holograms to be distributed along the tape. Data can be distributed across the tape width in several ways. A multifaceted spinning mirror is shown in Figure 2-3. Such a component is essential for achieving high recording rates. However, a galvanometer mirror could replace the spinner in a TORAM system designed for NASA. In either case, the one-dimensional holograms would be distributed across the tape as shown in Figure 2-4. There would be from 500 to 1500 holograms along each track across the tape width, and successive tracks would be separated by 1.0 to 1.5 mm along the tape (parallel to the direction of tape translation).

It is even possible that the data could be distributed across the film width by mounting the tape transport on a fixture which steps the film perpendicular to film motion. In this configuration the one-dimensional holograms would be aligned parallel

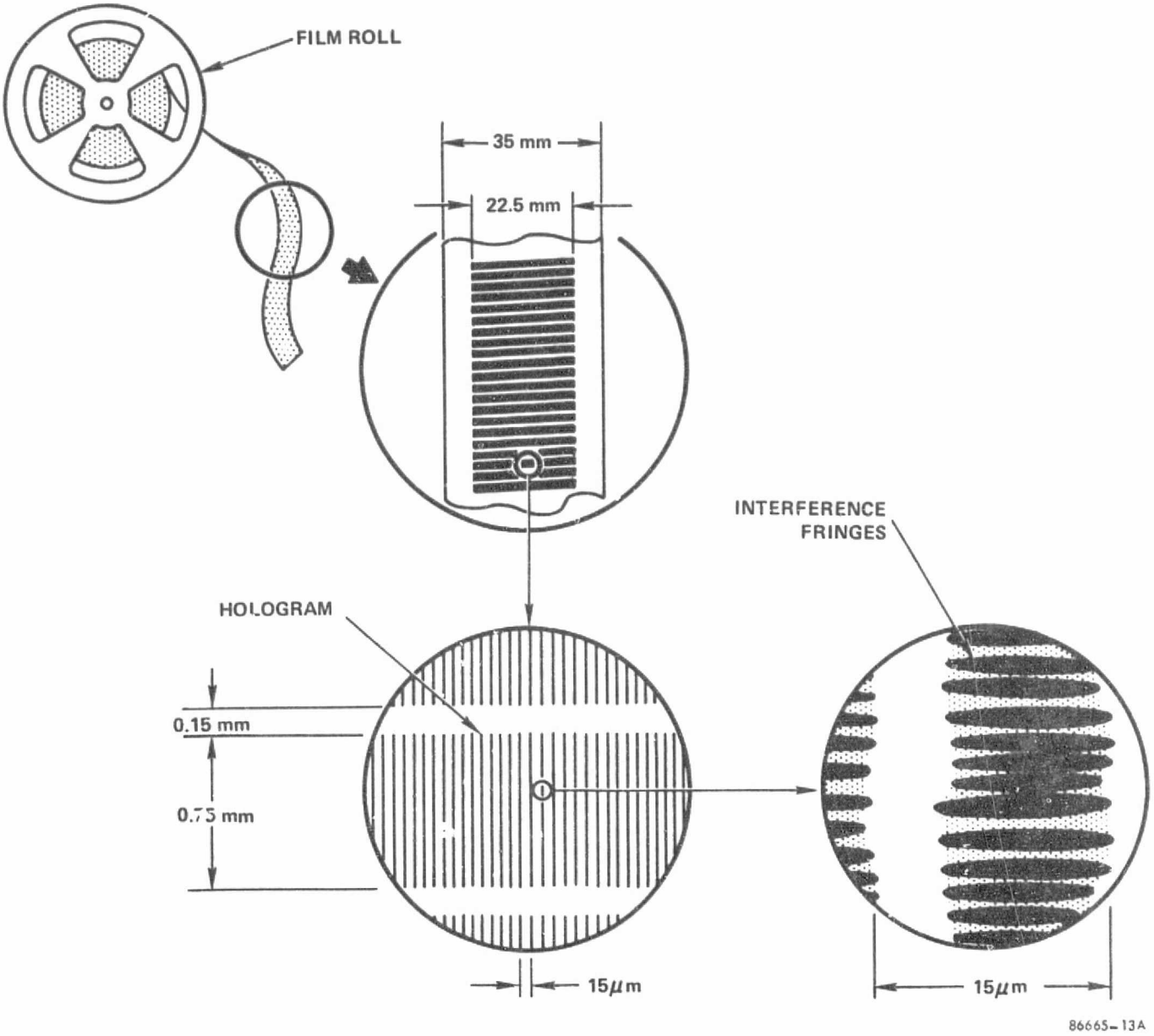

FIGURE 2-4. REPRESENTATIVE TORAM DATA FORMAT WITH ONE-DIMENSIONAL HOLOGRAMS

to the film width dimension, and about 25 tracks would be distributed across the film width. This approach is referred to as incremental transverse tape translation (ITTT).

Important trade-offs between this type of across-track distribution and those types with moving mirrors can be cited. With moving mirrors, every hologram can be recorded or accessed as the tape is translated once through the read station. With ITTT, only those holograms in any one track can be recorded during one full tape wind cycle. As many as 25 wind-rewind cycles would be required to fill the tape with data. Tape and transport wear would be much more of a problem in this case. Once the data is recorded, any word or small block of data on any one track could be accessed with about the same access time with either approach. However, a readout or erasure of the full tape contents would require many wind-rewind cycles with ITTT. The transform lenses required for the moving mirror approach must have a larger space-bandwidth product along the scanning dimension (as high as 5000 for 1500 well-resolved holograms per film width). With the ITTT approach, the lens requirements can be very modest; off-the-shelf lenses can even be considered.

2.2.3 Description and Status of Key TORAM Components

From Figure 2-2, the key components of a TORAM system can be identified. These and other system components are listed below:

1. Laser (e.g., an argon-ion at 514.5 nm)
2. Beam-forming optics (signal and reference)
3. Linear acousto-optic page composer (with 128 elements)
4. Across-film hologram distributor (moving mirror or ITTT)
5. Transform lenses
6. Tape transport
7. Photoplastic tape

8. Photodetector array (128 elements)
9. Acousto-optic light modulator for exposure control
10. Acousto-optic beamsplitter for frequency shift compensation, Z-ratio control, and beam position correction during readout
11. Data handling and control electronics (including MUX/DEMUX hardware)

2.2.3.1 Status Overview

Items 2, 9, 10, and 11 in the list above are quite conventional and require no special attention. Significant differences in the requirements for TORAM components compared to corresponding components for a Wideband Recorder/Reproducer will be identified and discussed in subsequent paragraphs.

2.2.3.2 Laser

At a 400 Mb/s input rate and with a photographic film which has a sensitivity of 1.4 $\mu J/cm^2$, the argon-ion laser in the Wideband Recorder/Reproducer must supply about 100 mW of CW power to record data at a 10^6 bit/cm^2 packing density. A Coherent Radiation Model 52 argon-ion laser is in use in the Phase I Wideband Recorder System (~1.0 watt output at 514.5 nm is available). We can translate these requirements to those of a TORAM system by assuming: 1) a 10^6 bit/s instantaneous record rate, 2) a photoplastic tape sensitivity of 75 $\mu J/cm^2$, 3) a packing density of 10^6 bits/cm^2, and 4) an overall optical system efficiency of $\eta_T = 0.02$ (the same as for the Wideband Recorder/Reproducer). With these parameters we find that the laser must supply about 13.5 mW for recording. It should be noted that this estimation allows a hologram exposure time of 26 μs, which corresponds to a laser duty factor of 26/128 = 0.2 (the same as for the Wideband Recorder/Reproducer). This constraint must be applied to limit smearing of the hologram during the exposure while the tape is moving. The smearing

is parallel to the holographic fringes so that fringe contrast is not degraded by the motion, but the hologram width is enlarged slightly.

For readout, we can use the expression for P_o in Table 2-2 with the following parameters:

$$S = 10^{-12} \text{ Joule/detector}$$

$$\nu = 10^{6} \text{ bit/s}$$

$$\alpha = 0.5$$

$$\eta_h = 0.01$$

$$\eta_o \eta_r \eta_g = 0.03$$

With these, we obtain $P_o = 6.7$ mW. The ten times lower value for S for the TORAM compared to the BORAM is consistent with the fact that the light integration time is over 100 times shorter for 128 bits/hologram compared to 128 x 128 bits/hologram. If the full power of the system laser (13.5 mW required for recording) is used, better SNR can be achieved.

A commercial argon-ion laser (the Spectra-Physics Model 162) can conceivably meet the requirements estimated above. This laser requires about 1000 watts of prime power and forced air cooling. A more efficient helium-neon laser might be a better choice, although some packing density may have to be sacrificed or else the focal power of the lenses may have to be increased. A Spectra-Physics Model 124A laser supplies over 15 mW with a maximum of 125 watts of prime power ($\eta_L \geq 10^{-4}$) without forced air cooling.

Higher input and output rates can be achieved with a correspondingly larger laser. For example, a 0.5 watt argon-ion laser can provide enough power for recording at 37 Mb/s and readout at 75 Mb/s. Prime power requirements are increased proportionately.

2.2.3.3 Page Composer

A linear array of 134 acousto-optic modulators spaced on 0.25 mm centers with 0.125 mm modulating element heights has been fabricated for the Wideband Recorder; this device is shown in Figure 2-5. This pc is formed with SF-8 dense flint glass (the acousto-optic material) to which a single large lithium niobate electro-acoustic transducer is bonded. The transducer is polished to a thickness in the 20 to 25 μ range, which corresponds to a piezoelectric resonance frequency near 140 MHz. The 134 channels are defined by evaporating 134 independent electrodes onto the exposed transducer surface through a mask in vacuum. Electrical contact to each independent electrode is achieved by attaching a printed circuit card, with a special matching pattern, to the transducer face of the glass block. A second vacuum evaporation step forms an electrical bridge between each transducer electrode and the corresponding electrode on the printed circuit card.

The diffraction efficiency of each element is $\eta_{pc} = 0.5$ with 0.25 watt of RF drive power at 140 MHz. The upper limit on drive power per element depends on the duty factor for holographic exposures. At 100 percent duty, 0.25 watt per element may overheat the glass. At a more typical 50 percent duty, this is not expected to be a problem, and $\eta_{pc} = 0.5$ can be achieved.

Only 128 of the 134 available modulators in the pc are connected to data channels. The other six may be used to include housekeeping information with each recorded hologram.

A linear pc of this type could be incorporated into a TORAM system without modifications. Per channel data rates of over 5 Mb/s (instantaneous) can be achieved; 15.6 Kb/s (instantaneous) at a 50 percent duty is required to keep up with a 1 Mb/s instantaneous recording rate. Exposure duty factors of less than 2 percent can be achieved, if required, at this data rate; correspondingly higher instantaneous laser power levels would be required.

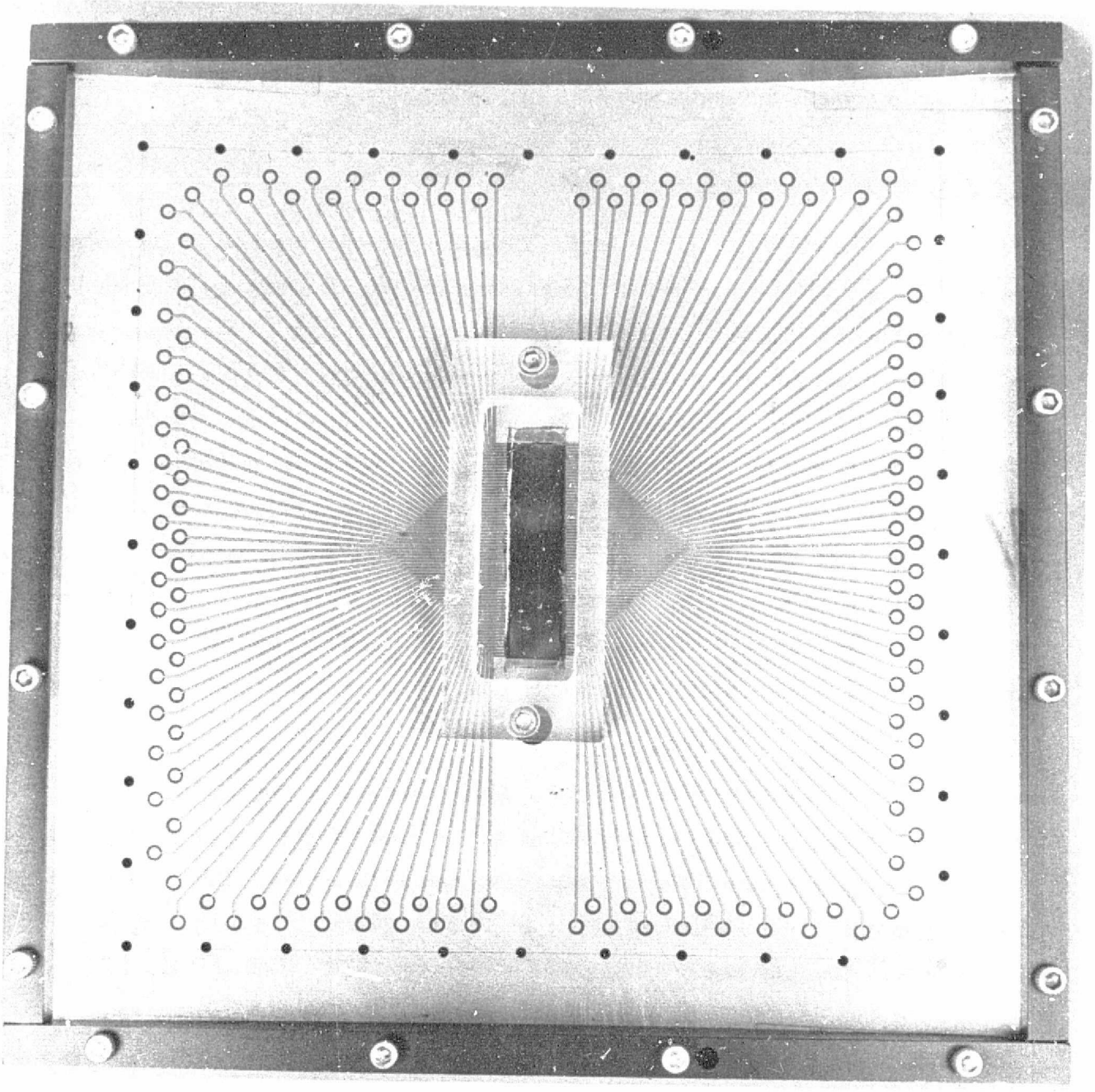

FIGURE 2-5. PHOTOGRAPH OF THE TRANSDUCER END OF A 134-ELEMENT ACOUSTO-OPTIC PAGE COMPOSER

Electrical crosstalk levels are at least 40 dB below signal levels in the present pc. Special printed-circuit card designs and interconnection procedures were developed to achieve this performance.

2.2.3.4 Multifaceted Spinning Mirror

The 40-facet spinner for the Wideband Recorder/Reproducer was designed to distribute up to 1600 holograms on 15 mm center spacings across 24 mm of 35 mm film through a scanning Fourier transform lens with a 75 mm focal length. The spinner scans both the signal and the reference beams. The spinner diameter is 140 mm and the height of each facet is 32 mm. A demagnified image of the signal plus reference beams encounters the central 26 mm of each facet. The images of the bits and of the reference beam are spread by an anamorphic optical system in the other dimension such that at each instant the incident beam spans across two facet widths. As the line scanned by one facet is ending, the next facet is already fully illuminated and the corresponding scanned pattern is just about to enter the recording aperture at the film. This feature eliminates any dead time between successive scanned lines at the expense of half of the available light.

For a 400 Mb/s recording rate, the spinner must rotate at 3050 r/min. For a 1 Mb/s recording or readout rate, the same spinner would have to rotate at only 3050/400 = 7.63 r/min, or about one revolution every 7.8 seconds. This can be checked by noting that during this interval, 40 rows of 1530 holograms, each containing 128 bits, are recorded. The total amount of recorded data is (40) (1530) (128) $\approx 7.8 \times 10^6$ bits during each revolution for a 1 Mb/s rate. A spinner which rotates this slowly could be very reliable in a spacecraft environment, but the very low rotational inertia tends to amplify mechanical jitter problems. The cost versus performance versus lifetime trade-offs between a spinner and a galvanometer are important.

2.2.3.5 Transform Lenses

As the spinner rotates through an angle of 9.0°, the incident light pattern is scanned through an angle of 18.0° into the entrance aperture of the first transform lens. The focussed light at the recording plane (the surface of the film) is telecentrically scanned across a distance of 24.8 mm. The scanned pattern at the film must be a diffraction limited, well-formed Fourier transform of the pattern incident on the spinner at each of 1600 positions along the scanned line. The second lens (the inverse transform lens) receives this scanned light pattern and must form a well-registered image of the light pattern incident on the spinner at the PDA. Not shown in Figure 2-2 is an "autoscan" configuration which descans the light. With the autoscan, the light pattern at the PDA can be condensed by a cylindrical lens to concentrate the available light onto the active PDA areas. Autoscan is described in References 6 and 7.

The principal requirements are associated with the ability of these two lenses to form the required light distribution in the Fourier transform plane (at the film) and with their ability to form high quality images of the data at the PDA while maintaining registration of the data image as the spinner rotates. Lenses which meet these requirements have been specially designed and fabricated for the Wideband Recorder/Reproducer. These lenses would meet any requirements anticipated for a TORAM system which incorporates a spinner or a galvanometer to distribute data cross about 25 mm of film. For shorter scans, the lenses are easier to design and fabricate.

2.2.3.6 Film Transport

A key parameter which significantly affected the design of the film transport for the Wideband Recorder/Reproducer is film speed. At 400 Mb/s, the required film speed is 1.83 meters/s. For the TORAM at 1 Mb/s and the same packing densities, the required film speed is only 4.6 mm/s. The tape transport for the TORAM can utilize basically the same layout, synchronization schemes, and spinner phase-lock schemes, but the drive requirements will be considerably different. The range over which film

position and speed are accurately controlled in the Wideband Recorder/Reproducer is from 0.01 to 2.4 meters/s. For the TORAM, this range must be dropped to around 0.5 to 50 mm/s. However, the control techniques can be very similar. Furthermore, the high speed capabilities of the present transport might be incorporated into the TORAM transport to provide the fastest possible random access and rewind speeds.

The present Wideband Recorder/Reproducer transport accepts only 35 mm film. Reels in cassette form for 100 feet of film and continuous loops of film can be used. It is designed for films with a 0.005-inch base thickness and can be modified for other thicknesses. The focal position repeatability (along the optical axis) is ±25 μm for both record and readout. The lateral position repeatability is ±50 μm. The servo tracking accuracy for readout is ±75 μm. Servo tracking is maintained by deriving an error signal from markers recorded on the edges of the film during the record cycle. It is essential to maintain phase lock between film motion and spinner position during readout; the servo system accomplishes this.

Although the design of a TORAM tape transport will have some important differences, the proven techniques and designs for the present film transport will be very useful.

2.2.3.7 Photoplastic Tape

The status of photoplastic tapes are discussed in Section IV.

2.2.3.8 Photodetector Arrays

Largely because of the requirements for net readout rates in the 40 to 400 Mb/s range, the PDA for the Wideband Recorder/Reproducer has been designed with 128 discrete hybrid photodetector-preamplifier units. A fiber-optic signal distributor samples the reconstructed light pattern in an image plane of the pc. The ends of 128 identical fibers are arranged along a line in this image plane (one fiber per bit position). These

fibers fan out in both dimensions from this plane. The opposite end of each fiber is inserted into a holder which directs the light onto the active portion of one photodetector-preamplifier unit. These units are arranged in a 16 x 8 array (10 inches x 6 inches) about 12 to 16 inches from the output image plane.

For data rates under 10 Mb/s, charge-coupled PDA's and linear self-scanned PDA's can perform the digital image sensing required in a TORAM system. Such PDA's are much smaller and lighter and require as much as 100 times less prime power. Previous experiments with 256 and 512 element linear self-scanned PDA's from Reticon have provided very encouraging performance data. In particular, a Model 512B unit optimized for 2.5 MHz clock rates on each of four output video lines (128 elements per line) was tested. At 2.5 MHz clock rates, the dynamic range was 18 to 20 dB, depending on which video line was tested. Nearest and next-nearest neighbor isolation at saturation was 14 dB. Neighboring element center spacings are 0.0254 mm, or 1 mil.

A linear array such as the Model 512B could be used in a TORAM system. With a 128-element pc having 0.25 mm element centers, a demagnification of about 1:2.5 would be required to match this spacing to every fourth diode (0.102 mm separations) which comprise each video channel. This demagnification takes place in the dimension orthogonal to the scanning dimension. With the autoscan arrangement, scaling of the data image on the PDA is not a problem. In the Wideband Recorder/Reproducer, rescaling optics are used.

A 1024-element array similar to the Model 512B is also available with eight video outputs (every eighth diode comprises one channel). The center spacings between neighboring elements are the same (0.0254 mm) so that successive elements of one video line are 0.203 mm apart. A very small demagnification would be required with this particular device.

With either a four-channel or an eight-channel PDA, off-center elements associated with the remaining channels can be used in at least two ways. The outputs of groups of four (or eight) channels can be summed to increase the signal associated with each bit, with some sacrifice of SNR. Alternatively, one element per bit can be used with redundant channels. That is, the PDA can be configured such that the pc image can be repositioned to the diodes corresponding to the different channels, in case of a failure (and to permit selection of the channel with the best performance).

2.2.3.9 Other Important Components

The beam-forming optics for both the signal and reference beams are conventional and typically can be off-the-shelf components. Space-bandwidth requirements on these components are quite modest since no data is on the beams transmitted through them. An important consideration is the optical efficiency of each of these components. Antireflection coatings can, of course, be applied to all surfaces to minimize losses.

In the Wideband Recorder/Reproducer two similar acousto-optic modulators are included to perform special functions. One of these provides exposure control (or shuttering). This unit externally modulates the CW laser beam with high efficiency ($\geq$70%) and high extinction ratio ($\leq 10^{-3}$). It can provide the required 65 ns pulses for exposure at 3.2×10^{6} pulse/second rate (20 percent duty) for recording at 400 Mb/s. An AOM which can provide 26 μs pulses at a 7.8×10^{3} pulse/second rate (20 percent duty) can meet the TORAM requirements at a 1 Mb/s input rate.

The other acousto-optic modulator functions as a beamsplitter and a Z-ratio controller as data is recorded; it also functions as a beam position corrector as data is reconstructed. For recording, the undiffracted light which is not frequency-shifted is directed into the signal path, and the diffracted light which is frequency-shifted is directed into the reference path. The frequency shift imparted to the reference beam is identical to that subsequently imparted to the signal beam. Therefore, the interfering beams form stationary fringes at the recording station. The amplitude

of the RF drive signal is adjusted to set the desired Z-ratio. For readout, a CW RF signal is applied to both AOM's. The frequency of the RF signal to the second unit is controlled by an error signal derived from a split photodetector which intercepts the undiffracted light transmitted through the film. This frequency control provides a slight angular adjustment to the readout beam at the film and corrects for film thickness variations which would otherwise cause a displacement of the data reconstructed at the PDA. A capability like this might be essential for a TORAM system.

2.2.3.10 Summary

The Wideband Recorder/Reproducer design and development effort has provided the basis for a promising alternative random-access holographic memory approach. With the exception of a suitable photoplastic tape and the associated charging and heating procedures, all of the key components have been developed and can be readily adapted for use in a TORAM system. We investigate the potential of such a system in the following text.

2.2.4 Potential of the TORAM Approach

In previous discussions, we observed that, with the exception of the photoplastic tape, all key components for a TORAM system can be adapted from corresponding Wideband Recorder/Reproducer components. In most cases, the TORAM requirements are less severe, particularly with regard to data rates, film speed, and laser power. We turn our attention to estimates of unit capacity and random access times.

2.2.4.1 Unit Capacity

A unit might consist of a reel or a cassette which contains a given length of photoplastic tape. Considerations of substrate breaking strength, scattering levels, thickness uniformity, dimensional stability, and compatibility with the photoplastic must be made to choose an appropriate tape thickness. For these discussions we choose a tape thickness of $t_t = 0.175$ mm, which is probably closer to an upper bound than to a lower bound. We select an inner spool radius of $R_i = 40$ mm; for thinner tape, a smaller inner radius might be used. The relationship between tape length L_t and outer radius R_o is given by,

$$L_t t_t = \pi (R_o^2 - R_i^2). \tag{2.7}$$

The total reel capacity Q_R is related to L_t, to the active film width W_f, and to the two-dimensional packing density ρ^2 by

$$Q_R = \rho^2 W_f L_t. \tag{2.8}$$

We use the same parameters cited earlier for the Wideband Recorder ($\rho^2 = 10^6$ bits/cm^2 and $W_f = 22.5$ mm) to obtain

$$Q_R = 2.25 \times 10^8 L_t \tag{2.9}$$

where Q_R is the unit capacity in bits when L_t is in meters. Reel capacity and spool radius as a function of tape length are given in Table 2-5. A capacity per reel above 10^{10} bits, and possibly as high as 10^{11} bits, appears feasible. Between 10 and 100 reels would be required in a TORAM system having a 10^{12} bit total capacity.

2.2.4.2 Random Access Times

With a tape cassette system, it is estimated that between 10 and 20 seconds would be required to change cassettes with an automatic or semiautomatic mechanism.

TABLE 2.5. REEL CAPACITY AND SPOOL RADIUS AS A FUNCTION OF TAPE LENGTH

Tape Length (L_t)		Reel Capacity (Q_R)	Reel Diameter ($2R_o$)		
Meters	Feet	Bits	cm	Inches	Comments
44.4	146	10^{10}	12.8	5.0	Feasible
444	1,460	10^{11}	32.5	12.8	Possibly Feasible
4,444	14,600	10^{12}	99.8	39.3	Impractical

TABLE 2.6. REEL CAPACITY AND RANDOM ACCESS TIME AS A FUNCTION OF TAPE LENGTH

Tape Length (L_t)	Reel Capacity (Q_R)	Random Access Time (T_{RMS})
Meters	Bits	Seconds
44.4	10^{10}	2.7
444	10^{11}	30.7
4,444	10^{12}	270.7

With open reels, more time would be required since the tape must be threaded through the read/record station.

Random access times to data on a tape in the system will be determined primarily by:

1. Length of tape
2. Across-track accessing technique
3. Forward and reverse tape speed (in search mode)
4. Data organization (average or rms distance to successive words or submits of data)

In order to make some estimates of what might be typical access times, we must assume values for certain operational parameters. The following choices are made:

Maximum Tape speed:	$V_{max} = 5$ meters/s
Time to accelerate to $\pm V_{max}$:	$T_{acc} = 2$ s
Distance traveled during T_{acc}:	$L_{acc} = 5$ meters
Time to stop from $\pm V_{max}$:	$T_{dec} = 2$ s
Distance traveled during T_{dec}:	$L_{dec} = 5$ meters
Time to synchronize for readout after reaching data:	$T_{syn} = 2$ s
RMS distance to next word:	$L_{RMS} = 0.3\ L_t$

The time required to translate the tape a distance L_{RMS} and synchronize to the data is,

$$T_{RMS} = T_{acc} + T_{dec} + T_{syn} + \frac{L_{RMS} - L_{ac} - L_{dec}}{V_{max}} . \qquad (2.10)$$

With the parameters selected above, we obtain,

$$T_{RMS} = 4 + 0.06\, L_t \qquad (2.11)$$

where T_{RMS} is in seconds when L_t is in meters. The results of such an estimative calculation is summarized in Table 2-6. This tabulation applies to both moving mirror and ITTT across-track access if all data subunits are indexed. In a pure search mode (nonindexed data), the ITTT approach is about 25 times slower and causes a corresponding larger amount of tape and transport wear.

To read the contents of a large fraction (10 to 100 percent) of a tape requires either much higher (X25) tape speeds or correspondingly more time with the ITTT approach.

2.2.4.3 Volume and Weight Requirements

The volume of tape required for the system parameters defined earlier can be obtained from

$$V_{Tape} = L_t t_t (W_f + \delta W) \qquad (2.12)$$

where $W_f + \delta W$ is the full width of the tape. For $Q_R = 10^{12}$ bits, we found that $L_t = 4444$ meters. For 35 mm tape and $t_t = 0.175$ mm, we find that $V_{Tape} = 0.0272\ m^3 = 0.96\ ft^3$. This is a small fraction of the overall system volume. This much tape weighs about $W_{Tape} = 78$ pounds = 35 kg, which is also a fairly small fraction of the overall system weight.

We estimate that a full 10^{12} bit TORAM system, including a controller and all data handling electronics, will weigh from 2500 to 4000 pounds and occupy from 120 to 160 ft^3. This estimate is based on an appropriate scaling of the existing Wideband Recorder/Reproducer system.

2.2.4.4 Power Consumption

The laser is an important item, as before, and the tape transport may require fairly large instantaneous power during acceleration. For input/output rates of 1 Mb/s, as little as 125 and as much as 1000 watts could be required by the laser, depending on whether a helium-neon (632.8 nm) or an argon-ion (514.5 nm) is selected. Based on the Wideband Recorder/Reproducer parameters, during acceleration the transport motors will require from 250 to 500 watts. It is conceivable that an energy storage mechanism could be designed which would provide an acceleration boost and then reclaim that energy during deceleration. Such a mechanism would eliminate the requirements for high peak power loads for the transport.

Overall power requirements for a 10^{12} bit TORAM system are estimated to be in the 2500 to 4000 watt range.

2.2.5 Technology Development

As emphasized earlier, the development of a suitable photoplastic tape with the related charging and heating techniques is key to the development of a TORAM system with read/write capabilities. The constraints imposed on the transport design by the charging and heating stations must be considered more carefully. A special configuration of a self-scanned PDA should be specified, fabricated, and tested. The design of a slowly rotating multifaceted mirror for across-track data distribution merits consideration, with particular emphasis on smoothness of rotation, lifetime, and reliability. Other techniques for scanning the accross-track dimension including a galvanometer-driven mirror should be investigated in greater depth.

2.3 DISC-ORIENTED RANDOM-ACCESS MEMORY (DORAM)

The TORAM type configuration modeled after the Wideband Recorder/Reproducer and shown in Figure 2-3 is also the basis for a DORAM system. The key differences between the TORAM and DORAM approaches are related to the techniques for data distribution and the recording material (no flexing of the substrate for the DORAM). A data block recorded as one-dimensional holograms on a disc can be distributed along a spiral (a single track) or as many nested circular tracks. Two-dimensional access is the R-θ type, rather than the X-Y variety of the BORAM and TORAM approaches. As the disc is rotated (θ access), it can be simultaneously translated along a radius (R access). The read/write material can be coated onto a rigid substrate which can then be attached to (or even part of) the disc. Nonrigid substrates can also be used.

Typically, the maximum random access time with the DORAM will be the time required for the continuously rotating disc to make one revolution.

2.3.1 Data Format

The one-dimensional holograms are recorded with the long dimension along a disc radius. With a spiral format, the pitch of the spiral is adjusted to separate adjacent tracks during one revolution (~1.0 mm/revolution). With a nested set of circular tracks, each track occupies an annular ring with the same width (~1.0 mm, including guard bands).

2.3.1.1 Fixed Disc Speed and Recording Rate

For a fixed disc speed and a fixed recording rate, hologram center spacings along the tracks decrease with radial position on the disc. The data packing density, therefore, increases inversely with radius. Given that ρ_{max} is the maximum achievable average packing density and that data are stored at ρ_{max} on the innermost track of

radius R_i, we can determine the relationship between R_i and the radius R_o of the outermost track in the following manner. The number of holograms and, thus, the quantity of data Q_{rev} recorded per revolution is fixed. For the innermost track we can write,

$$Q_{rev} = 2\pi R_i W_t \rho_{max} \tag{2.13}$$

where W_t is the center spacing between adjacent tracks. Similarly, for the outermost track we can write,

$$Q_{rev} = 2\pi R_o W_t \rho_{min} \tag{2.14}$$

where ρ_{min} is the packing density in this track. Then by dividing Equation (2.14) by (2.13) we obtain,

$$\rho_{min} = \frac{R_i}{R_o} \rho_{max} . \tag{2.15}$$

The average overall packing density is then,

$$\rho_{av} = \frac{R_i \rho_{max}}{R_{av}} = \frac{2R_i}{R_o + R_i} \rho_{max} \tag{2.16}$$

where $R_{av} = (R_o + R_i)/2$. The total number of tracks is,

$$N_t = \frac{R_o - R_i + W_t}{W_t}, \tag{2.17}$$

where R_o and R_i are measured to the centers of the outer and inner tracks, respectively. The total quantity of data per disc can be written as,

$$Q_D = A_{ac} \rho_{ac} \tag{2.18}$$

or

$$Q_D = \pi \left[\left(R_o + \frac{W_t}{2} \right)^2 - \left(R_i - \frac{W_t}{2} \right)^2 \right] \left(\frac{2R_i}{R_o + R_i} \right) \rho_{max} \tag{2.19}$$

where A_{ac} is the total area covered by holograms. Equation (2.19) reduces to,

$$Q_D = 2\pi R_i (R_o - R_i + W_t) \rho_{max} \tag{2.20}$$

which can be written,

$$Q_D = Q_{rev} N_t \tag{2.21}$$

by combining Equations (2.14), (2.17), and (2.20). We can now differentiate Equation (2.20) with respect to R_i to obtain,

$$\frac{\partial Q_D}{\partial R_i} = 2\pi \rho_{max} (R_o - 2R_i + W_t) . \tag{2.22}$$

We set $\partial Q_D / \partial R_i = 0$ to solve for the value of R_i which maximizes Q_D. We obtain,

$$R_i = \frac{R_o + W_t}{2} . \tag{2.23}$$

For a fixed speed disc and fixed rate data, only the outer 50 percent of the disc radius will contain data for the optimum disc capacity. Note, however, that this represents 75 percent of the available disc area. We find with Equations (2.16) and (2.23) that,

$$\rho_{av} = \frac{2(R_o + W_t)}{3(R_o + W_t)} \text{ and } \rho_{max} \approx \frac{2}{3} \rho_{max} \tag{2.24}$$

where $W_t \ll R_o$ is assumed. Also, with Equations (2.15) and (2.23) we obtain,

$$\rho_{min} = \frac{R_o + W_t}{2R_o} \rho_{max} \approx \frac{1}{2} \rho_{max} \tag{2.25}$$

which is consistent with the outer track length being about twice the inner track length, $2\pi R_o \approx 2(2\pi R_i)$.

2.3.1.2 Constant Packing Density

We now turn our attention to a disc format with a fixed packing density of ρ_{max} in all tracks. One way to achieve such a distribution would be to record holograms at a fixed rate but with the rotational speed of the disc varied to maintain constant along-track hologram center spacings. Another way would be to fix the disc speed but to vary the rate at which holograms are recorded with radial position.

The main advantage of this approach is that $\rho_{av} = \rho_{max}$. Therefore, more data can be put on a disc of a given diameter. The radius of the inner track is constrained mainly by two considerations. The first is that the dynamic range of disc speeds (or recording rates) is approximately R_o/R_i. The second is that as R_i becomes very small, the ratio W_t/R_i becomes large so that the outer portion of a hologram moves through a read station at a notably higher rate than the inner portion. The extreme is $R_i = 0$, which clearly cannot be used. Practical considerations will probably dictate that $R_i/W_t > 10$ and $R_o/R_i < 5$.

The penalties of this approach can apply either to the precision servo-mechanism and motor design for the disc drive or to the buffering and logic circuitry which are required to provide precisely variable recording rates. As an initial choice, it appears that placing the burden on the data handling electronics is more reasonable since additional mechanical complexities should be avoided for a spacecraft environment.

The quantity of data per disc with this approach is given by,

$$Q'_D = \pi(R_o + R_i)\ (R_o - R_i + W_t)\ \rho_{max}' \qquad (2.26)$$

which when compared to Equation (2.20) indicates an increase by the ratio $(R_o + R_i)/2R_i$, assuming the same R_o and R_i values. With this approach the improvement can be even better if $R_i < (R_o + W_t)/2$ is practical, as it may well be.

2.3.2 Capacity Per Disc

For this discussion we will consider only a fixed speed disc with a fixed recording rate. It will be recognized that improved net packing densities can be achieved at the expense of system complexity with the constant packing density approach.

We combine Equations (2.20) and (2.23) to obtain,

$$Q_D = \frac{\pi}{2} (R_o + W_t)^2 \rho_{max} \tag{2.27}$$

which for $R_o \gg W_t$ reduces to

$$Q_D = \frac{\pi}{2} R_o^2 \rho_{max} \tag{2.28}$$

We again choose $\rho_{max} = 10^6$ bits/cm^2 and define the overall disc diameter to be,

$$D_D = 2 (R_o + W_t + r_p) \tag{2.29}$$

where r_p is the excess at the outer periphery of the disc which is used for clamping the recording media to the disc and for disc handling. We choose $W_t = 1$ mm and $r_p = 4$ mm to obtain

$$D_D = 2R_o + 10 \tag{2.30}$$

where D_D and R_o are expressed in mm. The results of calculations with Equations (2.28) and (2.30) are tabulated in Table 2-7. A DORAM with 10^9 bits per 20-inch diameter disc appears to be achievable goal. A system with 10^3 such discs accessed by a refined and expanded version of a jukebox for 12-inch LP record would achieve a 10^{12} bit total capacity.

With Equation (2.17) we can determine that there would be $N_t = 126$ nested tracks (annular rings each $W_t = 1$ mm wide). Each track would contain $Q_{rev} = 7.93 \times 10^6$ bits, obtained from Equation (2.13). As a check on the numbers, we get $Q_D = 10^9$ bits/disk by multiplying N_t by Q_{rev}, as prescribed by Equation (2.21).

TABLE 2-7. DISC CAPACITY ON A FUNCTION OF DISC GEOMETRY

Disc Capacity (Q_D)	Outer Track Radius (R_o)		Disc Diameter (D_D)		
Bits	mm	inches	mm	inch	Comments
10^8	79.8	3.14	160	6.30	Feasible
10^9	252	9.92	514	20.2	Feasible
10^{10}	798	31.4	1606	63.2	Impractical

2.3.3 DORAM System Overview

2.3.3.1 Photoplastic Charging and Heating

Techniques for charging and heating the photoplastic on a disc before and after the recording station must be developed. The surface of the disc on which the photoplastic is coated must be free of supports which protrude above the photoplastic layer. Such a requirement can be met easily with rigid substrates, and can very likely be met with nonrigid substrates.

2.3.3.2 Rational Speed and Random Access Modes

The disc rotational speed is a function of packing density, data rates, and data format. For the fixed speed, fixed data rate case, the disc makes one full rotation as data is recorded or retrieved in a time,

$$T_{rev} = \frac{Q_{rev}}{\nu} \qquad (2.31)$$

For $\nu = 1$ Mb/s and $Q_{rev} = 7.93 \times 10^6$ bits, we find that $T_{rev} = 7.93$ seconds. This is the time per revolution for a continuous record or readout rate of 1 Mb/s (instantaneous). For the spiral format, the full contents of a disc could be read without interruption. For the nested ring format, the disc would probably have to be rotated twice as fast ($T_{rev} = 3.97$ seconds), and data would be read every other revolution. During alternate revolutions the disc would be translated radially to the adjacent track. A data channel with a large buffer would be required to receive 7.93×10^6 bits at 2 Mb/s and clock it out at 1 Mb/s.

A random access mode would probably operate as follows. The disc rotational speed would be fixed such that the instantaneous readout rate would be in the 2 to 5 Mb/s range. If the data were indexed, an accessing command would activate an appropriate radial position adjustment to bring the requested track to the read station.

After synchronization is achieved, the requested data would be read. If the requested data is in more than one track, then more than one radial adjustment and synchronization interval would be required. If any radial adjustment can be completed in an interval shorter than one revolution period, then random access times will be in the 1- to 4-second range, with indexed data. If the data are not indexed, the spiral configuration would be selected so that the read head would have the freedom to scan the full disc without interruption for incrementing between nested tracks. Random access times as long as 150 seconds, but more typically 30 to 50 seconds, would be required with this nonindexed approach.

A fast search mode is possible with a rapidly rotating disc. Data subunit identifiers would have to be included periodically in the spiral track. However, when the requested data is located, the disc will overrun as it is decelerating and will have to be reversed and stabilized before data reading can commence. More detailed considerations will have to be made before the feasibility of such a mode can be determined.

2.3.3.3 Volume and Weight Considerations

A 10^{12} bit DORAM system with the photoplastic on a glass substrate can be compared to a BORAM approach with glass. Since a parallel plane charging plate will be omitted from the discs, only about half the volume and weight of glass is required. The overall volume occupied by 10^3 discs each having an overall diameter of 0.514 meter and a thickness of 10 mm is 2.07 m^3 or 73.3 ft^3 (about the same as the BORAM). The weight of these discs for 1.5 mm thick glass would be about 1400 kg or 3100 pounds. It is estimated that the entire DORAM system with glass substrates would weigh from 5000 to 7000 pounds and occupy from 120 to 160 ft^3.

If lighter and thinner flexible substrates are used, the overall system weight drops to the 2500 to 4000 pound range. The volume falls in the 100 to 150 ft^3 range for this case.

2.3.3.4 Power Consumption

The DORAM approach can be compared to the TORAM to estimate power consumption. The only important differences are the absence of an across-track deflector and probably smaller drive motors for the DORAM. Overall consumption for a 10^{12} bit DORAM system should be in the 2000 to 3500 watt range.

2.3.4 Technology Development

The only difference from the TORAM is related to the disc drive and access mechanism and to the photoplastic material configuration. Constraints imposed on the disc and disc drive design by the heating and charging requirements of the photoplastic require particular attention. Note that with no moving mirror scanner, as for the ITTT case with TORAM, the optics are relatively simple.

2.4 FICHE-ORIENTED RANDOM-ACCESS MEMORY (FORAM)

An operational system for recording human readable (HR) and machine readable (MR) data on 148 mm x 104 mm film chips (or fiche) has been delivered to the Air Force (RADC) by Harris Corporation. The mechanisms for precisely transporting the fiche as data are recorded on them and read from them were developed as part of the HRMR program. An off-line automatic film processor was included with this system. A more advanced version of the HRMR system is soon to be delivered. This advanced HRMR system will include a faster fiche transport, a storage and retrieval appartus for over 10^4 fiche, and an off-line automatic film processor. The designs for the fiche handling equipment developed for the HRMR systems can be adapted to the requirements of a FORAM system.

2.4.1 Basic System Configuration

The configuration of Figure 2-2 depicts the basic arrangement for a FORAM, except that the indicated tape transport would be replaced by a flat-bed X-Y fiche

transport. The rotating mirror scanner indicated in Figure 2-2 can be replaced by a servoed galvanometer driven mirror. Because of clearance problems with the fiche transport, the autoscan configuration would be difficult to implement. One alternative is to do without descanning at the PDA and provide extra laser power for readout. A second alternative, which minimizes the required laser power, is to include a second servoed scanner at the position occupied by the PDA in Figure 2-2. This second scanner would descan the reconstructed data patterns and provide a stationary image at the PDA. Cylindrical optics could be used after the second scanner to concentrate the light from each page composer element onto the corresponding PDA element, as indicated in Figure 2-3. Note that a galvanometer driven mirror can replace the spinning multi-faceted mirror with minor adjustments in the details of the scanning procedure.

The other components and procedures for recording and retrieving data with the FORAM approach are essentially the same as for the TORAM approach described earlier. It is quite conceivable that a FORAM system could be changed to a TORAM system by replacing the fiche transport with a tape transport; the inverse is also conceivable (TORAM to FORAM). The compatability of the basic system approach to tapes, fiche, and even disc offers an important measure of flexibility for accommodating read/write materials which might become available in the future. This interchangeability also offers the potential for increasing data transfer rates by converting from a fiche to a tape format, if photoplastic tapes are successfully developed.

Many of the design relations in Table 2-2, along with Equations (2-2)-(2-6) for the TORAM approach, are applicable to the FORAM approach.

2.4.2 Data Format

In Table 2-8 we compare a number of alternative data formats for 148 mm x 104 mm fiche. One extreme is Format Number 1 with no scanner, shown in Figure 2-6. The system is significantly simpler without a scanner, but the penalties are:

TABLE 2-8

COMPARISON OF DATA FORMATS ON 148 mm x 104 mm FICHE

Format Number	Number of Files Parallel to Long Edge	Number of Holos/Scan	Minimum Scanner Space-Bandwidth (Single-Rayleigh)	Number of Holos/File	File Width (mm)	Excess Width for Guard Bands (mm)	Number of Bits/File (User and Overhead)	Number of Bits/Fiche (User and Overhead)
1	85	No Scanning	No Scanner	8.7×10^3	1.0 (Center Spacings)	19.0	1.1×10^6	93.5×10^6
2	23	250	750	30×10^3	3.75	17.75	3.8×10^6	87.4×10^6
3	11	500	1,500	60×10^3	7.5	21.5	7.7×10^6	84.7×10^6
4	7	750	2,250	90×10^3	11.25	25.25	11.5×10^6	80.5×10^6
5	6	1,000	3,000	120×10^3	15.0	14.0	15.4×10^6	92.4×10^6
6	4	1,500	4,500	180×10^3	22.5	14.0	23.0×10^6	92.0×10^6

Common Parameters

* Overall fiche size: 148 mm x 104 mm
* Number of user plus overhead bits per hologram: 128
* Hologram centers within each file: 1.0 mm x 15 μ
* Number of scan tracks per file (on 1.0 mm centers): 120
* Excess length for guard bands: 28 mm

89678-73

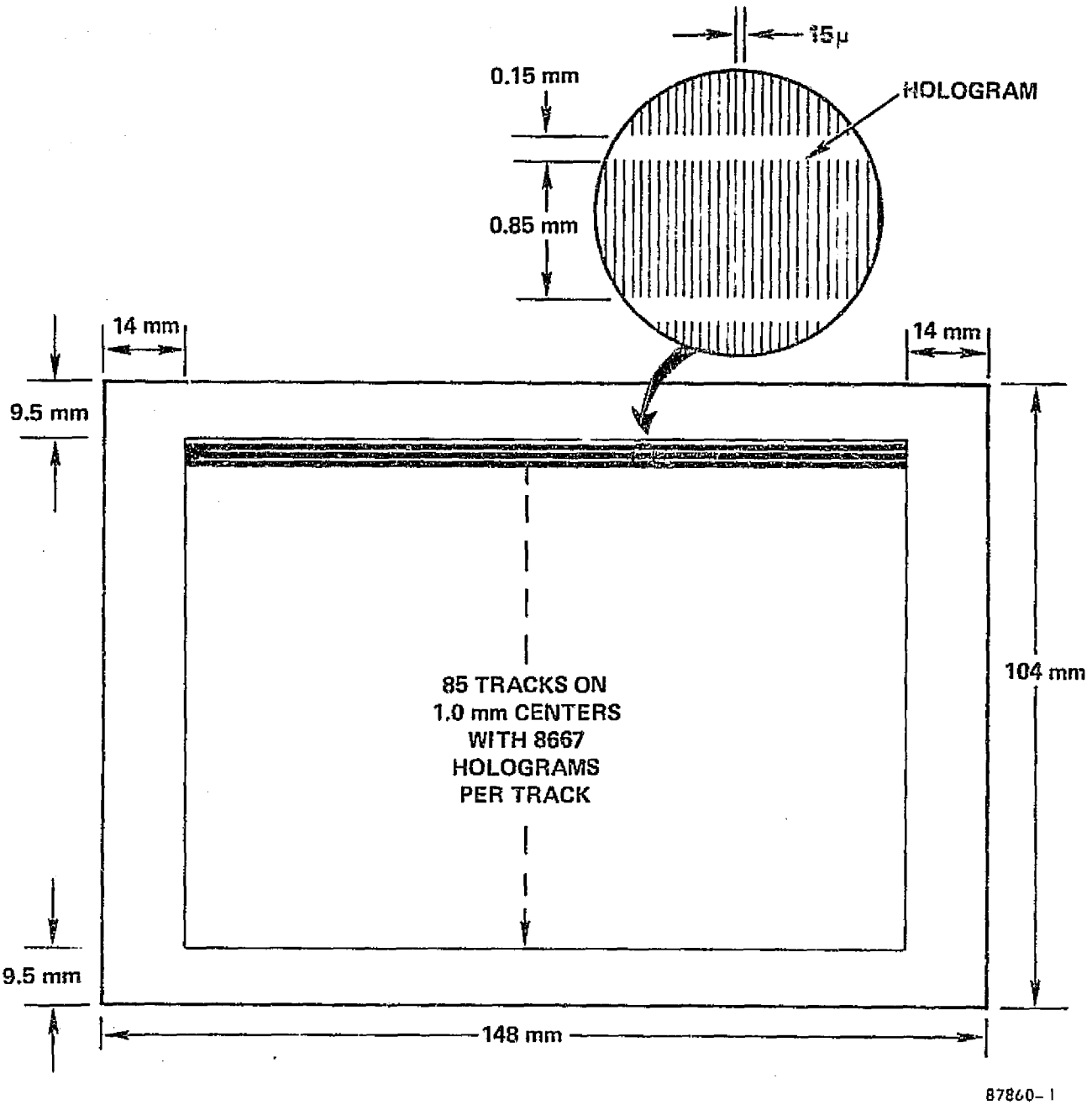

FIGURE 2-6. FICHE FORMAT NUMBER 1 FROM TABLE 2-8 (NO SCANNER)

1. Many tracks (85 in this example) must be accessed by the X-Y fiche transport.
2. Only 1.1×10^6 bits are accessed as the fiche is translated its full active length.
3. The rate of fiche translation required for effective data transfer rates over 1.0 Mb/s is excessive, especially since the number of acceleration-deceleration cycles at the ends of the tracks is large when the full fiche is being recorded or read.

This approach can be compared to the ITTT approach with the TORAM system.

The other extreme is Format Number 6, which is basically four files of data arranged the same as in the TORAM approach; refer to Figure 2-4 and imagine four strips of tape laid in parallel and bonded together. With this format, the requirements on the transform lenses and the scanner are severe; each must operate with a space-bandwidth of 4500, or greater, along the scanned line.

Formats Number 3 and Number 4 represent reasonable compromises. Format Number 3 is illustrated in Figure 2-7. Note that ample fiche area is provided around the periphery for handling and special identifying symbols. Some of this excess are may be used for alignment markers. It may be necessary to include synchronization markers along one edge of each file. This might reduce the number of files for this format from 11 to 10; the corresponding reduction in total data per fiche is from 84.7×10^6 bits to 77.0×10^6 bits. Trade-offs of this type will be investigated early in the proposed program.

2.4.3 Status of Key FORAM Components

Most of the components required for a FORAM system are the same as for a TORAM system; see Paragraph 2.2.3. The one outstanding difference is that a fiche transport replaces the tape transport. Correspondingly, the data format is different, as described above. We briefly review the status of the components of a FORAM in Table 2-9.

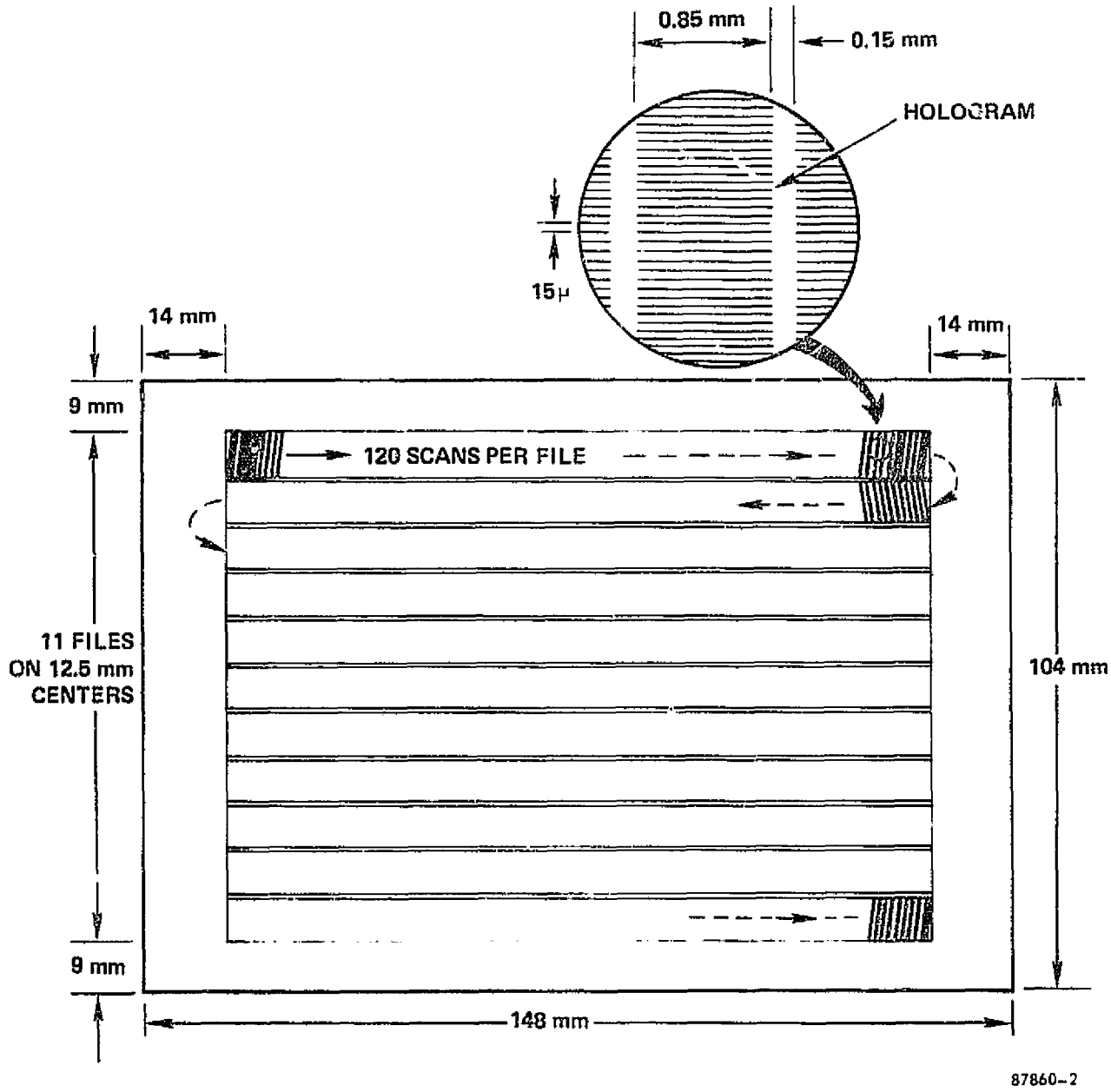

FIGURE 2-7. FICHE FORMAT NUMBER 3 FROM TABLE 2-8 WITH A SCANNER THAT RECORDS 500 HOLOGRAMS PER SCAN

TABLE 2-9

STATUS OF FORAM COMPONENTS

Component	Description	Status
Laser	Argon (514.5 nm) or He-Ne (632.8 nm)	Commercially available
Beam-forming optics and hardware	Common lenses, mirrors, mounts, and filters	Commercially available
Transform lenses (Format Number 3 or 4)	Space-bandwidth along scan ≤ 2250	Similar lenses with 5000 space-bandwidth along scan designed and under fabrication for Wideband Recorder
Linear acousto-optic page composer	128 elements on 0.25 mm centers	Two completed for Wideband Recorder
Acousto-optic light modulator	Exposure control	In use on Wideband Recorder
Acousto-optic beam splitter and readout beam positioner	Reference/signal intensity ratio control; few spots of deflection	In use on Wideband Recorder
Scanning mirror	a. Galvanometer drive or multifaceted spinner	a. Commercially available; in use at Radiation
	b. Cam drive	b. Similar to existing designs
Fiche transport	X-Y platen with positive fiche holddown	Three similar devices completed and in use on HRMR systems
Recording material	a. Photographic film	a. Commercially available
	b. Photoplastic fiche	b. Not available at present
Film processor	Automatic, off-line	Commercially available; in use on HRMR and on Wideband Recorder
Photodetector array	a. Self-scanned monolithic units of up to 1024 elements	a. 128-element device in use on HRMR
	b. Discrete hybrid units with fiber optic distributor	b. Nearing completion for Wideband Recorder
Controller	PDP-11/40 with extra disc storage and magnetic tape storage	Commercially available; similar unit in use on HRMR
Special control and data handling electronics	Set static system parameters; MUX/DEMUX circuitry; servo loops; PC and PDA drive, etc.	In use on Wideband Recorder or HRMR; conventional electronics

89678-72

We have used all of the components required to configure a FORAM system with photographic film. For the FORAM system with Format Number 3 or 4, the lens performance requirements are much less difficult than for the Wideband Recorder/Reproducer format. In fact, in feasibility tests of the Wideband Recorder/Reproducer system, off-the-shelf lenses performed satisfactorily for up to 500 holograms per scan for a full input data array (128 bits plus the reference beam). We anticipate that the FORAM system can be configured with such lenses for Format Number 3.

2.4.4 Potential of the FORAM Approach

A goal of configuring a 10^{12} bit memory is taken to generate some key performance parameters for the FORAM approach.

2.4.4.1 Fiche Capacity and Fiche Storage and Retrieval

A basic unit or block of data is the amount which can be recorded on one fiche. We are considering total data at this point (user plus overhead).

From Table 2-8 we see that for Format Number 3, each fiche can contain 84.7×10^6 total bits. To store 10^{12} bits, we therefore, must make provision for 11,806 fiche.

One particular fiche storage and retrieval unit which merits consideration is the REMKARD unit, manufactured by Image Systems, Inc., and marketed by Remington-Rand. Each REMKARD unit stores 750 fiche. Multiple units can be stacked with a command fiche input/output terminal. Special procedures for automatically loading a retrieved fiche into the FORAM and routing a recorded fiche from the FORAM to the REMKARD units have not been developed, but hardware for doing this is feasible. Random access times to any fiche in any of several REMKARD units is about 3 seconds rms.

Additional time would have to be allowed for automatic insertion into the FORAM; this interval could be of the order of 3 seconds, also. Thus a 6 second rms random access time to any fiche is envisioned.

With 750 fiche per REMKARD unit, a total of 11,806/750 = 16 units would be required for a 10^{12} bit memory (recall that this 10^{12} bit capacity includes user and overhead data). Two stacks of eight units with a common fiche input/output terminal between them would be a reasonable configuration. A similar configuration (one stack of nine units) has been assembled for the new HRMR system.

It is interesting to observe that at a 1 Mb/s average data transfer rate, it would take around 85 seconds to read or record a full fiche. For many applications, queuing of fiche could be considered so that only the time required for insertion of fiche would be required between reading or recording cycles. An extra 3 seconds after each 85 second full fiche interval would reduce the effective data transfer rate by less than 4 percent, or else require a corresponding increase in the instantaneous rate to keep up with a specified fixed rate near 1 Mb/s.

2.4.4.2 Volume and Weight Requirements

The total volume and weight of 11,806 fiche each 7 mils thick is comparable to that of the tape for a TORAM system (about 1 foot^3 and under 80 pounds). The storage and retrieval unit would occupy approximately three standard 6-foot equipment racks (~100 feet^3) and would weigh approximately 1500 pounds.

We estimate that a full 10^{12} bit FORAM system, including a controller and data handling electronics, will weigh from 3,000 to 5,000 pounds and will occupy from 180 to 230 feet^3. This estimate is based on an adaptation of the existing Wideband Recorder/Reproducer and HRMR systems.

2.4.4.3 Power Consumption

The storage and retrieval mechanism for FORAM will require about 1000 watts more power than for BORAM or TORAM. Otherwise, FORAM can be compared to TORAM. Overall power requirements for a 10^{12} bit FORAM system are estimated to be in the 3500 to 5000 watt range.

2.4.5 Technology Development

As for BORAM and TORAM, the development of photoplastic fiche and the related charging and heating techniques is key to the development of a FORAM system with read/write capabilities. A successful implementation of the stacked REMKARD assembly on the HRMR program will adequately demonstrate that technology. A special configuration of a self-scanned PDA must be specified, fabricated, and tested. A galvanometer-driven mirror must be configured and servoed to the motion of a fiche transport to demonstrate scan rates near 30 scans/second, space-bandwidth in excess of 1500, and the required stability and repeatability.

2.5 OTHER READ/WRITE MASS MEMORY TECHNOLOGIES

We now briefly review more conventional approaches for the development of mass memories.

2.5.1 Presently Available Magnetic Tape and Disc Systems

We review certain magnetic tape and disc mass memory systems in this section. These data can be compared to the projected performance of the various holographic read/write memories.

2.5.1.1 Mass Tape Memory

One magnetic tape memory system - the Terabit Memory from Ampex - with a total capacity in excess of 10^{12} bits is commerically available. Certain key parameters for this system are summarized below:

Maximum capacity	3×10^{12} bits
Capacity per reel	4.6×10^{10} bits
Number of reels per module	2
Number of modules	32
Number of tape transport units	2
Maximum data transfer rate	36 Mb/s
Number of read/write heads	64
Read/write head life	100 hours
Tape width (standard video)	2 inches
Tape length per reel	3,800 feet
Tape life	
Search	50,000 cycles
Read/Write	2,000 cycles
Random access time to data on a specified reel	
Average	15 seconds
Maximum	45 seconds
Number of simultaneous search operations	6
Total steady-state power consumption	30 kW
Approximate total system weight	45,000 pounds
Approximate total system volume	1,900 feet^3

This system also requires compressed air and vacuum.

The power, weight, and volume figures noted above include all electronics required to access any subunit of data, a system controller (typically a PDP-10), and a 10^8 bit staging disc memory. The staging disc is used to store subunits of data accessed from tapes and permits 15 to 20 ms random access times to such 10^6 bit subunits, once they are loaded onto the disc. The 100 hour read/write head life is only consumed when reading or writing is taking place; the heads are withdrawn from the tape during search operations.

The capacity of the above system can be reduced to 10^{12} bits by using only 11 modules and one tape transport unit. The power, weight, and volume figures are reduced to approximately 15.3 kW, 19×10^3 pounds, and 775 feet^3.

The magnetic tape used is standard 2-inch wide video tape. In the search mode, it is translated at speeds up to 25 meters/s (or 1000 inches/s).

2.5.1.2 IBM 3330-11 Disc Unit

This system consists of up to 8 discs (modules) each with a capacity of 3.2×10^9 bits for an overall capacity of about 2.6×10^{10} bits. Data transfer rates are 6.4 Mb/s. Random access times are in the 7 to 50 ms range. The weight of the system is in excess of 6000 pounds. It occupies a volume of over 160 feet^3. Power consumption figures are not available.

To achieve a 10^{12} bit capacity with systems of this type would require $40 \times 8 = 320$ modules and 40 controllers. The weight and volume requirements would be expanded to 240×10^3 pounds and 6.4×10^3 feet^3.

2.5.1.3 STC-8000 Series Disc Unit

This system is quite similar to the IBM unit described above. The major difference is a data packing density about twice that of the IBM unit. The weight and volume requirements are roughly halved.

2.5.2 Emerging Technologies

Several other memory approaches have the potential for mass memory applications and are in various stages of development. The following list is not exhaustive but provides a representative sampling of the emerging technologies. Certain key advantages (*) and problem areas (†) are identified by the symbols defined here:

Magnetic bubbles

* Moderate densities (~10^5 bits/cm^2)
* Nonvolatile
* Submillisecond random access within any block
* Relatively low weight and volume
* Lower power consumption
† Small signal levels
† Low data transfer rates (~100 kHz)
† Material nonuniformities
† Different bias field requirements for similar devices from a single batch

Magneto-optics

* High density (~5 x 10^6 bits/cm^2)
* Nonvolatile
* Tape or disc formats
* Moderate to high data transfer rates (1-10 MHz)
† Submicrosecond laser pulses required at a high rate
† Precise control of energy per pulse required to guarantee switching and prevent film damage
† Low optical efficiency

Charge-coupled devices

* Moderate density (10^4-10^5 bits/cm^2)
* Moderate to high data transfer rates (1-10 MHz)
* Silicon technology (MOS)
* Commercial devices available
† Volatile
† Serial data access, but data recycling preserves the data

Semiconductor (LSI)

* Submicrosecond random access within data blocks
* Moderate density (10^4-10^5 bits/cm^2)
* Silicon technology
* Moderate to high data transfer rates (>1 MHz)
* Commercial devices available
† Relatively high power consumption
† Volatile

When the data is volatile, means must be provided to keep the proper voltages connected to all elements of the memory. Thus, the CCD and LSI memories would require megawatts to preserve data in a 10^{12} bit memory; this consideration eliminates such approaches at present.

2.6 SUMMARY AND CONCLUSIONS

Table 2-10 summarizes the potential parameters of the systems discussed in this section. Parameters for both glass and plastic substrates are listed for the BORAM and DORAM approaches. The two magnetic disc approaches are not considered feasible for a 10^{12} bit memory; they are included mainly to permit certain comparisons. Note that the magnetic discs offer random access times of around 30 ms, but the size and weight of enough large discs for a 10^{12} bit memory are excessive.

TABLE 2-10

POTENTIAL PARAMETERS FOR VARIOUS APPROACHES TO A 10^{12} BIT READ/WRITE MEMORY

Feature \ Read/Write Memory Approach	Optical Technology (Holographic)						Magnetic Technology		
	BORAM		TORAM	DORAM		FORAM	Ampex Terabit Memory System	IBM 3330-11 Disc System	STC 8000 Series Disc System
	Glass	Plastic		Glass	Plastic				
Capacity per unit (or block)	10^7	8×10^7	10^{11}	10^9	10^9	8×10^7	4.5×10^{10}	3.2×10^9	6.4×10^9
Number of units in 10^{12} bit memory	10^5	12,500 fiche (16 Remkard Units with 6.25×10^{10} bits each	10	10^3	10^3	12,500 fiche (16 Remkard Units with 6.25×10^{10} bits each)	22	320	160
Organization	Single block per unit	Two stacks of 8	Tape cassettes	Refined jukebox	Refined jukebox	Two stacks of 8	Tape reels all on-line	Discs all on-line at once	Discs all on-line at once
Instantaneous data transfer rates (Mb/s)	1	1	1	1	1	1	12	6.4	6.4
Typical access time to a unit (seconds)	20	6		15	15	6	On-line	On-line	On-line
Typical random access time within a unit	5μs	5μs	31 sec	3 sec	3 sec	2 sec	30 sec	30 ms	30 ms
Nominal local area packing density (bit/cm^2)	10^6	10^6	10^6	10^6	10^6	10^6	0.08×10^8	-	-
Estimated volume of memory material (ft^3)	72	1.2	1.0	73	1.2	1.0	-	-	-
Estimated volume of full system (ft^3)	175	140	140	140	125	210	775	6400	3200
Estimated weight of memory material (lbs)	6500	100	80	3100	100	80	-	-	-
Estimated weight of full system (lbs)	10,500	3250	3250	6000	3250	4250	19,000	240,000	120,000
Estimated power consumption (kW)	4.5	4.5	3.3	2.8	2.8	4.0	15.3	?	?

89678-74

The Ampex Terabit Memory (magnetic tapes) is the only available read/write system which can be configured for a 10^{12} bit memory capacity. The size, weight and volume requirements of this memory are notably higher than the projections for all of the optical approaches. Note that even though all the data are on-line, the typical random-access time is still around 30 seconds. The data transfer rate can be as high as 12 Mb/s. The data transfer rates for the optical approaches can only be increased by increasing laser power and storage material translation speeds. These changes would increase volume and weight only slightly; however, power requirements could quadruple as transfer rates are increased from 1 to 12 Mb/s. Conversely, a reduction in data rate from 12 to 1 Mb/s for the Ampex system would not significantly reduce the volume, weight, or power requirements. The Ampex system power requirements could only be reduced notably by correspondingly increasing the random-access times. System volume and weight would not be notably reduced with this change.

Based on the system considerations presented in this section and on the results of previous related programs with NASA and the Air Force, we conclude the following:

1. At data transfer rates near 1 Mb/s, the optical approaches require much less volume, weight, and power than the magnetic approaches.
2. At rates near 10 Mb/s, the optical approaches still require much less volume and weight, but the power requirements are comparable to those of the magnetic approaches.
3. Until the system applications are more precisely defined, it is not clear that: a) microsecond or millisecond random-access to pages in a block or unit of data is necessary, b) subsecond delays between recording and readout are necessary, and c) erase-record cycle times of a few seconds are necessary.

4. Because of the proven performance of the key system components, the TORAM and FORAM approaches are preferred over the BORAM and DORAM approaches

5. Because the development of read/write photoplastic fiche appears less risky than the development of photoplastic tape, the FORAM approach is preferred for a holographic read/write memory.

6. The FORAM approach can be straightforwardly converted to a TORAM approach with higher data transfer rate potential if the feasibility of high resolution photoplastic tapes can be proven.

7. The volume of any 10^{12} bit optical memory will be in the 100 to 240 ft^3 range, with the FORAM at the upper end (with the REMKARD storage and retrieval approach).

8. The weight with plastic storage materials will be in the 3000- to 5000-pound range, with FORAM near the upper end.

9. The power requirement will be in the 3.0 to 5.0 kW range with FORAM near the middle.

10. The amount of overhead data required will be determined by measuring raw system error rates and matching the various error correction coding schemes to a given data format and to error sources and statistics.

11. The total capacity of a FORAM or TORAM system depends primarily on how many fiche or how many tape reels can be made accessible to the basic recorder or reproducer system.

12. With storage material processing remote from the record station (with photoplastics or photographic film), the reader could be separate from the recorder; the system designs could be significantly affected if such an approach can be matched to a particular application.

Overall, we conclude that the most important performance features of the read/write holographic random-access memory system required by NASA-MSFC can be demonstrated with a FORAM system. These most important features include:

- Capacity - 10^{12} bits is feasible
- Random-Access Time - less than 5 seconds to a block of about 0.8×10^{8} bits
- Input/Output Bit Rates - over 1 Mb/s with the capability for higher rates
- Measurement of Raw Bit Error Rates
- Error Correction Codes - capability to implement with software control
- Life Cycles of Page Composer and Photodetector Array - no fatigue with selected approaches
- Volume, Weight, and Power Requirements - notably lower than with the best available magnetic technology
- Moving Parts - no high r/min or high speed components required
- Key Components - well developed, with the exception of photoplastic fiche.

Finally, an interesting observation concerning an application for either a TORAM or a FORAM with only photographic film can be made. Suppose, for example, that a TORAM recorder is on board a space station. Further suppose that data are collected at an average rate of 2 Mb/s. At this rate it would require almost 14 hours to

fill a single 10^{11} - bit tape. Therefore, less than two such tapes would be required to store all data accumulated in each 24-hour period. If the space station were serviced on a monthly basis by the Shuttle, then fewer than 60 tapes would have to be brought up and returned each time to keep the recording system supplied. The space station could have a tape reader for verification and for on-board use of the collected data. One or more ground-based readers would utilize the tapes returned by the Shuttle. The volume and weight of 60 tapes, each with a 10^{11}-bit capacity, could be of the order of 50 cubic feet and 200 pounds; this represents a very small fraction of the Shuttle cargo capacity.

2.7 REFERENCES

1. "Updated Optical Read/Write Memory System Components," Final Technical Report, prepared under Contract Number NAS 8-26672 by Radiation, Electro-Optics Operation,* August 1973.

2. "Optical Read/Write Memory System Components," Final Technical Report, prepared under Contract Number NAS 8-26672 by Radiation, Electro-Optics Operation,* March 1973.

3. "Updated Optical Read/Write Memory System Components," Final Technical Report, prepared under Contract Number NAS 8-26672 by Radiation, Electro-Optics Center,* Feburary 1972.

4. "Optical Read/Write Memory System Design," Final Technical Report, prepared under Contract Number NAS 8-26360 by Radiation, Electro-Optics Center,* February 1971.

5. Vander Lugt, A., "Design Relationships for Holographic Memories," Applied Optics 12, July 1973, pp. 1675-1685.

*Now Electro-Optics Department, Harris Electronic Systems Division

6. Bardos, A. M. and R. G. Zech, "Wideband Holographic Digital Recording and Readout," Final Technical Report, prepared under Contract Number F30602-71-C-0365 for RADC by Radiation, Electro-Optics Operation,* August 1973.

7. Montgomery, R. M. and J. W. Watkins, "High Data Rate Holographic Recording Using Acousto-Optic Input Devices," Proceedings of the 1972 Electro-Optics System Design Conference, New York, September 1972, pp. 295-308.

8. Bardos, A. M., R. M. Montgomery, and H. N. Roberts, "Gigabit/Second Recording with Holography," Proceedings of the 1973 Electro-Optics System Design Conference, New York, September 1973.

9. Bardos, A. M., "Wideband Holographic Recorder," Applied Optics, 13, April 1974, pp. 832-840.

*Now Electro-Optics Department, Harris Electronic Systems Division

SECTION III

BREADBOARD HOLOGRAPHIC RECORDER/REPRODUCER

SECTION III

BREADBOARD HOLOGRAPHIC RECORDER/REPRODUCER

The systems and design considerations discussed in Section II provided the basis for design, analysis, and experimental activities in support of the development of a breadboard holographic recorder/reproducer, whose intended use is as the key subsystem of a holographic mass memory (HOLOMEM). In this section we discuss the principle of operation, major components, subsystems, and various test data.

As the basic concepts applicable to the recording and reconstruction of analog holograms of Fourier transforms of digital data blocks are well established, the focus of the experimental study reported here is on the development and improvement of key system components and their integration into an operational breadboard holographic recorder/reproducer. Particular emphasis was placed on the investigation of

1. Synchronized Scanning Deflection Techniques with performance goals of 40 scans/s with a maximum retrace interval of 7.5 ms, 1500 resolvable positions per scan, a full rotation angle of 4.2°, linearity of 0.2 percent, and repeatability of 0.05 percent.

2. Linear Self-Scanned Photodetector Arrays with performance goals of 4 Mb/s instantaneous data transfer rates, center spacings matched to the AOPC, detector saturation at 632.8 nm of 2 pJ, a minimum signal-to-noise ratio of 18 dB and neighboring detector isolation of at least 20 dB.

3. Linear Acousto-Optic Page Composers with performance goals of 70 percent (instantaneous) diffraction efficiency with less than 10 mW of RF drive power per channel, center spacings between elements of 0.25 mm, and 0.2 Mb/s per channel (instantaneous) modulation rates.

To appreciate the role of the most important breadboard components, it is helpful to study the conceptual schematic for a future fiche-oriented version of the HOLOMEM shown in Figure 3-1. The input to the system is a laser beam which is first split into two beams, the signal and reference beams, and then shaped with a combination of cylindrical and spherical lenses to form the wavefront shown emerging from the Beam Forming Optics block in the drawing. This wavefront forms the input to an acousto-optic page composer (AOPC). The AOPC is a carefully polished block of glass or crystal with a number of thin metal transducers bonded on one side. These transducers, driven by a high frequency RF oscillator, transmit an RF signal to the glass or crystal and produce compression waves. A sinusoidal wave pattern is created along the axis perpendicular to each transducer, forming a diffraction grating with the refractive index gradients of the compression waves acting as the structure of the grating. When light is incident on this grating, it is diffracted by the grating at an angle corresponding to the RF frequency used and the speed of sound in the AOPC material. The diffracted light forms the output data pattern of the page composer. (The beams diffracted by the AOPC may be thought of as logical "ones"; absence of a diffracted beam then corresponds to a logical "zero".)

As shown in the conceptual schematic, the signal and reference beams are both formed in the AOPC. A cylindrical lens then recollimates the wavefront in one dimension. The spherical lens following the cylindrical lens forms an optical Fourier transform of the signal and reference beams at the spatial filter plane located one focal length away from the spherical lens. This filter, which is a rectangular slit, blocks stray light and shapes the signal and reference beams to form a one-dimensional hologram irradiance pattern. The next lens also acts as a Fourier transform lens, in this case making the galvanometer mirror surface an approximate image plane of the AOPC data pattern (signal). The galvanometer then scans a row of succeeding data patterns across the next transform lens on the upper half of the lens, while the reference beam is scanned simultaneously across the bottom half of the lens. At the film plane

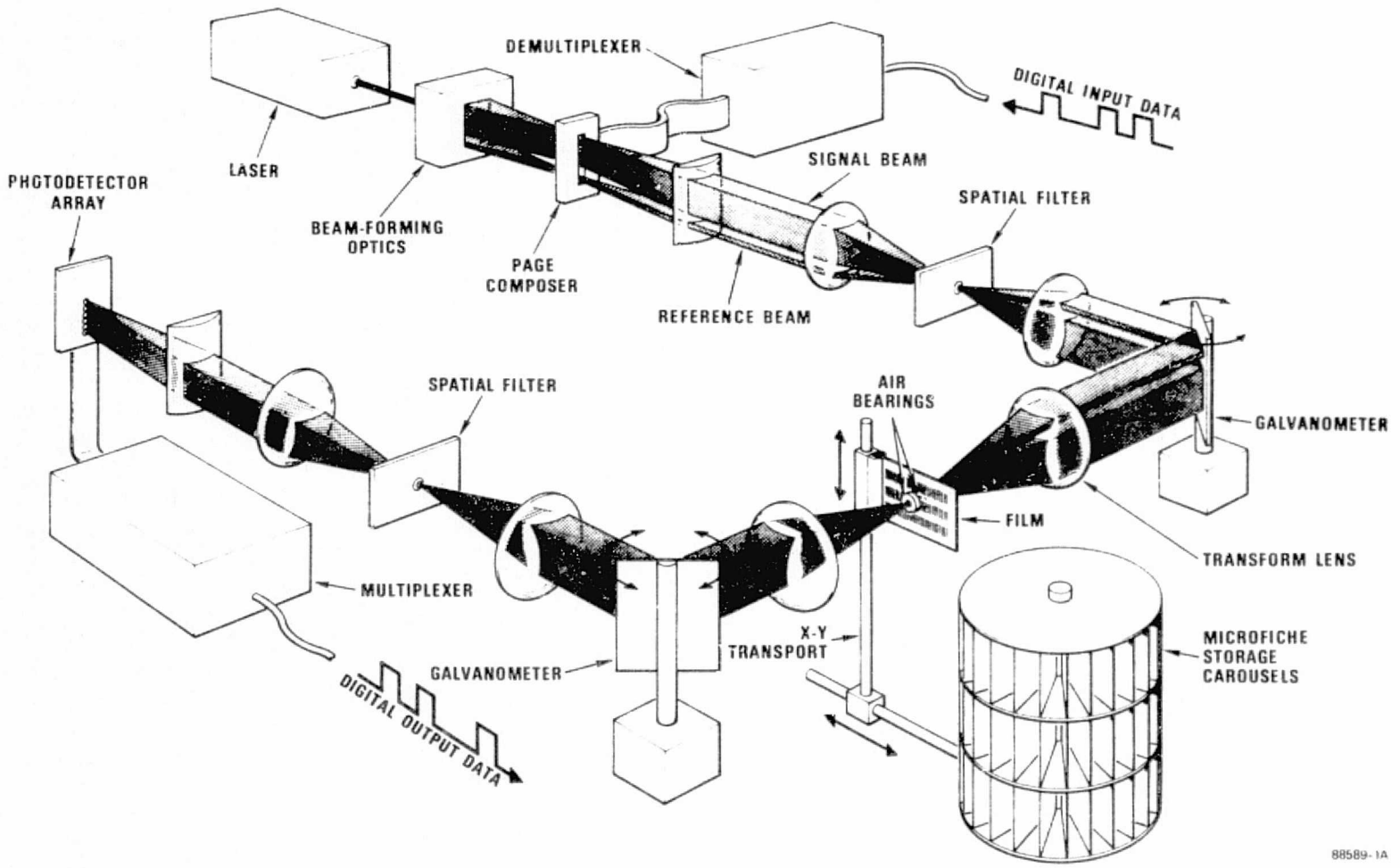

FIGURE 3-1. CONCEPTUAL SCHEMATIC FOR THE HOLOGRAPHIC MEMORY SYSTEM

the reference and signal beams interfere to become a row of successive holograms on film located between two air bearings. This completes a brief description of the holographic recording process.

To read out the holograms, that part of the AOPC which creates the reference beam is activated. The reference beam is incident on the first scanning galvanometer mirror. As the galvo scans, the reference beam illuminates a line of holograms and reconstructs the transform of the signal at the film plane. The signal transform is Fourier transformed onto the second galvanometer, which acts as another image plane of the AOPC data pattern. This galvanometer is driven so that its motion exactly counteracts the motion of the first galvanometer; the effect is to hold the output data pattern stationary after it is reflected off of the second galvanometer. This output pattern is transformed and filtered exactly as it was before the first galvanometer. A cylindrical lens collects the light in one dimension to focus the output data on a photodetector array.

Note that in Figure 3-1 there is a perfect symmetry about the film plane. The transform lenses are exactly alike on both sides of the film, as are the galvanometers. There is a transform filter plane with a spatial filter just before the first galvanometer and a similar filter plane is available after the second galvanometer. A cylindrical lens recollimates the light after the AOPC and a similar lens condenses the light on the photodector array. The AOPC and the photodetector array are conjugate planes.

3.1 MAJOR COMPONENTS

3.1.1 Synchronized Scan/Descan Subsystem

3.1.1.1 Comparison of Alternate Approaches

As our conceptual discussion suggested, a fundamental requirement of the HOLOMEM system concept is the ability to record a row of holograms across a film record. This implies scanning the signal and reference beams together across the entrance pupil of a Fourier transform lens, which in turn scans a row of holograms across the recording film plane within a film transport. In reading out the holograms, the reference beam scans the row and another Fourier transform lens forms an image plane of the reconstructed signal. The problem with this signal is that it is scanning along with the scanning reference beam, though clearly it would be desirable to hold the output signal stationary in space. For this reason, the scan-descan subsystem concept of Figure 3-2 was developed.

Very simply, the scan-descan assembly consists of two scanning mirrors driven in a manner so that a movement of the top mirror is exactly canceled by a movement of the bottom mirror. The performance goals for these scanners were: a 40 scans/s ramp frequency with a maximum of 7.5 ms for the retrace interval, 1500 resolvable positions per scan, a 4.2 degree full rotation angle, 0.2 percent linearity, and 0.05 percent repeatability; these goals assume a minimum mirror size of 25 mm in height by 7.5 mm in width. The next step is to determine the most effective approach to the problem.

The first possibility was to use a spinner assembly with a number of precisely-aligned facets mounted along the perimeter of a ring mounted on a motor shaft. Then the holograms would be read out by a beam scanned by one side of the assembly while the reconstructed signal is imaged on another side of the same assembly and descanned there. Though this approach is feasible, it creates some optical problems in bending the optical path back on itself to strike the spinner in two places and the

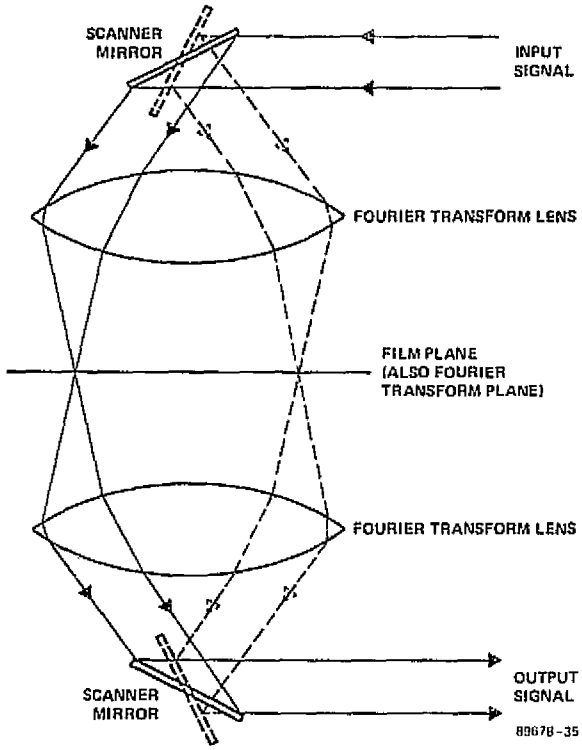

FIGURE 3-2. THE SCAN-DESCAN SUBSYSTEM

spinner assembly itself can cost upwards of $40,000. For this reason, the spinner approach was dropped in favor of a scan-descan system using two separate scanners.

Aeroflex Laboratories, Incorporated, was contacted to determine the usefulness of a second approach, brushless dc torque motors. The limiting characteristic of these motors at 40 Hz, regardless of the angular scanning range, is the inertia of the motor itself. Even with the very low rotor inertia of 1.13 gm-cm^2, this results in a corner frequency of about 90 Hz owing to the motor design. Using a rule of thumb suggested by Aeroflex that the corner frequency is approximately equal to the reciprocal of the desired settling time, this means that it would take longer than 10 ms for the scanner to settle. Optically, a sawtooth input would degenerate into a sine wave, and the nonlinearity would become much larger than 0.2 percent of the total angular deflection.

Servo motors have an even more severe problem than this for conventional devices, according to the Singer Servomotor catalog. Even at best, frequencies of as low as 2 cycles/s cause severe deterioration in the motor response. For sawtooth waveform inputs of the kind required for a truly linear scan, then, servo motors do not appear to be of much use.

For cam-driven mechanisms, the requirements are much more exacting than the last two approaches, as generally a much larger inertia must be rotated by the drive mechanism. In contrast to the other two techniques, however, the limitation of a low corner frequency can be overcome somewhat by adapting the geometry of the cam so that the uniform circular motion of a drive motor is translated into a variety of scanning waveforms. Nevertheless, a linear sawtooth drive is still a major problem to achieve at this high a frequency and this kind of resolution. It appears that a substantial development of cam drivers would be necessary before any accurate determination of cam driver capabilities for optical scanning could be made. For this reason, this method of scanning was dropped from consideration.

The final category of scanner devices considered in this subsystem was galvanometers. According to General Scanning Incorporated, a manufacturer of moving-iron galvanometer scanners, the scan frequency of 40 Hz is readily achievable as long as the ratio of the mirror inertia to the galvanometer's armature inertia is held to a minimum.

Before continuing with this evaluation, however, some analysis of the galvanometer mirror mount moment of inertia should be made. To begin, we note that a thin rectangular slab mirror of the kind illustrated in Figure 3-3 rotating about its center of mass has a moment of inertia of

$$I_1' = m_1 \frac{w^2}{12} \tag{3.1}$$

where m_1 is the mass of the mirror. This mass can be expressed as $m_1 = \rho_1 t_1 w \ell_1$, where ρ_1 = the density of the mirror material, and we have

$$I_1' = \rho_1 t_1 \ell_1 \frac{w^3}{12}$$

For the first of the two mirror mounts in Figure 3-3, Section a of the mount's moment of inertia can be expressed in two parts, I_2' and I_2'', where $I_2 = I_2' - I_2''$. Here I_2' is defined as the moment of inertia of the half-cylinder with radius r_1 and I_2'' the moment of inertia of a slab of thickness t_2 rotating about an axis displaced a distance $t/2$ from its center of mass. For the full cylinder, the moment of inertia is $m_2 r_1^2/2$, with $m_2 = \rho_2 \pi r_1^2 \ell_2$ and ρ_2 as the density of the mount material. If only half the cylinder is present and located as pictured, the mass is halved and it rotates about an axis translated approximately $r_1/2$ from its center of mass. Then we have that

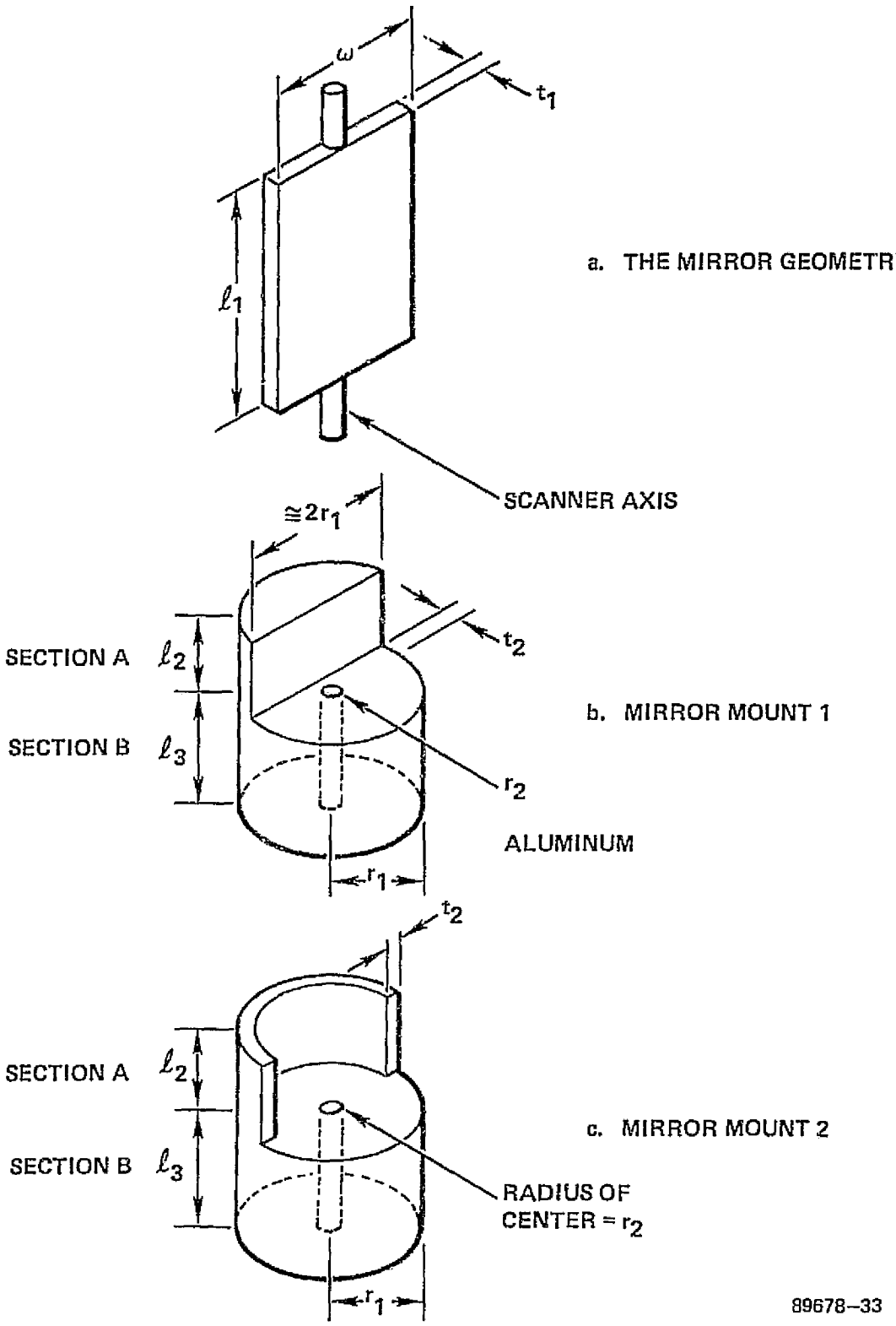

FIGURE 3-3. GALVANOMETER MIRROR MOUNT CONFIGURATION

$$I_2' = \pi \rho_2 \ell_2 \frac{r_1^2}{2} \left(\frac{r_1^2}{2} + \frac{r_1^2}{4} \right), \text{ or:} \tag{3.2}$$

$$I_2' = 3\pi \rho_2 \ell_2 \frac{r_1^2}{8} = \frac{3}{8} \pi \rho_2 \ell_2 r_1^2$$

I_2'' is given by

$$I_2'' = \left(\rho_2 t_2 \ell_2 \cdot 2r_1\right) \left(\frac{4r_1^2}{12} + \frac{t_2^2}{4} \right), \text{ or:} \tag{3.3}$$

$$I_2'' = \left(2\rho_2 t_2 \ell_2 r_1\right) \left(\frac{r_1^2}{3} + \frac{t_2^2}{4} \right)$$

Then we have that

$$I_2 = \rho_2 \ell_2 r_1 \left[\frac{3}{8} \pi r_1 - 2 \left(\frac{r_1^2}{3} - \frac{t_2^2}{4} \right) \right] \tag{3.4}$$

For ρ_1 = the density of glass for the mirror = 2.6 gm/cm^3, ρ_2 = the density of the aluminum mount material = 2.7 gm/cm^3, ℓ_1 = 2.54 cm, ℓ_2 = 1.27 cm, ℓ_3 = 1.27 cm, w = 0.75 cm, $t_1 = t_2$ = 0.318 cm, r_1 = 0.635 cm, and r_2 = 0.25 cm, the total moment of inertia for this mount is

$$I_4 = 1.1 \text{ gm-cm}^2$$

Section b of the first mount can be thought of as a cylinder with radius r_1 with a cylinder of radius r_2 bored out of its center. The expression for the moment of inertia of this section is, then

$$I_3 = \pi \rho_2 \frac{\left(r_1^2 - r_2^2\right)}{2} \ell_3 \tag{3.5}$$

The moment of inertia of the complete mount is therefore given by

$$I_4 \overset{\circ}{=} I_1 + I_2 + I_3, \text{ or:}$$

$$I_4 = \rho_1 t_1 \ell_1 \frac{w^3}{12} + \rho_2 \left[\ell_2 r_1 \left(\frac{3\pi r_1}{8} - 2\left(\frac{r_1^2}{3} + \frac{t_2^2}{4} \right) \right) + \pi_3 \frac{\left(r_1^2 - r_2^2 \right)}{2} \right] \tag{3.6}$$

For ρ_1 = the density of glass for the mirror = 2.6 gm/cm^3, ρ_2 = the density of the aluminum mount material = 2.7 gm/cm^3, ℓ_1 = 2.54 cm, ℓ_2 = 1.27 cm, ℓ_3 = 1.27 cm, w = 0.75 cm, $t_1 = t_2$ = 0.318 cm, r_1 = 0.635 cm, and r_2 = 0.25 cm, the total moment of inertia for this mount is I_4 = 1.1 gm-cm^2. This is the moment of inertia of the mirror mount used throughout most of the galvanometer evaluation phase of the program.

A second mirror mount was later designed to be used on the galvanometer in the breadboard system, and is pictured in Figure 3-3(c). Again, I_1 is the moment of inertia of the mirror, and I_3 is the moment of inertia of Section b of the mount. Section a, however, is calculated from the definition of the moment of inertia

$$I_5 = \int r^2 \, dm \tag{3.7}$$

where r is the radial distance of the infinitesimal mass dm of the mirror mount from the scanner axis. In this mirror mount we can write

$$dm = \rho_2 \ell_2 \cdot dr \cdot r \cdot d\theta \tag{3.8}$$

Inserting this relation in the last equation, this yields

$$I_5 = \rho_2 \ell_2 \cdot \int_{r_1 - t_2}^{r_1} \int_o^{\pi} r^3 \, d\theta \, dr, \text{ or:} \tag{3.9}$$

$$I_5 = \pi \rho_2 \ell_2 \cdot \frac{\left(r_1^4 - (r_1 - t_2)^4 \right)}{4}$$

The equation of the moment of inertia of the second mirror mount assembly is

$$I_6 = I_1 + I_3 + I_5, \text{or:}$$

$$I_6 = \rho_1 t_1 \ell_1 \frac{w^3}{12} + \pi\rho_2 \left(\ell_3 \cdot \frac{\left(r_1^2 - r_2^2\right)}{3} + \frac{\left(r_1^4 - \left(r_1 - t_2\right)^4\right)}{4} \right) \qquad (3.10)$$

With $\rho_1 = 2.6$ gm/cm^3, $\rho_2 = 2.7$ gm/cm^3, $\ell_1 = 4.0$ cm, $\ell_2 = 4.0$ cm, $\ell_3 = 1.27$ cm, $w = 2.2$ cm, $t_1 = t_2 = 0.16$ cm, $r_1 = 0.48$ cm, and $r_2 = 0.24$ cm, a size which was designed according to the hologram parameters discussed in detail in Paragraph 3.1.3, the moment of inertia $I_6 = 2.18$ gm-cm^2.

To judge the impact of these moments of inertia, Figure 3-4 is helpful. Adapted from General Scanning Incorporated's literature on their G-300 series of galvanometers, it depicts the degradation of the scanner corner frequency as the ratio of the mirror inertia to the galvanometer's armature inertia is held to a minimum. First note that a typical galvanometer unloaded corner frequency is 250 Hz, which according to Aeroflex's rule means that a sawtooth flyback time is approximately 4 ms, well below the required 7.5 ms at a 40 Hz scan frequency. For the first mirror mount designed, the ratio of I_4 (= 1.1 gm-cm^2) to the G-300 galvanometer's armature inertia of 3.7 gm-cm^2 is 0.30. Reading off the graph, this indicates a loaded corner frequency of ~0.88 x 250 Hz = 220 Hz, or a flyback time of 4.5 ms. For the second mirror mount, $I_6 = 2.18$ gm-cm^2, and the ratio of inertias is 0.59. This lowers the loaded corner frequency to about 0.80 x 250 Hz = 148 Hz, with a flyback time of 6.8 ms, still well within the 7.5 ms requirement. This indicates that what appears to be the limiting factor in galvanometer usage, the moment of inertia of the mirror and mirror-mount assembly, does not prevent their use in the breadboard system.

Further information on the General Scanning line of galvanometers indicated that the manufacturer's G-300 PDT temperature-regulated servo-controlled galvanometers, as well as possibly some of their G-100 and G-300 standard unservoed

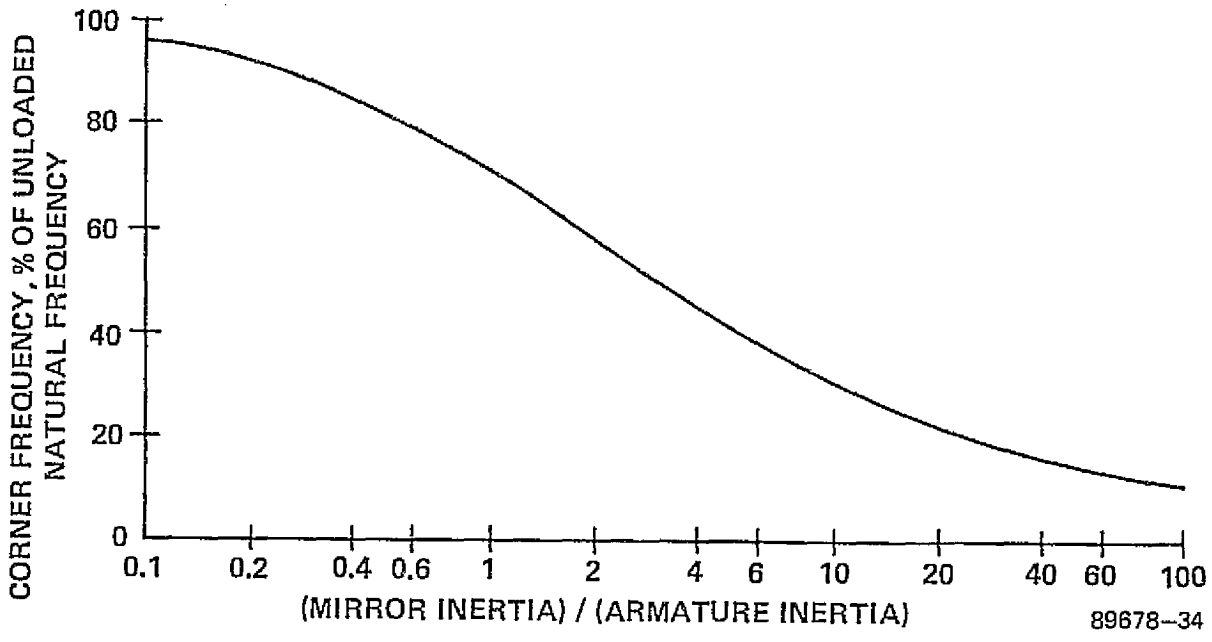

FIGURE 3-4. OPERATING GALVANOMETER CORNER FREQUENCY (EXPRESSED AS A PERCENT OF UNLOADED NATURAL FREQUENCY) AS A FUNCTION OF THE RATIO OF MIRROR INERTIA TO GALVANOMETER ARMATURE INERTIA

galvanometers, would meet all the required scanner specifications. A number of these scanners were acquired, and became the subject of more detailed scanner experiments.

3.1.1.2 Galvanometer Testing In Open-Loop Operation

As a starting point for galvanometer evaluation, the performance of selected General Scanning galvanometers designed for use without feedback was investigated. The galvanometers tested were the G-330, the Z-460, and the G-100PD; all were driven with a wave generator providing the signal input and a General Scanning RAX-100 unit the input waveform amplification and conditioning.

In terms of scan angle, both the G-330 and Z-460 galvanometers were found capable of a mechanical scan angle of over 25°, whereas the G-100PD ranged over 40°; the peak-to-peak scan angle is a function of the input RAX-100 damping resistance, and graphs of this effect appear in Figures 3-5 and 3-6. From this information it is clear that the galvanometers can easily provide the required 4.2° scan angle.

For a second test of the galvanometers, the response of the scanners to a range of frequencies within the test range was determined. For all of these investigations, mirror mount 1 of Figure 3-3 was used, and the peak scan amplitude was set to correspond to a mechanical scan angle of $5^{\circ} \pm 0.1^{\circ}$. As Figure 3-7 illustrates, for three typical signal damping resistances spanning the range of those available on the RAX-100 driver the G-330 shows substantial resonance problems, even replacing the 1.1 gm-cm^2 with a special "shaved" mount trimmed to a bare minimum of mount material and an estimated 0.03 gm-cm^2 moment of inertia resulted in the almost identical performance curve set of Figure 3-8. In both cases it is clear that the response falls off rapidly at frequencies above resonance. In addition, as damping resistance is increased, the resonant frequency decreases as expected; unfortunately, the amplifier could not be varied enough to obtain critical damping.

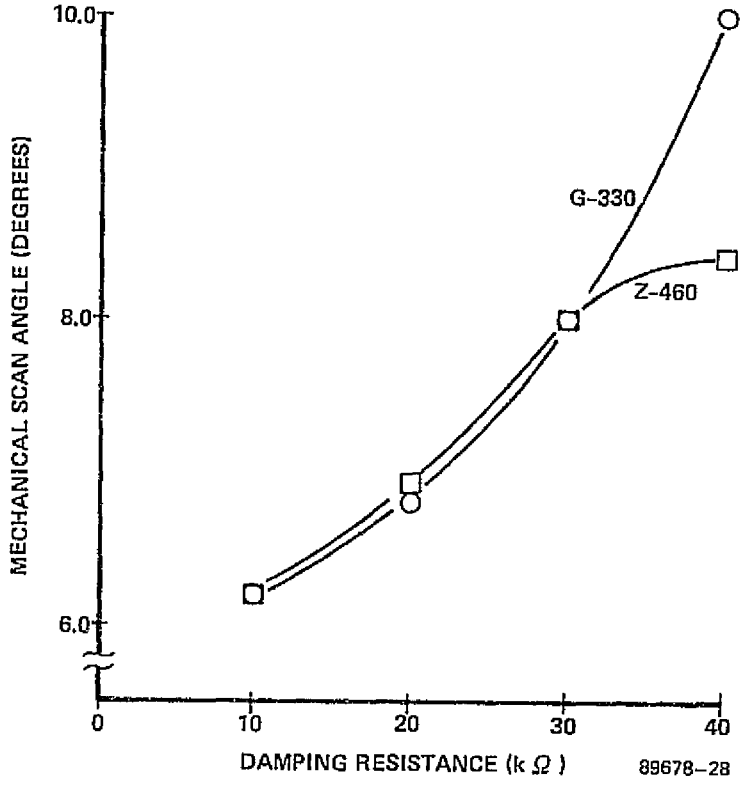

FIGURE 3-5. MECHANICAL SCAN ANGLE AS A FUNCTION OF DAMPING RESISTANCE FOR THE G-330 AND Z-460 GALVANOMETERS

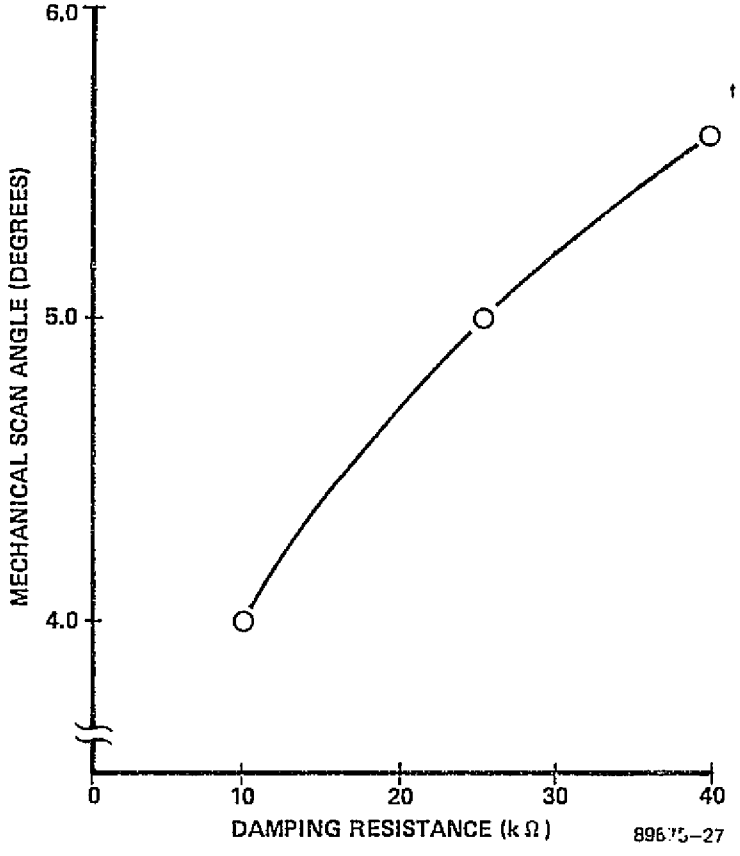

FIGURE 3-6. MECHANICAL SCAN ANGLE AS A FUNCTION OF DAMPING RESISTANCE FOR THE G-100 PD GALVANOMETER

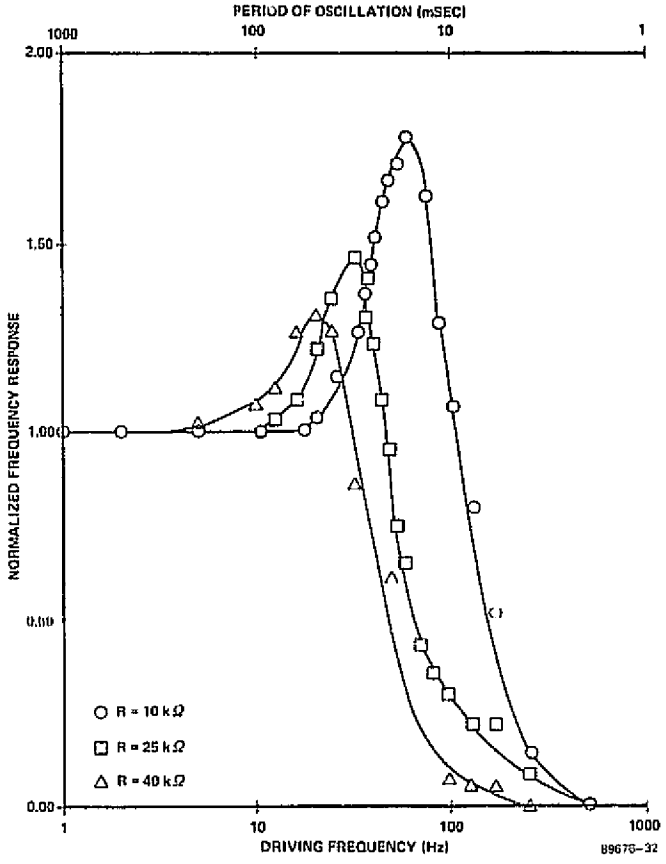

FIGURE 3-7. FREQUENCY RESPONSE OF THE G-330 GALVANOMETER WITH STANDARD MOUNT I

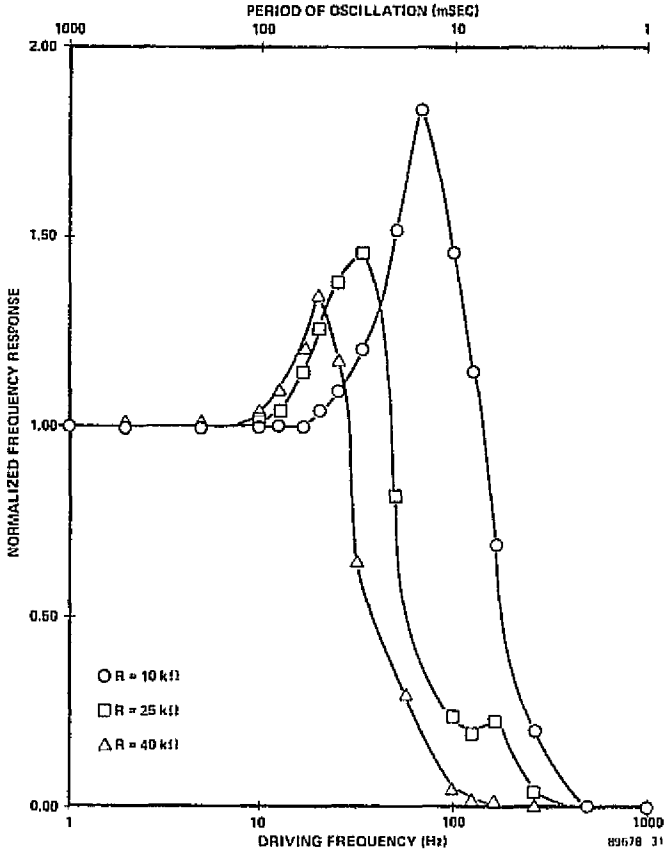

FIGURE 3-8. FREQUENCY RESPONSE OF THE G-330 GALVANOMETER WITH SHAVED MOUNT

The Z-460 galvanometer, when response is indicated in Figure 3-9, is intended for closed-loop operation in conjunction with a General Scanning servo-controller. This may explain the extremely strong response of the galvanometer at resonance, which may be the result of an understandable decrease in internal damping in a device designed for use with feedback. Without feedback, then, this galvanometer would not be suitable for use in the present system.

The G-100PD galvanometer's response while scanning a 3.2 mm x 3.2 mm x 1 mm is pictured in Figure 3-10 and illustrates that critical damping is achievable in this case. The observed resonant frequency of approximately 1000 Hz is high enough to allow use of the system, but the G-100PD has a major disadvantage in that its armature inertia is too small for the size of the mirror mount assembly required for this application; 0.011-0.015 gm-cm^2 is typical for the G-100 series armature inertia. Reference to Figure 3-4 makes it clear that even the "shaved" mount would place severe restrictions on the galvanometer performance.

To determine the linearity of the scan, the experimental configuration of Figure 3-11 was used. In this system the galvanometer mirror is at the first focal point of L_1, and it scans a collimated beam of light across L_1's entrance pupil. Because the scanner is at the focal point, L_1 can focus this scanned beam on a flat field, which in this case is a 200 cycles/inch Ronchi Ruling used as a spatial reference for the scan. Lens L_2 then forms the image of the galvanometer plane on a stationary photomultiplier (PMT), and a cylindrical lens C focuses the image on the PMT aperture. By displaying the signal from the PMT on an oscilloscope, the linear spatial reference of the Ronchi Ruling can be compared to any nonlinearities in the corresponding time intervals between successive peaks in the PMT output.

Once this apparatus was implemented, the G-330 and G-100PD galvanometers were tested by driving them with a ramp waveform with a 17.5 ms rise time and a 7.5 ms fall time; the RAX-100 driver/amplifier was set to a 40 kΩ damping resistance. By measuring the time intervals between successive 0.13° positions of the

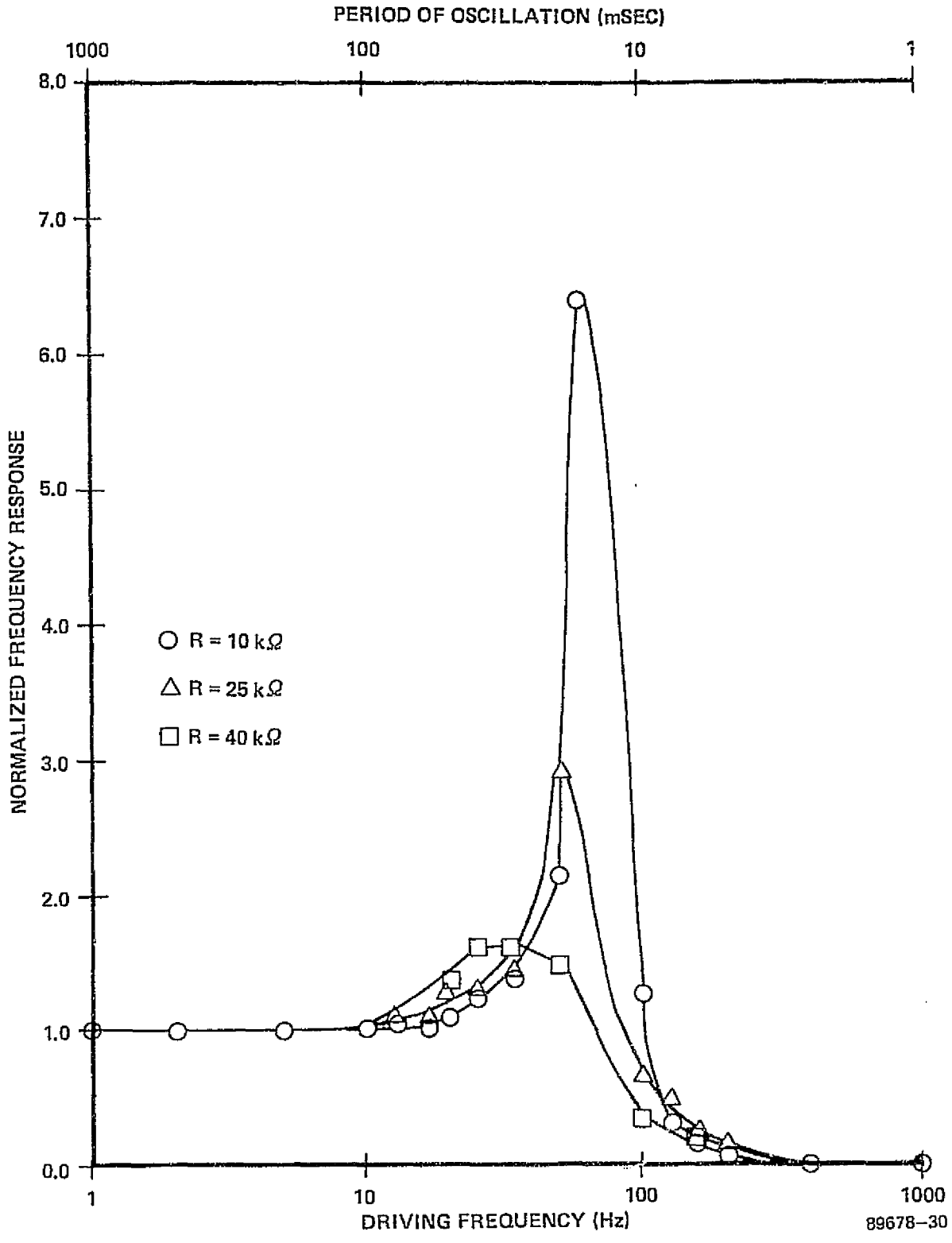

FIGURE 3-9. FREQUENCY RESPONSE OF THE Z-460 GALVANOMETER

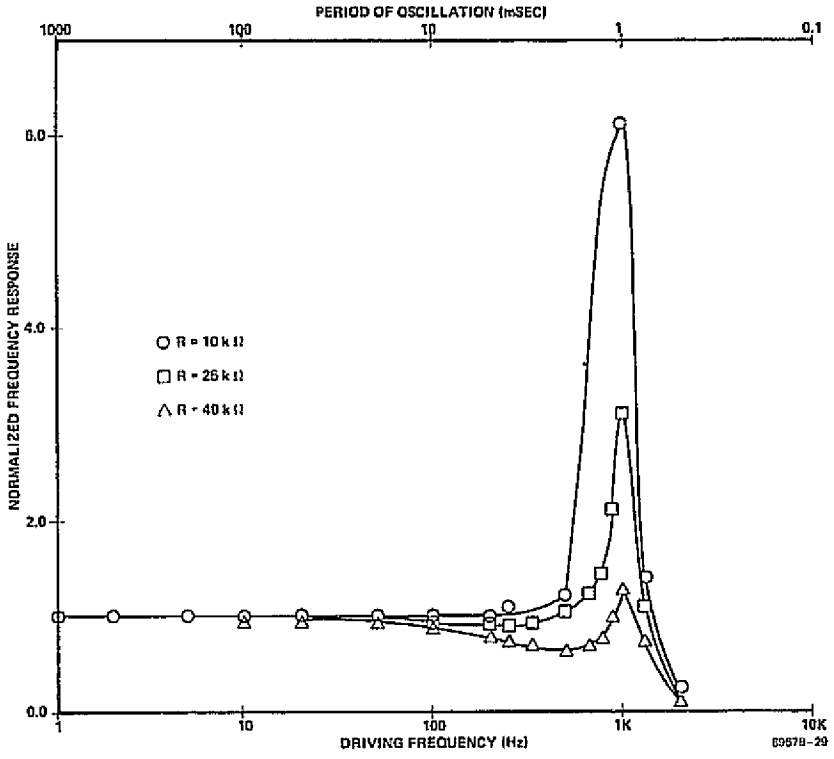

FIGURE 3-10. FREQUENCY RESPONSE OF THE G-100 PD GALVANOMETER

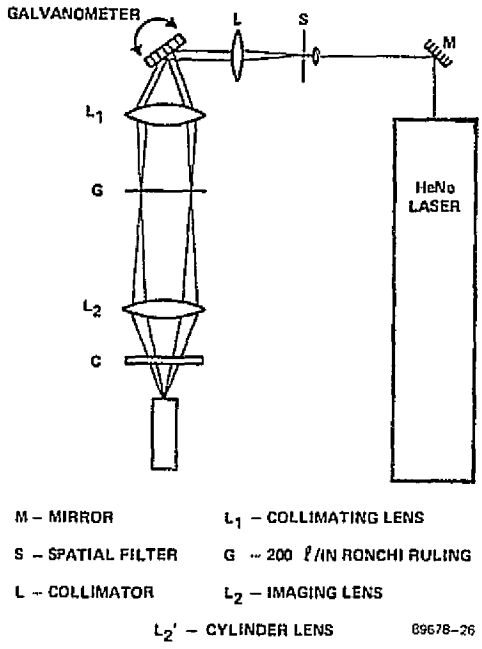

FIGURE 3-11. GALVANOMETER TEST ASSEMBLY FOR MEASURING SCAN LINEARITY AND REPEATABILITY

scan, the scan velocity at each position was calculated and the data plotted in Figures 3-12 and 3-13. As the first graphs show, for the G-300 the galvanometer is scanning at a frequency too close to resonance for a truly linear scan to be achieved. The G-100PD's performance is considerably better, but again, it is limited by mirror size and low armature inertia.

To achieve the required characteristics of performance for the scan-descan subsystem, the galvanometers cannot be run open loop. The G-330 and Z-460 models fail as the result of resonance at the 40 Hz scan frequency, and the G-100PD fails because of its marginal performance with a much smaller mirror than would be needed in the present system. At this point open-loop testing was discontinued in favor of galvanometer operation with electronic feedback.

3.1.1.3 Galvanometer Testing in Closed-Loop Operation

The galvanometers of the General Scanning line which are designed to run with position and velocity feedback and with sufficient armature inertia to swing large mirrors are in the G-300 PD series. These were used in conjunction with temperature regulation units mounted on the G-300's, the mirror mount number 1 of Figure 3-3 with a moment of inertia of 1.1 gm-cm^2, and CCX-100 electronic servo controllers for signal processing of the waveforms used as inputs to the galvanometers, as well as the feedback unit for the galvos. In addition, before any testing was begun, the standard PD-203 circuit card of each CCX-100 was altered to change R15's 100 Ω value to 10 Ω and C16 from 0.001 μF to 0.0005 μF. These changes were recommended by General Scanning to minimize settling time after the start of the scan.

As a first step in analyzing these galvanometers, the maximum angular excursion of the scan was measured to be in excess of 30° peak-to-peak at the required 40 Hz scan frequency. The problem here was that this is close to the maximum guaranteed angular field of the galvanometer, and a 40 Hz ramp input to the G-300 PD produced an optical scan which was linear for only 20 percent of the total scan time.

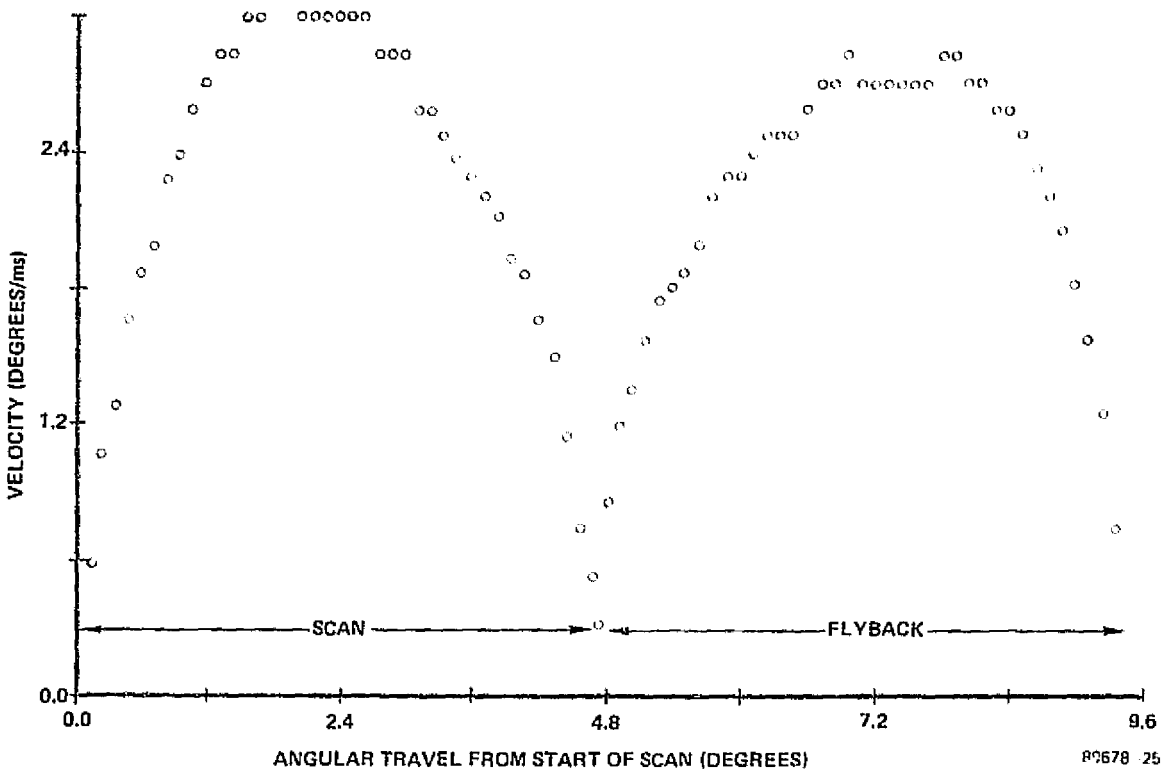

FIGURE 3-12. ANGULAR VELOCITY AS A FUNCTION OF SCAN ANGLE FOR THE G-330 GALVANOMETER

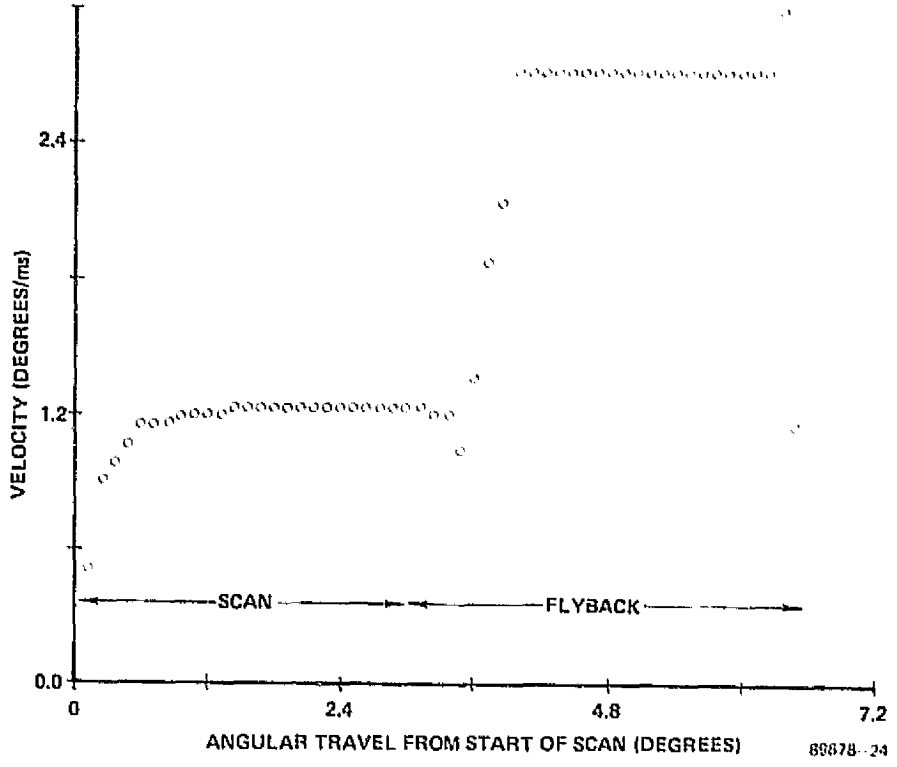

FIGURE 3-13. ANGULAR VELOCITY AS A FUNCTION OF SCAN ANGLE FOR THE G-100 GALVANOMETER

Backing the scan angle down to 20°-25° resulted in considerable improvement over the 30° performance.

To allow a more detailed evaluation of the scan properties, a G-300 PD galvanometer was placed in the testing system of Figure 3-11 as before. The angular deflection of the device was measured using a mirror placed in front of the galvo so that the collimated laser light as scanned by the galvanometer was reflected on the wall. With proper geometrical considerations, the ruler measurement in inches was made equal to the peak-to-peak angular deflection of the galvanometer in degrees, with an accuracy of 0.1°. (To aid in further analysis, the position output of the galvanometer, available as a signal from the CCX-100, was monitored and plotted against this angular deflection as shown in Figure 3-14). Once again, the photomultiplier tube response to the light moving across a Ronchi Ruling provided a timing calibration for each angular portion of the scan.

Linearity was the next specification investigated. Linearity is defined as the maximum angular error from the best straight-line fit for the curve of angular deflection versus time elapsed within the preflyback region of the scan, expressed as a percentage of the total angle used in the scan. Initially, it was thought that a graph of angular position versus time elapsed during the scan would yield the necessary information about linearity. As Figure 3-15 illustrates for a 4.5° peak-to-peak deflection, our scan is extremely linear. A scan velocity versus time elapsed in scan curve for the same data illustrates more clearly where ringing occurs (Figure 3-16; the flyback region is pictured in Figure 3-17).

The velocity scan for a 40.4 Hz, 10.2° peak-to-peak angular deflection is illustrated in Figure 3-18. In this case, flyback took up approximately 3.35 ms; this appears to be the shortest flyback possible for any frequency of the galvanometer, at least when used with a CCX-100 and the present ramp input. The time required for the galvanometer to settle down to the linear region of the scan (after flying back) is about 3.26 ms, which also refers to an angular loss of about 1.73°; here we have defined the

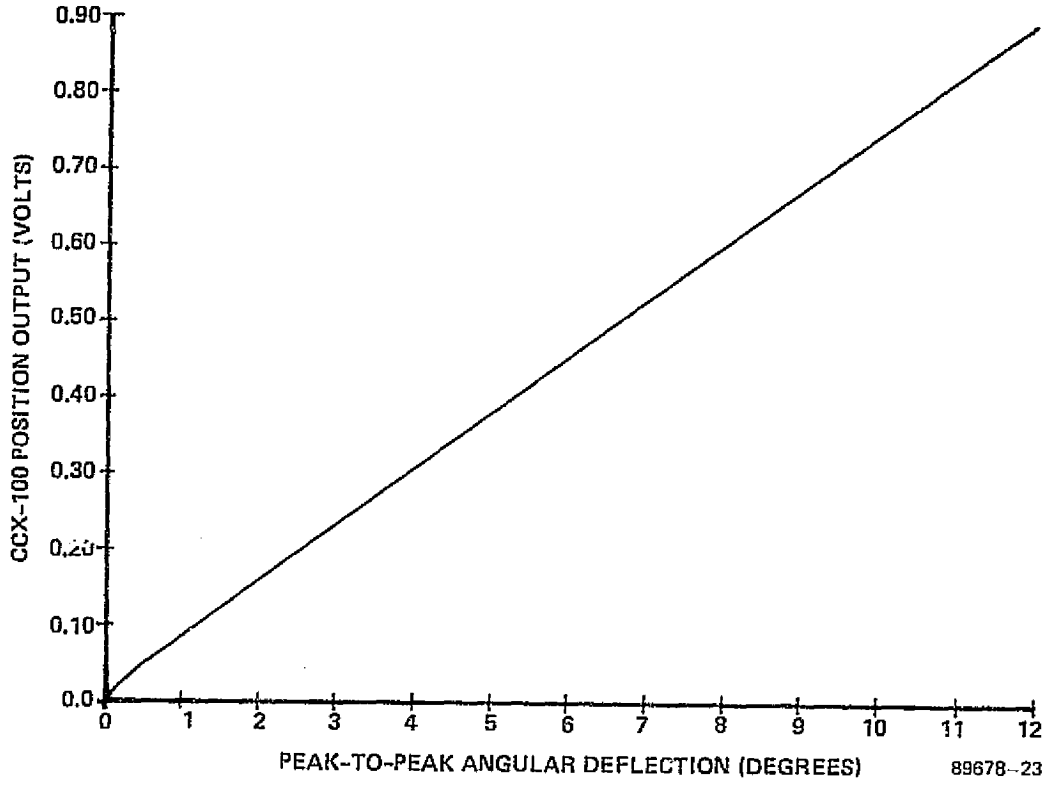

FIGURE 3-14. PEAK-TO-PEAK ANGULAR DEFLECTION AS A FUNCTION OF POSITION OUTPUT FROM THE CCX-100

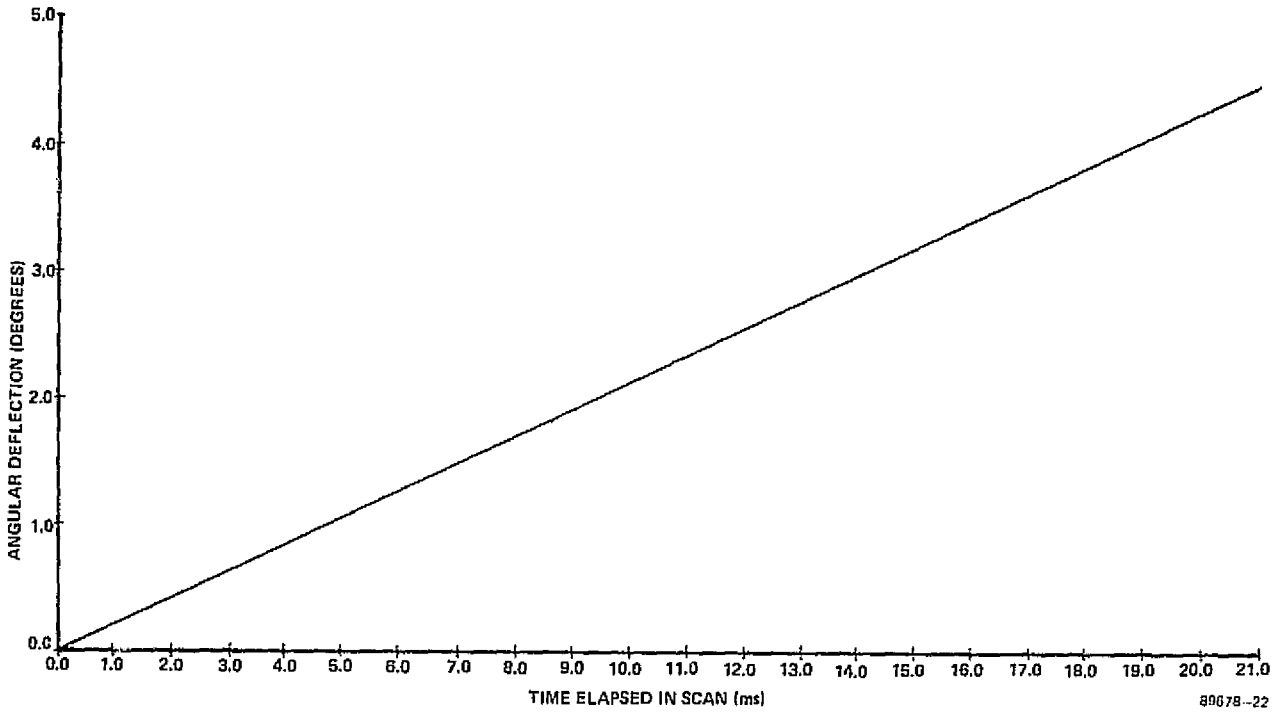

FIGURE 3-15. ANGULAR DEFLECTION AS A FUNCTION OF TIME ELAPSED IN SCAN FOR A 4.5° PEAK-TO-PEAK SCAN ANGLE

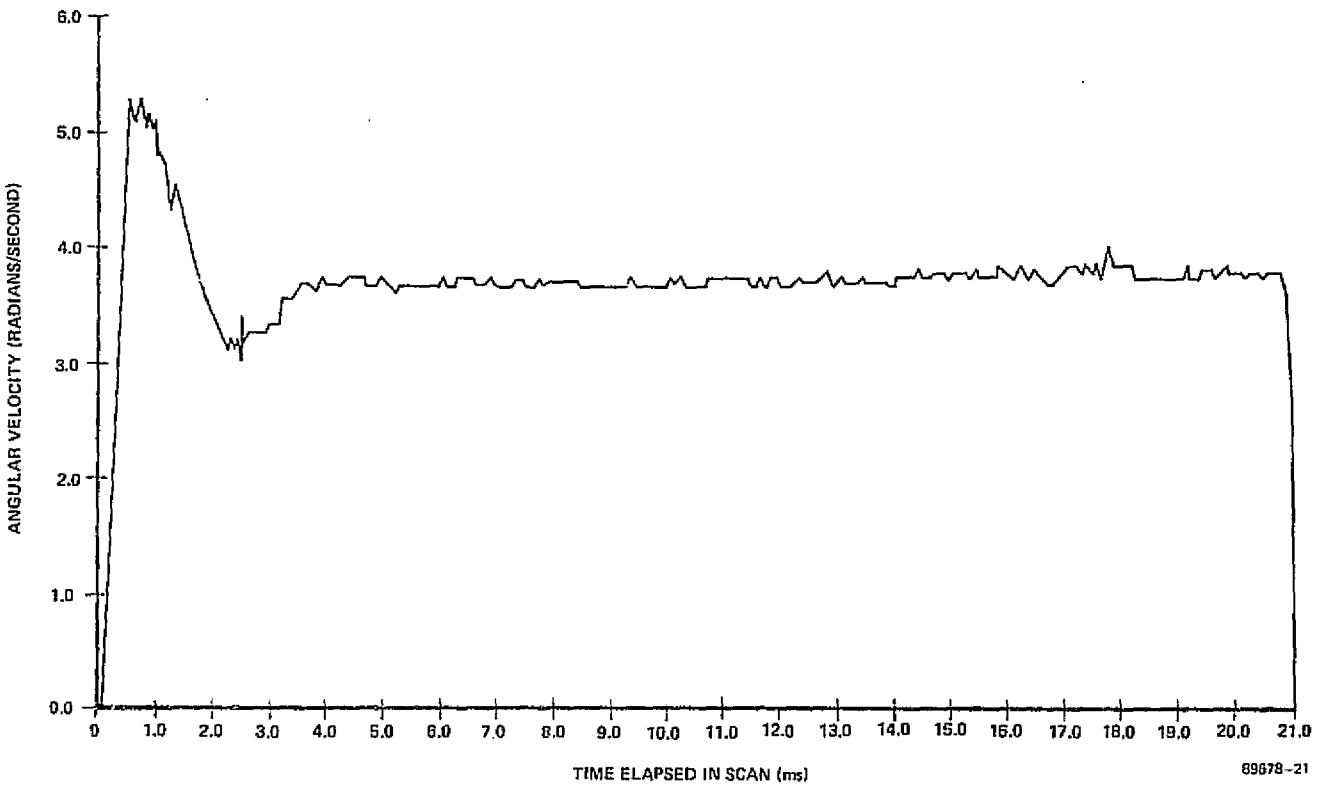

FIGURE 3-16. SCAN VELOCITY AS A FUNCTION OF TIME ELAPSED IN SCAN FOR A 4.5° PEAK-TO-PEAK SCAN ANGLE, SCAN REGION

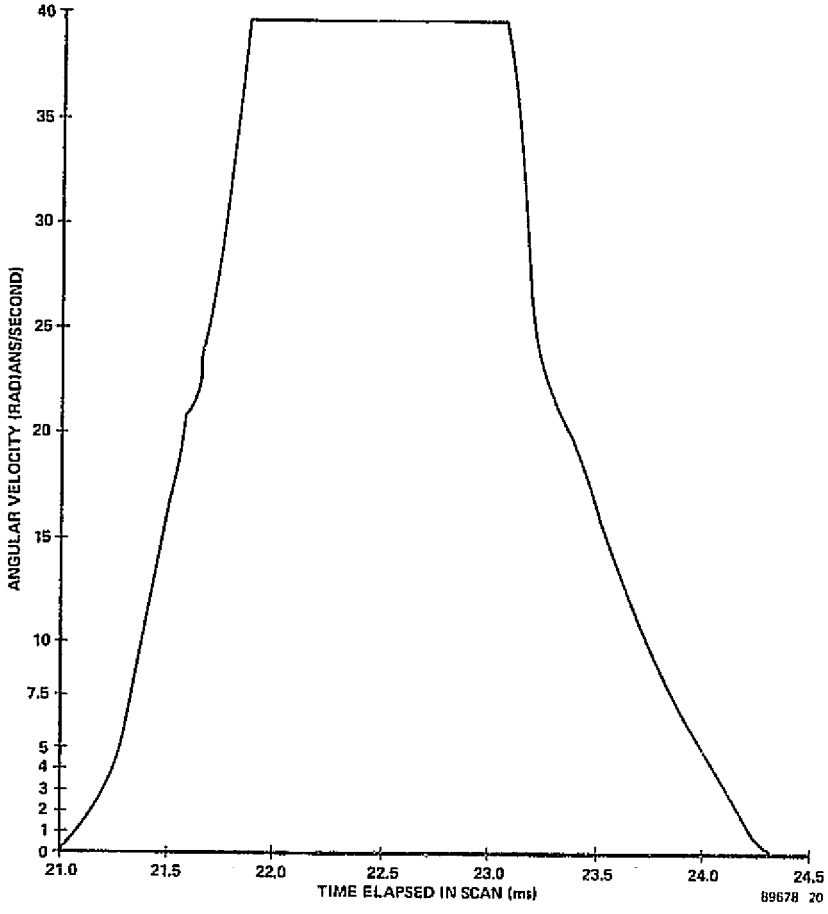

FIGURE 3-17. SCAN VELOCITY AS A FUNCTION OF TIME ELAPSED IN SCAN FOR A 4.5° PEAK-TO-PEAK SCAN ANGLE, FLYBACK REGION

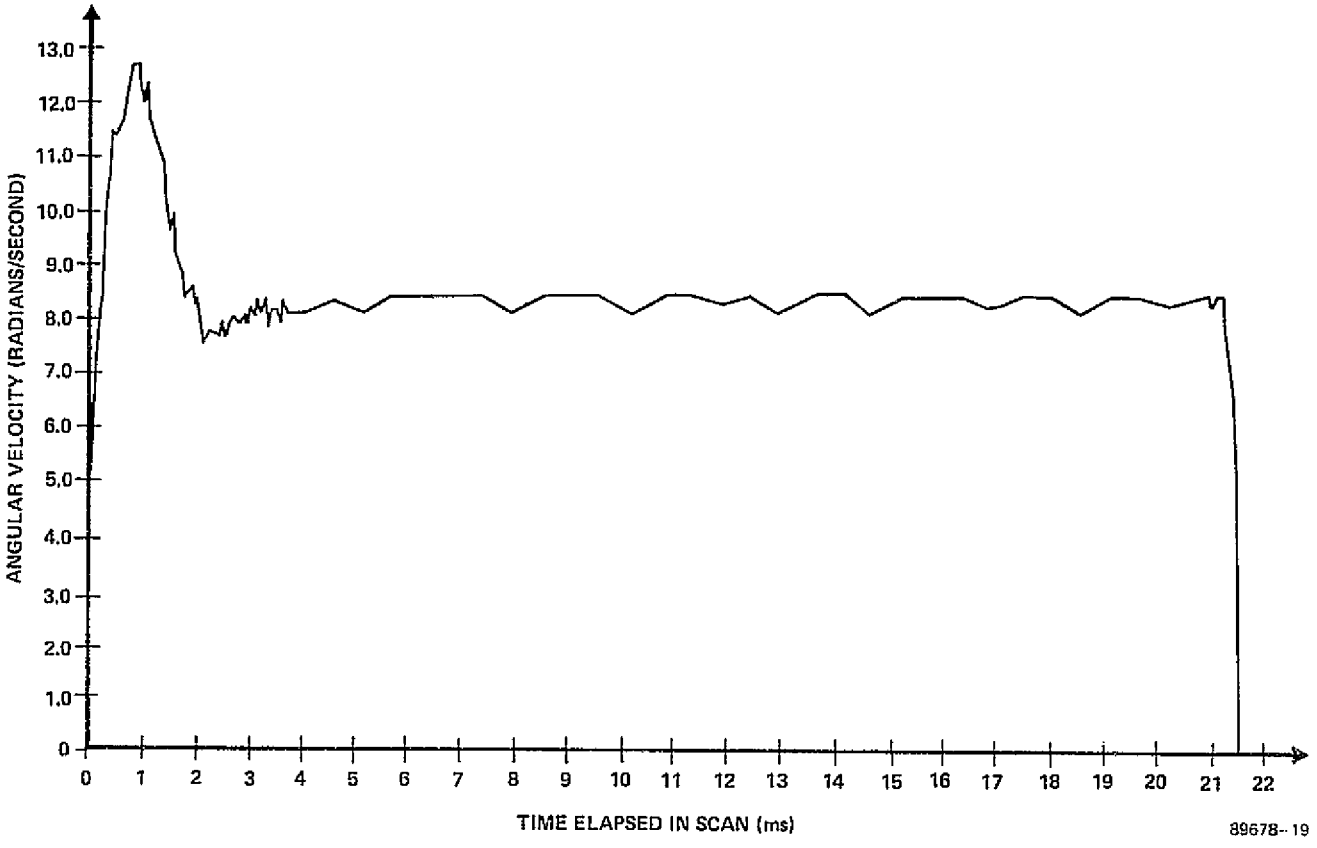

FIGURE 3-18. SCAN VELOCITY AS A FUNCTION OF TIME ELAPSED IN SCAN FOR A 10.2° PEAK-TO-PEAK SCAN ANGLE

"linear region of the scan" as that region where the scan velocity fluctuates by no more than ±5%. The total settling time plus flyback, including the small nonlinear region at the end of the scan is 6.77 ms, with a total angular loss of 1.78°. Again, this 6.77 ms appears to be a fundamental limitation with the present apparatus, as is the loss of approximately 17-18 percent of the angular scan in settling. There is some flexibility if the linearity is allowed to grow marginally larger, offering as much as 1 ms less settling time and 4.6 percent more useful angular sweep while retaining a linearity of about 0.05 percent. This does, however, make the linearity less uniform at the beginning of the sweep. In either case, since the linearity specification was 0.2 percent, these data indicate that the G-300 PD's performance is well within the required specification limit; the G-300 PD also satisfies the requirement that the flyback time for a 40 Hz ramp be less than 7.5 ms total (including settling time).

Next, we evaluated repeatability of the scan; this is a short-term repeatability, the fluctuation in the temporal position of a given portion of the scan, and it is given by the maximum timing error (equivalent to a maximum angular error) expressed as a percentage of the total useful scan time (again equivalent to the amount of angle actually used). To measure this, a wave generator was used to provide a 20 kHz sine wave to match the frequency of the photomultiplier tube output trace from the scan across the Ronchi Ruling. It was fitted to the PMT trace by adding the two signals on a Tektronix 475 oscilloscope, and adjusting the 20 kHz wave generator signal until the beat frequency was minimized. Finally, the two traces were observed separately, with the sine wave signal providing a stable reference alongside the short-term fluctuations of the PMT trace. As this approach adds all the errors of the oscilloscope trigger stability, the photomultiplier tube stability, and the actual galvanometer fluctuations, the repeatability was measured as a percentage fluctuation of the time between peaks on the PMT trace, and is shown in Figure 3-19 with the fluctuations in the flyback region estimated (they may have varied as much as 100 percent). The repeatability for the 10 percent peak-to-peak fluctuation translates to a 0.03 percent repeatability when expressed as a percent of the total time available in this "repeatable" region. Again,

as with the linearity, there is some margin of flexibility for what is defined as the "repeatable" region, though uniform repeatability is assured only in the region indicated. Since the repeatability is required to be 0.05 percent, the G-300 PD satisfies this specification.

The final remaining need is to demonstrate that the scanners have 1500 resolvable spots per scan. In this case, the inverse of the linearity is one means of measuring this. The number of spots (i.e., resolvable positions) for each scan is therefore equal to $\frac{1}{0.0005} = 2000$ resolvable positions. Hence, the G-300 PD galvanometers with the 1.1 gm-cm^2 mirror mount, temperature regulation, and feedback from the CCX-100 servo controller, fulfill all system requirements.

A summary of scanner specification and the performance of the General Scanning G-300 PD galvanometer is given in Table 3-1.

3.1.1.4 Performance of the Scan-Descan Subsystem

The final step in assembling the scan-descan system is to assemble two identical scanners as shown in Figure 3-2 and test the performance of the system. In the final assembly, the scanners were mounted as in the photograph of Figure 3-20 with two 4-inch EFL, f/2 Super Baltar lenses as the Fourier transform lenses between them. The scanners are mounted upside down with respect to each other so that the same waveform can be used as the input to each galvanometer, while still providing the mechanical compensation to hold the output signal position stable.

To test the magnitude of the stability, the scanning beam was focused onto a 300 cycles/inch Ronchi Ruling to yield approximately 514 μradians resolution per ruling crossing. With the best matching of the output waveforms of the G-300 PD's, the results of detecting this data appear in Figure 3-21. In the upper oscilloscope photo only one galvanometer is scanning, whereas in the lower photo both galvanometers are scanning; the upper trace in each photo is the photomultiplier output and the bottom one the position output from the CCX-100 for a single galvanometer. As is evident from the

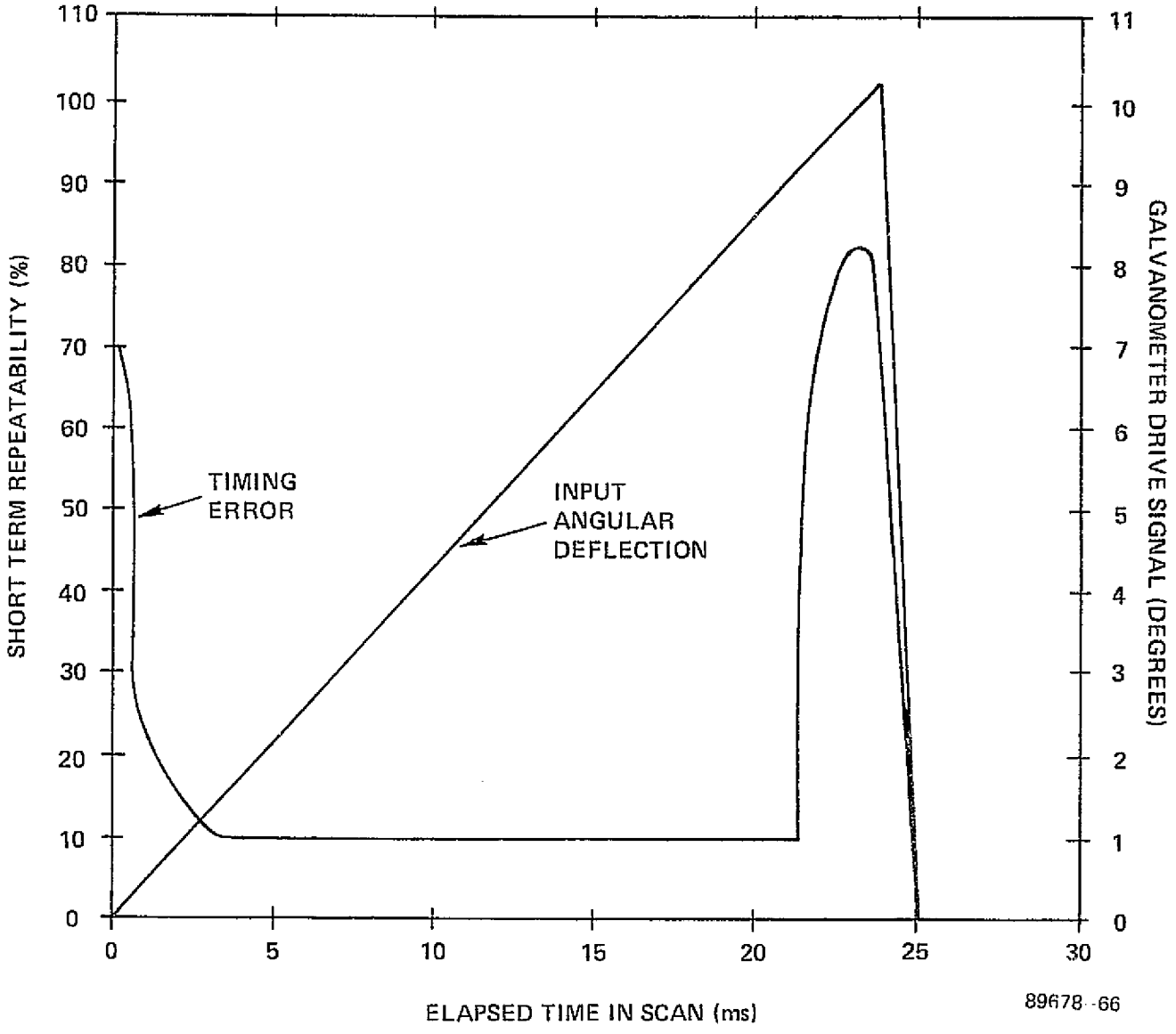

FIGURE 3-19. SHORT TERM SCAN REPEATABILITY AND ANGULAR SCAN POSITION AS FUNCTIONS OF TIME ELAPSED IN SCAN

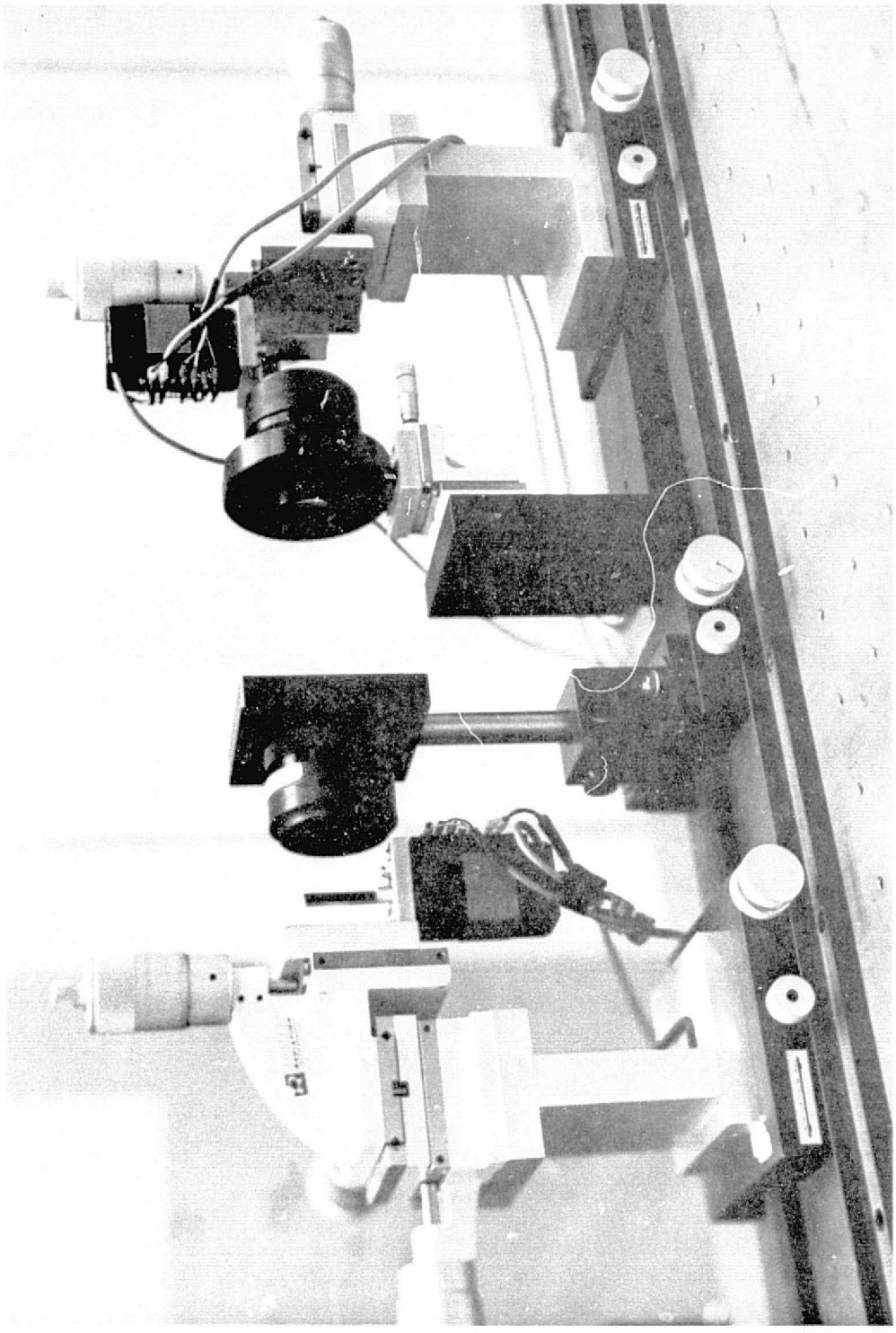

89678-101

FIGURE 3-20. PHOTOGRAPH OF THE FABRICATED SCAN-DESCAN SUBSYSTEM

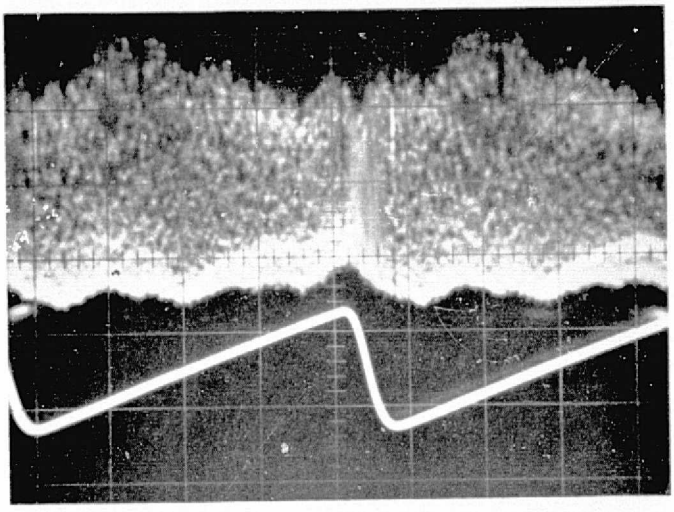

a. SINGLE GALVANOMETER SCANNING

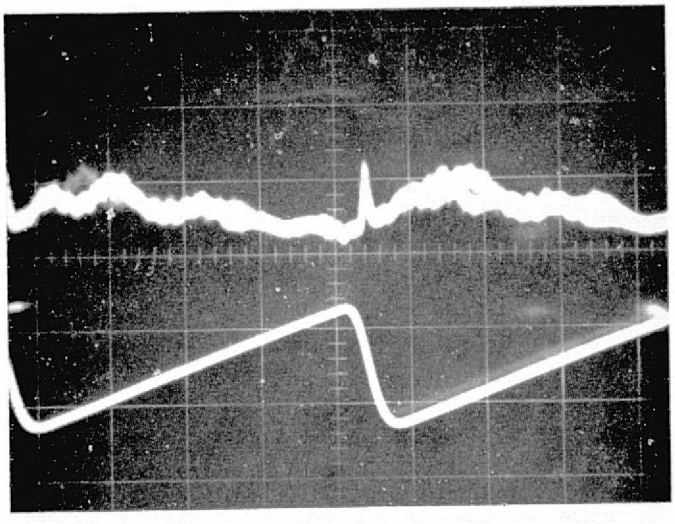

b. BOTH GALVANOMETERS SCANNING

89678–43

FIGURE 3-21. POSITION OUTPUT FROM A GALVANOMETER (BOTTOM TRACE) AND TRACE OF SCAN ACROSS A 300 CYCLE/INCH RONCHI RULING (TOP TRACE)

TABLE 3-1

SCANNER PERFORMANCE CHARACTERISTICS*

PARAMETER	SPECIFICATION	G-300 PD PERFORMANCE
Retrace Interval	7.5 ms max	<6.8 ms
Full Rotation Angle (Peak-to-Peak)	4.2°	>30°
Linearity	<0.2%	<0.05%
Repeatability	<0.05%	<0.03%
Number of Resolvable Positions Per Scan	>1500	2000

*For a minimum mirror size of 25 mm x 7.5 mm and a 40 Hz ramp waveform input.

photographs, the scan-descan subsystem holds the signal stable to less than 514 μradians total drift. A higher-frequency grating of 1000 cycles/inch was used in place of 300 cycles/inch grating to obtain the photograph in Figure 3-22, and it is again evident that for most of the scan the position output is stable to its correspondingly more accurate 154 μradians (per line crossing). In further tests, this accuracy was maintained for days, after equipment shutdown and restarted a day later. In this dimension, then, the scan-descan performance is excellent.

For scan stability in the direction transverse to the scan direction, the ruling was rotated 90° from its original position and similar results were obtained for the scan-descan performance when the scanners were properly mechanically aligned.

The scan-descan subsystem thus fully satisfied all requirements for this component of the holographic memory system.

3.1.2 The Photodetector Array

A major component of the breadboard system is the photodetector array (PDA) for reading out the reconstructed hologram data. The performance goals were 4.0 Mb/s instantaneous data transfer rates, 2×10^{-12} joules of incident light energy at 632.8 nm for detector saturation, 18 dB signal-to-noise ratio, and 20 dB isolation between neighboring detectors.

3.1.2.1 Fiber Optic-Coupled PDA

The first possibility evaluated for such a system involved an array of 128 hybrid photodetectors with fiber-optic coupling to the data image plane. For such an array of detectors to be capable of a total 4.0 Mb/s instantaneous data rate, each detector must attain a 31.25 kHz clock rate. One impact of this on the detectors is that, regardless of the available bandwidth of a detector, the effective bandwidth is 70-90 kHz for the purpose of calculating the noise equivalent power (NEP) for each unit. The only exception occurs when a detector itself limits the bandwidth, as in the case, for

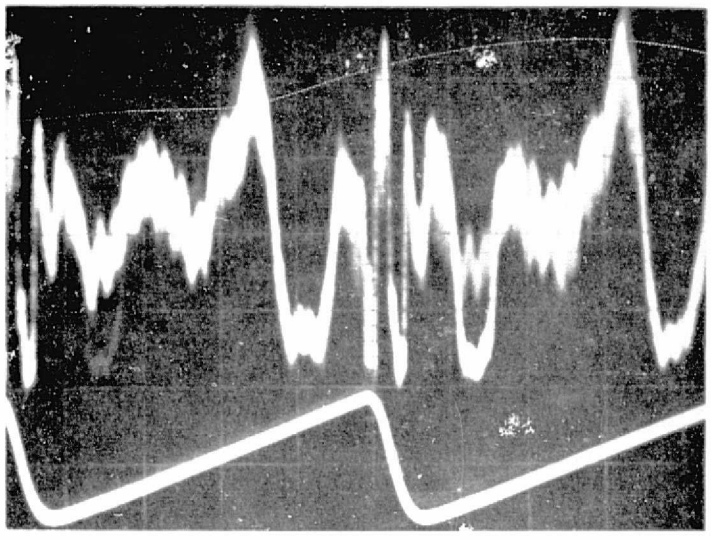

89678–42

FIGURE 3-22. POSITION OUTPUT FROM A SINGLE GALVANOMETER (BOTTOM TRACE) AND TRACE OF SCAN ACROSS A 1000 CYCLE/INCH RONCHI RULING (TOP TRACE) FOR BOTH GALVANOMETERS SCANNING

example, of the MDA_{320} unit from Meret which only operates from dc to 60 kHz. Another result of this is that the maximum signal per detector for a 2×10^{-12} joules light saturation level is

$$2 \times 10^{-12} \text{ joules} \times 31.25 \times 10^{3}/\text{s} = 62.5 \times 10^{-9} \text{ watts}$$

These two results make it possible to calculate an NEP (see NEP_2 in Table 3-2) based on the characteristics of the present system, as well as a SNR for each detector based on the maximum signal. While this SNR is an important "figure of merit" for the detectors, its actual value will be different than this in use, owing to the use of the fiber-optic signal distributor, the incident radiation being less than the saturation level, and any signal-processing techniques in the readout electronics. Nevertheless, it can be used as a basis for comparison.

Based on the tabulated comparison summarized in Table 3-2 between three typical hybrid photodetector preamplifier units which have been used in past similar applications, the MDA_{320} outperforms either the MDA_{321} or the C30816, primarily because of its low NEP, and the limiting 60 kHz bandwidth. The MDA_{320} also is superior as far as responsivity is concerned; it is 10 times more sensitive than the C30816. It is also, not unexpectedly, the most expensive of the three. A 128 element array of the MDA_{320} units would cost $13,824, as compared to a cost of approximately $9,600 for an identical array of either the MDA_{321} or C30816 units. This recommends the use of the MDA_{321} with its acceptable 21 dB SNR and lower sensitivity, but with a gain of a factor of 32 in risetime capability. With signal processing, these trade-offs should not create a significant problem area.

To implement fiber-optic coupled detectors in a practical system, their large size makes it necessary to connect each one to a separate fiber-optic cable. A linear array of these fiber-optic cables assembled as pictured in Figure 3-23 would then be used to relay the optical signals to the individual detectors. To guarantee the performance of such a device, several design factors must be considered.

TABLE 3-2

HYBRID PHOTODETECTOR PREAMPS

CHARACTERISTICS	UNITS	MDA_{320}	MDA_{321}	C30816
Responsivity (at 632.8 nm)	mV/μW	>300	>35	6
NEP_1	W/(Hz)1/2	6×10^{-13}	2×10^{-12}	3×10^{-12}
Available bandwidth	MHz	0-0.06	0-1.5	0-10.0
Bandwidth (in use)*	kHz	60	70	70
NEP_2 (in use)	Watts	1.47×10^{-10}	5.3×10^{-10}	7.95×10^{-10}
SNR at saturation	dB	26.0	21.0	19.0
Risetime	ns	<8000	<250	35
Cost/unit (1-4)	$	195	93	95**
Cost/unit (100-199)	$	108	74	65**
Manufacturer	---	Meret, Inc.	Meret, Inc.	RCA

*Bandwidth for 128 detectors, each operating at 31.25 kHz, to give a net data rate of 4 Mb/s.

**Price quote as of late 1973; these prices are undoubtedly higher now.

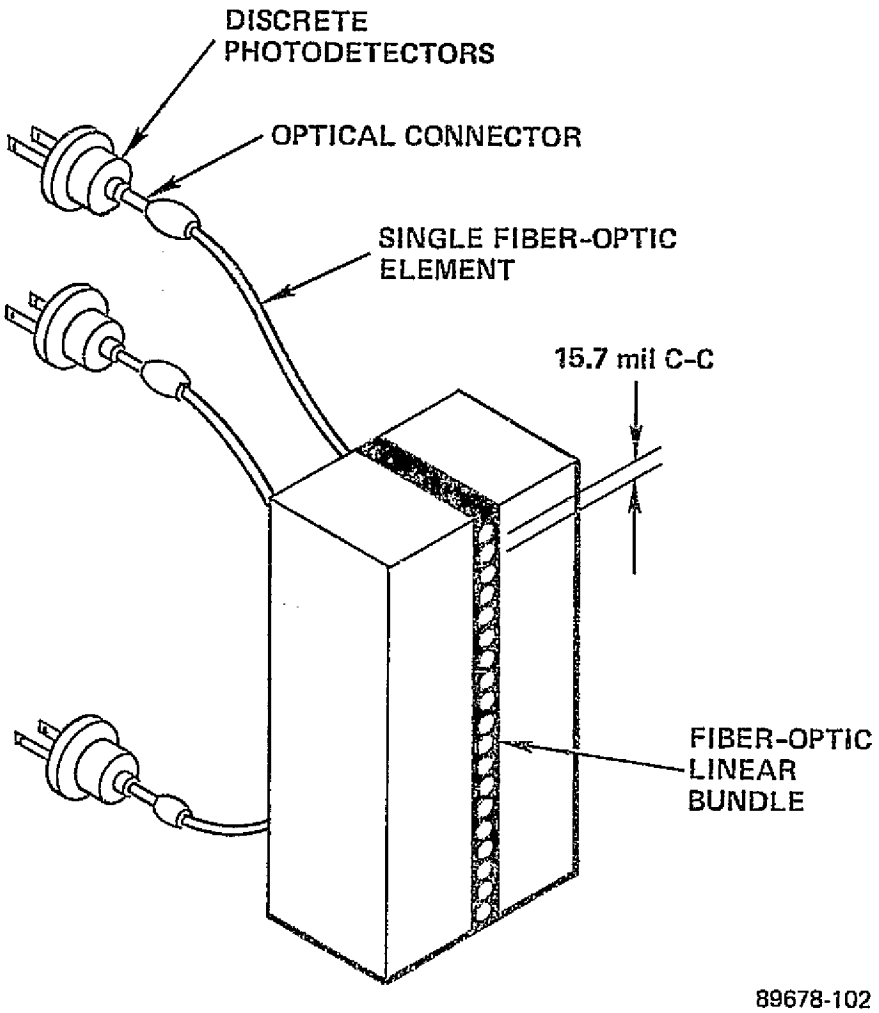

FIGURE 3-23. A FIBER-OPTIC SIGNAL DISTRIBUTOR

The first of these, the array spatial duty cycle, is the ratio of the fiber clear aperture to the fiber center-to-center spacings. Clearly, the larger the element spacing the greater the detector-to-detector isolation; however, this must be balanced against the expected data channel spacing errors, channel jitter, and noise considerations. In view of this, a spatial duty factor of 64 percent has been chosen as a compromise value in practice.

A second consideration is the uniformity of the fiber transmittance from one channel to the next. During experimental studies, it was found that the variation of fiber diameters was the main cause of transmittance nonuniformity; to achieve a maximum transmittance fluctuation of less than 5 percent from fiber to fiber, the fiber diameters were selected to an accuracy of plus or minus 0.0001 inch. The fiber lengths could then be trimmed for final adjustment of their transmittances.

A third factor of importance for fiber arrays was the optimum connection of fibers to their detectors. Although a number of methods have been evaluated to accomplish this, the most effective was to cut the ends of the fibers with a razor blade and then insert them into disposable hypodermic needle tips. These tips could then be plugged into mechanical couplers in front of the detectors with final detector-fiber connection achieved through the use of an optically clear, nonrigid selastic material on the detector surface. This provided a deformable interface between the optical fiber and the detector. Also, because the selastic has a low power "lensing" effect and index-matches the fiber to the detector to a degree, the optical coupling efficiency between fiber and detector was increased 25 to 30 percent over simple mechanical coupling techniques. Each fiber must also be polished on the input end, as well as protected by a protective sleeving of "RTV", a silicone compound, wherever possible.

Using these techniques, fiber-optic arrays have been successfully fabricated with over 5 MHz per channel data rates and less than 10^{-6} bit error rates.

3.1.2.2 Reticon Photodiode Array

As the above descriptions show, the major drawbacks to the use of discrete detectors are the high cost of the materials and the complexity of producing a fully-integrated fiber-optic array. For these reasons a second photodetector array alternative, the solid-state self-scanned photodiode array developed as an off-the-shelf component from Reticon Corporation, was evaluated.

The Reticon arrays are units having 64, 128, 256, 512, 1024, 1728, and 1872 elements in the size range used for most applications. The 256 and 512 element arrays have two and four output lines, respectively, each of which is capable of approximately 18 dB SNR and 15-19 dB isolation between adjacent detectors at 2.5 MHz data transfer rates per output video line. A typical 24 mil x 1 mil detector element aperture requires a saturation exposure of:

$$0.21\ \mu W - s/cm^2 = 2.1 \times 10^{-7}\ J/cm^2 \text{ for tungsten light.}$$

The detector area is:

$$24\ \text{mil} \times 1\ \text{mil} = 1.50 \times 10^{-4}\ cm^2,$$

So the total saturation exposure is:

$$31.50 \times 10^{-12}\ J/\text{detector}.$$

This, however, does not apply for the 632.8 nm Helium-Neon laser light intended for use on the breadboard; to correct for that, Reticon has supplied data showing that their detectors are 3.6 times more sensitive to He-Ne light than to tungsten illumination. Therefore, the total saturation exposure is approximately 8.75 pJ/bit. It should also be noted that even if the detector size was changed by masking, the saturation exposure requirement will not change because it is determined by the underlying charge storage "bucket" size below the silicon detector surface. With the exception of a marginal decrease in adjacent-detector isolation and a slightly higher saturation exposure, a dual video line 256-element array such as the RL256EBH detector (with 24 mil x 0.5 mil detector elements on 2 mil centers) meets all the necessary requirements, including a net

5 MHz data rate. In addition, the price of the RL256EBH is about $1500, and even with support hardware the total materials cost is less than $3000. Implementation of the detector array can be made with off-the-shelf circuit cards, many of which are available directly from Reticon.

Therefore, we decided to use the RL256EBH array because of cost and convenience considerations. If higher data rates or SNR were required, the hybrid photodetectors would have been required; however, the Reticon array easily satisfies the present breadboard requirements.

Experimental evaluation of the RL256EBH occurred after the total breadboard system was constructed; hence, the results of these tests are reported in Paragraph 3.3.2.

3.1.3 Acousto-Optic Page Composer

Optical recording of digital data requires that electronic data be converted in some way into optical data (by temporal or spatial beam modulation) and properly formatted for recording. The device which performs this function, both in holographic and direct spot recording schemes, is an acousto-optic page composer. (Figure 3-24).

3.1.3.1 Acousto-Optic Devices (General)

An acousto-optic (AO) device is a block of transparent material (various types of glass and crystals, for example) which deflects or modulates a laser beam. In the AO device a strain pattern associated with propagating acoustic waves exists. The acoustic waves are generated by an electromechanical transducer bonded to one face of the crystal. When connected to an appropriate RF source, a refractive index variation characteristic of a grating is produced in the transparent material. Light passing through the grating is diffracted in the Bragg mode if the angle of incidence of the light corresponds to the Bragg angle, as determined by the acoustic beam. The Bragg angle is defined as

$$\theta_B = 1/2 \frac{\lambda}{\Lambda} = 1/2 \frac{\lambda}{V_A} f \qquad (3.11)$$

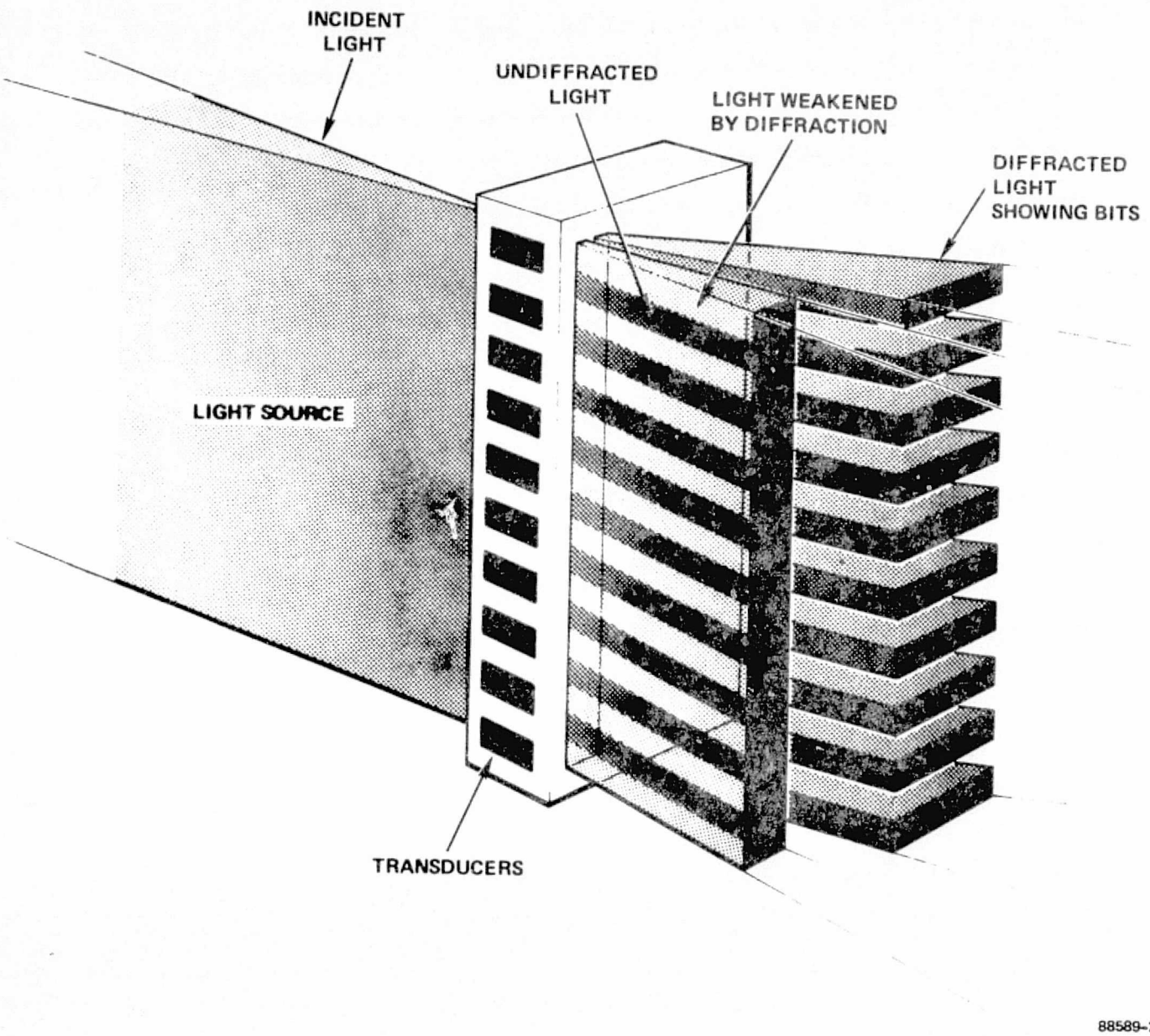

FIGURE 3-24. THE ACOUSTO-OPTIC PAGE COMPOSER (FUNCTIONAL DRAWING)

where λ is the wavelength of light and Λ is the acoustic wavelength, given by $\Lambda = V_a/f$, V_a is the acoustic velocity of the material and f is the transducer frequency. This diffraction mode produces two main output beams as shown in Figure 3-25. One beam, the undiffracted or transmitted component, does not interact with the acoustic wave. The other beam, the diffracted component, interacts with and is modulated or deflected by the acoustic wave.

Amplitude modulation of the acoustic wave is used to modulate the intensity of the diffracted light. Frequency modulation of the acoustic wave produces an angular deflection of the light beam, since the diffraction angle is proportional to the spatial frequency of the acoustic wave. This proportionality is evident in Equation 3.11. These principles are the basis for several acousto-optic devices.

3.1.3.1.1 Acousto-Optic Modulator (AOM). Amplitude modulation of the acoustic wave in the AO material results in an amplitude modulation of the diffracted light beam. Figure 3-25 is a schematic diagram of an acousto-optic modulator (AOM).

The shuttering transitions and/or overall light level used to record holograms are produced by passing the light beam through an AOM. High-rate recording requires that the rise time associated with these transitions be as short as possible. Since the rise time of a change in light level produced by an AOM depends on the propagation time of the acoustic wave through the optical beam, the rise time can be minimized by using a very small light beam. This is achieved in an AOM by focusing the beam (in one dimension) into the active region of the AOM. This is also shown in Figure 3-25.

3.1.3.1.2 Acousto-Optic Beam Splitter (AOBS). To produce the reference and signal beams necessary for holographic recording, an AO beam splitter is used. As the signal to this device is constant, rise time considerations are not important. However, another

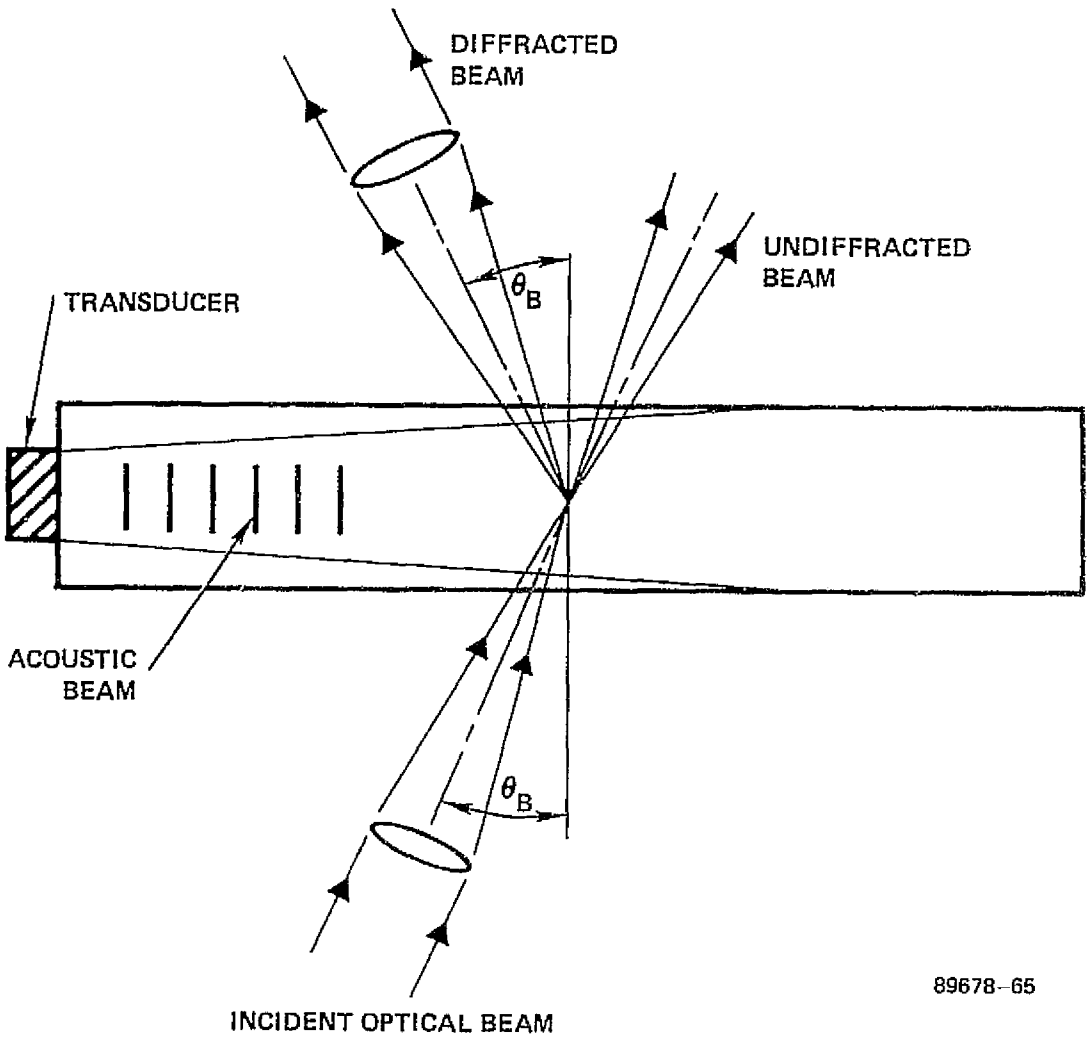

FIGURE 3-25. DIFFRACTION OF LIGHT BY AN ACOUSTO-OPTIC MODULATOR

characteristic of acousto-optic devices becomes significant. As a light beam interacts with a propagating acoustic wave, a Doppler frequency shift (equal in magnitude to the RF acoustic frequency) is induced in the diffracted light. Since holographic recording requires a high degree of temporal coherence between reference and signal beams, this frequency shift would ordinarily have a severe impact on fringe contrast, and hence diffraction efficiency and signal-to-noise ratio. This problem is solved by using the diffracted, frequency-shifted light as the reference beam and the undiffracted light as an illumination source for another AO device, the page composer, to form the signal beam. Driven by the same RF source as the AOBS, the page composer imparts to the signal beam a frequency shift identical to that of the reference beam. Thus, temporal coherence is preserved and interference between reference and signal beams can be optimized.

3.1.3.1.3 Acousto-Optic Page Composer (AOPC). In a multichannel optical system, several operations must be performed to allow successful recording. First, the information carried by the high data rate electronic signals must be demultiplexed, allowing a reduction in the required per channel data rates. Second, a formatting operation to prepare the data for recording must be performed. Finally, a conversion of the channelized data from the electronic to the optical domain must be accomplished.

To produce simultaneously many optical channels of data, a multichannel AO device is needed. The key component in performing this conversion is the acousto-optic page composer (AOPC). The AOPC imparts temporal as well as spatial modulation to the optical beam; thus, the electronic signal information is impressed on the optical beam. Except for its multichannel nature, this device is essentially identical to an acousto-optic modulator. The light beam is focussed to a line in the interior of the AOPC to minimize signal rise time, just as the light beam is focussed into an AOM for the same reason. Figure 3-26 is a simple diagram of a one dimensional AOPC, which is composed of a linear array of transducers attached to a block of an acousto-optic material. The

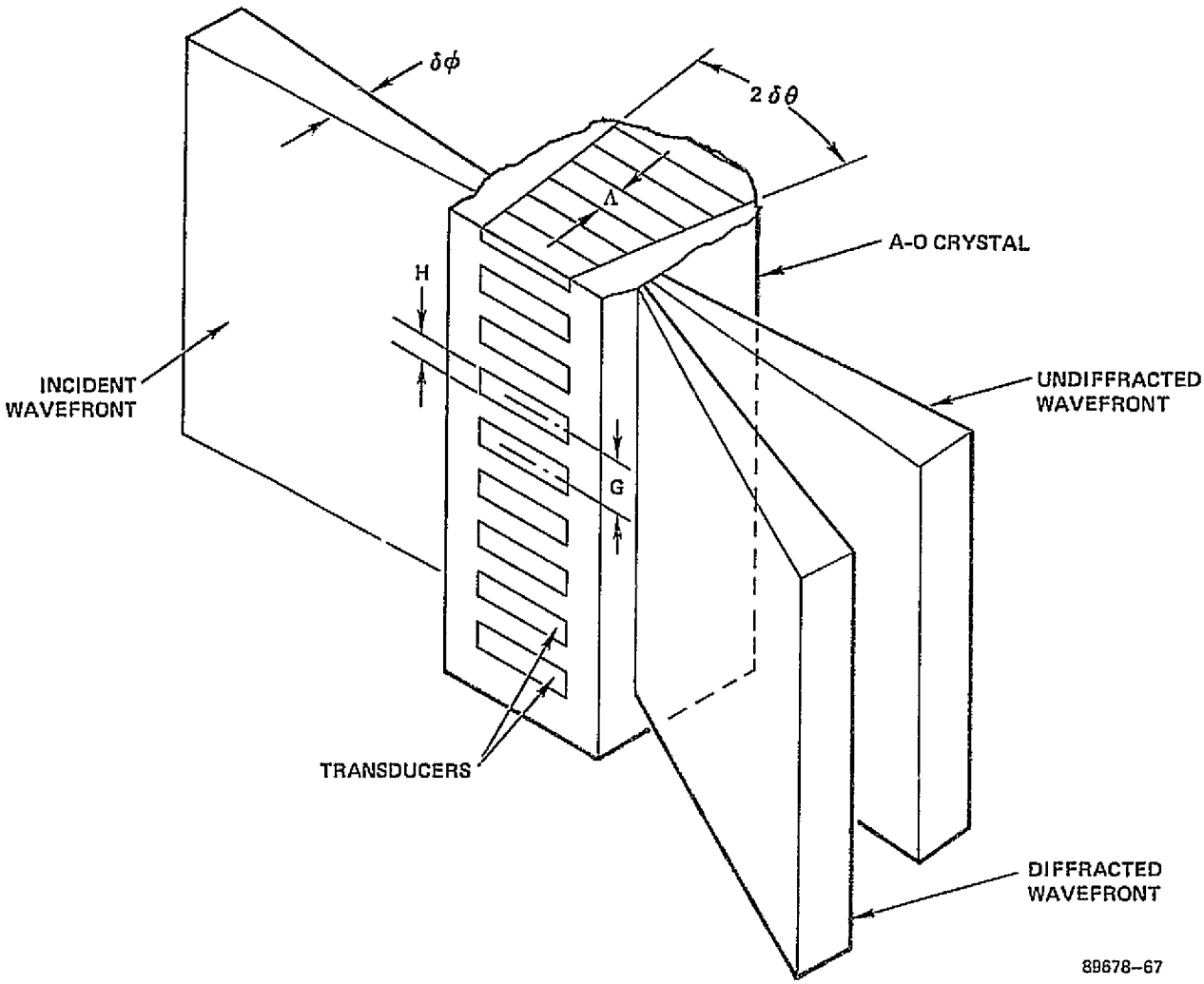

FIGURE 3-26. SCHEMATIC OF A ONE-DIMENSIONAL AOPC

illumination is provided by focussing a collimated beam with a cylinder lens to form a line source; the diffracted light beams form a linear array of optical data channels, whose intensity correspond to the demultiplexed electronic data.

Several factors must be considered during the design of an acousto-optic page composer. The AOPC must be capable of efficiently modulating the optical signals. Because diffraction efficiency is a function of the RF drive signals, higher efficiencies are obtained by increasing the RF drive power. However, high levels of drive power can cause significant heating effects which negatively affect system performance. A thermal gradient in the acousto-optic material can seriously degrade the optical quality of the diffracted beams or even fracture the acousto-optic material. A trade-off between high efficiency and tolerable thermal degradation is always necessary.

The AOPC must provide a rise time consistent with user data rates. Short rise times require a high RF carrier frequency, a large bandwidth and a short transit time. The increases in carrier frequency and bandwidth raise the level of the electronic channel-to-channel crosstalk and correspondingly reduce the extinction ratio that the AOPC can achieve. Various trade-offs are required to ensure that these parameters are within acceptable bounds.

The characteristics of the AOPC device can also vary significantly from one acousto-optic material to another. Several factors determine the choice of an acousto-optic material. First, the material should have a high figure of merit; good efficiency can then be obtained at low RF drive levels. Second, the optical quality of the material must be high; this ensures that any aberrations introduced by the crystal are minimal. Finally, the difficulty of fabrication for a given material must also be considered. Some acousto-optic materials, although capable of providing high performance levels, require delicate care during the polishing and coating stages of fabrication. Thus, these materials pose a high risk of breakage which must be considered.

The AOPC performance is also affected by transducer design. The transducers must provide good heat transfer characteristics to minimize thermal degradations. The RF

switching characteristics and rise times of the AOPC are determined by the drive electronics and transducer circuitry; their design must provide a frequency response that satisfies performance goals. The geometry of the transducer array influences the resolution achieved with subsequent imaging optics. Thus, the effect of the transducer size and spacing on optical performance must be given careful consideration during the design stage.

The illumination conditions for the AOPC must be determined that satisfy the Bragg angle and angular bandwidth requirements. The convergence angle of the incident optical beam must be chosen to provide rise times (i.e., acoustic transit times) consistent with system requirements. These parameters interact to determine both the efficiency and shape of the diffracted beams obtained in the final AOPC device.

The final design should represent a combination of acousto-optic material and transducer geometry that yield optimum operational parameters. The fabrication of the AOPC device must then proceed with great care if these design goals are to be achieved.

3.1.3.2 Analysis and Trade-Offs

In the selection of an acousto-optic material for an acousto-optic page composer, a variety of optical, acoustical, electrical, and mechanical properties must be considered. The key parameters include acoustic power and diffraction efficiency requirements, separation between modulated and unmodulated output beams, acoustic Q, optical beam diffraction, acoustic beam spreading, acoustic and optical losses, and experimental and fabrication difficulties. The AO materials considered were SF-8, SF-59, T_eO_2 (paratellurite), and As_2S_3 (Arsenic Trisulfide) glasses and TeO_2 and $PbMoO_4$ (lead molybdate) crystals.

3.1.3.2.1 Acoustic Power and Diffraction Efficiency. The diffraction efficiency η_i of an acousto-optic device, is defined as the ratio of diffracted to incident light power; the maximum efficiency for a given acoustic power can be calculated from

$$\eta_1 = \sin^2\left[\frac{\pi}{\lambda \operatorname{Cos}\theta_B}\left(\frac{M_2 P_a}{2}\ \frac{L}{H}\right)^{1/2}\right] \qquad (3.12)$$

where

λ = wavelength of light in vacuum

L = acousto-optic interaction length (transducer length)

H = transducer width

P_a = acoustic power

M_2 = acousto-optic figure of merit of the AO material = $\frac{n^6 p^2}{V^3 \rho}$

θ_B = Bragg angle

h = index of refraction

ρ = material density

Figure 3-27 shows the geometry of the acousto-optic device. For the purpose of comparison the transducer was chosen as L = 10 mm and H = 0.150 mm. Table 3-3 lists various AO materials as well as giving the figure of merit, power required for 70 percent diffraction efficiency, and diffraction efficiency for 10 mW of input acoustic power. Red light at $\lambda = 632.8$ nm (helium-neon laser) is assumed. With the exception of the TeO_2 shear mode all the materials are operated in the longitudinal acoustic mode. The calculations show both TeO_2 (shear) and As_2S_3 require less than 10 milliwatts drive for 70 percent diffraction efficiency. Also, the diffraction efficiency for a given RF power level improves as the wavelength of the light decreases.

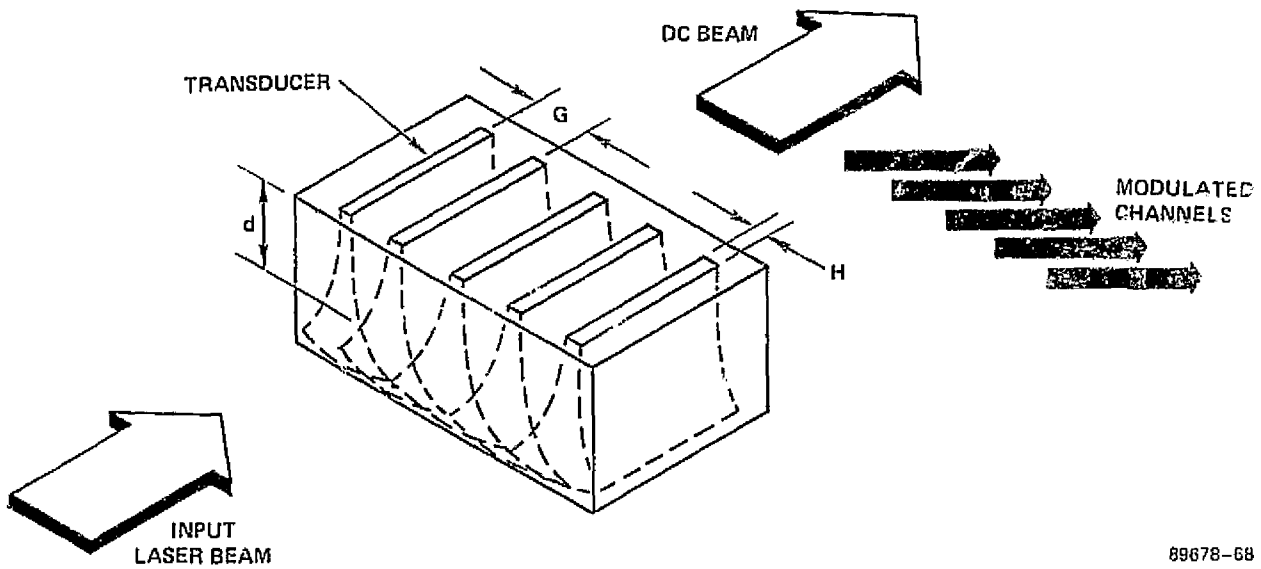

FIGURE 3-27. INTERACTION GEOMETRY OF AN ACOUSTO-OPTIC PAGE COMPOSER

TABLE 3-3

ACOUSTIC POWER VERSUS DIFFRACTION EFFICIENCY
FOR SELECTED ACOUSTO-OPTIC MATERIALS

Material	M_2 (10^{-15} s^3/Kg)	P_a for $\eta_1 = 70\%$ (mW)	η_1 for P_a = 10 mW
SF-8	~4.5	300 nW	3%
SF-59	19	62.9	15%
As_2S_3	433	2.8	---
TeO_2 (glass)	23	52.0	18%
$PbMoO_4$	36.3	32.9	27%
TeO_2 <110> (Shear)	793	1.5	---
TeO_2 <001> (longitudinal)	34.5	34.6	26%

3.1.3.2.2 Diffraction Effects and Acoustic Q. In order to achieve high per channel data rates in an acousto-optic page composer, a low modulator rise time is required. The rise time can be roughly defined as the time taken for an acoustic wave to propagate through the light beam. Rise time can be minimized by focusing the optical beam as it passes through the acousto-optic material. However, it is essential that the diffracted and undiffracted beams be sufficiently separated in angle to permit distinction between the two beams. Finally, in addition to transducer geometry and acoustic power, diffraction efficiency is a function of a parameter termed the acoustic Q.

A general rule relating the Bragg angle with the optical diffraction angle, or cone angle, is that the beam waist at the optical beam should be approximately three acoustic wavelengths. This results in a double Rayleigh resolution between the diffracted and undiffracted beams, permitting the two beams to be easily separated.

With reference to Figure 3-26, another parameter which influences the rise time of the modulator is defined as the diffraction beam spread ratio a:

$$a = \frac{\delta\phi}{\delta\theta} = \frac{2\lambda L}{\pi\omega_o \Lambda} \tag{3.13}$$

where

$$\delta\phi = \frac{\lambda}{\pi\omega_o}$$

is the inverse of the F-number and

$$\theta_D = 2\delta\theta = \frac{\Lambda}{L} \tag{3.14}$$

is the acoustic diffraction angle caused by the limited transducer aperture. The beam waist radius is ω_0. For low values of the beam spread ratio the rise time (10 percent to 90 percent) approaches

$$t_r \approx 1.3 \frac{\omega_o}{V} \tag{3.15}$$

where V is the acoustic velocity. When the beam spread ratio exceeds unity, with constant ω_0, the rise time increases linearly with transducer length. This change in rise time is due to the increase of transit time of the acoustic wave across the light beam, which is a function of L for an incidence angle other than zero. Generally, in an optimum design, the beam spread ratio is near unity.

The Klein-Cook factor Q, known as the acoustic Q, is given by

$$Q = \frac{2\pi\lambda L}{n\Lambda^2} \tag{3.16}$$

The efficiency of an acousto-optic modulator is greatest for devices with a high Q. However, as Q increases the modulator becomes less capable of efficiently diffracting light rays entering the device at angles other than the Bragg angle. This means that the extreme rays of a focusing beam (used to reduce rise time) are less efficiently diffracted than central rays because of this deviation from Bragg incidence. In general, to ensure the most efficient operation as a Bragg modulator, the requirement is that $Q \geq 4\pi$. An equation giving the normalized diffraction efficiency η_2 of an angular and frequency misaligned Bragg modulator is

$$\eta_2 = \text{sinc}^2 \left(\frac{\propto Q}{4}\right)$$

with

$$\propto = \frac{\Delta f}{f} + \frac{2\theta}{\theta_B} \tag{3.17}$$

where $2\theta/\theta_B$ is the angular deviation of light from the Bragg angle and $\Delta f/f$ is the frequency deviation ratio. The net diffraction efficiency of an acousto-optic modulator is

$$\eta = \eta_1 \eta_2 \tag{3.18}$$

where η_1 is the power diffraction efficiency defined by Equation 3.12.

Table 3-4 gives calculated values for θ_B, θ_D, and Q for each material at an acoustic frequency of F = 100 MHz, an optical wavelength of λ = 632.8 mm, an interaction length of L = 10 mm, and a transducer width of 0.15 mm.

3.1.3.2.3 Acoustic Beam Spreading and Attenuation. The preceding calculations were all for single channel devices. When a linear array of modulators is fabricated the interference of adjacent channels owing to spreading of the acoustic beams and acoustic attenuation must be considered. This will result in the determination of a minimum permissible channel-to-channel separation distance based on optical, acoustic and geometric considerations of the modulator design.

In order to get the maximum benefit from the acoustic beam power, the optical beam should be close to the transducer. Unfortunately, this puts the optical beam in the near-field region of the acoustic beam, resulting in distortion of the output optical beam. If the distance to the optical beam from the modulator is large enough to reduce the distortion, the beam is then in the Fraunhofer (far-field) region, which is defined by the condition

$$d \gg \frac{H^2}{\Lambda} \tag{3.19}$$

where

d is the distance from the transducer to the optical beam and

H is the transducer width.

However, after the acoustic waves have propagated a near-field distance, the acoustic channels begin to overlap. Figure 3-27 shows this interaction geometry. When the

TABLE 3-4

OPTICAL AND ACOUSTIC PARAMETERS
FOR SELECTED ACOUSTO-OPTIC MATERIALS

Material	V_a (mm/μs)	n	θ_B (mrad)	θ_D (mrad)	Q
SF-8	3.93	1.68	4.78	3.93	15
SF-59	3.26	1.94	5.00	3.26	19
As_2S_3	2.60	2.61	4.66	2.60	22
TeO_2 (glass)	3.27	2.02	4.80	3.27	36
$PbMoO_4$	3.63	2.26	3.86	3.63	13
TeO_2 <110> (Shear)	0.62	2.26	22.6	0.62	458
TeO_2 <001> (longitudinal)	4.20	2.26	3.33	---	10

modulator is operated within the weak interaction region, the mixed channels can be retrieved by appropriate imaging since the diverging acoustic field merely imposes a predictable quadratic phase shift to the optical wavefront. However, for acoustic devices operated in the strong interaction region, the acousto-optic process becomes nonlinear with acoustic power and nonretrievable optical cross-channel interference occurs as the acoustic channels overlap.

As a compromise between these two extremes, d can be chosen as

$$d = \frac{H^2}{\Lambda} \quad . \tag{3.20}$$

This puts the optical beam at the edge of the acoustic near field.

The acoustic diffraction angle of concern here is defined as the half angle to the first intensity minimum of the acoustic beam in the far field, and is taken as

$$\theta_A \approx \sin\theta_A = \frac{\Lambda}{H} \quad . \tag{3.21}$$

The depth d into the material to the overlapping of the first minimum from adjacent channels is given by

$$d = \frac{G}{2\tan\theta_A} \approx \frac{G}{2\theta_A} \tag{3.22}$$

where

G is the channel-to-channel separation distance.

Combining the two equations for d yields

$$G \approx 2H \tag{3.23}$$

Table 3-5 gives the calculated values for θ_A and d for various A-O materials, again for F = 100 MHz and H = 0.15 mm. Also given are the published values of acoustic attenuation Γ, which are extrapolated to 100 MHz.

TABLE 3-5

ACOUSTIC PARAMETERS
FOR SELECTED A-O MATERIALS

Material	Λ (μm)	θ_A (rad)	d (μm)	Γ (dB/mm)
SF-8	39.3	.265	566	---
SF-59	32.6	.220	682	1.20
As_2S_3	26.0	.175	857	0.17
TeO_2 (glass)	32.7	.220	682	0.32
PbM_oO_4	36.3	.244	615	0.015
TeO_2 <110> (shear)	6.2	>1.0	87	0.29
TeO_2 <001> (longitudinal)	42.0	.284	528	0.015

3.1.3.2.4 Optical Losses. The optical losses of an acousto-optic device include reflection losses at the two glass-air interfaces and the absorption and scattering losses in the A-O material. The reflection losses can be estimated at each surface by using the approximate expression for reflectance at an air-dielectric interface

$$R = \left(\frac{n-1}{n+1}\right)^2 \tag{3.24}$$

The absorption and scattering losses can be estimated by measuring the transmittance of a known length of material or by extrapolating values from the literature. Table 3-6 gives the reflectance R and transmittance T for a 20-mm thick sample of various A-O material at λ = 632.8 mm. Also given is the total optical insertion loss.

The reflection losses from the surfaces can be reduced by the use of anti-reflection (AR) coatings. A common AR coating used is MgF (magnesium fluoride) $\lambda/4$ thick. A general single layer coating of this type can reduce reflection losses per surface to 0.5 percent to 1.0 percent. Multilayer coatings of various refractory oxides, tuned to a specific wavelength and angle of incidence, can further reduce reflective losses to 0.15 percent to 0.25 percent per surface.

3.1.3.2.5 Phase Randomization. Holographic data recording makes use of a lens to form the Fourier transform of the page composer data. A reference beam is interfered with the transformed data beam at the transform plane to form a hologram of the data pattern. The recording plane coincides with the transform plane.

A result of the Fourier transform process is the formation of a high intensity dc spike in the transform plane which far surpasses in intensity the level of the signal spectrum frequency components in the transform. A faithful recording on film of the dc spike consumes the greater part of the linear dynamic range of most films, resulting in the frequency components of the data being recorded near the noise level of the film. The net effect is to minimize the capability for reproduction of the digital data in the hologram.

TABLE 3-6

OPTICAL LOSS AT λ = 632.8 mm
FOR SELECTED A-O MATERIALS

Material	n	R (percent)	T (percent)	Total Insertion Loss (dB)
SF-8	1.68	6.5	99.7	0.60
SF-59	1.94	10.3	97.8	1.0
As_2S_3	2.61	19.9	38.4	6.1
TeO_2 (glass)	2.02	11.4	>97	>1.2
PbM_oO_4	2.26	15.0	>99.9	>1.4
TeO_2 (crystal)	2.26	14.9	>99	>1.45

The dc spike can be reduced to the level of data frequency components by means of phase randomization. As the phase of the diffracted light is the same as that of the RF source, if the separate channels are driven by a randomly phased RF source, the dc power components of the data bits are spread over the entire signal spectrum. This results in a more uniform amplitude distribution which, in turn, allows a more efficient use of the film dynamic range for recording and subsequent data reconstruction. In addition, channel-to-channel crosstalk can be minimized by incorporating a pseudo-random phasing scheme in which one of four phases is supplied to the RF drivers for each channel. A constraint is that adjacent channels must be $\pm\pi/2$ out of phase, which minimizes coherent additions owing to channel crosstalk.

3.1.3.2.6 Comparisons. The selection of the optimum A-O material for an acousto-optic page composer depends a great deal upon system requirements. For minimum acoustic power requirements, the TeO_2 single crystal <110> sheer mode ranks first and the As_2S_3 second. These two materials also rank in the same order in terms of ease of separation of the modulated and unmodulated beams and also in terms of the Q for most efficient acousto-optic interaction. However, when ranked according to minimum interchannel interference resulting from diffraction spreading of the acoustic beam, As_2S_3 ranks first with SF-59 glass and TeO_2 glass second and with the TeO_2 single crystal having the worst beam spreading of any material considered. If the optical losses are considered, there is no clear choice among the A-O materials other than As_2S_3; the absorption of visible radiation by As_2S_3 makes it the most lossy of the A-O materials.

Fabrication difficulties must also be considered. The TeO_2 single crystal <110> shear mode device must be very carefully oriented to avoid acoustic beam walk-off. The As_2S_3 glass is a soft material and very difficult to polish; it is difficult to effectively bond a transducer to this material. Both SF-59 and SF-8 glass devices have

been fabricated, and present minimal polishing, transducer bonding and fabrication difficulties.

Two materials were chosen for experimental evaluation: TeO_2 <110> shear mode, and SF-59 glass. The TeO_2 single crystal, operated in the shear mode, had the lowest acoustic and optical power requirements. The SF-59 glass was chosen as representative of a composite of the A-O materials; i.e., those with intermediate acoustic power requirements, acoustic beam spreading and optical losses. This group includes the TeO_2 glass and the TeO_2 <001> longitudinal mode and $PbMoO_4$ single crystals.

3.1.3.2.7 Experimental Results.

3.1.3.2.7.1 SF-59 Acousto-Optic Page Composer. A 128 element SF-59 AOPC, shown in Figure 3-28, was fabricated with the following operational parameters:

Center Frequency:	82 Mhz
Interaction Length:	7 mm
Optical Aperture:	0.56 mm
Q:	8.7

For evaluation, the optical beam was expanded to illuminate all the channels and then focused in one dimension as it entered the AOPC. With an acoustic-to-optical beam spread ratio a close to 1/2 and with impedance matching, the AOPC required 160 mW per channel for 70 percent diffraction efficiency. The higher power requirement than expected is related to the modest values of the a and Q parameters. With $a \approx 0.5$ and $Q \approx 9$, the maximum throughput is only ≈80 percent. Thus, for a net 70 percent diffraction efficiency the instantaneous diffraction efficiency has to reach a level of 87 percent. This corresponds to a theoretical power requirement of 140 mW, which is close to the experimental value. The remaining discrepancy is believed to be due to cable and circuit card losses.

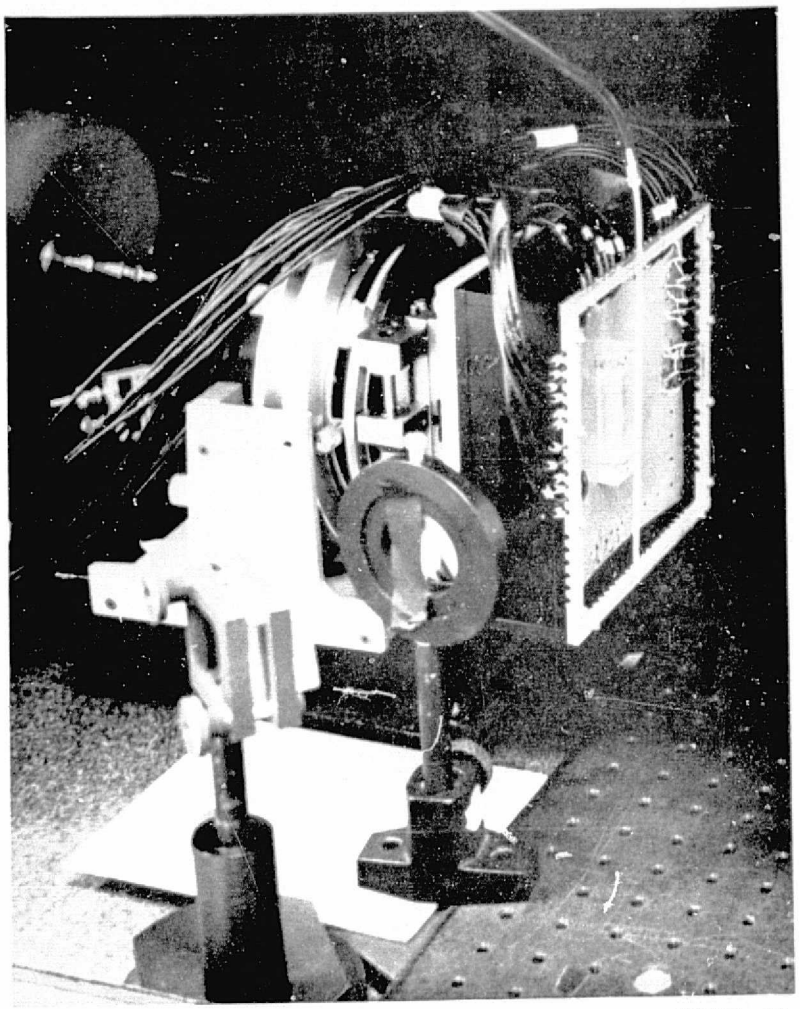

89678–64

FIGURE 3-28. 128-ELEMENT SF-59 AOPC

3.1.3.2.7.2 TeO_2 Acousto-Optic Page Composer. The TeO_2 fast shear wave provides both a high acousto-optic figure of merit and isotropic properties. Also, the estimated power requirement is very low. Using a TeO_2 crystal in this mode, a 32 channel AOPC was fabricated with the following operational parameters:

Center Frequency:	140 MHz
Interaction Length:	6 mm
Optical Aperture:	1.5 mm
Q:	42

The device was tested with an optical beam spread of approximately 1/3 the acoustic beam spread. The acoustic power for 70 percent light diffraction into the first order was measured as 36 mW, which is 17 percent higher than the theoretical value of 30 mW. A major part of this discrepancy was again assumed to be from losses in cables and circuit cards.

3.1.3.2.8 Summary. Table 3-7 summarizes important parameters for the fabricated and tested AOPC's; theoretical, as well as experimental, results are given. For comparison, parameters and performance of an SF-8 AOPC are also included. We note that RF drive power requirements are relatively low but higher than expected. Overall performance obtained with these AOPC's is less than ideal, but nonetheless good. However, further analysis and experiment are necessary to solve remaining problems and to optimize performance.

TABLE 3-7

SELECTED ACOUSTO-OPTIC
PAGE COMPOSER DATA

AOPC	L	H	f_o	d	P(70 percent) Measured	P(70 percent) Theory
SF-8	7 mm	0.15 mm	90 MHz	0.35 mm	500 mW	319 mW
SF-59	7 mm	0.15 mm	82 MHz	0.56 mm	160 mW	108 mW
TeO_2 (FS)	6 mm	0.15 mm	140 MHz	1.5 mm	36 mW	26 mW

3.1.4 Fourier Transform Lenses and the Data Format Considerations

The lens which forms the Fourier transform of the data pattern from the page composer must be a high quality, coated lens designed for infinite conjugates (i.e., for the imaging of infinitely distant objects) and of sufficiently large aperture relative to its focal length to accommodate the full scan angle. At a 4.2° mechanical scan angle, the field coverage is $2 \times \tan 4.2^{\circ} \times \text{EFL} = 0.15 \cdot \text{EFL}$. If we choose a standard 4-inch EFL, f/2 minimum Super Baltar lens as the transform lens, this makes the field coverage equal to about 15 mm. At f/2, there is a full 2-inch aperture available at the entrance pupil of this lens, indicating that 35 mm of mirror aperture is available to scan this field. The transform lens thus has enough aperture to accommodate the scan angle.

Once a transform lens has been selected, the next step is to establish the mirror size format required to form holograms of the appropriate size. As the requirement is to form holograms 1.5 mm high on 15 μm center-to-center spacings, if we leave space between the holograms in both dimensions, a conservative hologram size is 800 μm high x 10 μm wide. To double Rayleigh resolve the bit spacing, note that

$$d = 2F^{\#}\lambda = 2\frac{f}{D_1}\lambda \quad , \tag{3.25}$$

where d = the bit spacing at the mirror plane, f = the effective focal length of the Fourier transform lens, D_1 = the clear aperture, determined by the spot to be resolved (in this case, D_1 = 800 μm), and λ = the wavelength of the illuminating laser light. In this case, then:

$$d = 2 \cdot \frac{100 \text{ mm}}{0.8 \text{ mm}} \times 0.6328 \text{ μm} = 158 \text{ μm}.$$

Thus the large dimension of the data entering the first Fourier transform lens is 158 μm x 128 elements = 20.2 mm. To resolve the other dimension, the 10 μm hologram width, we use

$$w = 2F^{\#}\lambda = 2\frac{f}{D_2}\lambda \qquad (3.26)$$

where w is the width of the bits at the mirror plane and D_2 is the applicable clear aperture, or 10 μm in this case. Therefore:

$$w = 2 \cdot \frac{100\ mm}{0.01\ mm} \times 0.6328\ \mu m = 12.7\ mm.$$

Since this is only a projection of the mirror surface, and the surface is positioned at 45° to the optical axis at its center position as illustrated in Figure 3-2, the actual required mirror width is 12.7 mm x $\sqrt{2}$ = 18.0 mm. Nevertheless, the size of the data is 20.2 mm high (with the bits on 158 μm center-to-center spacings) and 12.7 mm wide. Since the scanning aperture available is 35 mm by the analysis above, there is more than enough room in a 4-inch EFL, f/2 Super Baltar lens to scan the data across the full field and yield holograms of the required dimensions.

3.1.5 Recording Material Selection

When selecting a recording material, the first consideration is that the recording material be a red-sensitive photographic film, since a Helium-Neon laser is intended for use on the breadboard. Secondly, since the medium is to be used for holographic recording, the emulsion must resolve >1000 cycles/mm to adequately record the hologram fringes. The final specification, exposure sensitivity, is dictated by the size of the hologram, the exposure time per hologram and the amount of available laser power; this will require some analysis.

First note that the proposed system requires approximately 500 holograms per scan of the galvanometer. If the frequency is 40 Hz, and the retrace time is 7.5 ms, this means that there is 17.5 ms of record time in the scan. The amount of time between the exposure of one hologram and the next is, therefore:

$$t = \frac{17.5 \text{ ms}}{500 \text{ holograms}} = 35 \text{ μs}$$

Based on this, a typical exposure time available to minimize the blur of the holograms while scanning would be 20 percent of the available time, or 7 μs. Next, take into account the size of the hologram: 1.5 mm high on 15 μm center-to-center spacings. If the hologram size itself is taken as 0.8 mm x 10 μm, then the total area per hologram is 8×10^{-5} cm^2. With 50 mW of available laser power from a Spectra-Physics Model 125 laser and a typical breadboard optical efficiency of one percent (for uncoated optics), this area can be filled with, at most, 0.5 mW of laser power. The available intensity is, then:

$$I = \frac{0.5 \text{ mW}}{8 \times 10^{-5} \text{ cm}^2} = 62.5 \text{ W/cm}^2$$

With an exposure time of 7 μs/hologram, then, the maximum energy available is 62.5 W/cm^2 x 7 μs = 625 ergs/cm^2 for a typical hologram density of D = 0.6.

The first two requirements, red sensitivity and high resolution, narrow the field of readily available materials from Eastman Kodak to 649F, SO-173, and SO-253 film. To produce a density of D = 1.0, 649F requires 900 ergs/cm^2, SO-173 400 ergs/cm^2, and SO-253 5-8 ergs/cm^2 according to published Kodak data. Because of the limitation on exposure energy available, 649F must be eliminated from consideration. SO-173 is a possibility, but SO-253 has considerably greater flexibility because of its extremely low exposure requirement. For these reasons, SO-253 was selected as the recording material for the present system.

3.1.6 The Film Transport

In considering the kind of film transport to be used in demonstrating the feasibility of the holographic storage concept, the initial specification for comparison is film transport speed. Since the hologram scans are to be stacked with minimum 1.5 mm

center-to-center spacings with a movement of one scan width for every 25 ms (corresponding to the galvanometer's 40 Hz scan frequency), the film speed must be 60 mm/s or faster. This relatively slow speed allows either the use of an X-Y planar transport, a reel-to-reel transport, or a rotating floppy disc type transport. Of the three, the floppy disc is the least expensive, the easiest to implement and involves the least risk; for these reasons it was selected for the breadboard system.

To identify fully the details of the transport specifications, it is helpful to first study the film recording format shown in Figure 3-29. Air bearings are used to hold the film flat to ±6 μm to guarantee that the holograms will remain in focus; experimental testing of the transport has, in fact, shown that spot sizes as small as 3.5 μm in diameter can be held in focus in such a transport, indicating that the present need to hold 10 μm spots in focus will not be difficult. Here the air bearings have a 0.375-inch aperture on the inside and a 1.00-inch aperture on the outside and are fabricated from a porous stainless steel; they are set in place so that there is a 0.75 mil gap between each bearing surface and the film surface. To determine the acceptance cone angle required by the bearings, an initial calculation shows that 500 holograms take up 500 x 15 μm = 7.5 mm of scan space. The 20.2 mm aperture required in the other dimension, therefore, is the largest aperture which must pass through the transport. This means that an entrance half-angle of

$$\tan^{-1}\left(\frac{20.2\ \text{mm}}{100\ \text{mm}}\right) = 11.4^{\circ}$$

is required on the air bearing cone. Accordingly, to satisfy this requirement while allowing room for diffracted light to pass through without reflecting off the cone, the half-angle of acceptance for the air bearing was set at 15°.

The film speed required is determined by the hologram spacing (1.5 mm), the scan speed (40 Hz), and the mean diameter of the air bearing opening with respect to the center of the film rotation (40 mm). The speed required is thus

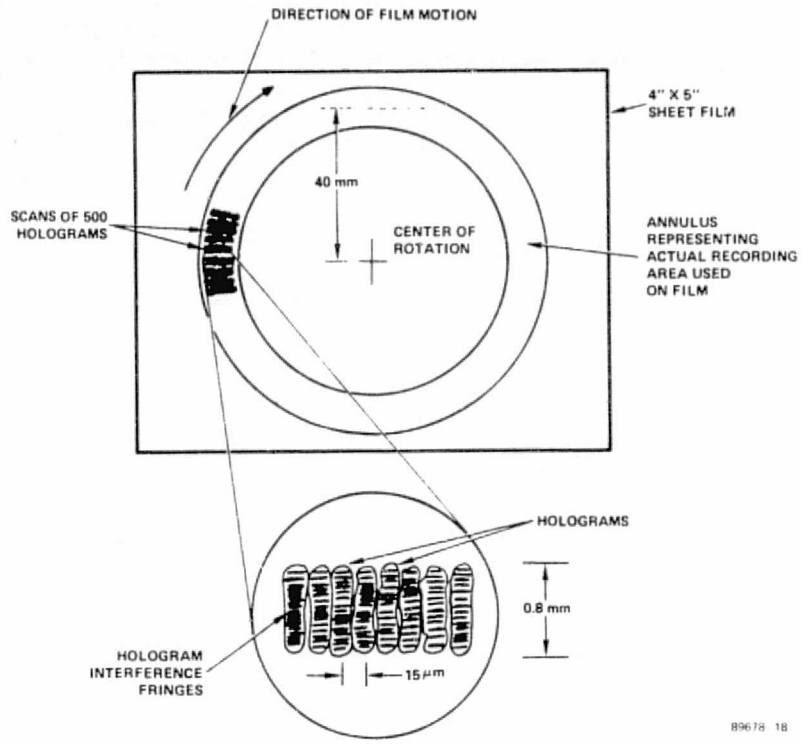

FIGURE 3-29. THE FILM RECORDING FORMAT

$$\text{film speed} = \frac{1.5 \text{ mm}}{25 \text{ ms}} \times \frac{\text{one revolution}}{2 \times \pi \times 40 \text{ mm}} = 0.24 \text{ r/s},$$

which corresponds to about 4 seconds per revolution.

The final version of the film transport implemented is a cassette-type module with shutters mounted on each half of the cassette; it is pictured in Figure 3-30 standing alone and in Figure 3-31 mounted in the center of the scan-descan subsystem. As designed, the cassette can be loaded in the darkroom, plugged into the recording plane, and the shutters opened for recording. For development, the cassette can be removed and taken to the darkroom to unload the film. It will handle any standard 4- by 5-inch sheet film.

3.2 THE BREADBOARD SYSTEM

3.2.1 The Recording Subsystem

3.2.1.1 Signal Path Optics

To begin the analysis of the breadboard system constructed using the components described previously, a discussion of the signal path optics is appropriate, since its format affects the rest of the subsystems. As Paragraph 3.1.3 showed, the size of the data on $GALVO_1$'s mirror is 12.7 mm wide by 20.2 mm high (for 128 data bits) with the bits on 158 μm center-to-center spacings. For the breadboard implementation of these components, a field of only 64 elements was used because high-quality, large aperture optics for imaging all 128 data bits as well as the reference beam were unavailable. This then narrows the required field size to 12.7 mm by 20.2 mm, but the 158 μm center-to-center spacing of the bits remains. To achieve this, we note that the acousto-optic page composer element center-to-center spacing is 250 μm; this means that, previous to the mirror on $GALVO_1$ it is necessary to have a $\frac{250}{158} = 1.6$ to 1 reduction in size of the data. As pictured in the top view of Figure 3-32, this is accomplished using a

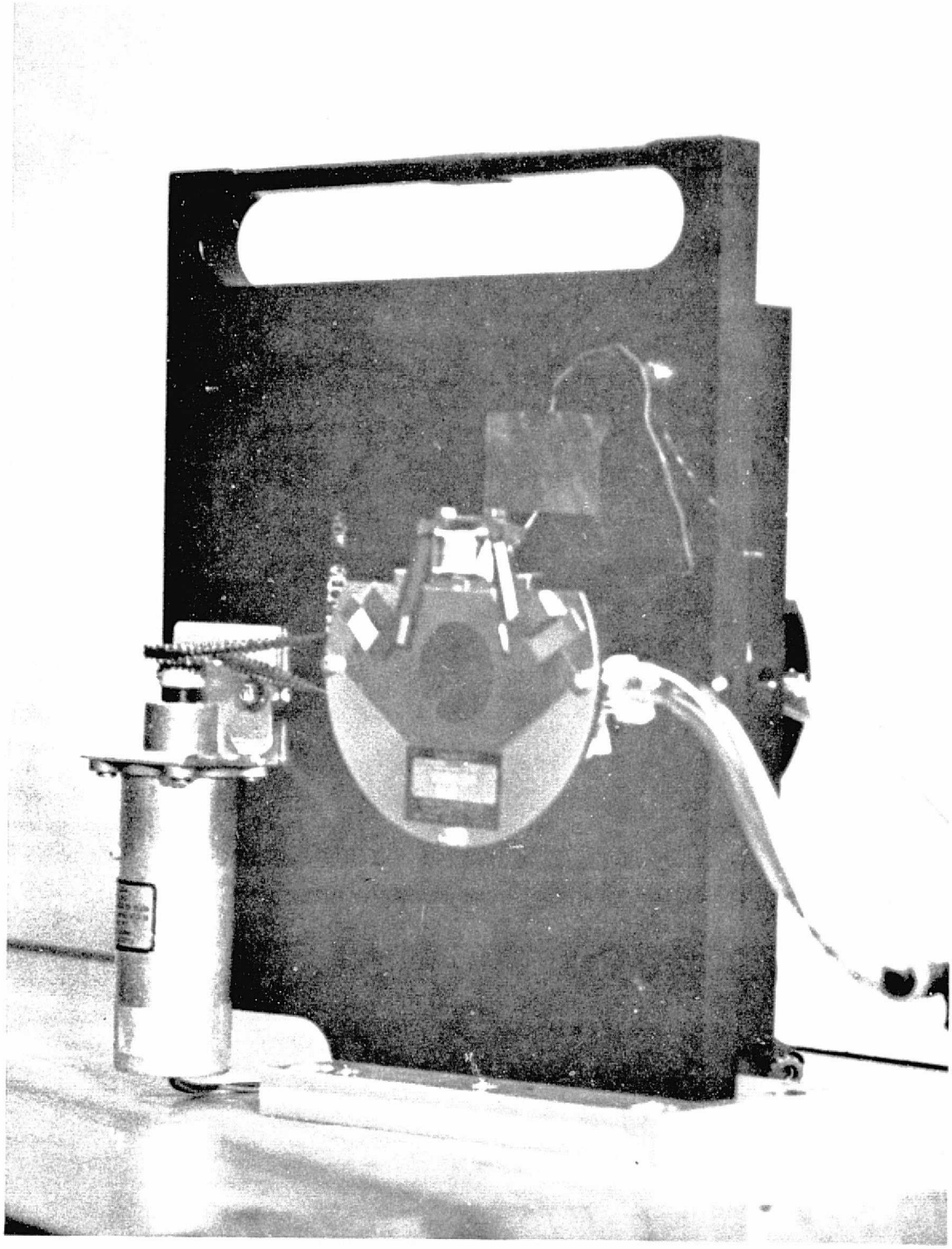

89678-40

FIGURE 3-30. THE FILM TRANSPORT

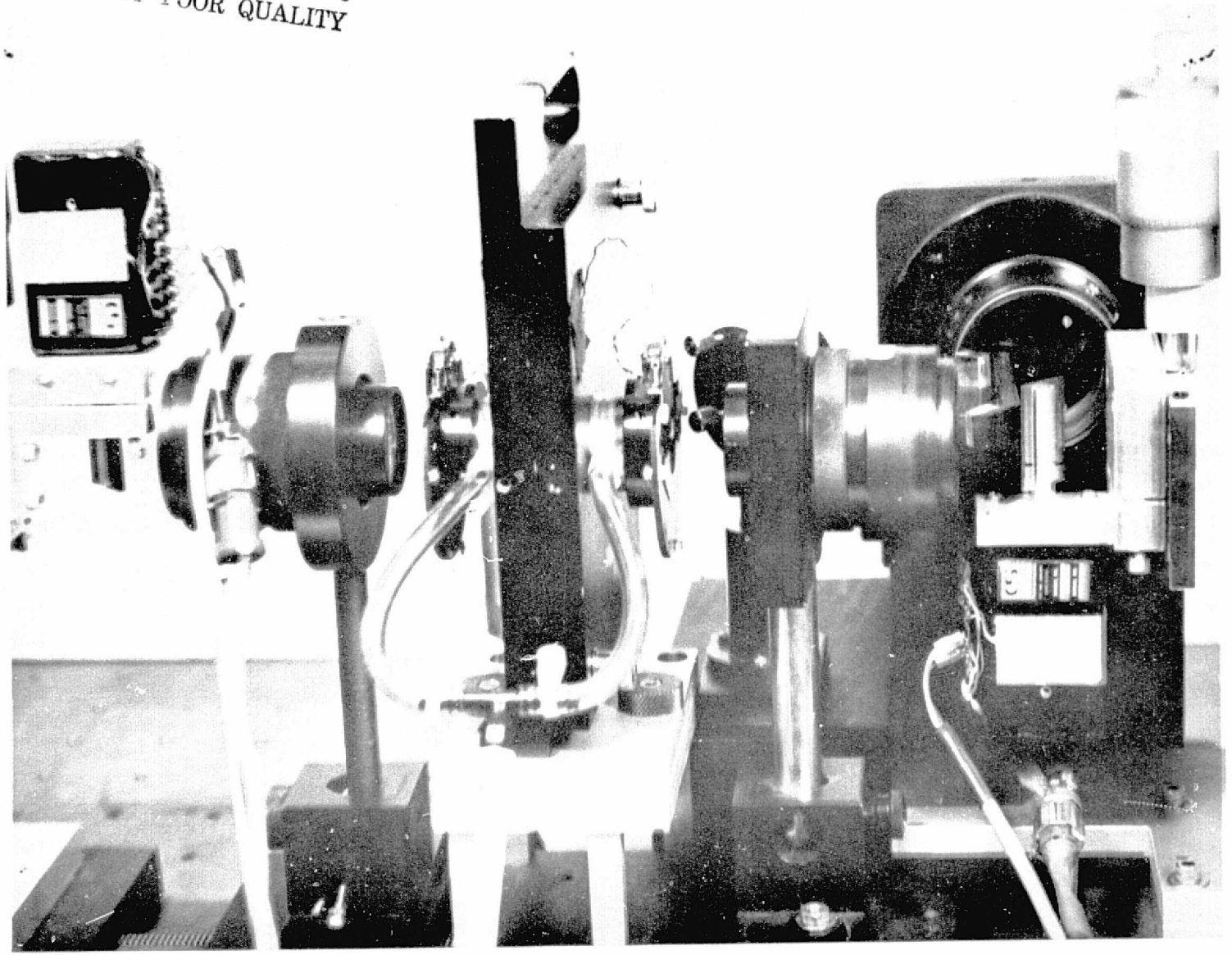

89678–41

FIGURE 3-31. THE FILM TRANSPORT IN THE RECORDING PLANE

6-inch EFL, f/2.8 Super Baltar for L_4 and a 10.0 inch EFL, f/2.5 lens for L_3 in a telescope configuration; this yields an effective reduction ratio of approximately 1.67, indicating that there will be some minor spreading in the hologram plane. Before L_3, L_1 (a 10X microscope objective) expands the entering beam to fill a 22-inch EFL lens L_2 where the beam is collimated in the 250 μm center-to-center spacing axis of the system. This completes our discussion of the requirements for one dimension of the data format.

In the other dimension, the requirement is to fill the 12.7 mm aperture on $GALVO_1$. This makes the aperture size on the entrance pupil of L_3 equal to 1.67 x 12.7 mm = 21.2 mm. To find the requirements which this places on the preceding lens elements, the first restriction to note is that the wavefront must focus in the AOPC plane in this dimension to minimize the travel time of the sound waves across the laser beam; the sharper the focus, the faster the AOPC can be switched on and off. This means that with the acousto-optic page composer placed at a total distance of 35 inches from L_3, that the size of the illuminated aperture on L_2 in Figure 3-32 (b) must be $\frac{22}{35}$ x 21.2 mm = 13.3 mm. A 40 mm focal length cylindrical lens C_1 collimates the beam from L_1 in this dimension at the required 13.3 mm size, and L2 focuses it in the AOPC. As a final fine adjustment on the illuminating wavefront size, a cylindrical lens C_2 of 40 mm focal length was placed before L_3's focal plane to add additional divergence to the wavefront entering L_4; this ensured overfilling of the $GALVO_1$ mirror aperture despite vignetting effects earlier in the subsystem.

3.2.1.2 Reference Beam Optics

For the reference beam the optical system is much less complicated than for the signal beam. As before, in the top dimension the reference beam must be placed at the extreme top of $GALVO_1$'s mirror with a 158 μm width; this ensures matching the size of the reference beam with the signal at the film transport where the holograms are formed. To do this, however, as Figure 3-33 (b) shows, a cylindrical lens "telescope" of 150 mm focal length C_4 and 80 mm focal length C_5 was used in an experimental

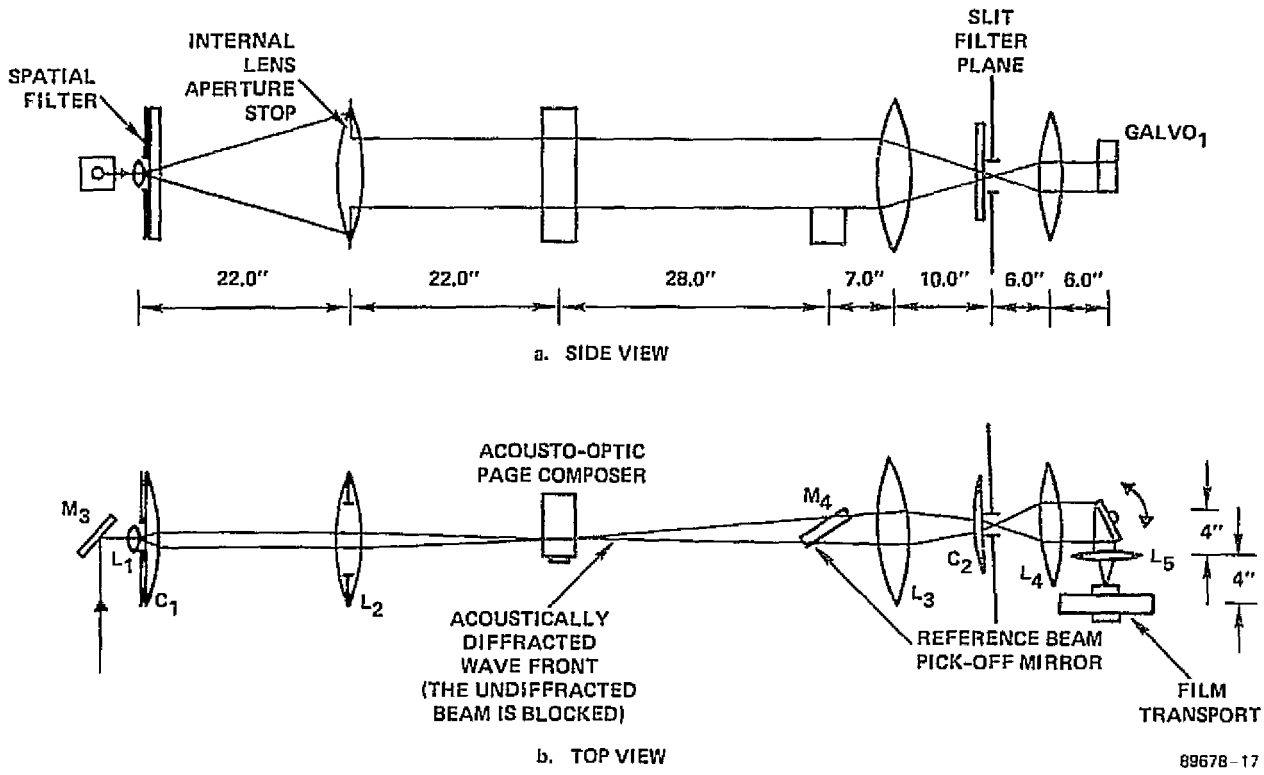

FIGURE 3-32. SIGNAL PATH OPTICS

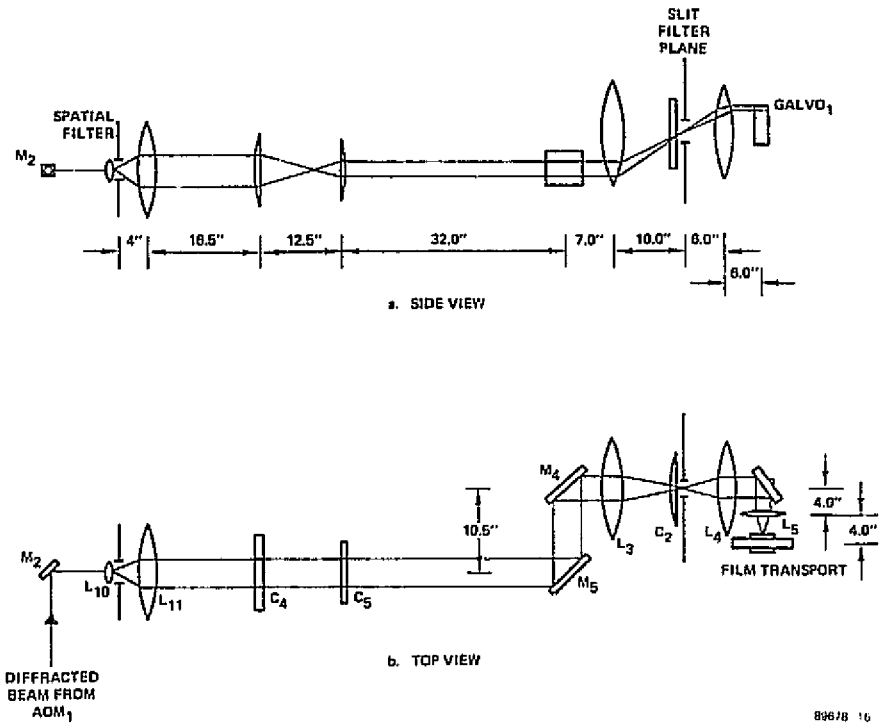

FIGURE 3-33. REFERENCE BEAM OPTICS

configuration. While the relative sizes of the Fourier transform of the data pattern and the reference beam transform in the film plane were monitored, the spacing of these two cylindrical lenses was changed until the divergence angle of the light emerging from C_5 was such that exact matching of the sizes took place. L_{11}, a 4 inch EFL collimating lens, and L_{10} a 5X microscope objective, provided the collimated wavefront input to C_4. Once again, C_2 provided additional refractive power after L_3 to ensure overfilling the 12.7 mm dimension of $GALVO_1$'s mirror in the other dimension.

One additional constraint on the reference beam is that its input beam be the diffracted beam from an acousto-optic modulator (AOM). The reason is that the data from the page composer is Doppler-shifted, and an optimum hologram interference pattern will not be obtained unless the frequencies of the reference and signal beams match exactly. Accordingly, the 83 MHz drive signal used to drive the AOPC was also used to drive the AOM that provided the reference beam signal.

3.2.1.3 Row Marker Optics

With the breadboard implemented to this point, it is possible to record successive rows of holograms on rotating 4 inch x 5 inch sheets of film. To recover this information dynamically, it is necessary to record a row marker at the beginning of each hologram row as pictured in Figure 3-34. In recording the holograms, a marker pulse is recorded on the film during the flyback and settling portion of a single scan of the first galvanometer; in readout, the marker pulse signal is detected and triggers the start of the galvanometer scan for the next row.

To record the marker dimensions pictured in Figure 3-34 the optics of Figure 3-35 are used. An acousto-optic modulator acts as a high-speed shutter for the system, lenses L_{12} (a 10X microscope objective) and L_{13} (a 4-inch EFL collimating lens) expand the beam and the cylindrical lens doublet of 100 mm EFL C_6 and 80 mm EFL C_7 generate the necessary wavefront curvature and aperture to form the required 100 μm x 1 mm marker spot at the film plane; the required lens spacings as labeled in Figure 3-35

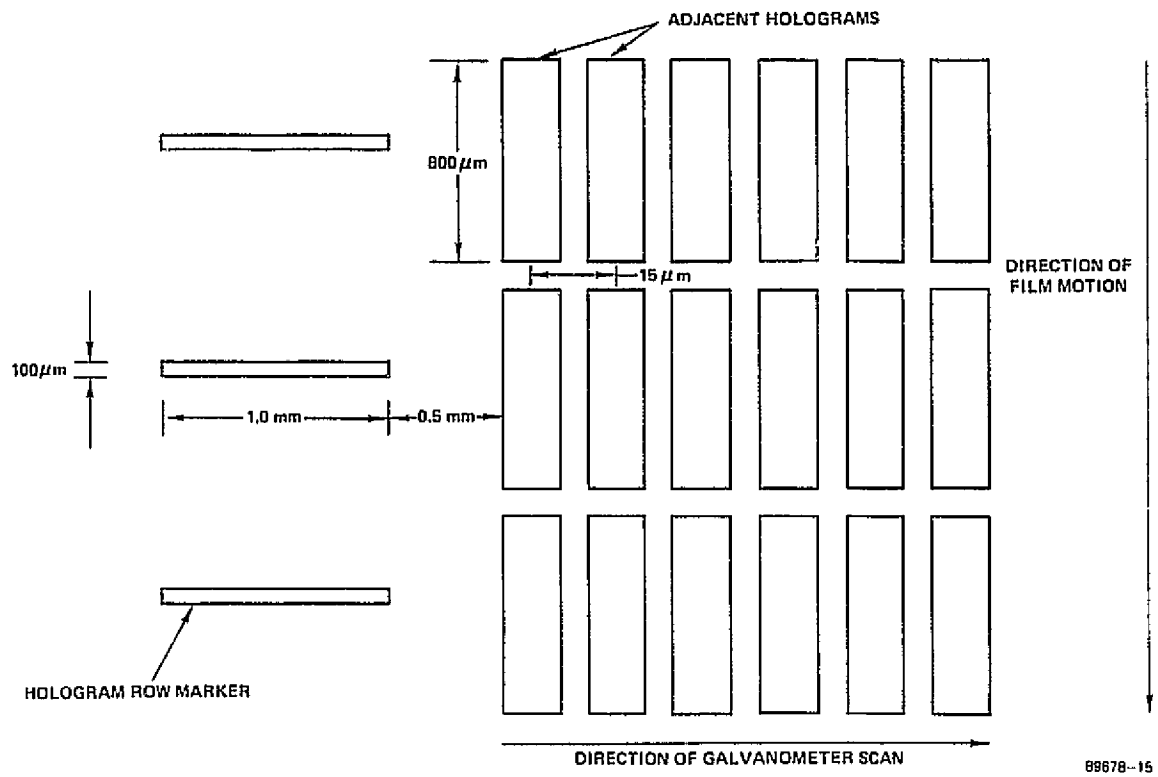

FIGURE 3-34. THE HOLOGRAM ROW RECORDING FORMAT

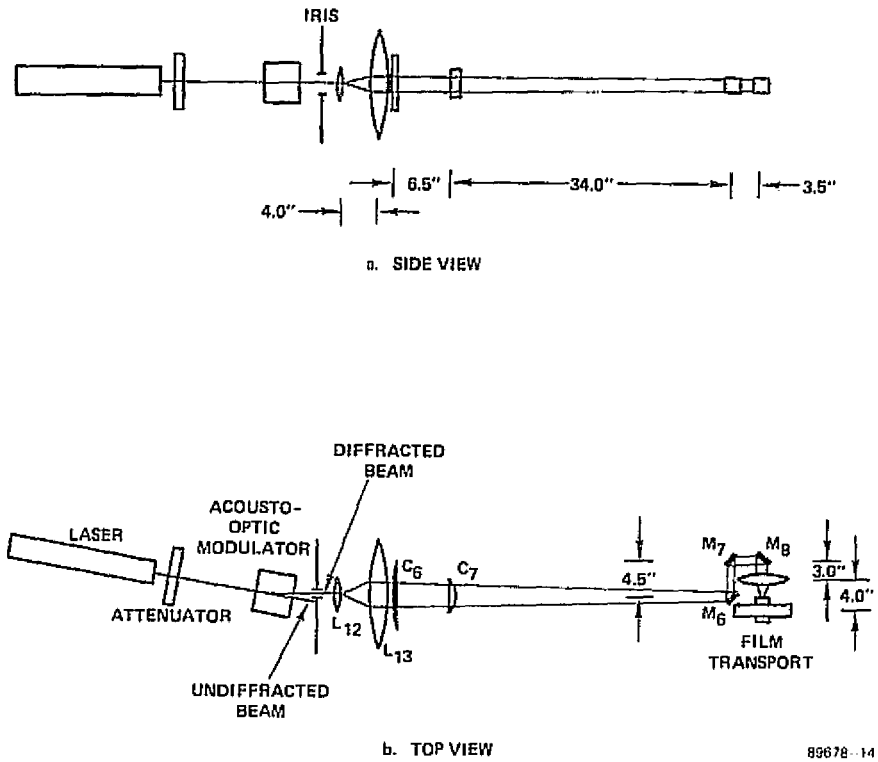

FIGURE 3-35. ROW MARKER OPTICS

were determined experimentally in the same way that the cylindrical lens doublet of the reference beam was positioned.

3.2.1.4 Electronic Considerations

The first electronics problem of fundamental importance for the recording subsystem is in transferring electronic data into the acousto-optic page composer. Because of the complications involved in changing data sequences from one hologram to the next, it was decided to maintain an identical data pattern input for all holograms. This data pattern is shown in Figure 3-36. Unfortunately, the Fourier transforms of digital data blocks like this have a very strong dc irradiance component in their spectrum. Since the K-ratio for a fixed reference beam irradiance would vary over the hologram (leading to recording nonlinearities and a decrease in signal-to-noise ratio) clearly a method of smoothing the data spectrum is desirable. Accordingly, a method of varying the electronic phase of the AOPC transducers (and, therefore, the complex phase of the wavefront diffracted by the acousto-optic cells) was implemented to alter the interference pattern produced by combining all the individual bit wavefronts at the transform plane.

To change the input phase structure to the page composer transducers, the first step is to choose the phase variation desired from one transducer to the next; in the present case $\frac{\pi}{2}$ was chosen as the phase difference step, where a phase difference of 2π corresponds to the two cycles being in step. Next note that electricity travels in coaxial cable at a speed of approximately 6 inches/nanosecond. So, for the 83 MHz carrier frequency driving the AOPC transducers, one wavelength of the electrical signal is 1/83 MHz = 12 nanoseconds in duration. A $\frac{\pi}{2}$ phase change is 3 nanoseconds in duration, corresponding to 18 inches of coaxial cable. By changing cable lengths and randomly connecting different lengths of cable to transducers as listed in Table 3-8, then, a randomized phase structure for the data pattern of Figure 3-36 was produced. The result was that the data spectrum made was uniform enough in intensity to allow the recording of holograms with only minor high carrier frequency bit rolloff.

TABLE 3-8

PHASE DIFFERENCE OF BIT RELATIVE TO BIT NUMBER 10

BIT NUMBER	PHASE DIFFERENCE
3	$\frac{\pi}{2}$
5	$\frac{\pi}{2}$
8	0
10	0
15	π
17	$\frac{3\pi}{2}$
24	π
28	π
30	$\frac{3\pi}{2}$
35	π
37	$\frac{3\pi}{2}$
41	$\frac{3\pi}{2}$
43	$\frac{\pi}{2}$
44	0
48	0

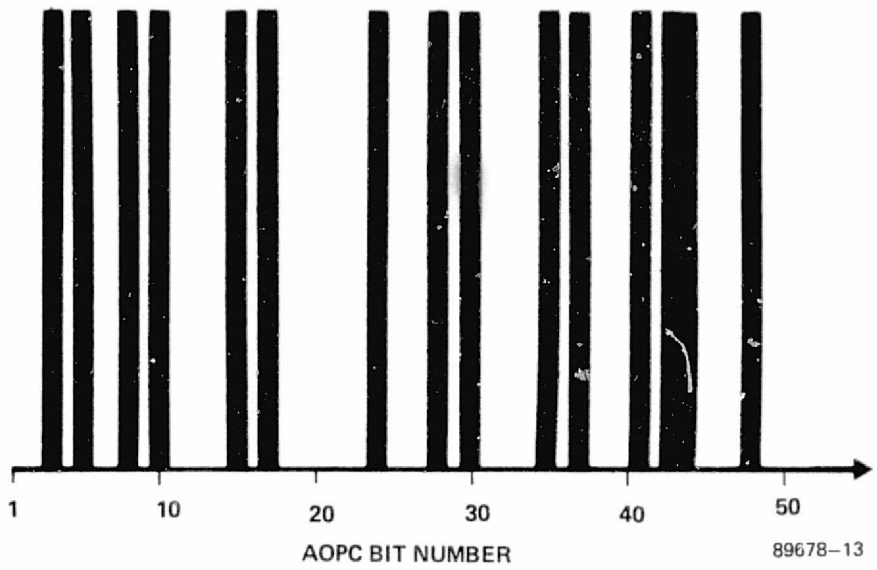

FIGURE 3-36. THE ACOUSTO-OPTIC PAGE COMPOSER DATA PATTERN

To record the holograms, the galvanometers were driven with a 5 volt peak-to-peak 40 Hz ramp waveform to scan 4.2° peak-to-peak, the reference beam and signal beam switched on for 8 μs every 40 μs, and the row marker beam was switched on for 5 ns for every flyback of the galvanometer. As Paragraph 3.1.5 showed, in order to separate adjacent hologram scans the film transport must rotate at a minimum speed of 0.24 revolutions per second, and for all experiments this was the speed used.

3.2.2 The Readout Subsystem

3.2.2.1 Optical Requirements

The primary optical requirement for the readout system is the imaging of the data pattern on to the photodetector array. To determine the optics required to do this, we begin with the observed experimental result that the page composer bits exhibit a "lens-like" effect as a result of the acoustic wave diffraction; this means that as far as the bits are concerned, the effective object plane for the bits is located 40 inches from L_3, or about 5 inches before the AOPC. These bits then are reimaged through the system; their position and magnification can be calculated using $ZZ' = f^2$ and $m = -\frac{Z'}{f}$, where Z is the object distance from the imaging lens involved and the first local plane of the lens, Z', the corresponding image distance from the second focal plane, and f is the focal length of the lens. Referring to Figure 3-32 we have imaging by:

L_3 $\quad Z = 30$ inches, $Z' = 3.3$ inches, $m_1 = -0.33$

L_4 $\quad Z = -7.3$ inches, $Z' = -4.9$ inches, $m_2 = 0.82$

L_5 and L_6 perform a unit magnification of this image, so the data will appear positioned 4.9 inches before $GALVO_2$. The net magnification of the bits is $m = m_1 m_2$, or $m = -0.27$ at this plane. Since the photodetector array has detector elements spaced on 50 μm center-to-center spacings and the page composer has 250 μm center-to-center spacings an additional demagnification of

$$m' = \left(\frac{50\ \mu m}{250\ \mu m}\right)\frac{1}{m} = -0.74$$

is required. To do this, a three-lens system of L_7 (400 mm focal length), L_8 (9-inch EFL) and L_9 (147 mm focal length) was set in a zoom lens configuration. L_8 and L_9 were moved until the maximum signal output was observable on the photodetector array read-out display. This then guaranteed the required demagnification with the experimentally derived lens spacings depicted in Figure 3-37. Finally, cylindrical lens C_3, with a 2 inch focal length, collected the light in the 24-mil width dimension of the detector elements.

In regard to the rest of the readout optics, the row marker was illuminated by the marker beam continuously during readout, and a photodetector was used for picking off the beam. In addition, to provide a signal for synchronizing the detector array start pulse with the best hologram position, the undiffracted reference beam signal was diverted to a detector. When the maximum hologram diffraction efficiency (and, therefore, the best place to read the holograms) was observed, the undiffracted reference beam is at its lowest intensity, yielding a reference point for the best hologram reading time.

A final consideration of importance is that the breadboard system has placed the AOPC data pattern 40 inches from the lens, L_3; if we were to form an exact Fourier transform of the data pattern at the slit filter plane (and therefore also at the hologram plane, since the slit filter is imaged directly onto the film), the AOPC data would have to be one L_3 focal length, or 10 inches, from L_3. The result is that a spherical phase factor has been added to the Fourier transform. With a perfect Fourier transform hologram, if the hologram is moved in the plane normal to the system optical axis during reconstruction, the reconstructed image remains motionless. In this sytem, however, the spherical phase factor reduces this translation invariance property. With film transports of the kind used in the present system, motor ripple amounting to sudden slips of up to 10 percent of a hologram length are possible; it is possible this could cause the reconstructed data bits to slip from one detector element to the next in readout. For this reason, a

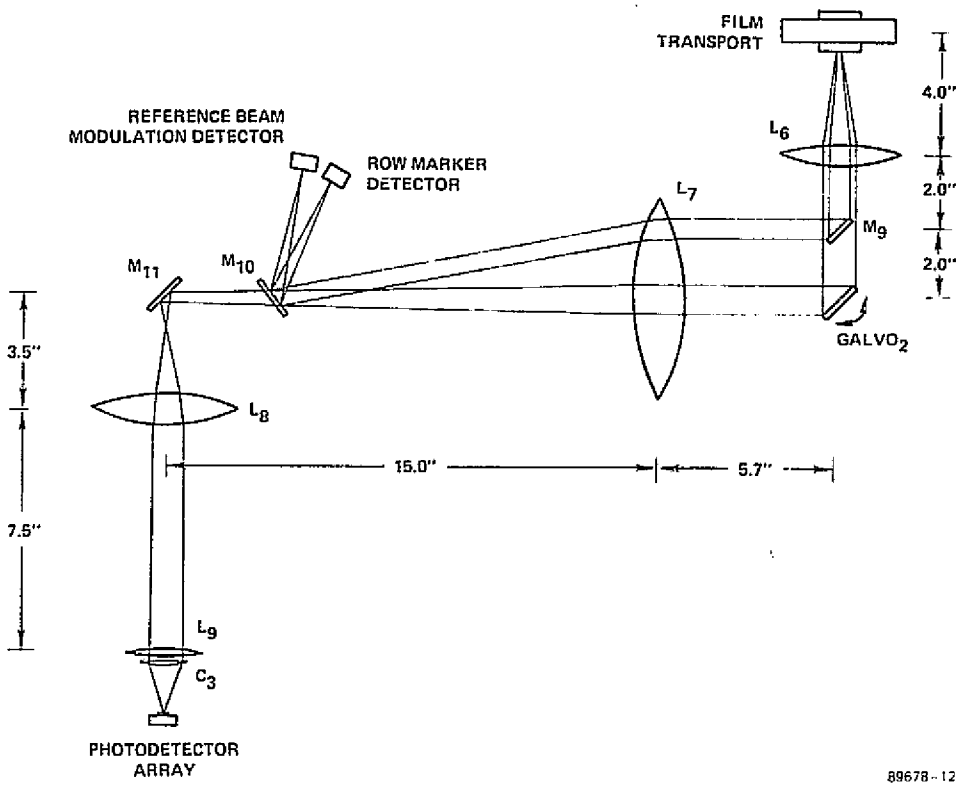

FIGURE 3-37. THE READOUT SUBSYSTEM

mathematical model of this Fourier transform phase error effect was derived (see Appendix 3A). But as the example in Appendix 3A (derived from the present system) illustrates, the effect is not severe enough in this case to be of concern; a bit translation of half a bit is expected at worst in the photodetector array image plane.

This completes our discussion of the optical subsystems of the breadboard. The complete optical top view schematic is shown in Figure 3-38; Figure 3-39 is a photograph of the actual components used in the system.

3.2.2.2 Electronics Considerations

To read out the data, the system was operated for all experiments at one-half the recording speed; this was not done because of an inherent speed limitation on any of the components, but because of a desire to integrate the detector array readout over a longer time period than would be available at 40 Hz scan rates. To begin readout, timing considerations require first switching the film transport on at a 0.12 revolution per second rate. The marker beam is on continuously, with the developed marker pulse on the film producing a 10 ms pulse every 50 ms. When the row marker has been passed, a total of 5 ms remains until the galvanometer scan is initiated. This in turn scans the reference beam across the film, and a switchable delay allows readout by the photodetector array to begin at any point in the scan (in 0.5 ms increments) after the start of the scan. The undiffracted reference beam modulation signal provides the proper timing for the start of each detector array readout; this signal is phase locked to a voltage-controlled oscillator which regulates the RL256EBH scan frequency. The detector integration time was fixed at 25.6 μs per hologram.

To display the data, the detector system divides the data into two video line readouts. In the present labeling system, the odd-numbered bits display on video line output No. 1 and the even-numbered bits on line No. 2. The resulting oscilloscope readout maps the input page composer bit pattern of Figure 3-36 onto the output display of Figure 3-40.

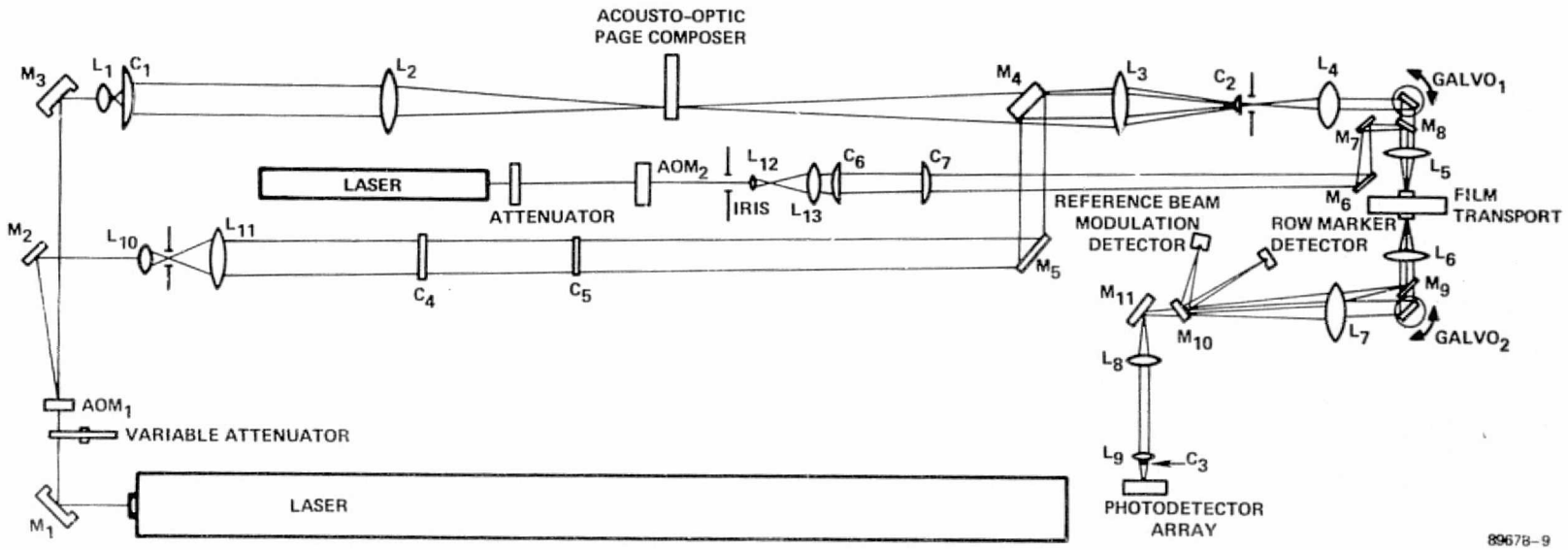

FIGURE 3-38. THE COMPLETE BREADBOARD OPTICAL SCHEMATIC

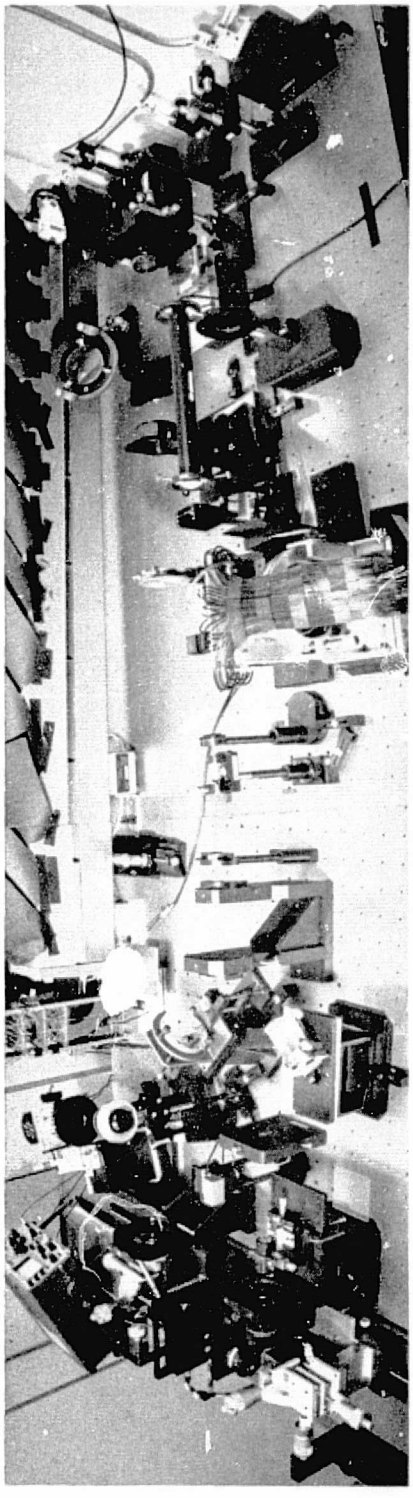

89678-39

FIGURE 3-39. PHOTOGRAPH OF THE BREADBOARD SYSTEM

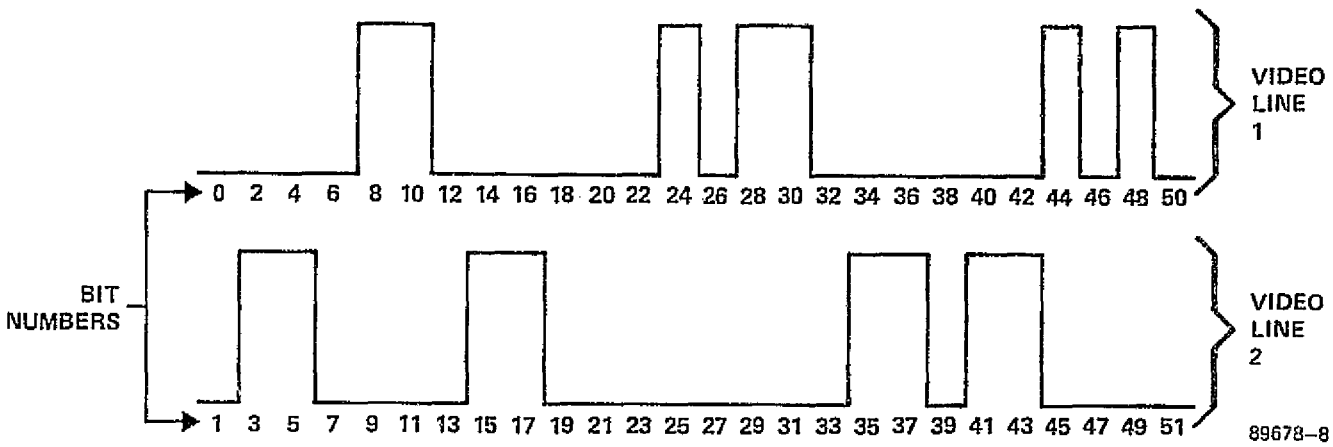

FIGURE 3-40. THE OSCILLOSCOPE DISPLAY READOUT FORMAT

3.2.3 Holographic Optical Elements

The optical system as defined in Paragraph 3.2.1 and 3.2.2 functioned adequately, but considerable improvement of system optical efficiency and the signal-to-noise ratio of the reconstructed data and a decrease in system complexity are possible with the use of three specially designed holographic optical elements (HOE). The first, an acousto-optic page composer illuminator, would simulate the effect of C_1 and L_2 of Figure 3-32 while breaking the laser beam up into 128 bits; the effect is to eliminate two lenses while increasing the optical efficiency by only sending laser light to the individual AOPC channels, rather than wasting energy by illuminating between channels. The second, a reference beam shaper, would replace the cylindrical lens doublet of Figure 3-33 and precisely match the required hologram size. The third is a photodetector array illuminator designed to filter and shape the reconstructed data pattern. An analysis of the requirements to record all three types of holographic optical elements appears in Appendix 3B.

Of these three types of holographic optical elements, only one, the transmissive acousto-optic page composer illuminator, was developed during the present investigation, and then only on 649F photographic plates. To make it, an electroformed gold mask with the same geometry as the 128-element AOPC array was placed in the AOPC plane. The same optical system which illuminated the AOPC was used to illuminate the AOPC mask; this transmitted beam formed the signal beam for this holographic optical element. The photographic plate used to record the HOE was placed with its surface normal to the optical axis, and the reference beam was a collimated beam incident on the plate at an angle of 22° to the surface normal. With this recording apparatus, several illuminators were recorded and well-resolved reconstructed spots were produced. Diffraction efficiences were typically less than 0.5 percent, as would be expected for the unbleached holograms which were evaluated. With bleaching, or dichromated gelatin HOE it is possible to obtain HOE with overall efficiencies in the 50-80 percent range.

3.3 SYSTEM EXPERIMENTAL RESULTS

Although most of the HOLOMEM activity stressed component development, the final stage of this activity included an evaluation of device performance in a complete, operational breadboard. We now discuss baseline experiments conducted using the components described earlier in the breadboard system of Paragraph 3.2.

3.3.1 Photographic Film Testing

The initial experiments on the breadboard system were made before the film transport had been fabricated, and for that reason single scans of holograms were recorded. For these experiments 649F film was used to record the holograms and only nonscanned single holograms were recorded. The results these experiments produced are summarized by the curves of Figure 3-41; the K-ratios are the ratios of the intensity of the reference beam to that of the signal beam. As Figure 3-41 shows, diffraction efficiencies of 0.2 percent to 0.3 percent are easily achievable for a variety of K-ratios. Since 0.5 percent peak diffraction efficiencies are typical, this indicates that the system is stable and the reference/signal overlap is accurate enough to record holograms suitable for system testing. By viewing the reconstructed data pattern with a microscope, it was found that the best reconstructions were achieved for K-ratios in the 10 to 15 range.

When the film transport was implemented, the recording material used was SO-253 film. Once again, the photographic evaluations were aimed at optimizing the holographic properties of the material. Using the 649F results as a guideline for holographic materials, the SO-253 tests focussed on the use of K = 13. The resulting hologram diffraction efficiencies for exposures in the 5.0-10.0 ergs/cm^2 range (for 632.8 nm Helium-Neon laser light) are plotted in Figure 3-42 together with a qualitative signal-to-noise ratio curve based on microscopic visual examination of the reconstructed data. Since the optimum hologram exposure is selected between the two curve peaks, 6.0 ergs/cm^2 was selected as the best choice for this material and recording configuration.

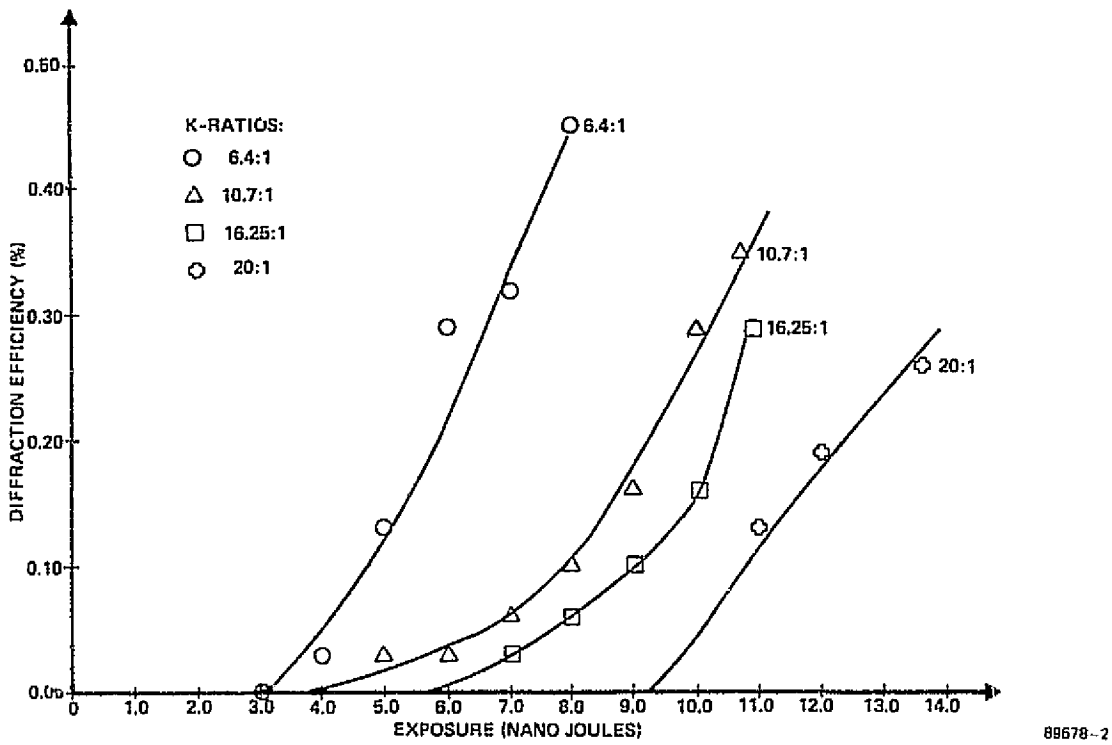

FIGURE 3-41. DIFFRACTION EFFICIENCY OF KODAK 649F HOLOGRAMS AS A FUNCTION OF HOLOGRAM EXPOSURE

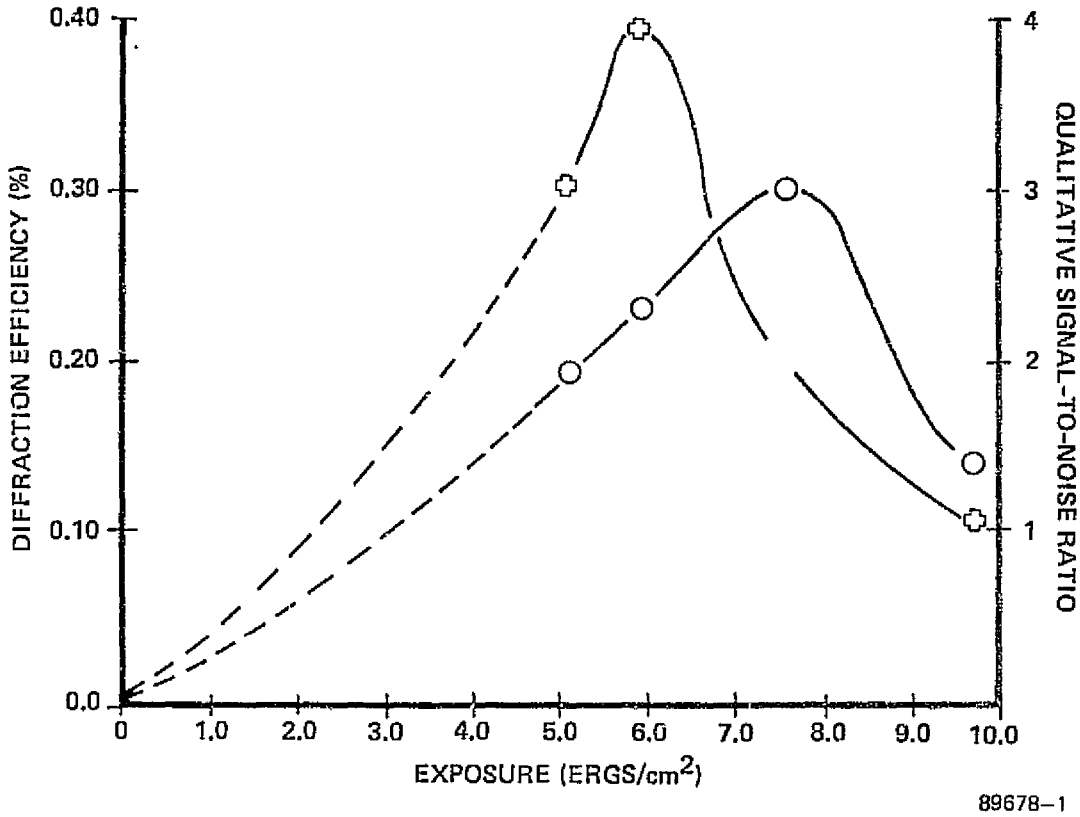

FIGURE 3-42. DIFFRACTION EFFICIENCY AND QUALITATIVE SNR OF KODAK SO-253 HOLOGRAMS AS A FUNCTION OF HOLOGRAM EXPOSURE

A magnified view of a section of a row of SO-253 holograms is shown in Figure 3-43. The long dark bands are the holograms and the narrow bands perpendicular to the hologram length are the hologram fringes.

Further photographic film testing also took place using the breadboard to record rows of holograms on Kalle photoplastic recording film. Though the material was not optimized for the relatively low spatial carrier frequency of the breadboard holograms, the reconstruction efficiency and qualitative signal-to-noise of these test holograms were comparable to those of the SO-253 holograms. A thorough experimental evaluation of photoplastic material, together with a more detailed discussion of these breadboard investigations, appears in Section IV.

3.3.2 Photodetector Array Readout

The first of a number of experimental tests on the photodetector array after the breadboard system was implemented involved verification of the saturation exposure per detector. When 15 data bits were incident in the photodetector array, the total amount of 632.8 nm laser energy in the 15 bits required to achieve detector saturation was 17 μW. By visual examination of the bit pattern it was estimated that the bit width to bit center-to-center spacing ratio was 0.20. Since the detector array was set to integrate the incident energy for 80 μs when this experiment took place, the saturation exposure requirement per detector was

$$E_{saturation} = 17\,\mu W \cdot \frac{1}{15\ bits} \times 80\,\mu s \times 0.20 = 18\ pJ/bit$$

This is more than twice the saturation exposure calculated in Paragraph 3.1.2 from Reticon's furnished data, but identical tests on different occasions confirm the accuracy of the result to within ±2 pJ/bit.

In a separate experiment with a single scanned spot, the 18 dB SNR and 19 dB adjacent detector isolation were confirmed at 2.5 MHz per video line data rates.

C-3

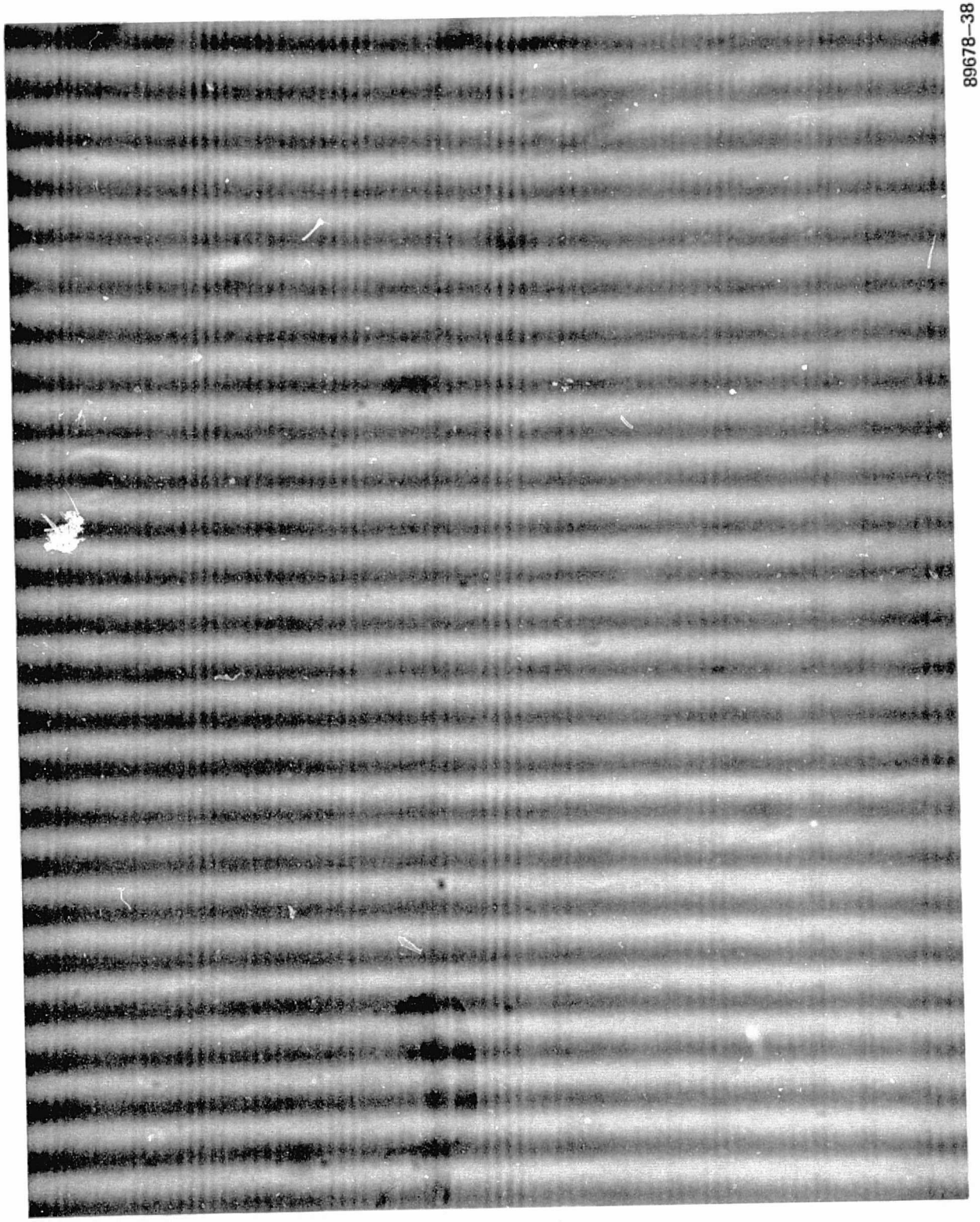

89678-38

FIGURE 3-43. A SECTION OF A ROW OF SO-253 HOLOGRAMS (MAGNIFIED)

As for the absolute data rate, the RL256EBH array read out all 256 elements in 80 μs. This corresponds to an absolute single detector data rate of $\frac{256 \text{ elements}}{80 \text{ μs}}$ = 3.2 Mb/s. The goal for readout for this component is 4 Mb/s, and the present system therefore operated at 80 percent of the required speed.

To evaluate the system characteristics, scanned holograms with approximately 6 ergs/cm^2 exposures of 632.8 nm laser light, K = 13, 0.6 percent diffraction efficiencies, and the data pattern of Figures 3-36 and 3-40 were reconstructed to image the data on the RL256EBH photodetector array. The oscilloscope display readouts for the image of the page composer pattern itself, a single hologram reconstruction with the film moving and the galvanometers scanning, and the averaged readout of a number of scanned holograms with the same bit pattern are shown in Figures 3-44 (a), (b), and (c), respectively. As these pictures show, the system throughput signal-to-noise ratio of Figure 3-44 (a) is about 7 to 1. A single hologram degrades this to between 3 and 4 to 1. Scanning the holograms has a minor degrading effect, but the indications are good that dynamic readout is easily achievable. Similar tests on other developed film samples show that identical results can be achieved with no adjustment of the breadboard components.

3.3.3 System Reliability Evaluation

After all system component performance had been optimized, the breadbaord configuration was finalized. During the following two months, the HOLOMEM breadboard was used to record over sixty SO-253 hologram discs, all of which displayed the same sharply-defined hologram fringes and high-quality photodetector array readout. Throughout the testing, the only system adjustments required were fine alignments of the mirrors M_4 and M_5 that were used to maintain the proper reference beam position. At no time, however, did any other component or subsystem require any realignment or adjustment. We therefore conclude that this system, although only a breadboard, is reliable and provides a uniformly high level of performance.

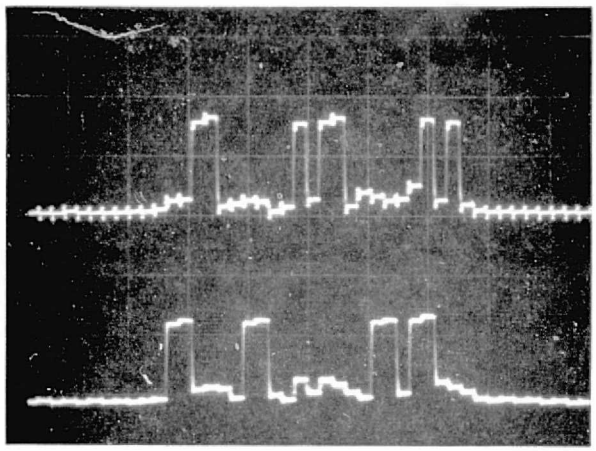

a. SIGNAL

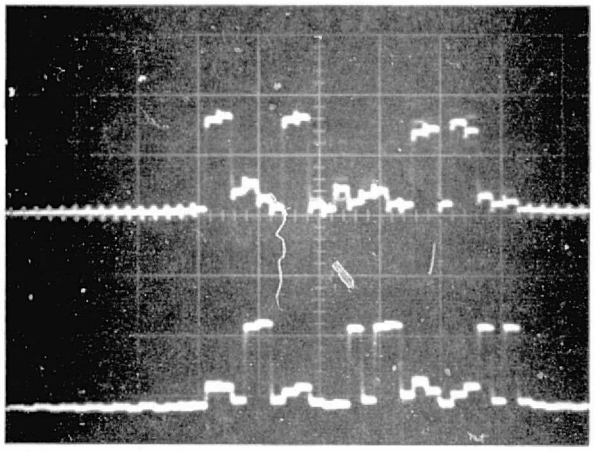

b. STATIC HOLOGRAPHIC READOUT

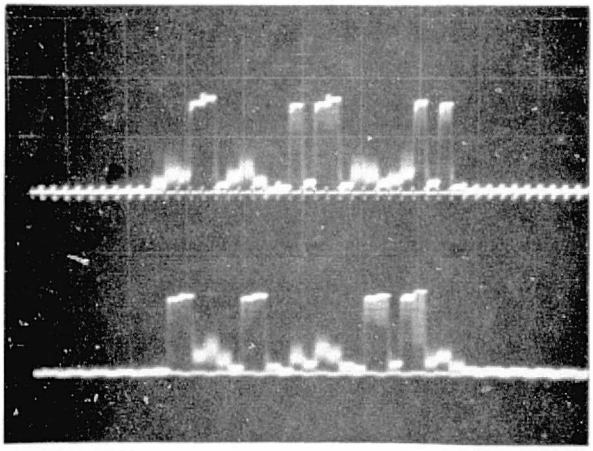

c. DYNAMIC HOLOGRAPHIC READOUT

89678–37

FIGURE 3-44. OSCILLOSCOPE DISPLAY READOUTS FROM THE RL256EBH PHOTODETECTOR ARRAY

3.4 REFERENCES

1. "Updated Holographic Memory System Components," Technical Proposal to NASA/MSFC, Electro-Optics Department, Harris Electronic Systems Division, May 1974

2. Product Literature, General Scanning, Incorporated, 1974

3. Brosens, P. J., "Fast Retrace Optical Scanning," Electro-Optics Systems Design, April 1971

4. Singer Servomotor Catalog, 1974

5. Meret Photodetector Catalog, 1974

6. Reticon Products Summary Brochure, Reticon Corporation, 1974

7. Adler, Robert, "Interaction Between Light and Sound," I.E.E.E. Spectrum, May 1967, pp. 42-54

8. Uchida, N. and N. Niizeki, "Acousto-Optic Deflection Materials and Techniques," Proc. I.E.E.E. 62, pp. 1073-1092

APPENDIX 3A

THE EFFECT OF FOURIER TRANSFORM PHASE ERRORS ON IMAGE TRANSLATION INVARIANCE IN TRANSFORM HOLOGRAPHY

APPENDIX 3A

THE EFFECT OF FOURIER TRANSFORM PHASE ERRORS ON IMAGE TRANSLATION INVARIANCE IN TRANSFORM HOLOGRAPHY

I. INTRODUCTION

In designing holographic recording systems, considerable effort has been made to produce an exact Fourier transform of the signal in the recording plane. Two major reasons for this are the increased packing density of the resulting recording and the insensitivity of the reconstructed image to translation when the hologram is out of exact alignment. Sometimes, however, it becomes necessary to move the recording plane out of an exact Fourier transform plane. The paraxial raytrace analysis below shows that the resulting translation problem can be reduced to a few simple design equations.

II. THE SIMPLEST CASE: A TWO-LENS IMAGING SYSTEM

The paraxial thin lens imaging equations are first used to trace rays through the system in the untranslated case, with geometry as pictured in Figure 3-45. Note that all rays traced are of the form (y, nv), where y equals the ray height, v equals the direction tangent of the ray, and the index of refraction n is assumed to be 1.0 throughout the system.

The first ray to be traced is the (0, 1) ray:

Plane P_o	$y_o = 0$	$v_o = 1.0$
L_1, before lens	$y_1 = t_o$	$v = v_o$
L_1, after lens	$y_1 = t_o$	$v_1 = v_o - \frac{y_1}{f_1}$
Plane P_2	$y_2 = t_o + t_1 v_1$	$v = v_1$

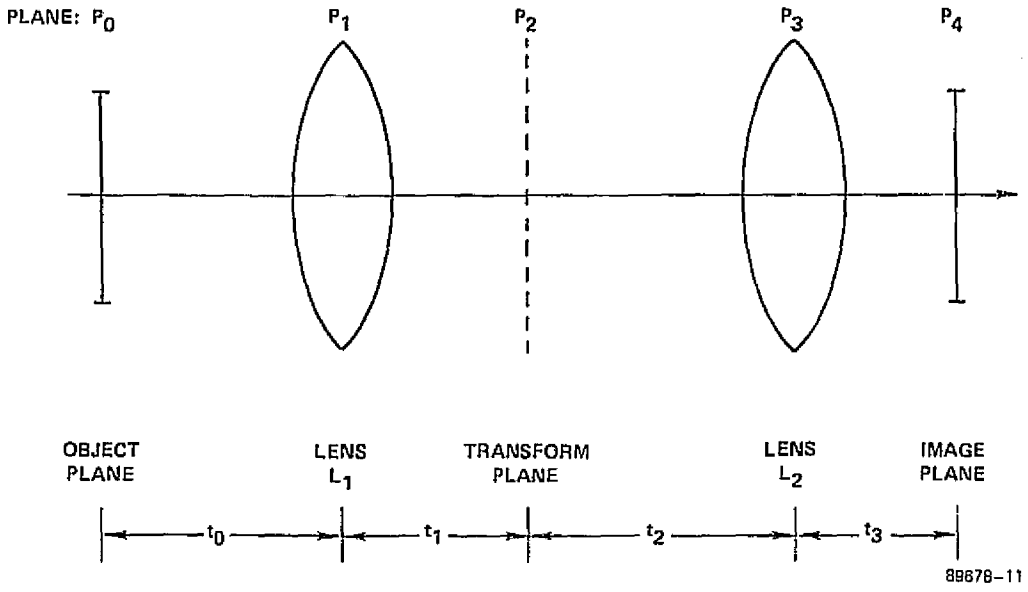

FIGURE 3-45. GEOMETRY FOR FOURIER TRANSFORM PHASE ERROR ANALYSIS

L_2, before lens	$y_3 = y_2 + t_2 v_1$	$v = v_1$
L_2, after lens	$y_3 = y_2 + t_2 v_1$	$v_3 = v_1 - \frac{y_3}{f_2}$

Writing out y_3 in full gives

$$y_3 = t_o + (t_1 + t_2)\left(1 - \frac{t_o}{f_1}\right) \tag{1}$$

and expanding v_3 yields

$$v_3 = 1 - \frac{t_o}{f_1} - \frac{y_3}{f_2} \tag{2}$$

Finally, the image plane must have $y_4 = 0$; hence

$$y_4 = 0 = y_3 + t_3 v_3, \text{ or}$$
$$t_3 = \frac{-y_3}{v_3} \ . \tag{3}$$

An example of these equations used in practice shows that, if $t_o = t_1 = f_1$ and $t_2 = f_2$, then $y_3 = f_1$, $v_3 = -f_1/f_2$, and $t_3 = f_2$, as expected. This is the classic two-lens imaging system.

Now suppose that the signal pattern in plane P_2 is recorded as a hologram, developed, and replaced with an alignment error of Δy_2. Then the above equations become:

Plane P_2	$y_2' = t_o + t_1 v_1 + \Delta y_2$	$v' = v_1$
L_2, before lens	$y_3' = y_2' + t_2 v_1$	$v' = v_1$
L_2, after lens	$y_3' = y_2' + t_2 v_1$	$v_3' = v_1 - \frac{y_3'}{f_2}$

Thus at the image plane we have that:

$y_4' = y_3' + t_3' v_3'$, or, written out:

$$y_4' = t_3' v_1 + (t_o + t_1 v_1 + \Delta y_2 + t_2 v_1)\left(1 - \frac{t_3'}{f_2}\right) \tag{4}$$

Another equation is needed to find the image coordinates t_3' and y_4', so the (0, 0) ray will be traced. It propogates straight through to P_2 unchanged. Therefore, if the plane is shifted by Δy_2:

Plane P_2	$y_2'' = \Delta y_2$	$v_2'' = 0$
L_2, before lens	$y_2'' = \Delta y_2$	$v_2'' = 0$
L_2, after lens	$y_3'' = \Delta y_2$	$v_3'' = -\dfrac{\Delta y_2}{f_2}$

At the image plane

$$y_4'' = \Delta y_2 + t_3' \left(-\frac{\Delta y_2}{f_2}\right), \text{ or}$$

$$y_4'' = \Delta y_2 \left(1 - \frac{t_3'}{f_2}\right) . \tag{5}$$

Subtracting Equation (5) from Equation (4), we have

$$0 = t_3' v_1 + (t_o + t_1 v_1 + t_2 v_1)\left(1 - \frac{t_3'}{f_2}\right) , \text{ or}$$

$$-(t_o + t_1 v_1 + t_2 v_1) = t_3' \left(v_1 - \frac{t_o + t_1 v_1 + t_2 y_1}{f_2}\right), \text{ or}$$

$$t_3' = \frac{(t_o + t_1 v_1 + t_2 y_1)}{\left[\dfrac{t_o + t_1 v_1 + t_2 v_1}{f_2} - v_1\right]} ,$$

which can be rewritten as

$$t_3' = \frac{-y_3}{\left[1 - \dfrac{y_3}{f_2} - \dfrac{t_o}{f_1}\right]} . \tag{6}$$

This is the same as Equation (3), meaning that the shift of plane P_2 does not change the position of the image: $t_3' = t_3$. The resulting image translation is given by Equation (5) with $t_3' = t_3$, since $y_4'' = \Delta y_4$ because $y_4 = 0$. Note also that $y_4' = y_4''$. In the exact Fourier transform case $t_3' = t_3 = f_2$, and $y_4'' = 0$ for any Δy_2, as expected.

III. OTHER IMAGING CONDITIONS

If the transform plane is imaged to a new transform plane, which is then used as the recording plane, several altered versions of the previous equations must be used. For these new equations, m_f equals the magnification of this new transform plane with respect to the old one, and t_2', f_2', v_3''', and t_3''' all refer to a new "second half" of the imaging system after the new transform plane. The equations are

$$y_3''' = m_f \left[t_o + (t_1 + t_2') \left(1 - \frac{t_o}{f_1} \right) \right] \tag{7}$$

$$v_3''' = \left(1 - \frac{t_o}{f_1} m_f - \frac{y_3'''}{f_2'} \right) \tag{8}$$

$$t_3''' = \frac{-y_3'''}{v_3'''} \tag{9}$$

$$\Delta y_4' = \Delta y_2 \left(1 - \frac{t_3'''}{f_2'} \right) \tag{10}$$

where y_2 equals the translation in the new transform plane. Finally, if the image plane is imaged to a final image plane with a magnification m_1, we have

$$(\Delta y_4)_{\text{final}} = m_1 (\Delta y_4)_{\text{original}} . \tag{11}$$

The major equations are (1), (2), and (3), for defining y_3, v_3, and t_3; Δy_4 is given by Equation (5) for the first and simplest case described. Equations (7) through (10) give the results if the transform plane is imaged and then translated, and Equation (11) treats the case of a magnified image plane.

IV. EXAMPLE: REFERENCE FIGURE 3-46

In one system, the virtual image of a page composer bit pattern is located 40" from a 10" lens. Ten inches further along the system is a transform plane which is imaged (with a magnification of $m_f = 2/3$) to a recording plane. Following that plane and 4" from it is a 4" transform lens, and the resulting image is demagnified to a photodetector array with $m_l = 1/5$. Listing the parameters, then, we have

$t_o = 40"$ $\quad f_1 = 10"$ $\quad m_f = 2/3$

$t_1 = 10"$ $\quad f_2' = 4"$ $\quad m_l = 1/5$

$t_2' = 4"$

Equations (7) through (11) are used to calculate our results:

$$y_3''' = \frac{2}{3}\left[40 + (10+4)\left(1 - \frac{40}{10}\right)\right] = -1.33"$$

$$v_3''' = \frac{2}{3}\left(1 - \frac{40}{10}\right) - \frac{(-1.33)}{4} = -1.67$$

$$t_3''' = -\frac{y_3'''}{v_3'''} = -0.80".$$

Suppose holograms 1000 μm = 40 mil long were recorded, and that Δy_2 = 10% of that, or $\Delta y_2 = 4$ mil. Then Equations (10) and (11) are used to get:

$$\Delta y_4' = \left(\frac{1}{5}\right)(4 \text{ mil})\left(1 - \frac{(-0.80)}{4}\right) = 0.96 \text{ mil} \quad .$$

In this example, the imaged bit spacing was 2 mil, so this amounts to a translation of about half a bit. This value has been demonstrated experimentally to be of the proper order of magnitude.

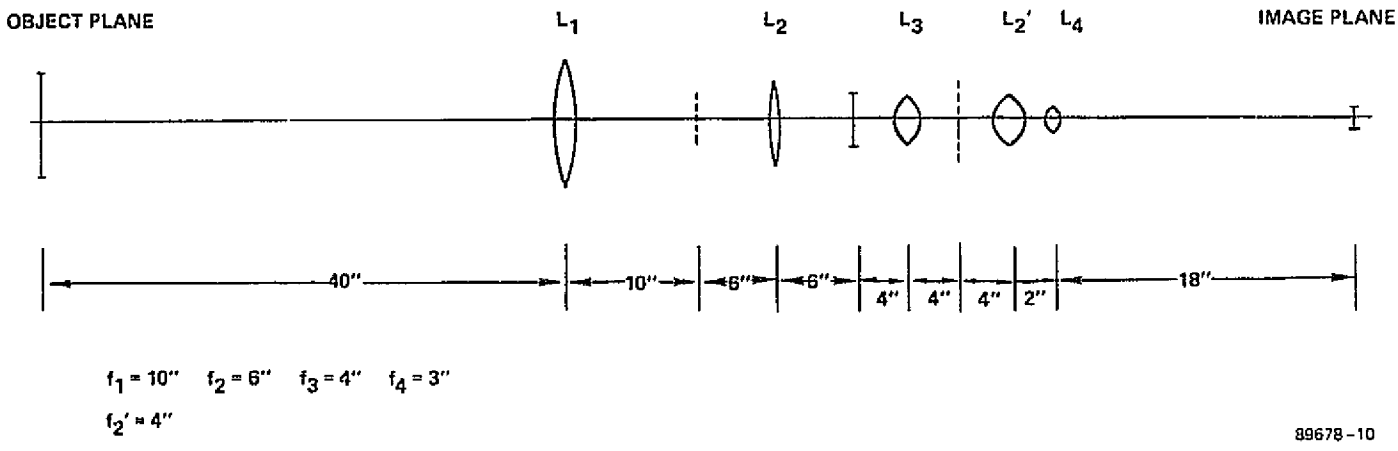

FIGURE 3-46. TRANSFORM PHASE ERROR EXAMPLE LAYOUT

V. THICK LENSES

To accommodate thick lenses, whenever a focal length f_i appears in an equation, substitute $1/\varphi_i$, where φ_i equals the power of the thick lens. This will still be a paraxial approximation, but it will provide a treatment applicable to most practical cases.

APPENDIX 3B

DESIGN PARAMETERS FOR THREE PROPOSED HOLOGRAPHIC OPTICAL ELEMENTS

APPENDIX 3B

DESIGN PARAMETERS FOR THREE PROPOSED HOLOGRAPHIC OPTICAL ELEMENTS

I. GOALS

Three types of holographic optical elements (HOE) were to be investigated for the present system: an acousto-optic page composer illuminator, a photodetector array illuminator, and a reference beam shaper. The general goals for all three include an improvement in system optical efficiency, a decrease in complexity, and an improved signal-to-noise ratio for the system output. As a philosophy for the development of these devices, an attempt was made to relate each component with the subsystem involved; for example, the AOPC illuminator will be generated using an AOPC mask and the cylindrical wavefront presently being used to illuminate it. In this way the original complicated and less efficient system will be used to produce HOE's which will simplify and improve it; a less specific goal is to generalize this idea to other coherent optical systems.

II. HOLOGRAM TYPES

Before discussing system considerations, an analysis of the types of holograms available is appropriate. Since system optical efficiency is important, a summary of the diffraction efficiency characteristics of thin, thick, and blazed holograms appears in Table 3-9. A discussion follows.

A factor that distinguishes thin from thick holograms is Q, which is less than 1 for thin holograms and greater than 10 for thick holograms:[2]

$$Q = \frac{2\pi\lambda_c t}{n\Gamma^2} \qquad (1)$$

TABLE 3-9

THEORETICAL HOLOGRAM DIFFRACTION EFFICIENCIES[1]

Thickness	Modulation Type	Mode of Use	(%) Maximum Efficiency
Thin	Absorption	Transmission	6.25
Thin	Phase (Unblazed)	Transmission	33.9
Thin	Phase (Blazed)	Reflection	100.0
Thick	Absorption	Reflection	7.2
Thick	Phase	Transmission	100.0
Thick	Phase	Reflection	100.0

where λ_c is the reconstruction wavelength, t = the emulsion thickness, n = the refractive index of the emulsion, and Γ = the separation of the interference fringes in the medium. Γ is given by[3]

$$\Gamma = \frac{\lambda_e}{2 \sin\left(\frac{\theta_R' - \theta_o'}{2}\right)}$$

Here λ_e is the effective wavelength of the recorded wavefront in the medium, and θ_R' and θ_o' are the angles of incidence of the reference and signal beams with respect to the normal of the emulsion surface. Assuming that the effective wavelength is the recorded wavelength (which means, for most purposes, that no shrinkage occurred in processing), then for the 6328Å light used in the present system, it is found that the separation of the reference and signal beams must be greater than 22° for a thick hologram to result.

a. Thin Holograms

Absorption holograms, whether thin or thick, have a low diffraction efficiency by their very definition: they absorb a high percentage of the incident light. Thin phase holograms are better, but still are not optimum, because of their impact on the system optical efficiency. In the thin category blazed holograms, working somewhat like blazed diffraction gratings, have produced up to 73 percent diffraction efficiency for plane wave holograms in photoresist and overcoated with aluminum[4] (with a reflectance of ~80%); higher efficiencies are expected when more reflective materials, such as silver (with a reflectance of ~93%), are used for coating the surface. The advantages are that a shallow angle between the object and reference is not only possible but recommended, and that because reflection is used to reconstruct, at no time does the object wavefront need to pass through the substrate of the photographic medium. Drawbacks include the

more complex recording and reconstruction geometry of any reflection hologram (with the reference and object beams incident from opposite sides of the emulsion), the difficulties of finding a reliable red-sensitive photoresist (Horizons Research has supplied one which produces a diffraction efficiency of 7.2 percent for holograms of a diffuse object),[5] the requirement to overcoat for peak efficiency, the bright and modulated background that appears in the image, and the nonlinear phase distortion of the image caused by the blazing process.[6]

b. Thick Holograms

The most obvious advantage of thick holograms is that they have a capability of 100 percent diffraction efficiency in either the transmission or reflection phase modes of operation. This is true even in conventional materials such as 649F, though dichromated gelatin is recommended over this because of the practical difficulties in producing high diffraction efficiencies in bleached 649F. The disadvantages of using this are that there is another step in the photographic process for this method, that plates must be dichromated shortly before use, and that because of its limited sensitivity, dichromated gelatin has been evaluated primarily in the orthochromatic region. This last problem may make it necessary to use a "contact printing" method along the lines suggested by Lin and Doherty,[7] in which a first hologram recorded in 649F at 6328Å is reconstructed at, for example, 5145Å and used to expose a dichromated gelatin hologram. This hologram can then be processed and returned to the system to be reconstructed in red. Fortunately, red-sensitization of dichromated gelatin is being investigated, and one recent report claims diffraction efficiencies of greater than 90 percent for ammonium dichromated gelatin

sensitized with methylene green and ammonium nitrate and exposed with 300 mJ/cm^2 at 6328Å.[8] Both dichromated gelatin methods are recommended, with special emphasis on the red-sensitive version because of its future advantages in other systems.

III. HOE DESIGN CONSIDERATIONS

a. General

Based on the requirement that the HOE's to be implemented result in equal or better optical efficiency for the present system, hologram diffraction efficiency specifications require thin blazed reflection or thick phase holograms to be used in all cases. An emphasis must be made on eliminating propagation of an object or image beam through the photographic substrate, in order to minimize holographic aberrations; as HOE stability is of fundamental importance, 0.25 inch thick glass is recommended for this purpose, which could severely aberrate the beam if the incident cone angle were too steep.[9] The HOE's under consideration must also fit into the present breadboard, and, if possible, should be recorded with the existing system. Finally, each HOE should be dielectric overcoated where possible to eliminate light losses and noise from unwanted reflections.

As an aid to following the design arguments, a drawing of the present NASA HOLOMEM configuration is included at the end of this Appendix.

b. The Acousto-Optic Page Composer Illuminator

The first of the design problems is defining the maximum comfortable size of a light bit within each acoustic channel. In Figure 3-47(a) a small section of the existing AOPC transducer array is illustrated to

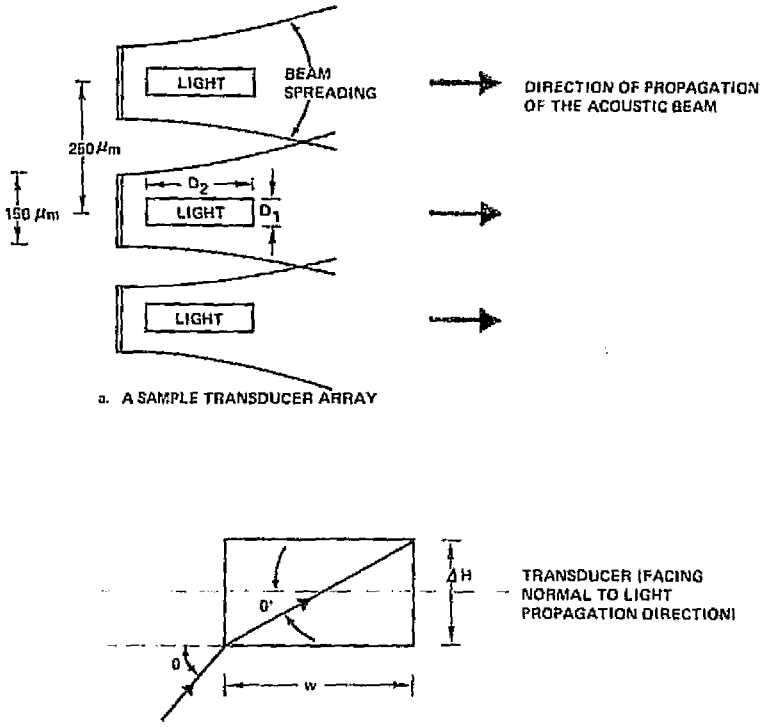

FIGURE 3-47. ACOUSTO-OPTIC PAGE COMPOSER DESIGN CONSIDERATIONS

help discuss this, showing the 150 μm width, the 250 μm center-to-center spacing, the acoustic beam spreading, and the suggested illumination of the transducers by individual laser bits. Here D_2 is defined by the distance to the far-field of the acoustic beams, given by

$$D_2 \leq \frac{d^2}{\Lambda} \tag{3}$$

where d is the transducer width, and Λ is the acoustic wavelength in the medium at the specified acoustic frequency. For a TeO_2 page composer (calculations are similar for SF-59 glass) operating at a carrier frequency of 90 MHz, $\Lambda \cong 23$ μm, and $d = 150$ μm, $D_2 \leq$ 978 μm. Next the present illumination system is checked for compatibility with this requirement (see Figure 3-32); if L_2 has its 2 inch aperture filled, the cylindrical wavefront incident on the page composer is an f/11 system, and the spot size = $2.44 \times f^{\#} \times \lambda \cong 17$ μm, so there is no problem in the D_2 dimension.

The D_1 dimension, the second design problem, comes into play because of the resolution requirements of the page composer illuminator: the signal-to-noise ratio of the AOPC's new output should be higher than that of the present output, which uses a single line of light to illuminate all the bits. The original transducer array artwork is available, and can be used in both this and the photodetector array illuminator to provide a special HOE object beam and increase the system bit resolution, but the smallest bit size allowable in the D_1 dimension must be calculated. This can be done noting Snell's law and using the transducer "window" pictured in Figure 3-47(b). Based on these, the smallest bit size is given by

$$d = \frac{\lambda \cdot w}{n \cdot \Delta H} \tag{4}$$

where λ = the illuminating wavelength in the medium outside the AOPC, w = the width of the transducer, n = the refractive index of the page composer crystal, and ΔH = the transducer height. With $\lambda = 6328\text{Å}$, w = 4 mm, n = 2.43 for TeO_2, and $\Delta H = 150$ μm, $d \cong 7$ μm. Masking down the bits to 7 μm is, therefore, allowable. To minimize the amount of extra work for this HOE, it is recommended that the present 150 μm opening be used for D_1, so that the original AOPC transducer mask can be used to form the HOE.

The layouts using this mask are illustrated in Figures 3-48 and 3-49. The first of these shows a typical transmission HOE, with the beams arranged to make recording and reconstruction relatively simple to implement with the present system; note that the reference beam for recording the HOE comes from the system reference beam with the cylinder lenses removed. In the second scheme, a reflection HOE is pictured. It is only slightly more complicated than the transmission HOE and might allow the use of a blazed hologram, while both it and the first HOE could be thick phase holograms. In both cases, the photographic emulsion is to face the AOPC to avoid letting the object or image beams pass through the HOE glass, and because the image beam will pass through the AOPC crystal in reconstruction, if d is the distance from the emulsion of the HOE to the page composer mask M_{AOPC} during recording, the distance d' from the HOE to the AOPC in reconstruction is given by

$$d' = d + \frac{t}{2}\left(\frac{1}{n} - 1\right) \qquad (5)$$

where t is the crystal thickness and n its refractive index.

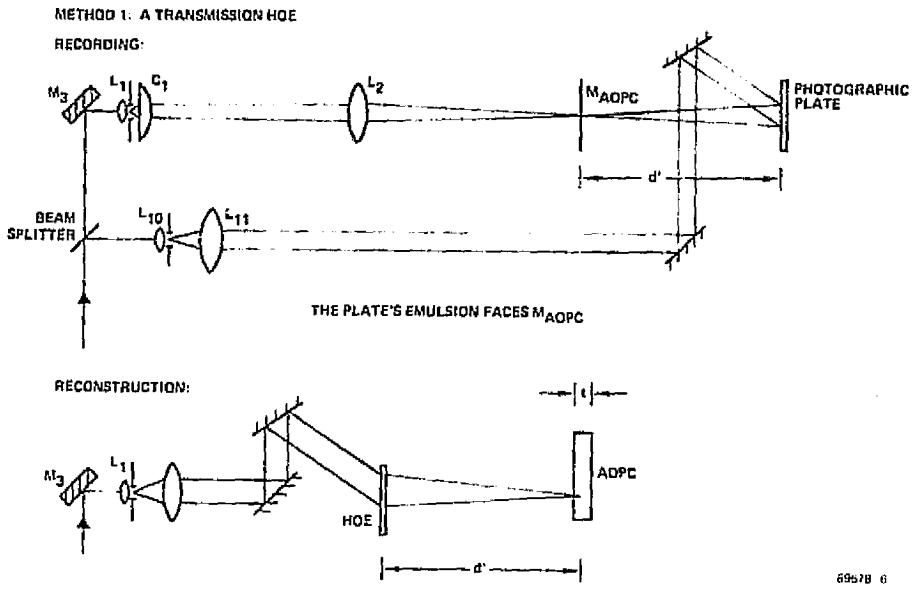

FIGURE 3-48. THE AOPC ILLUMINATOR, METHOD 1

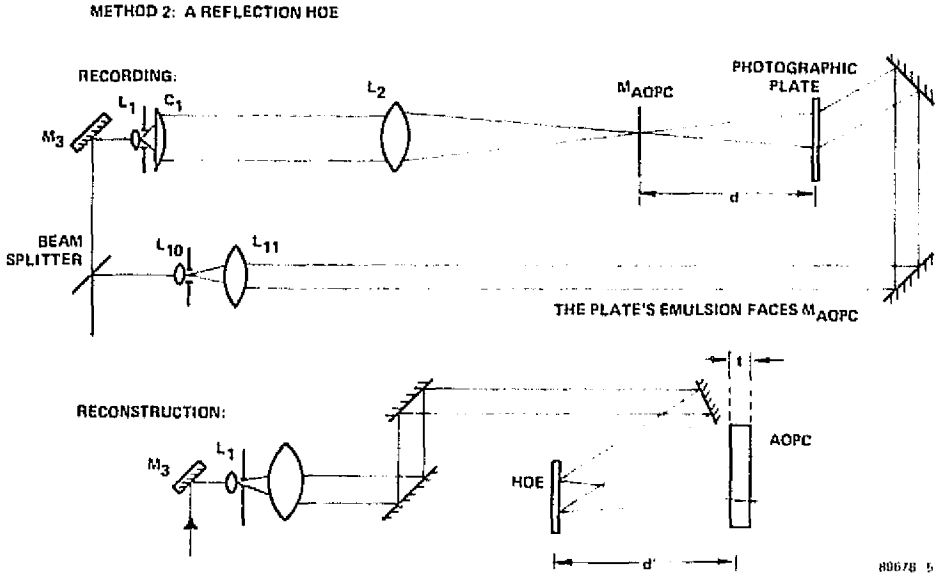

FIGURE 3-49. THE AOPC ILLUMINATOR, METHOD 2

One problem that may surface when this HOE is used is the effect of illuminating an AOPC transducer "window" with a converging instead of collimated wavefront along the D_1 - axis, the result of reconstructing the conjugate wavefront of the object in Figures 3-48 and 3-49. This may distort the Fourier transform of the beam, though preliminary experiments indicate that this is not a problem.[10]

c. The Reference Beam Shaper

There are two basic possibilities for this HOE pictured in Figure 3-50. The first method uses the existing cylinder lenses C_4 and C_5 to form the object beam, with a reference beam separated from the collimated beam at L_{11}; this could be adjusted for equal path lengths if necessary by extending the object beam out to the right side of the main path and bringing it back again. This layout is simple to use and requires no major system modifications. The second concept, which would require an etalon in the laser to allow several resonator lengths of path difference in the recording beams, avoids the disadvantage of the first HOE when the object beam passes through the HOE substrate. Here the object beam illuminates M_{ref}, a special mask 10 μm x 800 μm in the film cassette plane, and passes back through the system to a spot in the original reference beam before M_5, where it forms a HOE. Because the emulsion faces M_5, neither recording nor reconstruction will require that the object beam pass through the glass. A major advantage here is that the beam shaping relies only on the quality of M_{ref}, and not on C_4 and C_5; the disadvantages are the need for an etalon and long recording paths. Both HOE's would use thick phase holograms, and would eliminate the two cylinder lenses from the system.

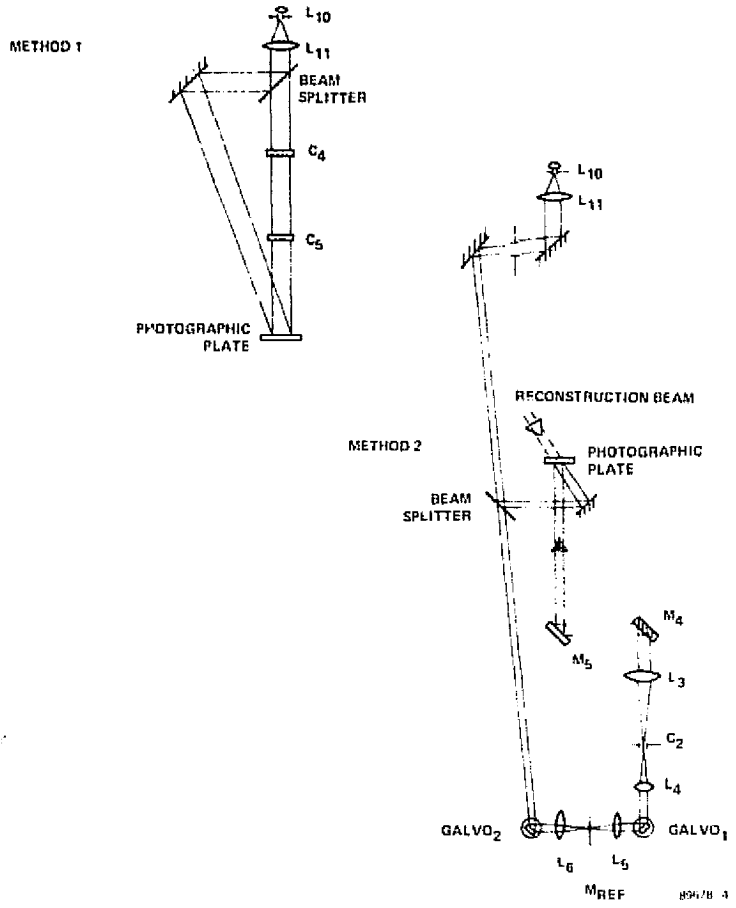

FIGURE 3-50. THE REFERENCE BEAM SHAPER

d. The Photodetector Array Illuminator

This is the most difficult of the HOE's to produce, because of the lack of space in the breadboard and because it must take the AOPC bits and filter them, ideally shaping them to fit the photodetector array elements more exactly. As a result, a two-step HOE recording process has been conceived that has the additional problem of requiring the object beam to pass through glass. Because of the nearly-collimated nature of the beam leaving $GALVO_2$, however, this should not produce the disastrous aberrations the AOPC HOE could have suffered.

The basic concept behind this HOE (shown in Figure 3-51) is that each 150 μm bit, when reconstructed from the film cassette, is to be filtered and shaped by the HOE. Because the PDA detector spacing-to-width aspect ratio is 4:1, a 5:1 aspect ratio is recommended in the output of this HOE. For this reason a new mask, M_{PDA}, must be made from the original AOPC transducer artwork, maintaining the 250 μm center-to-center spacing but with an opening of only 50 μm for each cycle. (Fringing with the existing mask will assure identical scaling of the mask.) This will be used later. As a first step, the original M_{AOPC} beam, placed to take the AOPC crystal thickness into account, must be passed through the system and bounced off $GALVO_2$ to a photographic plate at PDA HOE No. 1 in Figure 3-51, Step One. It is required that $\theta \cong 20^\circ$ and $\theta' \cong 45^\circ$ (brought in beyond $GALVO_2$) to assure good diffraction efficiency. The angular offset of beam No. 1 is produced by adjusting the offset control on the CCX-100 for $GALVO_2$. It is recommended that this first HOE be placed before L_7 because of space limitations.

STEP ONE: RECORD A HOLOGRAM OF THE ORIGINAL AOPC BITS

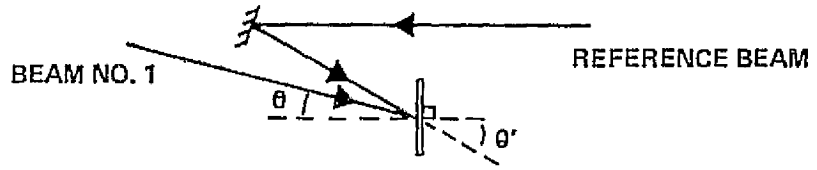

BEAM NO. 1 IS PRODUCED BY THE THROUGHPUT OF THE ORIGINAL AOPC MASK

STEP TWO: RECORD THE PDA ILLUMINATOR HOE USING PDA HOE NO. 1

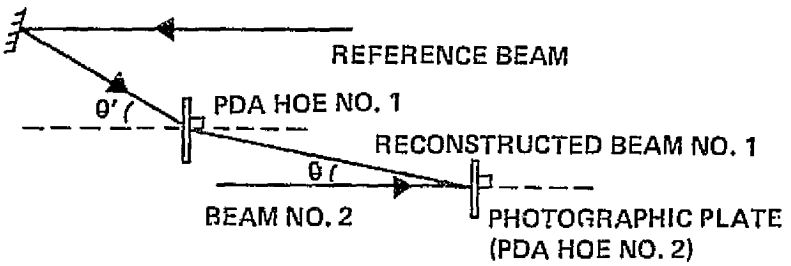

BEAM NO. 2 IS PRODUCED BY THE THROUGHPUT OF THE SPECIAL M_{PDA} MASK

STEP THREE: RECONSTRUCTING PDA HOE NO. 2

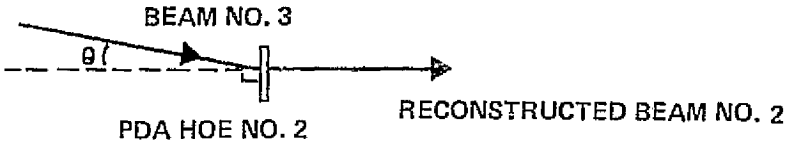

BEAM NO. 3 IS PRODUCED BY RECONSTRUCTING BITS FROM THE FILM CASSETTE HOLOGRAMS

89678–3

FIGURE 3-51. THE PHOTODETECTOR ARRAY ILLUMINATOR

As a second step, the special M_{PDA} mask is inserted in the page composer plane (again taking the AOPC crystal thickness into account), and passed through the system and off $GALVO_2$ with its CCX-100 reset to normal angular offset; the PDA readout should be checked at this point to confirm proper scaling of M_{PDA}. Next, as Step 2 of Figure 3-51 shows, PDA HOE No. 1 is reconstructed and used as the reference beam for PDA HOE No. 2, in which the M_{PDA} beam is the object beam. Because of space conditions, PDA HOE No. 2 is to be recorded after L_7 with $GALVO_2$ translated slightly toward $GALVO_1$ to allow the two beams for PDA HOE No. 2 to coincide. After recording, $GALVO_2$ must be translated back, and any offset in reconstruction can be adjusted with M_{11} and the translation controls at the PDA. Finally, to reconstruct, the CCX-100 on $GALVO_2$ is returned to the offset angle of Step 1, and the reconstructed bits are transformed by PDA HOE No. 2 into M_{PDA}-type bits.

A major problem with this method, besides the obvious difficulties of maintaining alignment between all the components, is the recording process: each individual M_{AOPC} bit must reconstruct only one M_{PDA} bit. This would ordinarily require one PDA HOE No. 1 and one PDA HOE No. 2 exposure for each such relationship, which could be done using a step-and-repeat procedure. Because of the nearly-collimated nature of the beam leaving $GALVO_2$, however, it may be possible to record all bit pair holograms at once. Alignment would be considerably easier in this case, but it will be necessary to determine the degree of noise that reconstructed "false bits" will generate when M_{AOPC} Bit No. 1, for example, reconstructs not only M_{PDA} Bit No. 1 but also all the others more faintly.

e. Hologram Size

The reference beam shaper and the PDA HOE have to focus fairly large spots. So for the worst-case it is necessary to go to the AOPC HOE to determine how large a photographic plate must be to resolve the bits. Because the 2-inch aperture of L_2 resolves the AOPC illuminating line in the present system, this means that a 2-inch aperture is all that will be required for all these HOE's.

IV. THICK HOLOGRAM RAYTRACE PROGRAM

Using the quantitative thick hologram theory of Reference 3 for calculating fringe separation and effective recording wavelengths, and the surface grating approximation of thick holograms in Reference 2, a thick hologram raytrace program has been generated for use on the HP30 desk computer. As shown subsequently, it can be used to test the alignment sensitivity and effect of emulsion shrinkage on the proposed HOE's.

Figure 3-52 shows the general format of the printout for three cases analyzing the effects of a 20 percent hologram shrinkage during processing of the various HOE types. Figure 3-52(a) is one method for producing a HOE of minimum Q for the AOPC illuminator, the reference beam shaper, and the only way for PDA HOE No. 2. Figure 3-52(b) is an alternative approach with the object and signal beams balanced to have hologram fringes normal to the emulsion for the AOPC illuminator and the reference beam shaper. Figure 3-52(c) is the case for PDA HOE No. 1. For 20 percent shrinkage, these three cases produce a misalignment of the image vector as indicated in Table 3-10.

As expected, the case for PDA HOE No. 1 is the most critical of the three. But because it need not have a high diffraction efficiency, swelling of the emulsion in ordinary 649F thick holograms should counteract this. Soaking in thriethanolamine is a possible solution.[11]

```
FOR THE REFERENCE VECTOR WITH
R1= 0.374    ,R2= 0      ,AND R3= 0.927    ,
THE OBJECT VECTOR WITH
O1= 0        ,O2= 0      ,AND O3= 1        ,
A RECORDING WAVELENGTH OF 0.6328  MICRONS,
AN EMULSION MAGNIFICATION OF 0.8  ,
AN EMULSION THICKNESS OF 12   MICRONS,
AN EMULSION REFRACTIVE INDEX OF 1.54    ,
AND A RECONSTRUCTION WAVELENGTH OF 0.6328  MICRONS,
THE EFFECTIVE WAVELENGTH IS 0.624917099   MICRONS,
THE FRINGE SEPARATION IS 1.342898282   MICRONS,
THE ALLOWABLE WAVELENGTH ERROR IS + OR - 0.591473707   MICRONS,
THE ALLOWABLE ANGULAR MISALIGNMENT IS + OR - 8.288550908   DEGREES,
AND Q= 13.74391988    .
FOR A RECONSTRUCTION VECTOR WITH
C1=-0.374    ,C2= 0      ,AND C3=-0.927    ,
THE RECONSTRUCTED IMAGE VECTOR HAS COORDINATES
I1= 4.71775E-03    ,I2= 0      ,AND I3=-0.999988871    .
```

a.

```
FOR THE REFERENCE VECTOR WITH
R1= 0.191    ,R2= 0      ,AND R3= 0.982    ,
THE OBJECT VECTOR WITH
O1= 0.191    ,O2= 0      ,AND O3=-0.982    ,
A RECORDING WAVELENGTH OF 0.6328  MICRONS,
AN EMULSION MAGNIFICATION OF 0.8  ,
AN EMULSION THICKNESS OF 12   MICRONS,
AN EMULSION REFRACTIVE INDEX OF 1.54    ,
AND A RECONSTRUCTION WAVELENGTH OF 0.6328  MICRONS,
THE EFFECTIVE WAVELENGTH IS 0.6328  MICRONS,
THE FRINGE SEPARATION IS 1.331180565   MICRONS,
THE ALLOWABLE WAVELENGTH ERROR IS + OR --0.573236677   MICRONS,
THE ALLOWABLE ANGULAR MISALIGNMENT IS + OR - 8.107821109   DEGREES,
AND Q= 13.98694653    .
FOR A RECONSTRUCTION VECTOR WITH
C1=-0.191    ,C2= 0      ,AND C3=-0.982    ,
THE RECONSTRUCTED IMAGE VECTOR HAS COORDINATES
I1=-0.191    ,I2= 0      ,AND I3= 0.981590037    .
```

b.

```
FOR THE REFERENCE VECTOR WITH
R1= 0.707    ,R2= 0      ,AND R3= 0.707    ,
THE OBJECT VECTOR WITH
O1= 0.374    ,O2= 0      ,AND O3= 0.927    ,
A RECORDING WAVELENGTH OF 0.6328  MICRONS,
AN EMULSION MAGNIFICATION OF 0.8  ,
AN EMULSION THICKNESS OF 12   MICRONS,
AN EMULSION REFRACTIVE INDEX OF 1.54    ,
AND A RECONSTRUCTION WAVELENGTH OF 0.6328  MICRONS,
THE EFFECTIVE WAVELENGTH IS 0.600695402   MICRONS,
THE FRINGE SEPARATION IS 1.447846739   MICRONS,
THE ALLOWABLE WAVELENGTH ERROR IS + OR - 0.661622863   MICRONS,
THE ALLOWABLE ANGULAR MISALIGNMENT IS + OR - 8.578990684   DEGREES,
AND Q= 11.82365275    .
FOR A RECONSTRUCTION VECTOR WITH
C1= 0.707    ,C2= 0      ,AND C3= 0.707    ,
THE RECONSTRUCTED IMAGE VECTOR HAS COORDINATES
I1= 0.356202575    ,I2= 0      ,AND I3= 0.934408757    .
```

89678-36

c.

FIGURE 3-52. HOLOGRAM RAYTRACE PROGRAM PRINTOUTS

An additional problem is the effect of misalignment of the reconstruction vector on the image, and this has been evaluated for $\pm 1^{o}$ misalignment along with the shrinkage effect. The results are summarized in Table 3-11.

Here PDA HOE No. 1 is again prominent, but as the reconstruction beam need not be moved between recording and reconstruction, the drop-off in diffraction efficiency because of Bragg misalignment should provide the reference needed to align this HOE.

TABLE 3-10. SHRINKAGE EFFECT ON RECONSTRUCTING HOE'S

Case	Misalignment of Image Vector (°)
AOPC HOE, Reference HOE, or PDA HOE No. 2	-0.27
AOPC HOE or Reference HOE	0.00
PDA HOE No. 1	-1.09

TABLE 3-11. EFFECT ON RECONSTRUCTED HOE'S OF EMULSION SHRINKAGE AND RECONSTRUCTION VECTOR MISALIGNMENT

Case	Image Vector Misalignment in Degrees for a Reconstruction Misalignment of:	
	$+1^{\circ}$	-1°
AOPC HOE, Reference HOE, or PDA HOE No. 2	+0.65	-1.20
AOPC HOE or Reference HOE	+1.00	-1.00
PDA HOE No. 1	-0.34*	-1.86

*This is negative owing to the combination of shrinkage and angular misalignment; at $+2^{\circ}$ reconstruction misalignment, this is $+0.40^{\circ}$.

REFERENCES

1. Cathey, W. T., Optical Information Processing and Holography, John Wiley and Sons, New York, (1974), p. 162.

2. Close, D. H. and Moss, G. E., Materials for Holographic Optical Elements, Technical Report AFML-TR-73-267, Hughes Research Laboratories, October (1973), p. 116.

3. Zech, R. G., Data Storage in Volume Holograms, Ph.D. Thesis (University of Michigan: 1974), p. 104.

4. Sheridan, N. K., Applied Physics Letters 12, 316 (1968).

5. Ralston, L. M., "Horizons Red-Sensitive Photoresist," Technical Memo dated May 6, 1974, Harris Electro-Optics Operations.

6. Kermisch, D., JOSA 60, 782 (1970).

7. Lin, L. H., and E. T. Doherty, Applied Optics 10, 1314 (1971).

8. Graube, Andrejs, "Holographic Dye-Sensitized Dichromated Gelatin," in Unconventional Photographic Systems, SPSE Symposium IV, edited by Kocher, A., and Eynard, R. A., Society of Photographic Scientists and Engineers, Washington, D.C., (1975), pp. 67-69.

9. Reddersen, B. R., "Distortion Effects in the ETL/MEGIS System, II. Plane Parallel Plate Aberrations," Technical Memo dated September 9, 1975, Harris Electro-Optics Operations.

10. Roberts, H. N., "Transform Plane Intensity Pattern for 100 percent Duty Page Composer," Technical Memo dated November 22, 1975, Harris Electro-Optics Operations.

11. Nishida, N., Applied Optics 9, 238 (1970).

SECTION IV

READ/WRITE RECORDING MATERIALS INVESTIGATION

SECTION IV

READ/WRITE RECORDING MATERIALS INVESTIGATION

The implementation of an unattended, generally unaccessible optical mass memory requires a reusable storage material. The recording medium must not only achieve a specified level of holographic performance, as measured in terms of diffraction efficiency and SNR ratio, but also be compatible with systems and operational requirements, chiefly those related to recyclability, performance consistency and reliability.

For a space-qualified mass memory system, we require an optical analog to magnetic tape (a "recording medium" that satisfies systems and operational criteria, but not the information storage specifications). As is well-known, available recording media do not fill this need. However, certain types of electrophotographic materials closely simulate the storage performance and systems behavior expected of a fully-qualified recording medium; specifically, we refer to photoplastic recording films.[1-5] Photoplastic recording films are closely related to high resolution electrophotographic films, except in two respects: a top coating of a thermoplastic with a relatively low glass transition temperature is added and, after charging and exposure, heat is used to develop the electrostatic latent image rather than a toner. Photoplastic recording films are phase recording media (that is, a recording media that modulates the phase rather than the amplitude of an incident beam of coherent light) that store information in the form of surface deformations in the thermoplastic layer. Since heating the thermoplastic layer significantly above its glass transition temperature leads to softening and a discharge of the electrostatic latent image owing to an ionic conductivity, the surface of the photoplastic recording film can be smoothed to its original planarity, thus rendering it ready for reuse. If it were not for changes with use in the behavior of the photoconductor, sensitizing dye(s), thermoplastic layer (and its components such as anti-oxidants and plasticizers) and conductive ground plane, a photoplastic recording film would be indefinitely recyclable.

Many practical problems still limit the use of photoplastic recording films, but remarkable progress has been made in improving both recyclability and performance consistency.

4.1 SCOPE OF THE INVESTIGATION

By way of an overview, the ideal recording medium has a high recording speed, a spectral sensitivity matched to a space-qualified laser (at this date only certain helium-neon, Nd-YAG and argon-ion lasers satisfy test criteria for use in space), resolution on the order of 1000 cycles/mm, holographic storage parameters comparable to those of the best Lippmann silver halide photographic emulsions, a capability for undergoing a large number of write/read/erase cycles and so forth. Photoplastic recording films satisfy, on an experimental basis, most of these requirements and, therefore, are primary storage material candidates for a holographic read/write optical mass memory.

Unfortunately, photoplastic recording films are essentially experimental recording materials, whose commercialization has been aimed at single recording applications such as holographic nondestructive testing and micrographics. Hence, there is no motivation to develop a photoplastic recording film capable of a large number of useful write/read/erase cycles. Also, commerically available photoplastic recording films are not optimized for high-density data storage, a factor that minimizes the cost of production and the performance of these recording media.

Despite the shortcomings of existing photoplastic recording films, they are the closest approximation to the type of recording material needed for the read/write holographic optical mass memory. Therefore, we acquired several photoplastic recording films (namely, the PVK/TNF-type photoplastic recording film made by Kalle AG and a new photoplastic recording film based on the Scott Graphics, Inc. transparent electrophotographic or TEP film) and designed a basic research program to measure various performance variables. The emphasis of this study was on reusable photoplastic recording films coated on flexible substrates. Most high performance photoplastic recording media

have a rigid glass substrate overcoated with a transparent conductor; this approach is not suitable for a mass memory application. As performance goals, we chose a spectral sensitivity of 100 $\mu J/cm^2$ at 632.8 nm and/or 514.5 nm, individual hologram recording times consistent with average data rates in excess of 1 Mb/s, a 500 cycle lifetime for each hologram location, and a 15 μm hologram center spacing along each scan track. Key experimental activities included the measurement of holographic parameters in both static and dynamic modes, the design and fabrication of a breadboard film transport having in-line charging and heat development stations, and environmental testing. The details, procedures and results of our experimental activities are summarized in Paragraphs 4.2 and 4.3. Further background is provided in Appendices 4A, B and C.

4.2 KALLE PHOTOPLASTIC RECORDING FILM

The only photoplastic recording film (PRF) that is both suitable for holographic recording and available as a commercial product is manufactured by Kalle AG of Wiesbaden-Biebrich, West Germany. Kalle, a Division of Hoechst AG, is a plastics company with both raw materials and finished products capabilities; it is also a primary source of reprographic materials in Europe. The Kalle PRF was developed primarily for rapid-access, holographic nondestructive testing (HNDT) applications. As HNDT applications generally do not require a write/read/erase recording material, the Kalle PRF is not optimized for data storage and retrieval. However, because its holographic recording properties and machine-handling problems closely simulated those of anticipated systems-qualified recording media, we performed an in-depth experimental characterization of the Kalle PRF. Baseline data and highlights of our investigation follow; further background is given in Appendix 4A.

4.2.1 Construction of Kalle AG Photoplastic Recording Film

The Kalle photoplastic recording film is a (planar) phase recording material coated on a 35 mm polyester film base. Holograms and spatial filters are recorded as surface deformations in a thin layer of thermoplastic. The construction of the Kalle PRF is shown in Figure 4-1. The PRF is constructed of three layers: a thermoplastic layer nominally 0.6 μm thick, an organic photoconductor layer approximately 0.9 μm thick, and a Hostophan® polyester substrate about 50 μm thick. There is no internal transparent ground plane. The thermoplastic is a plasticized polystyrene, whereas the organic photoconductor is believed to be polyvinyl carbozole (PVK) photosensitized with trinitrofluoronone (TNF). The cosmetic quality of the Kalle PRF is excellent. There are generally no visible scratches or blemishes. The optical transmission of the PRF varied from an average value of 90 percent by ±4%. Film thickness varied from an average value of 55 μm by about ±4%.

4.2.2 Photoplastic Recording System

The holographic storage process for the Kalle PRF is shown schematically in Figure 4-2. Three steps are required for recording: charging, exposure, and development. During the charging process, the top surface of the PRF is charged by a corona spike at a potential of 20 kV. This step performed in the dark creates a potential gradient across the PRF. For exposure, some irradiance distribution (e.g., hologram interference fringes) is allowed to illuminate the charged PRF for a given time. In illuminated regions of the organic photoconductor (OPC) layer, charge carriers are created. These carriers are swept to the interfaces of the OPC by the potential gradient across the film, thereby causing a modulated charge density to appear. Development is accomplished by heating the charged and exposed PRF above the glass transition temperature of the thermoplastic. Above the glass transition temperature of the thermoplastic, the electrostatic and surface tension forces cause the thermoplastic to flow. The flow continues until these two forces are equalized or the temperature drops below the glass transition

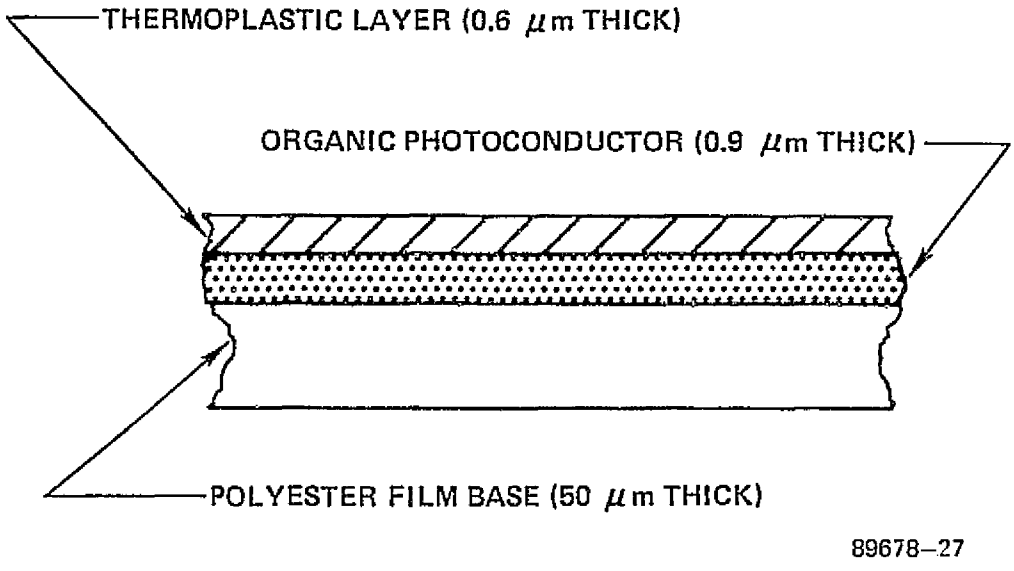

FIGURE 4-1. CONSTRUCTION OF KALLE AG PHOTOPLASTIC RECORDING FILM

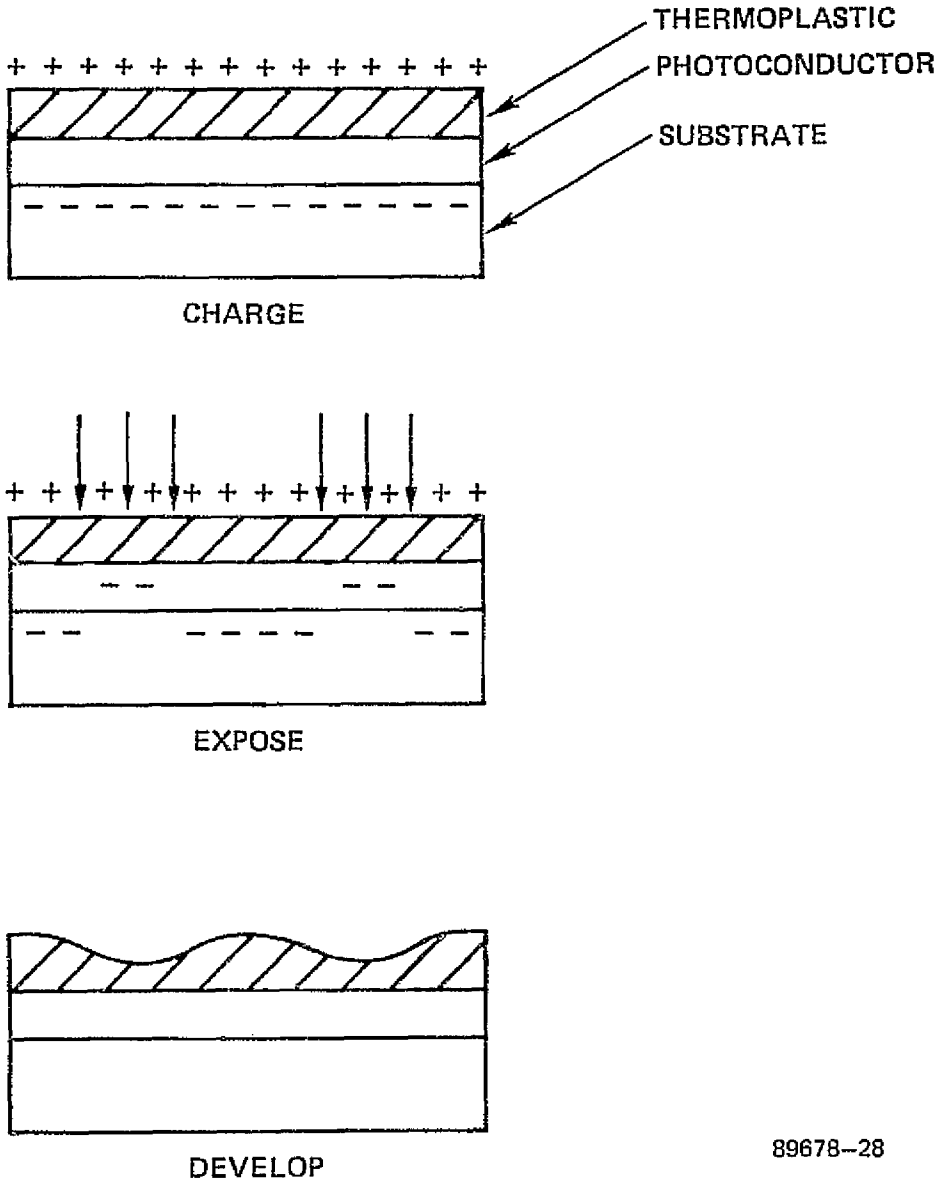

FIGURE 4-2. HOLOGRAPHIC STORAGE PROCESS FOR KALLE AG PHOTOPLASTIC RECORDING FILM

point. The heating and subsequent cooling of the thermoplastic layer surface cause deformations which correspond to the initial modulated charge density.

Holograms were recorded on the Kalle PRF using two different recording systems. A static system was used to determine basic holographic performance. A dynamic system was used to demonstrate the feasibility of a tape-oriented random-access memory (TORAM).

The static recording system could record a single hologram on the PRF with the film stationary. The PRF sample was supported by a vacuum platen fabricated from NESA® glass (a glass coated with a transparent conductive coating of indium-tin oxide). The transparent coating on the platen allowed exposure and readout of transmission holograms. Electrical contacts were made to the conductive coating; hence, the coating itself provided both a ground plane for the charging process and a resistive load that a current pulse heated during the development process. The vacuum platen secured the film and ensured good thermal contact.

The corona charging unit consisted of a single charging spike at a potential of approximately 20 kV. The spike was separated from the surface of the PRF by approximately 1 cm. The corona spike was chosen instead of the more usual corona wire because of the extremely high voltages required to charge the externally-grounded Kalle PRF. These high voltage levels caused frequent failure of corona wires. No noticeable difference in charging between the two methods was observed, except for the increased lifetime of the spike unit. Timing control of the corona high-voltage supply guaranteed repeatable charging times.

The dynamic recording system was designed to perform charging, exposure and development operations for a photoplastic film moving at velocities consistent with a 1 Mb/s data transfer rate. A photograph of the breadboard film transport system is shown in Figure 4-3. The charging, exposure and development stations are indicated. The vacuum capstan and film tensioning motors are powered by external power supplies

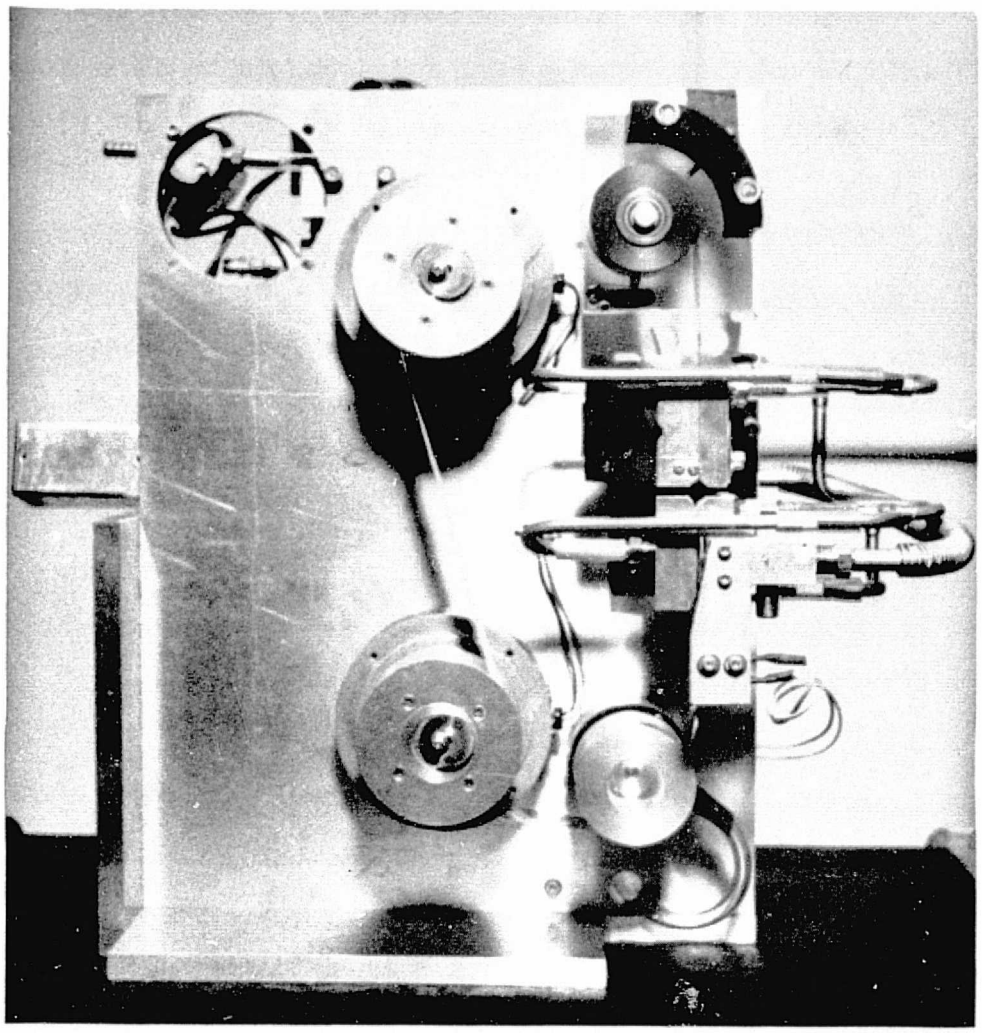

89678–1

FIGURE 4-3. PHOTOGRAPH OF PHOTOPLASTIC RECORDING FILM TRANSPORT

controlled from a console panel (not shown). Solenoid actuation and system power are also provided at the console, in addition to the film velocity control.

A schematic diagram of the tape drive is shown in Figure 4-4. The motion of the PRF through the transport is illustrated. The location of the charging, exposure and development stations are shown, together with the necessary air lines. The supply reel and takeup reel accomplish the storage of unused and developed PRF, respectively. Air pressure gauges were used to monitor the air pressure at the bearings.

The charging station consisted of a single corona spike approximately 1 cm from the surface of a grounded aluminum cylinder which supported the PRF. The aluminum cylinder, supported on an insulated plastic bearing, was only 20 mm in width to ensure that no tendency for high voltage arc existed. To isolate the high voltage present during charging the corona assembly was separated from the film drive frame by a 40 mm thickness of nonconductive plastic. In operation, the corona unit was raised to the designated voltage and left on during exposure. When passed through the charging station, the PRF was charged to a prescribed level.

The exposure station consisted of an air bearing that constrained the film surface to movement in the lateral dimension of less than ±12 μm. The air bearing was fabricated from Porex,® a porous plastic that provides a smooth diffusion of the air passing through it. The bearing provided a reasonably uniform distribution of air pressure to support the photoplastic film between pneumatic layers. An entrance window was provided in the air bearing to allow the signal and reference beam to illuminate the charged PRF. An exit window/mirror combination on the back of the air bearing permitted separation of the diffracted beam for subsequent imaging.

The development station was also an air bearing. The development station provided heated air to raise the temperature of the PRF thermoplastic layer above its glass transition temperature. The heated air could be vented for readout by solenoid action. The temperature of the heated air was controlled by a voltage proportioning heater assembly. Temperature was stabilized within 0.5° C at the desired operating temperature.

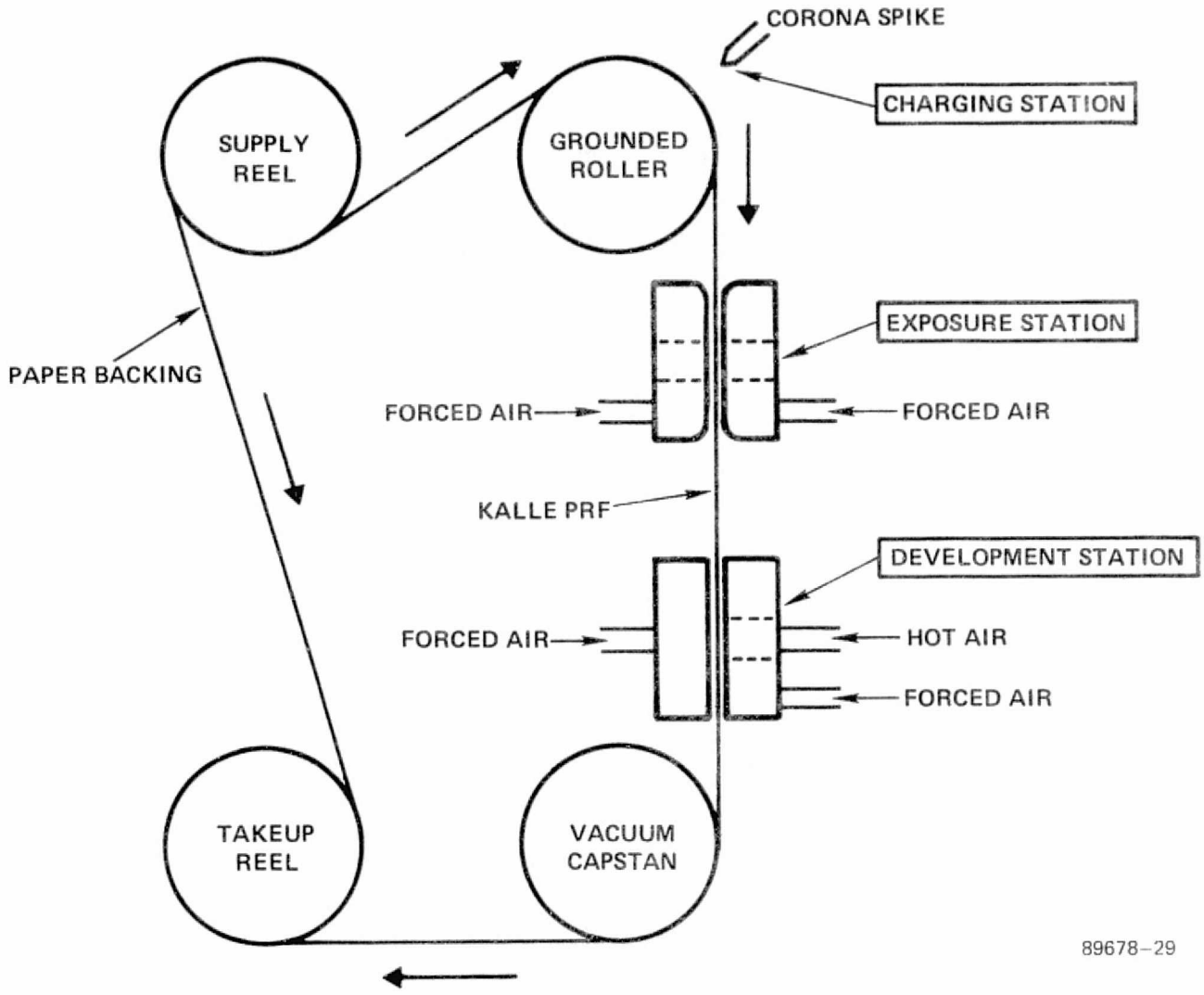

FIGURE 4-4. SCHEMATIC OF PHOTOPLASTIC RECORDING FILM TRANSPORT

The film transport handled the PRF adequately. A length of PRF cycled through the film transport five times had no visible scratches or blemishes. The stresses on the PRF during handling produced no discernible effects. No smearing of the surface relief patterns occurred and no imprinting of relief patterns in the polyester substrate was observed. These effects were probably minimized by the protective paper backing of the film. This backing prevents any layer of PRF from direct contact with adjacent layers. As indicated in Figure 4-4, the protective paper backing was automatically unwound from and rewound on the PRF by the film transport.

The stability of the dynamic recording system was fully tested. A series of grating holograms were recorded on a conventional silver halide film using the film transport. Exposure times ranged from 5 to 30 ms. Film velocities were consistent with the 1 Mb/s data transfer rate. The diffraction efficiencies of dynamically recorded amplitude holograms (Kodak 649F film was used for this test procedure) reached the 6 percent level, which is approximately the theoretical maximum and indicated that the system had sufficient stability.

A holographic interferometer was used to generate the irradiance distribution for exposure. The same interferometer was used for both static and dynamic testing. A helium-neon laser ($\lambda = 632.8$ nm) was used for exposure. The laser beam was split into signal and reference beams to form the holographic interferometer. The signal and reference beams were then spatially filtered, expanded and collimated. The two beams were combined at the exposure plan to form a sinusoidal irradiance pattern. The irradiance of the beams was uniform over a 1 cm^2 area in the exposure plane.

4.2.3 Kalle PRF Holographic Properties

The holographic properties of the Kalle photoplastic recording film were investigated using both static and dynamic recording systems. The diffraction efficiency of grating holograms was measured for recordings made with the static system. The diffraction efficiency (DE) and signal-to-noise ratio (SNR) obtained for Fresnel holograms

recorded with the static system were also measured. In addition, diffraction efficiency of grating holograms recorded dynamically was measured.

The simple holographic interferometer described in Paragraph 4.2.2 was used for all experiments. The spatial frequency of the interferometer was 750 cycles/mm, which corresponds to the maximum spatial frequency response of the Kalle PRF. The normalized spatial frequency response for the PRF is shown in Figure 4-5. The maximum response is seen to occur at 750 cycles/mm with a 3 dB full bandpass of 500 cycles/mm.

Grating holograms were recorded with static system. The NESA® glass substrate had a nominal resistance of 65 ohms/square. The diffraction efficiency as a function of exposure was measured with corona voltage V_c and heat development energy E_d as parameters.

The DE levels of holograms recorded under the same experimental conditions varied. Deviations from the average level by factors as large as 2 were noted. Some of the inconsistencies were traced to the high sensitivity of the charging process to the relative humidity level. A portable dehumidifier was used to stabilize the relative humidity of the recording laboratory at 46 percent. Holograms were recorded at equal time intervals. This action maintained the substrate temperature at the same level for the start of each cycle. To average the effects of the fluctuations, five holograms were recorded for each set of experimental parameters. The average DE for each set was calculated discarding the highest and lowest DE levels.

The experimental data are summarized in Figures 4-6 through 4-14. Figures 4-6 through 4-9 illustrate the sensitivity of DE on the corona charging voltage V_c. The heat development energy E_d was held constant at 4 J/cm^2. Each set of data was generated by charging with the designated V_c, exposing to the holographic interference pattern for a net exposure E, and developing with a heat pulse of energy E_d. A maximum DE of 4.3 percent was obtained for V_c = 18 kV and E = 21 $\mu J/cm^2$. Lower DE was obtained for changes of the corona voltage V_c from its optimum value of 18 kV.

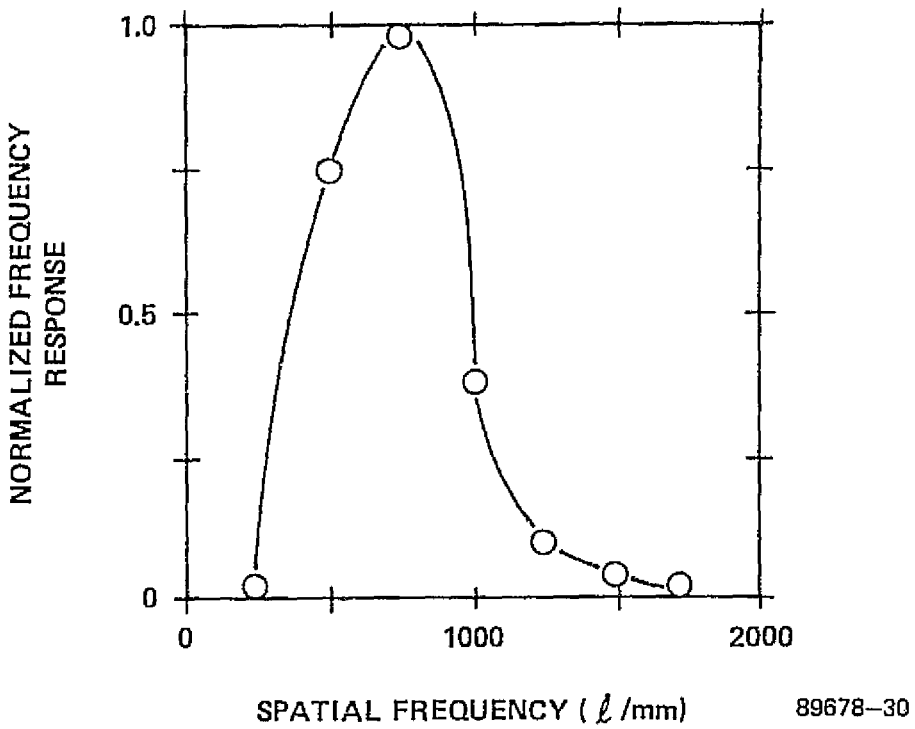

FIGURE 4-5. NORMALIZED SPATIAL FREQUENCY RESPONSE OF KALLE PHOTOPLASTIC RECORDING FILM

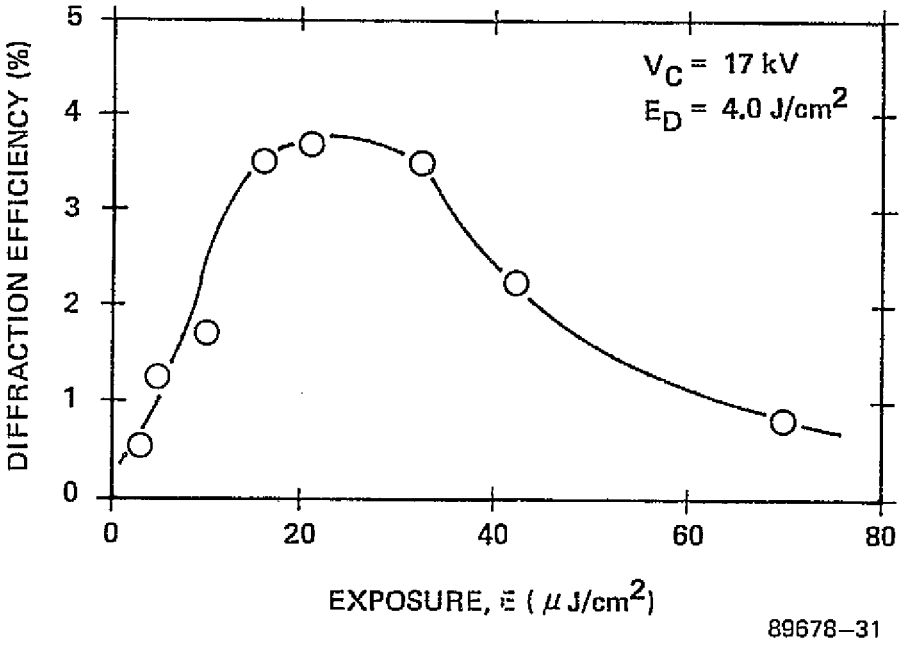

FIGURE 4-6. DIFFRACTION EFFICIENCY AS A FUNCTION OF EXPOSURE WITH V_c = 17 kV and E_d = 4 J/cm^2

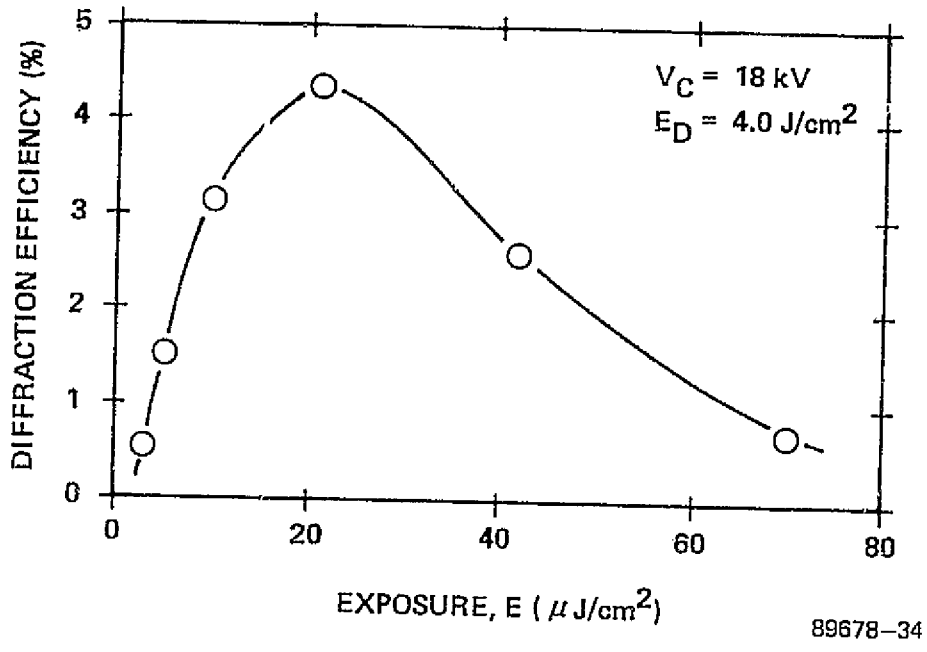

FIGURE 4-7. DIFFRACTION EFFICIENCY AS A FUNCTION OF EXPOSURE WITH V_c = 18 kV AND E_d = 4 J/cm^2

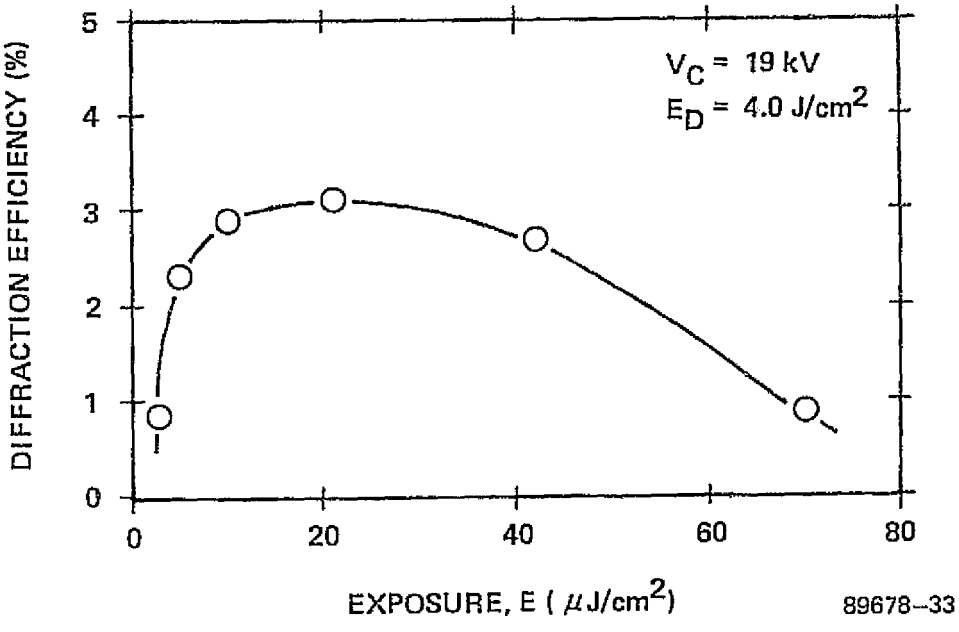

FIGURE 4-8. DIFFRACTION EFFICIENCY AS A FUNCTION OF EXPOSURE WITH V_c = 19 kV AND E_d = 4 J/cm^2

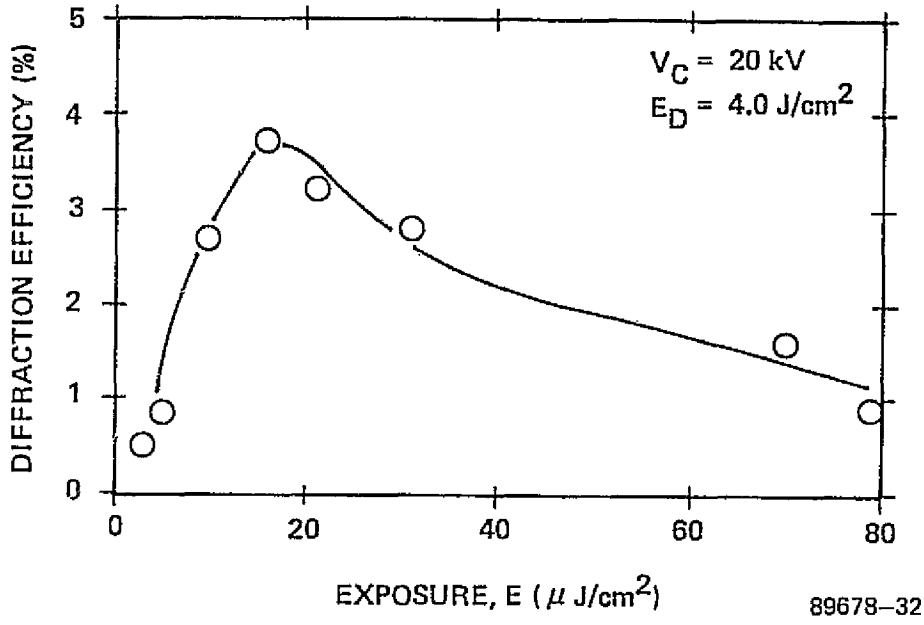

FIGURE 4-9. DIFFRACTION EFFICIENCY AS A FUNCTION OF EXPOSURE WITH V_c = 20 kV AND E_d = 4 J/cm^2

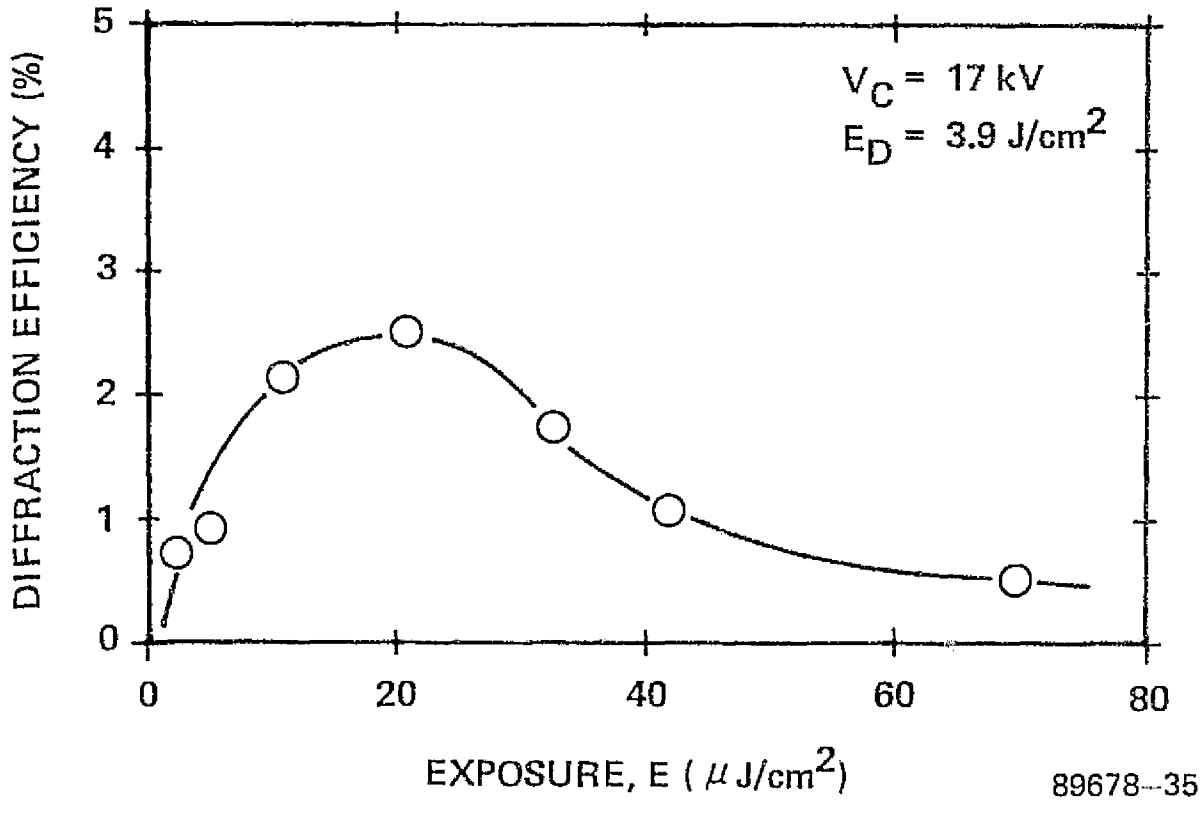

FIGURE 4-10. DIFFRACTION EFFICIENCY AS A FUNCTION OF EXPOSURE WITH V_c = 17 kV AND E_d = 3.9 J/cm^2

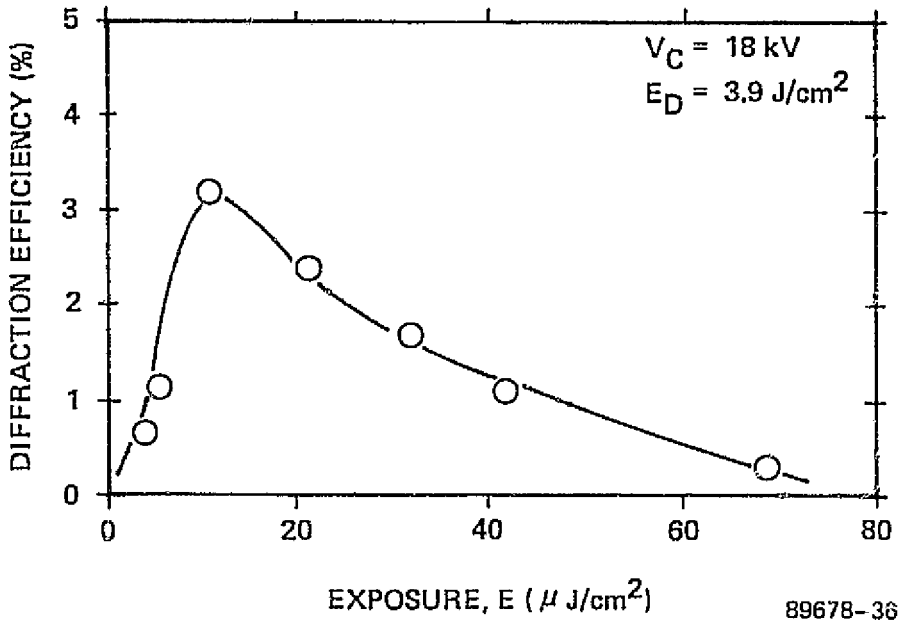

FIGURE 4-11. DIFFRACTION EFFICIENCY AS A FUNCTION OF EXPOSURE WITH V_c = 18 kV AND E_d = 3.9 J/cm^2

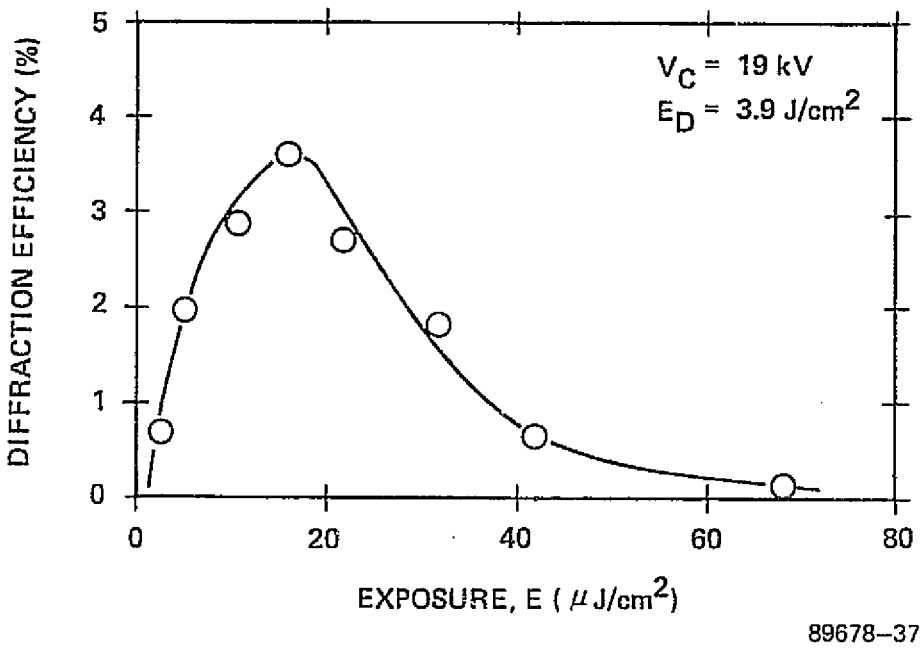

FIGURE 4-12. DIFFRACTION EFFICIENCY AS A FUNCTION OF EXPOSURE WITH V_c = 19 kV AND E_d = 3.9 J/cm^2

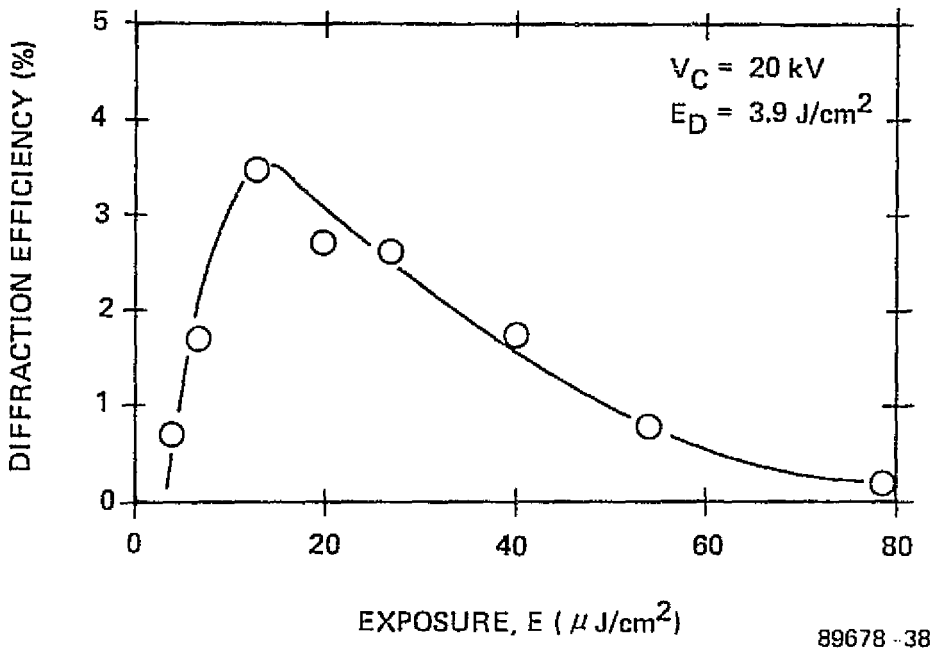

FIGURE 4-13. DIFFRACTION EFFICIENCY AS A FUNCTION OF EXPOSURE WITH V_c = 20 kV AND E_d = 3.9 J/cm^2

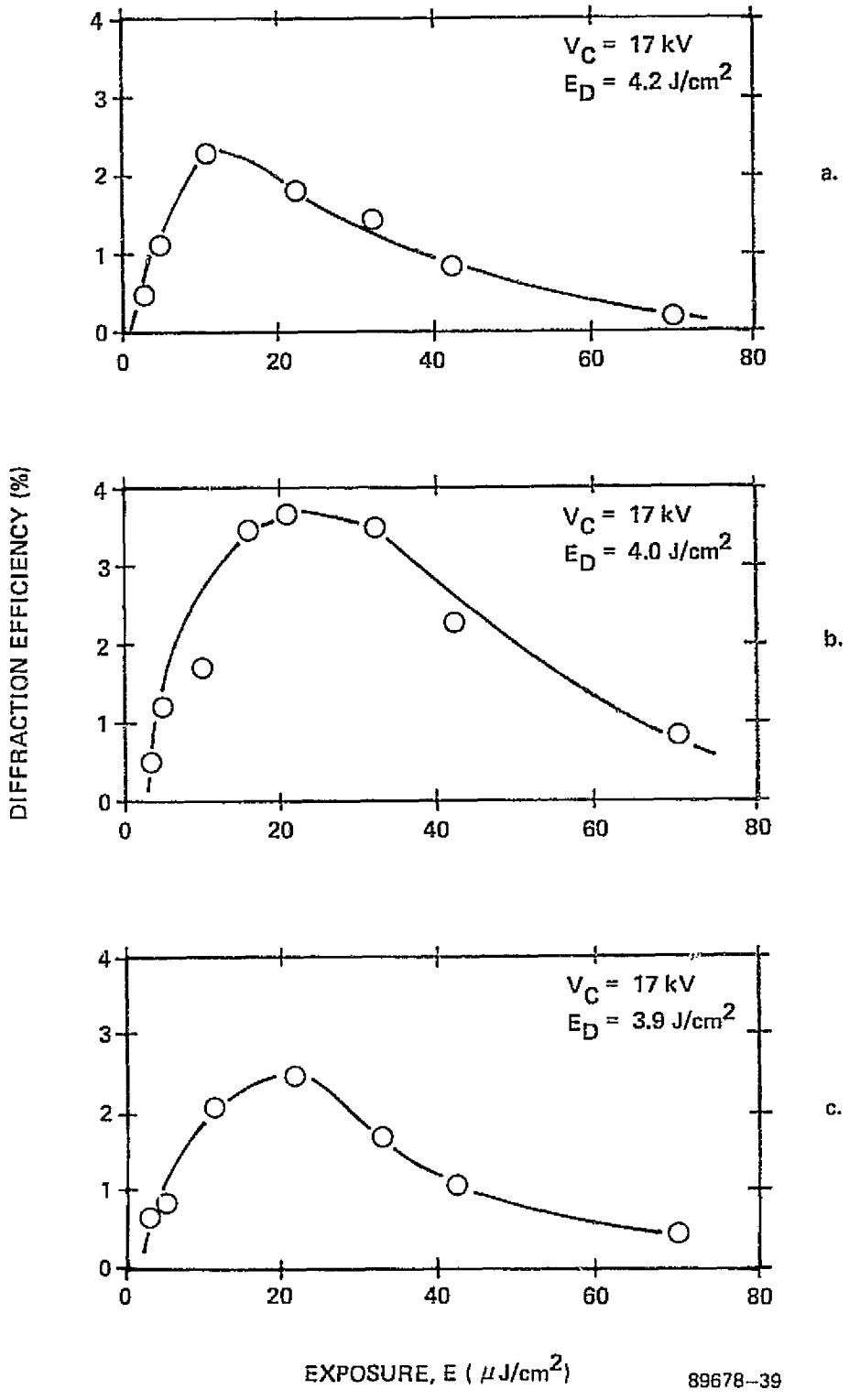

FIGURE 4-14. DIFFRACTION EFFICIENCY AS A FUNCTION OF EXPOSURE WITH DEVELOPMENT ENERGY E_d AS A PARAMETER

Figures 4-10 through 4-13 show the change in DE level for different corona charging voltages and for a heat development energy E_d of 3.9 J/cm^2. This small change in development energy reduced the diffraction efficiency obtained to 3.6 percent. The maximum DE for these test conditions also occurs at a higher charging voltage V_c; that is, the corona charging voltage had to be increased to obtain the maximum efficiency at the lower heat development energy. The need for increased charging levels exists because of the decreased thermal forces present during development. To achieve the same phase modulation level, the decreased thermal forces had to be balanced by an increase in the electrostatic forces. The electrostatic forces were increased by charging with a higher initial potential value.

The diffraction efficiency of a hologram recorded on PRF is clearly dependent on heat development energy. This is illustrated by Figure 4-14, where diffraction efficiency as a function of exposure for three heat development energies is plotted. The corona charging voltage V_c was fixed at 16 kV for this series of tests. The effects of heat development energies were 3.9, 4.0, and 4.2 J/cm^2 are shown in Figures 4-14(a), 4-14(b), and 4-14(c), respectively. A maximum DE of 3.7 percent was obtained for the heat development energy of 4.0 J/cm^2. We observe that the diffraction efficiency decreased by about 35 percent when the PRF was developed with energies of either 3.9 or 4.2 J/cm^2.

The data storage performance of the Kalle PRF was investigated by recording Fresnel holograms of a diffuse data mask with an opaque center. The packing density was 3 Mb/cm^2 with a signal bandpass of about 100 cycles/mm. The beam ratio K was varied while maintaining the charging voltage V_c at 19 kV and the heat development energy E_d at 4 J/cm^2. The diffraction efficiency and associated SNR for K ratios of 1, 2, 5, 10, 25 and 100 as a function of exposure E are shown in Figures 4-15 through 4-20. The variation of SNR and DE with exposure is typical of planar phase recording media. The best overall storage performance was obtained for K = 5 and E = 13 μJ/cm^2. The diffraction efficiency for this K-ratio and exposure value was 2.4 percent and the corresponding SNR was 13 dB.

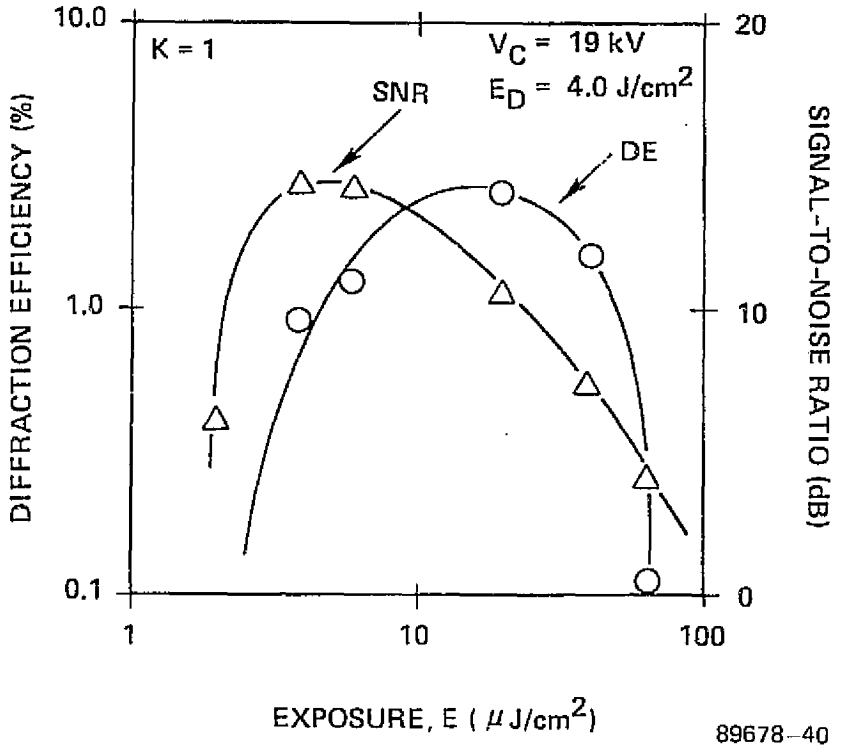

FIGURE 4-15. DIFFRACTION EFFICIENCY AND SIGNAL-TO-NOISE RATIO FOR FRESNEL HOLOGRAMS AS A FUNCTION OF EXPOSURE WITH K = 1

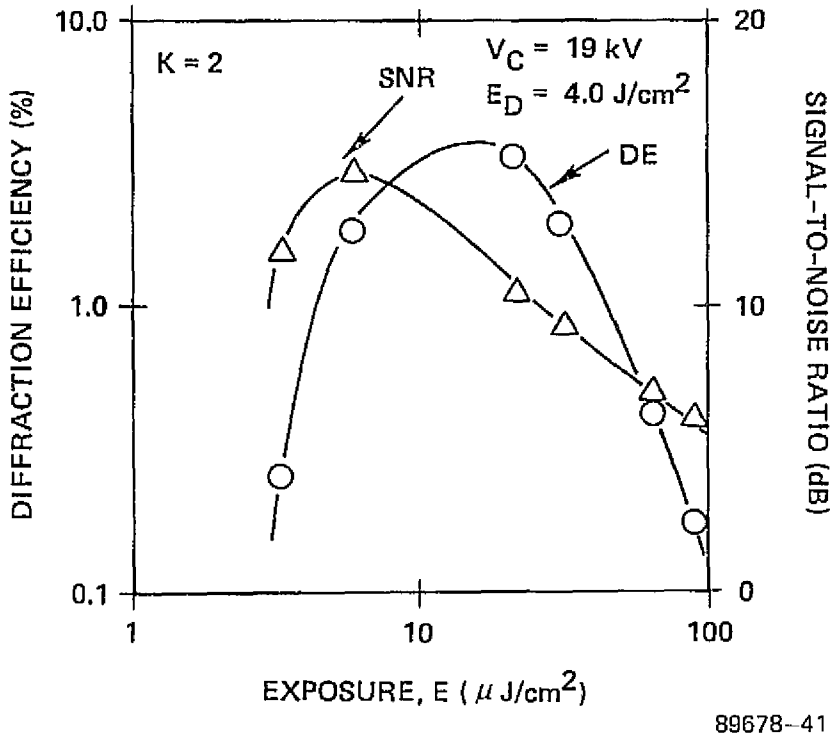

FIGURE 4-16. DIFFRACTION EFFICIENCY AND SIGNAL-TO-NOISE RATIO FOR FRESNEL HOLOGRAMS AS A FUNCTION OF EXPOSURE FOR K = 2

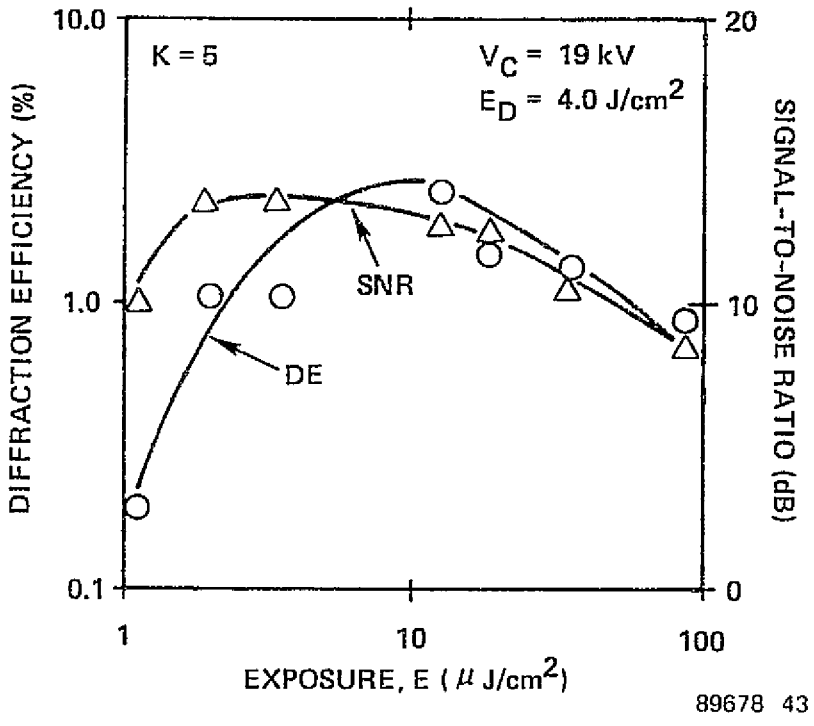

FIGURE 4-17. DIFFRACTION EFFICIENCY AND SIGNAL-TO-NOISE RATIO FOR FRESNEL HOLOGRAMS AS A FUNCTION OF EXPOSURE FOR K = 5

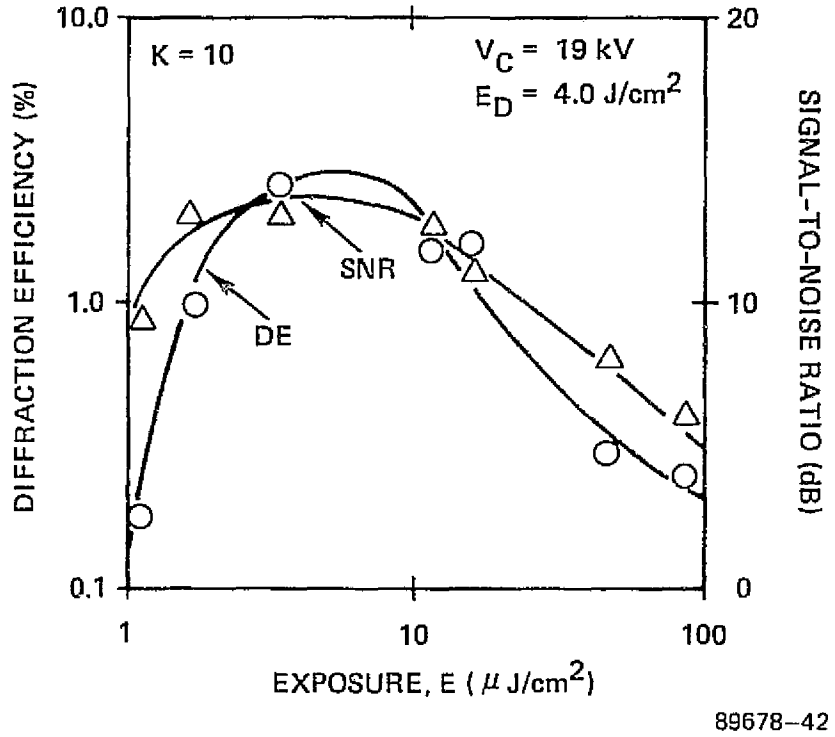

FIGURE 4-18. DIFFRACTION EFFICIENCY AND SIGNAL-TO-NOISE RATIO FOR FRESNEL HOLOGRAMS AS A FUNCTION OF EXPOSURE FOR K = 10

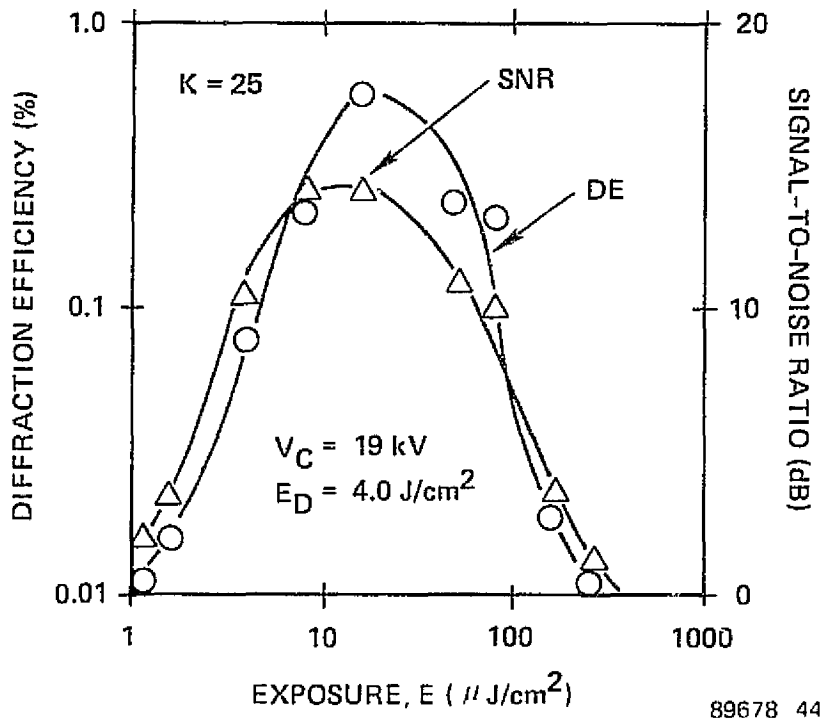

FIGURE 4-19. DIFFRACTION EFFICIENCY AND SIGNAL-TO-NOISE RATIO FOR FRESNEL HOLOGRAMS AS A FUNCTION OF EXPOSURE FOR K = 25

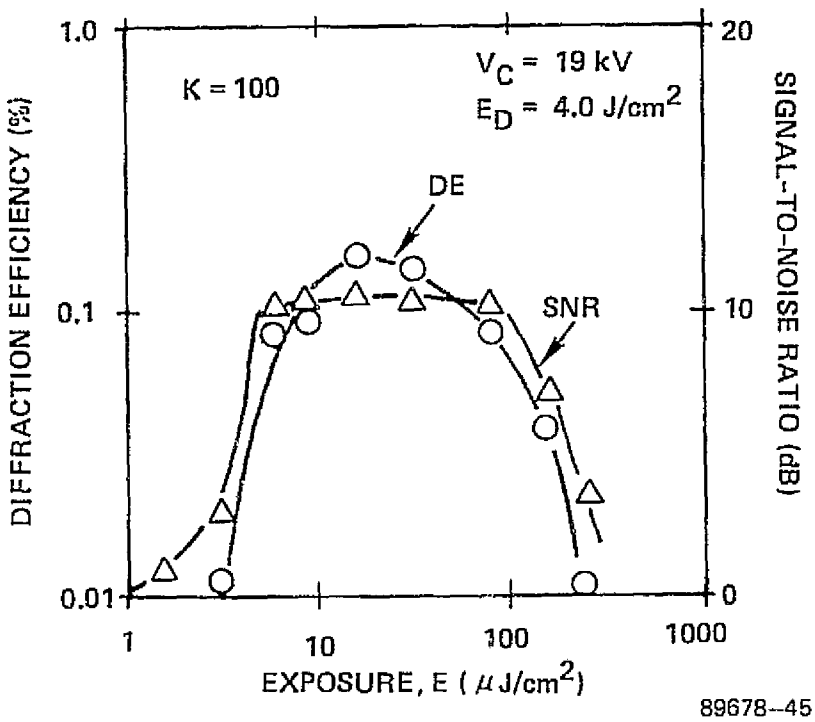

FIGURE 4-20. DIFFRACTION EFFICIENCY AND SIGNAL-TO-NOISE RATIO FOR FRESNEL HOLOGRAMS AS A FUNCTION OF EXPOSURE FOR K = 100

Grating holograms were recorded dynamically on the film drive system. Charging, exposure, and development were accomplished with the film moving at speeds consistent with a 1 Mb/s data transfer rate; the film velocity was approximately 4.5 mm per second. Measurements were made to determine the optimum corona voltage V_c and development temperature T_d for dynamic recording. The dependence on charging voltage observed for the dynamic experiments was not as critical as those observed during the static recording. However, increases in charging voltages never produced the decrease in diffraction efficiency observed in the static tests. This condition is indicative of undercharging (see Paragraph 4.2.7). The exposure temperature T_d has the same impact as during the static recording tests. The optimum recording conditions were determined and used for all experiments.

Diffraction efficiency as function of exposure for grating holograms recorded dynamically on the film transport is shown in Figure 4-21. A maximum diffraction efficiency of 0.94 percent was obtained with an exposure of 40 $\mu J/cm^2$. Charging voltage was 19 kV and the development temperature was 57° C.

The cause for the optimum exposure to double from the static exposure case can be explained by the undercharging condition. The recording sensitivity or apparent speed of an electrophotographic material is dependent on the surface voltage. The higher the surface voltage, the lower the exposure needed to obtain a given level of modulation in the electrostatic latent image. Thus, if the PRF were undercharged, an increase in exposure level from the optimum charging case would be necessary to produce the same electrostatic modulation.

4.2.4 Recyclability of Kalle PRF

The write/read/erase property of a photoplastic film is a primary attraction for its use as an optical mass memory recording material. The recycling capability of the Kalle PRF was investigated as a key part of the overall study. The static recording system was used to record, read, erase and rewrite holograms.

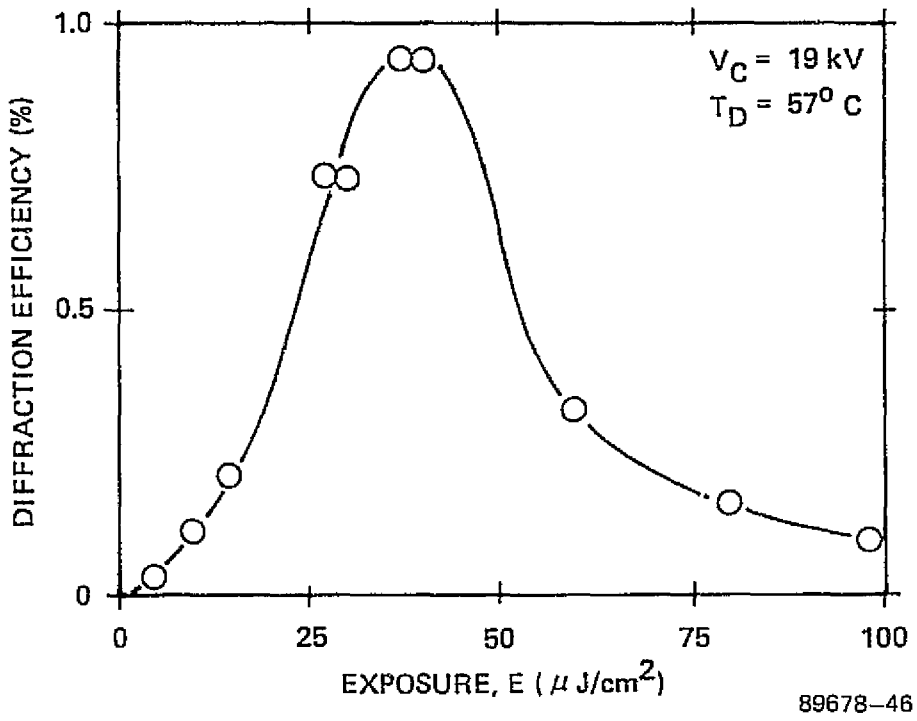

FIGURE 4-21. DIFFRACTION EFFICIENCY AS A FUNCTION OF EXPOSURE FOR HOLOGRAMS RECORDED IN THE DYNAMIC MODE

The simplest technique for hologram erasure is to apply the development current pulse long enough to allow the surface tension forces to smooth the surface of the thermoplastic layer. For Kalle PRF, the necessary erasure pulse was 2.2 times as long as the 130 millisecond development pulse. This recycling technique required erasing the recorded hologram, recharging directly and recording again. However, no second generation holograms could be recorded with this technique. The probable cause for this failure is the residual surface charge from the first recording (recall that there is no internal ground plane).

A technique was developed that did permit the recording of up to 10 holograms in the same area of the photoplastic recording film. The steps of the process were:

1. Record the hologram on a selected crea of the PRF
2. Recharge with a negative voltage
3. Expose the PRF to a uniform beam of laser light
4. Apply an erasure pulse
5. Return to Step 1

This technique produced the highest quality multigeneration holograms.

Ten recording cycles were achieved using this technique on the static system. A Fresnel hologram of a diffuse data target with an opaque center was recorded for several cycles. After each recording cycle, the DE and SNR was measured. The hologram was then erased using the technique described previously, and a subsequent recording carried out. The normalized diffraction efficiency and SNR as a function of recording cycle number is shown in Figure 4-22. A dramatic decrease in normalized diffraction efficiency and SNR is seen for subsequent recordings. The decrease is probably due to volatilization of the thermoplastic plasticizer when heated during

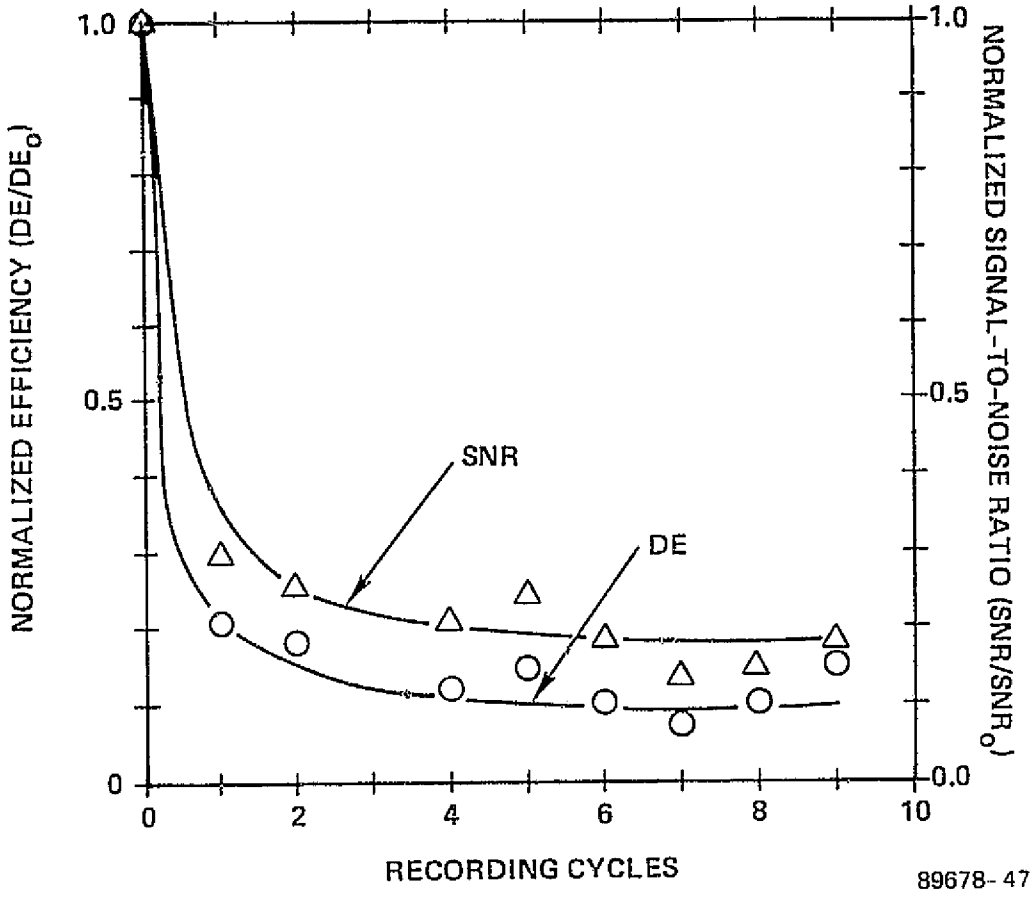

FIGURE 4-22. NORMALIZED DIFFRACTION EFFICIENCY AND SIGNAL-TO-NOISE RATIO AS A FUNCTION OF RECORDING CYCLE NUMBER

development and erasure. The loss of plasticizer increases the surface tension in the thermoplastic layer at a given development temperature; that is, the glass transition temperature increases, thereby altering the flow characteristics of the thermoplastic layer during subsequent recordings.

Fresnel holograms of a standard 1951 Air Force Resolution Target were also recorded on the Kalle PRF. Photographs of the reconstructions obtained for the first and second recordings are shown in Figure 4-23(a) and 4-23(b), respectively. Resolution and image quality are seen to be dramatically decreased in the second recording.

Figure 4-24 illustrates the degradation of the second write cycle when a two-dimensional data mask is recorded as a phase-randomized Fourier transform hologram. Intermodulation and scatter noise are seen to increase significantly from the levels of the first write cycle.

Hologram erasure was also accomplished by using only laser light. A grating hologram recorded in the static system was exposed for 200 ms to the 514.5 nm light from an argon-ion laser. The 300 mW direct laser beam fully erased the exposed portion of the hologram. There was no detectable latent image.

4.2.5 Adjacency Effects for Microholograms Recorded on Kalle PRF

Microholograms were recorded on the Kalle PRF to determine the existence of adjacency effects. The holograms were recorded using the HOLOMEM breadboard (as described in Section III) and the static photoplastic recording system. The HOLOMEM system was used to record phase-randomized one-dimensional Fourier transform microholograms on the Kalle PRF. The microholograms, approximately 1 mm long and 8 μm wide, were recorded on 15 μm centers. The interferometrically recorded holograms had a center spatial frequency of approximately 400 cycles/mm.

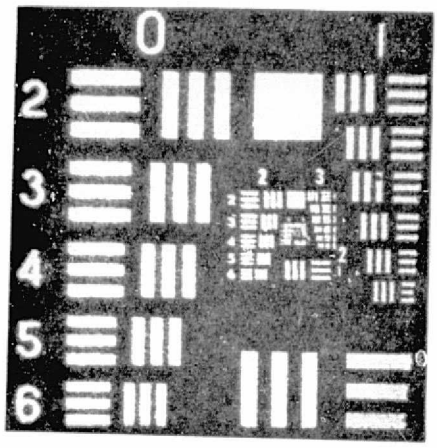

a. FIRST RECORDING

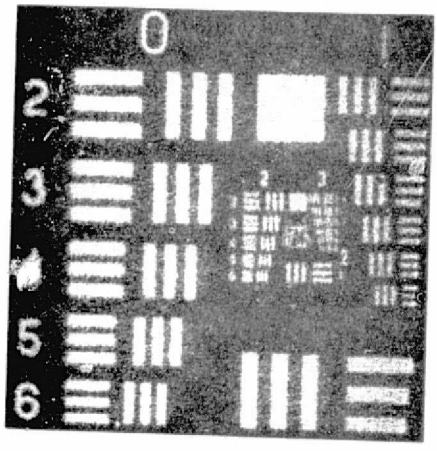

b. SECOND RECORDING

89678–60

FIGURE 4-23. RECONSTRUCTIONS FROM FIRST AND SECOND RECORDINGS OF A FRESNEL HOLOGRAM OF A 1951 USAF RESOLUTION TARGET

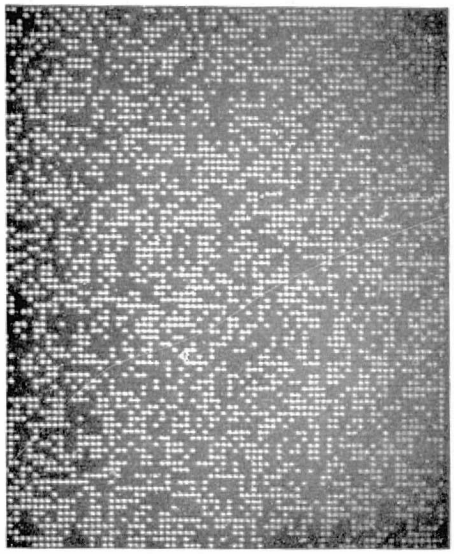

a. FIRST RECORDING

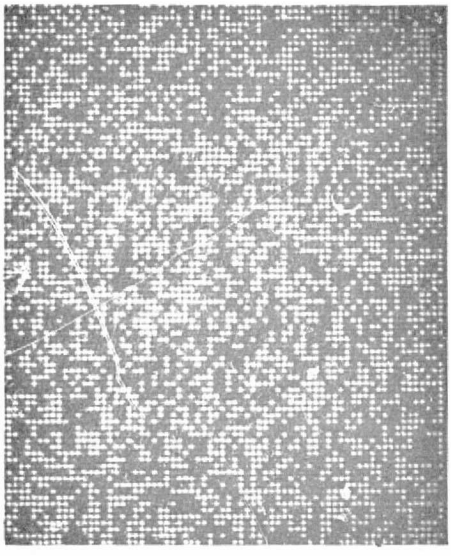

b. SECOND RECORDING 89678–61

FIGURE 4-24. RECONSTRUCTIONS FROM FIRST AND SECOND RECORDINGS OF A PHASE-RANDOMIZED FOURIER TRANSFORM HOLOGRAM OF A DIFFUSE DATA MASK

The static photoplastic recording system was positioned in the Fourier transform plane of the HOLOMEM breadboard. The film was charged using a corona voltage V_c of 18 kV. The charged PRF was then exposed to a single scan line containing approximately 400 microholograms. Each microhologram was exposed with a K ratio of 10 to an average level of 20 $\mu J/cm^2$. The exposed PRF was then developed with a heat pulse of 4 J/cm^2.

The recorded blocks of digital data were read out in the HOLOMEM breadboard. The maximum diffraction efficiency achieved was 0.6 percent with a corresponding SNR of 5 dB. Photographs of the throughput data bits and the reconstructed data bits are shown in Figure 4-25. Bit decision levels could probably be successfully made from the reconstructed data bits. The relatively low diffraction efficiency is due to the falloff in spatial frequency response of the Kalle RFP at 400 cycles/mm.

Extinction between adjacent PRF microholograms recorded along the scan was good. An interference microphotograph of the microholograms is shown in Figure 4-26. The 400 cycle/mm interference fringes are clearly resolved and there is no evidence of any coupling between adjacent holograms.

4.2.6 Environmental Properties of Kalle PRF

The environmental factors affecting the storage performance of the Kalle photoplastic recording film were carefully investigated. Properties examined included shelf-life degradation and archivability. Sample age for the shelf-life test ranged from 2 years stored at ambient conditions to recently received film samples. Samples for the archival storage tests were newly recorded holograms.

The shelf-life tests were accomplished by recording holograms on the differently-aged PRF samples. Comparison of the diffraction efficiency and SNR of the holograms showed no noticeable degradation. Shelf-life for the Kalle PRF material is considered, therefore, to be good. This is generally expected for electrophotographic materials.

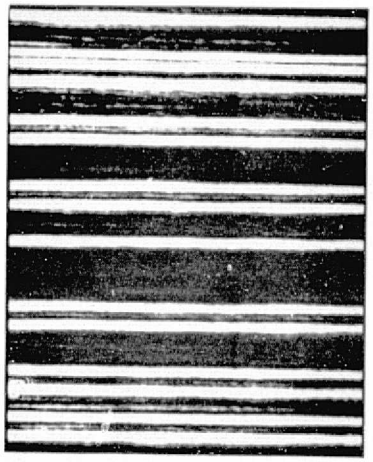

a. THROUGHPUT BIT PATTERN

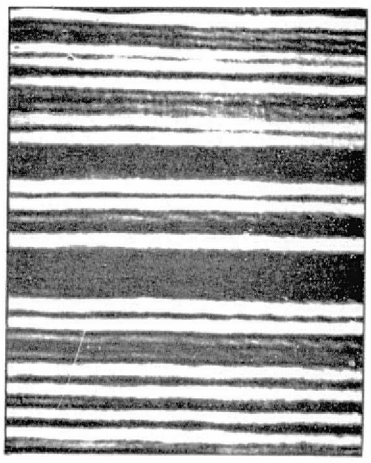

b. RECONSTRUCTED BIT PATTERN

89678–62

FIGURE 4-25. THROUGHPUT AND RECONSTRUCTED DIGITAL DATA BLOCKS

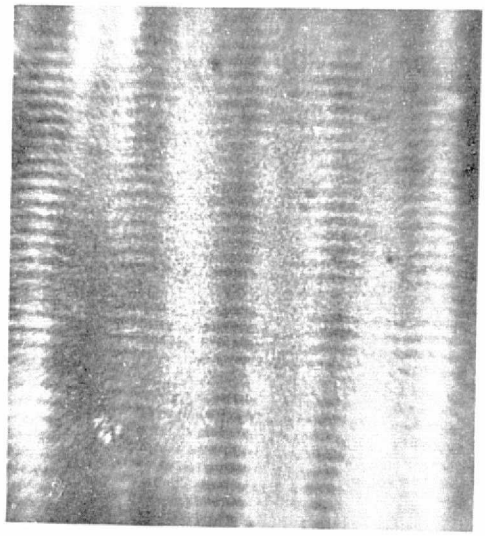

HOLOGRAPHIC FRINGE PATTERN 1000 X ACTUAL SIZE
(KALLE PRF)

89678–63

FIGURE 4-26. INTERFERENCE PHOTOMICROGRAPH OF A SECTION OF A MICROHOLOGRAM

Archival storage properties were investigated by subjecting newly recorded holograms to different environments. The temperature and relative humidity were controlled in an environmental chamber. A typical degradation of normalized diffraction efficiency for holograms recorded on PRF and subjected to ambient conditions of storage is shown in Figure 4-27. (Normalized diffraction efficiency is defined as the diffraction efficiency at a particular time divided by the initial diffraction efficiency.) For storage conditions with a room temperature (RT) of 24° C and a relative humdity (RH) of 37 percent, the efficiency decreases by 50 percent after 50 minutes.

The normalized diffraction efficiency as a function of time for other storage conditions is shown in Figures 4-28 and 4-29. For a hologram stored in an environment at 30° C and 20 percent relative humidity, the 50 percent (3 dB) falloff in diffraction efficiency occurs after 75 minutes. For storage at 40° C and 30 percent relative humidity, the same degradation occurs in less than 3 minutes.

The effect of relative humidity on normalized diffraction efficiency is illustrated in Figure 4-30. Here, the normalized diffraction efficiency as a function of temperature is shown for relative humidities of 10 percent and 50 percent. The data were collected by allowing the environmental chamber to stabilize at the chosen temperature and relative humidity. The hologram was then conditioned in this environment. The diffraction efficiency of the hologram was measured after 5 minutes. The high relative humidity caused degradation of diffraction efficiency to occur at lower temperatures, as is shown in Figure 4-30.

The archival storage properties of the Kalle PRF are clearly quite poor in an uncontrolled environment. The cause for the poor environmental integrity of the Kalle PRF is probably the low glass transition temperature of the thermoplastic layer. Since the glass transition region is broad, cold flow of the thermal plastic layer can occur at relatively low temperatures. This cold flow reduces the depth of the surface deformations in the thermal plastic, thus decreasing the diffraction efficiency. We add that in several instances holograms stored in an office environment were observed to fade over a 24-hour period. The mechanism responsible for this behavior is not understood.

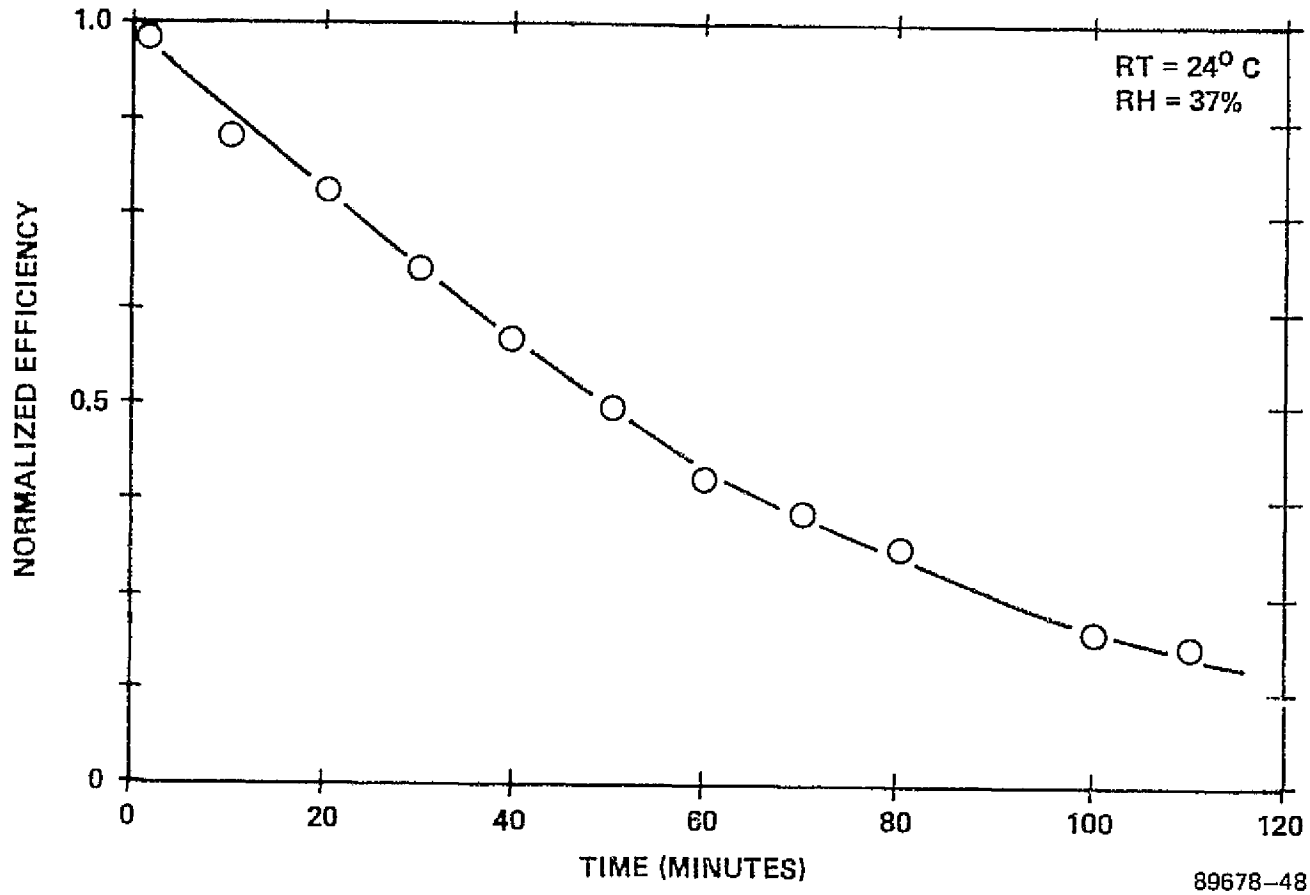

FIGURE 4-27. NORMALIZED DIFFRACTION EFFICIENCY AS A FUNCTION OF TIME FOR RT = 24° C AND RH = 37%

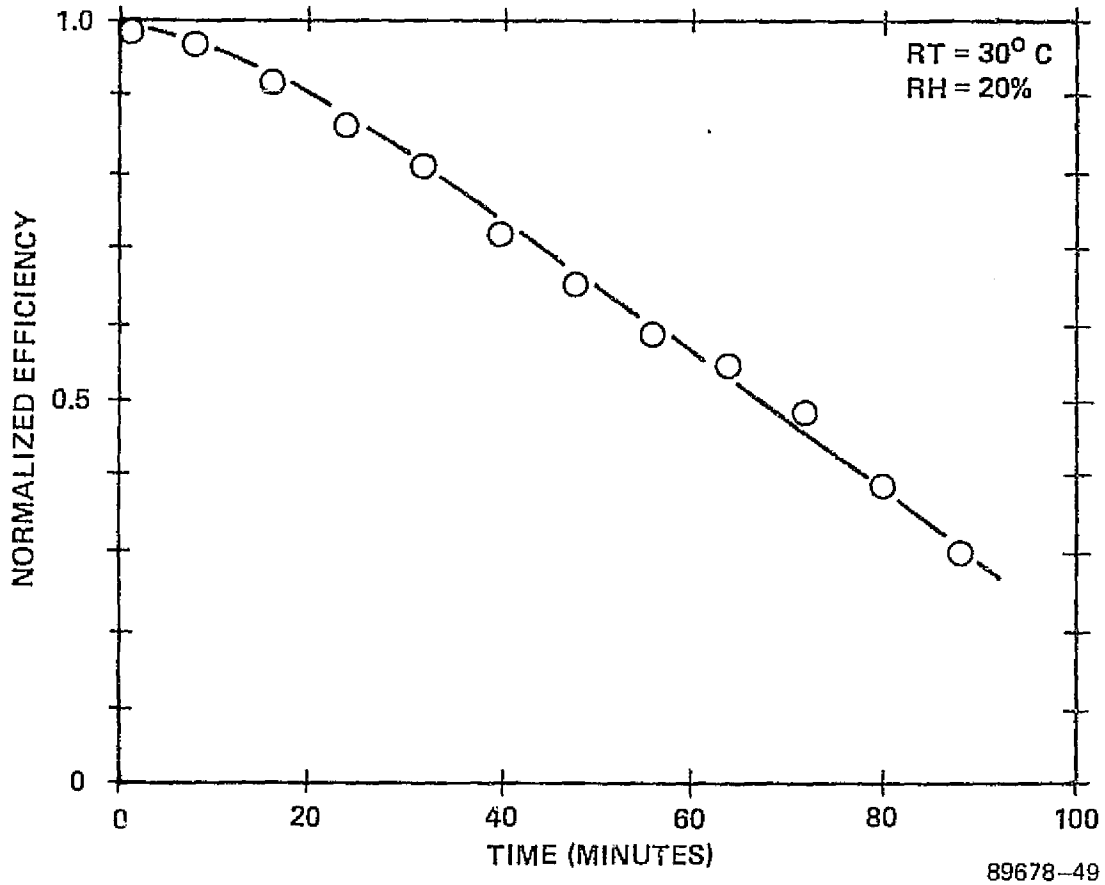

FIGURE 4-28. NORMALIZED DIFFRACTION EFFICIENCY AS A FUNCTION OF TIME FOR RT = 30° C AND RH = 20%

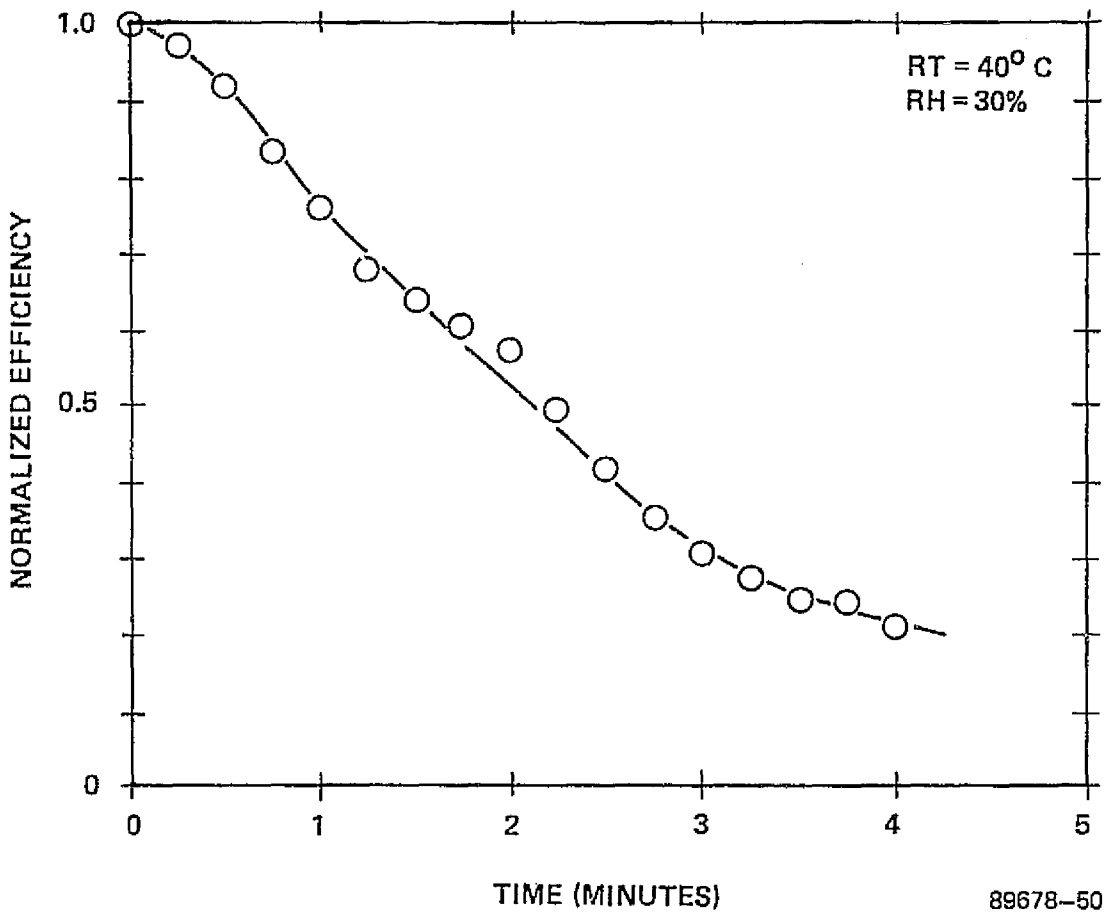

FIGURE 4-29. NORMALIZED DIFFRACTION EFFICIENCY AS A FUNCTION OF TIME FOR RT = 40° C AND RH = 30%

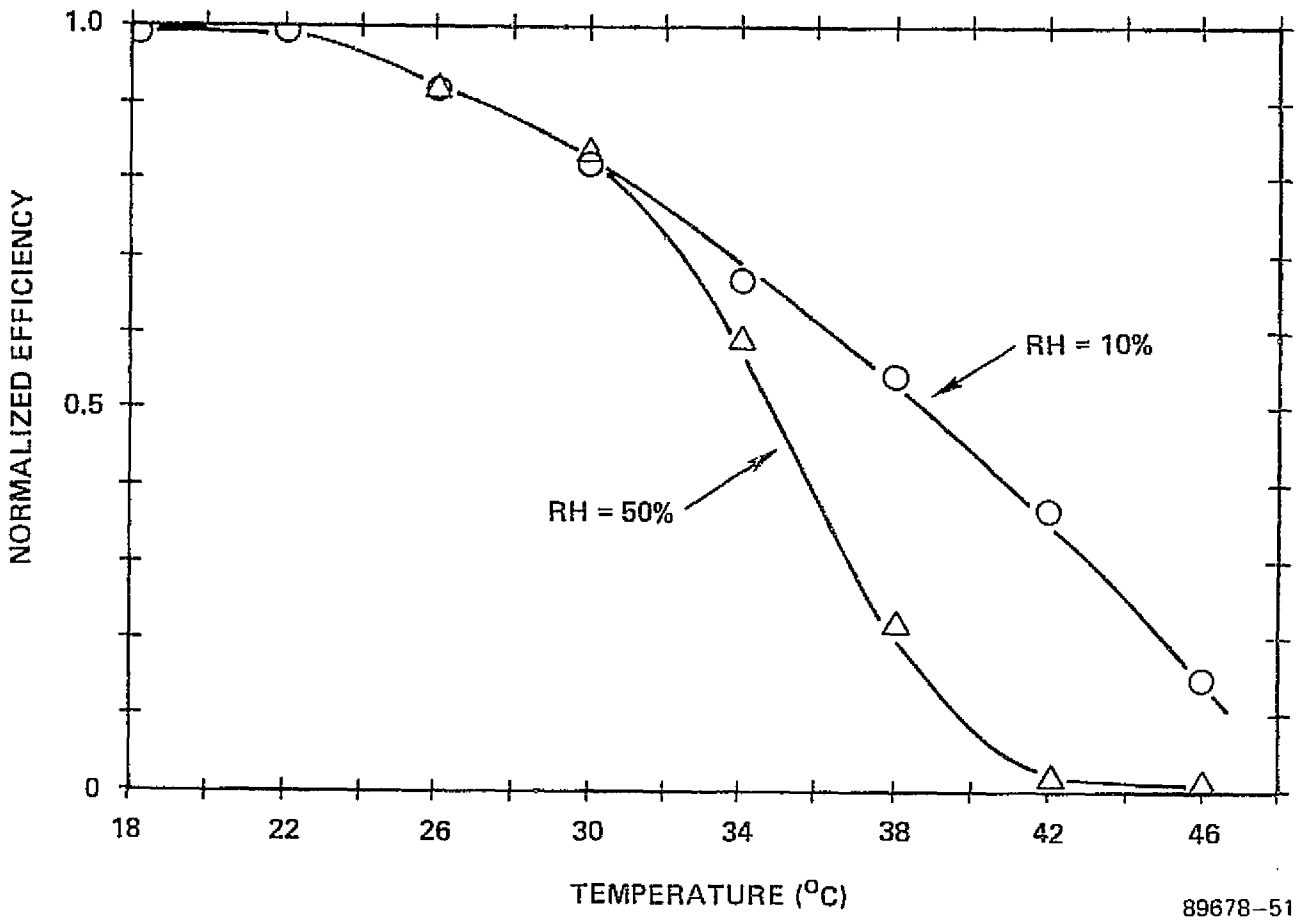

FIGURE 4-30. NORMALIZED DIFFRACTION EFFICIENCY AS A FUNCTION OF TEMPERATURE WITH RELATIVE HUMIDITY AS A PARAMETER

4.2.7 Causes for Inconsistent Holographic Performance

The holographic performance of the Kalle photoplastic recording film was observed to be quite inconsistent. As noted in Paragraph 4.2.3, the diffraction efficiency for a given set of experimental conditions could vary about some typical value by a factor as large as 2. Variations in any of the three steps necessary to form a photoplastic hologram could be responsible for the inconsistencies we observed. In this paragraph, the charging, exposure and development processes are examined to explain the observed inconsistent performance.

The charging process is considered the most probable cause of performance inconsistencies. In this step, the photoplastic recording film is subjected to a high voltage corona discharge which charges the surface of the film to a saturation level. Here, saturation level is defined as the surface voltage of the PRF at which further charges emanating from the corona are repelled. At saturation, the kinetic energy of the charged particles is equal to the potential energy at the PRF surface.

A calculation based on a simple model representing the Kalle PRF layers as capacitors can be used to obtain approximate values for the surface voltage of the PRF. Since the voltage across a planar capacitor is proportional to its thickness/dielectric constant quotient, then

$$V_p/V_{tp} = d_p \epsilon_{tp}/d_{tp} \epsilon_p \qquad (4.1)$$

where V_p is the voltage across the polyester layer, V_{tp} is the voltage across the thermal plastic photoconductor layer, d_p (d_{tp}) is the thickness of the polyester (thermoplastic-photoconductor layer) and ϵ_p (ϵ_{tp}) is the dielectric constant of the polyester (thermoplastic-photoconductor) layer. We note that the surface voltage necessary for optimum hologram recording on photoplastic media of the PVK/TNF type, which have an internal ground plane, is approximately 300 V. Let us assume that the 300 V is also a representative value for the voltage across the Kalle thermoplastic-photoconductor and that the

dielectric constant for the thermoplastic and polyester are the same. Then $\epsilon_{tp} = \epsilon_p$ and the voltage V_{PRF} across the Kalle PRF can be expressed as

$$V_{PRF} = V_p + V_{tp} = V_{tp}\left[1 + d_p/d_{tp}\right] \tag{4.2}$$

For a polyester thickness of 50 μm and a 1.5 thermoplastic-photoconductor thickness, approximately 10 kV must be developed across the Kalle PRF to maintain a 300 V potential drop across the thermoplastic layer. The high charging levels are required because of the additional thickness of polyester base which must be charged. This is a direct consequence of the absence of an internal ground plane.

Variations in total film thickness are seen to cause changes in the voltage V_{tp} across the thermoplastic-photoconductor. The voltage change is related to thickness change of the film layers. For measured film thickness data, the variation in V_{tp} could have a 10 percent spread. The impact of a 10 percent change in V_{tp} on holographic performance is significant, as previous experimental data have shown.

The saturation voltage level for the film could also be affected by changes of other parameters. These parameters include relative humdity changes in the charging chamber, dust concentration and surface quality of the PRF. Of these parameters, the relative humidity is the most critical. These changes are difficult to control unless a special environment is available.

The exposure and development processes are controlled more precisely. The 8 percent total variation in the absorption of the Kalle PRF mentioned in Paragraph 4.2.1 could effectively change the exposure level. However, examination of diffraction efficiency data shows this change to be minimal. Development with either the current pulse in the static system or the heated air in the dynamic system was repeatable to within 0.5 percent; this is an acceptable level.

Two major variants account for the differences in performance between holograms recorded statically and those recorded dynamically. First, the charging and development processes were performed differently in the two recording systems. The charging process with the dynamic system moved the charged film from the ground plane roller, whereas the static system allowed the charged film to remain in contact with the ground plane. Second, development with heated air in the film transport was for a longer time than development with a current pulse in the static system.

Application of Gauss' Law shows that removal of the charged film from the grounded roller decreases the electric field in the photoplastic by a factor of two. The reduction in field would be roughly equivalent to charging in the static system with half the optimum corona voltage. Diffraction efficiency is decreased because of the lower charging level.

The dynamic recording system developed the charged and exposed PRF for a longer time than the static system: approximately a 1 s development time for the tape system, compared to a 30 ms development time for the static system. The rate at which the deformation of the thermoplastic layer proceeds and the length of development have an effect on the resulting diffraction efficiency of the hologram. For a given rate of deformation, there is an optimum development time. Appendix 4B contains a thorough analysis of this effect. Previous experimental work with other photoplastic recording films indicate that shorter development times yield higher diffraction efficiency holograms.

4.2.8 Summary and Conclusions

The performance of the Kalle photoplastic recording film is acceptable for certain rapid-access, nonarchival data storage applications. The most obvious application would be as a single use recording material for holographic nondestructive testing (HNDT). The Kalle PRF was designed and is marketed for this application. The in situ formation of a hologram, combined with high exposure sensitivity, make the Kalle PRF ideally suited

for HNDT. Unfortunately, it is not as well suited for holographic data storage and retrieval. Overall systems specifications for the HOLOMEM storage material are not met by the Kalle PRF. The inconsistent holographic performance, limited recyclability and short archival life of the Kalle PRF minimize the attractiveness of this material as a candidate recording medium for high-density holographic data storage. The high charging levels necessary and the low glass transition temperature of the thermoplastic are the chief problem areas.

The present experimental work has demonstrated several key features of a write/read/erase recording media of significance to the NAS Optical Mass Memory Program. They are:

- A photoplastic recording material on a flexible substrate can be used for recording holograms dynamically in a tape transport system.
- A photoplastic recording material can be used in record one-dimensional microholograms with no detectable adjacency effects.
- Localized erasure of holograms on photoplastic film can be accomplished by exposure to pulsed laser light.

Photoplastic recording materials have great potential value for high-density data storage applications. Although the Kalle PRF did not satisfy systems and operational requirements, other photoplastic recording films are being developed which could (see Appendix 4C). Further investigation of other photoplastic recording films, however, should be limited to those that possess two features not present in the Kalle PRF. First, the PRF should have a transparent internal ground plane. This will allow lower charging voltages to be used and should eliminate many of the inconsistencies observed for the noninternally grounded Kalle PRF. Second, the photoplastic recording film should have a relatively high glass transition temperature, on the order of 80° C or more. This will improve both recyclability and archival storage properties.

4.3 SCOTT GRAPHICS PHOTOPLASTIC RECORDING FILM

As our study of the Kalle PRF proceeded, it became clear that a transparent internal ground plane was a crucial recording and systems requirement. To obtain the desired PRF, we considered the following alternatives:

1. Acquire a polyester film base coated with a transparent conductor and develop techniques for coating the photoconductor and thermoplastic layers, or
2. Modify an existing electrophotographic film that had achieved production status.

The first alternative was rejected because of high risk. It is not possible, in general, to do extensive solution coating on a flexible substrate without a considerable expenditure of resources and time. Even then, there is no guarantee that the resulting PRF will meet specifications or be reproducible. The second alternative was attractive for several reasons: low risk; security of supply; availability; and a minimum impact on resources and time.

At the time, only Scott Graphics (Holyoke, MA) had available a high-resolution (organic photoconductor) electrophotographic film which appeared suitable for holographic data storage. [Later, about 1976, Coulter Information Systems (Bedford, MA), would also begin the production of a high-speed, high-resolution (inorganic/photoconductor) electrophotographic film.] We recognized that the Scott Graphics film required only the addition of a thermoplastic layer to form a photoplastic recording film. Hence, we acquired various samples of Scott Graphics electrophotographic films coated with a thermoplastic we supplied. A detailed experimental study was performed to characterize this new photoplastic recording film. The results of this investigation were quite positive; they are reported in succeeding paragraphs.

4.3.1 Construction

The Scott Graphics PRF is based on a proprietary electrophotographic film, which is often referred to as a transparent electrophotographic, or TEP film[6-7]. The construction of a typical TEP film is shown in Figure 4-31(a). It is comprised of a polyester substrate, a transparent conductive layer and a photoconductive layer, which is an organic photoconductor (OPC) in a polymeric matrix and a sensitizing dye. Spectral response is determined by the type of dye in the OPC layer. To convert the TEP film to a photoplastic recording film, a 1 μm thick thermoplastic top layer was added. Figure 4-31(b) shows the resultant PRF construction. In this system, the photoconductor is believed to be a derivative of m-phenol and diamamine, rather than polyvinyl carbozole (PVK). The thermoplastic, in all cases, is similar to Foral 105, a product of Hercules, Inc.

The resistivity of the conductive coating is about 1000 ohms/square. This is sufficiently low to make an excellent grounding plane, but is too large to permit development by resistive heating; therefore, in use, the film was held by vacuum to a NESA® glass substrate having a resistivity of about 75 ohms/square. The indium-tin oxide layer of the NESA® glass was etched with zinc powder and hydrochloric acid to create isolated 10 mm^2 pads. A vacuum groove around each pad ensured good contact with the film base. Two silver electrodes along opposite edges of each pad provided connections to the electrical source which supplied the current pulses used to heat the pads. Development and erasure of holograms were accomplished through resistive heating with short voltage pulses. Heating pulse durations for development were 200 ms.

4.3.2 Mechanism of Hologram Formation

A hologram is recorded in the Scott Graphics photoplastic recording film as surface deformations in the thermoplastic layer. The surface deformations correspond to the spatial variations of the exposure pattern which, in this research, was generally a holographic interference pattern. The recording process, which can be described with the aid of Figure 4-32 consists of three steps:

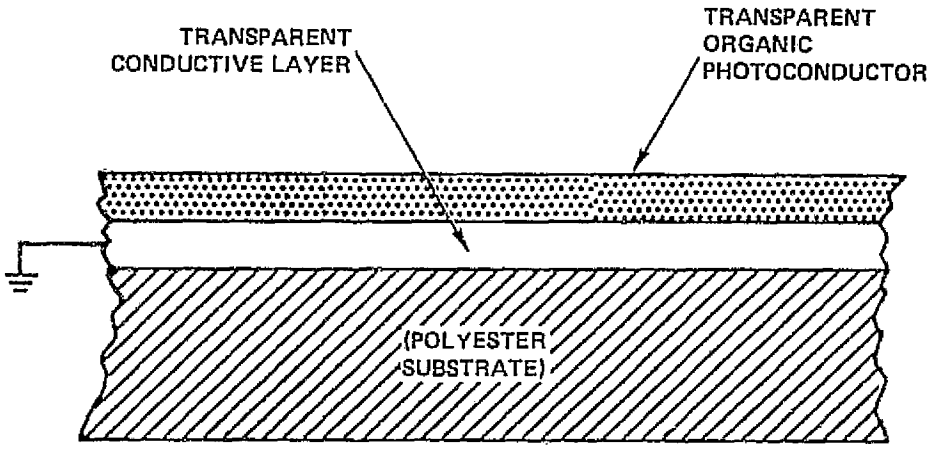

a. CONSTRUCTION OF A TRANSPARENT ELECTROPHOTOGRAPHIC (TEP) FILM

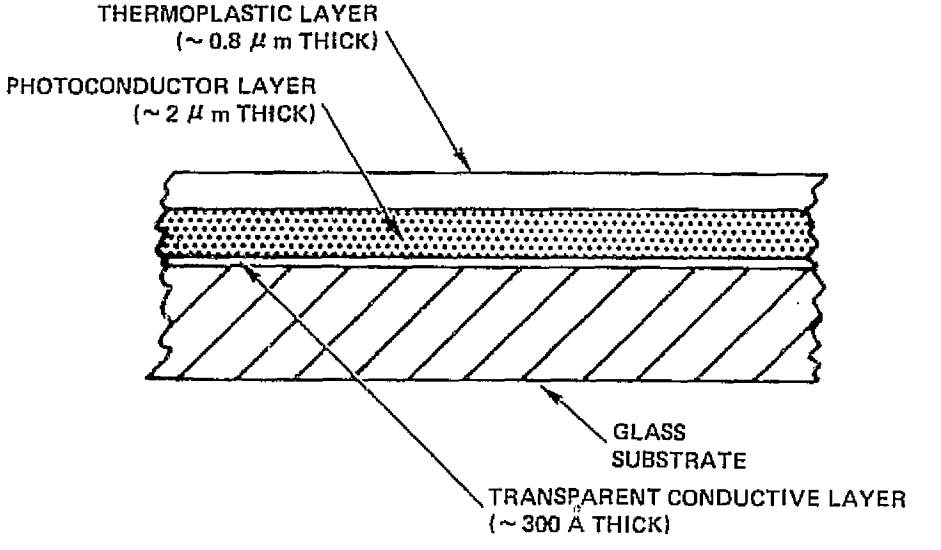

b. CONSTRUCTION OF A PHOTOPLASTIC RECORDING MEDIUM

FIGURE 4-31. CONSTRUCTION OF SCOTT GRAPHICS ELECTROPHOTOGRAPHIC MEDIA

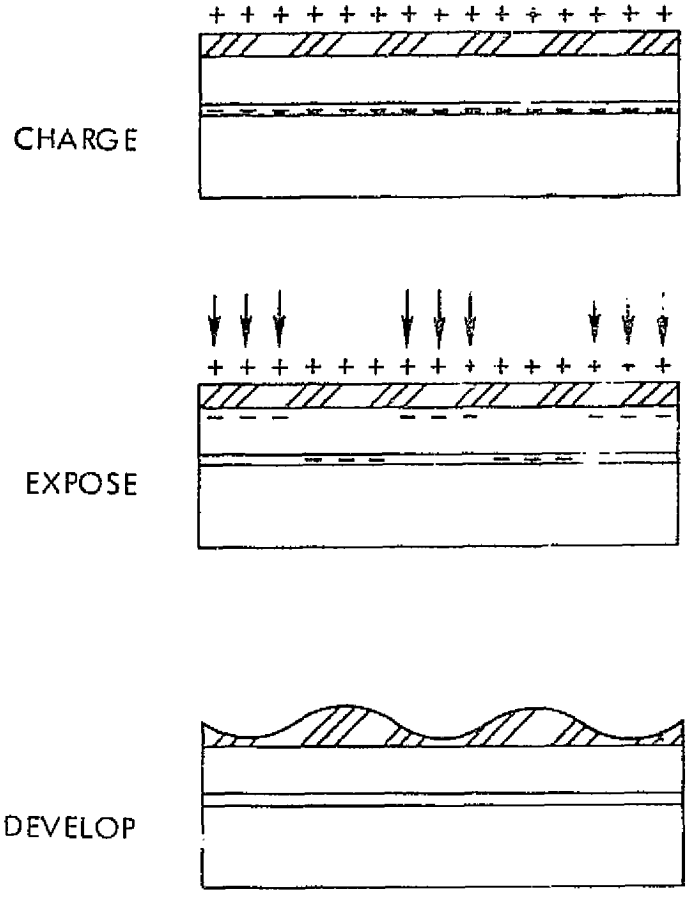

FIGURE 4-32. METHOD FOR RECORDING ON PHOTOPLASTIC RECORDING MEDIA

1. The photoplastic recording film is charged in darkness to a uniform potential by a corona discharge device.

2. The PRF is exposed to light causing a variation of the surface charge density of the photoconductor which corresponds to the variation in the exposing illumination. In the illuminated regions, displacement of charges from the transparent electrode to the photoconductor/thermoplastic interface reduces the electrostatic surface potential at the free surface of the thermoplastic layer.

3. The PRF is developed by raising the temperature of its thermoplastic layer above the glass transition temperature, and then rapidly lowering this temperature to the ambient level. This produces surface deformations related to the original irradiance distribution used to record the hologram.

In the first step, the medium is "sensitized" for recording. The corona discharge device, consisting of a thin wire (approximately 4 mils in diameter) at a voltage of about 10 kV and an electrically grounded shield, deposits a uniform charge distribution on the thermoplastic. After this sensitization step, the recording material must be handled in darkness. After exposure, the photoplastic medium is developed by lowering the viscosity of the thermoplastic layer by heating. The material then deforms in a manner related to the surface charge density distribution. To lower the viscosity of the thermoplastic, the temperature is raised to approximately 80° C. Rapid cooling to room temperature forms spatially varying surface deformations which remain stable until intentional erasure. Erasure requires more energy than development; it is achieved by applying the same voltage used for development, but for a longer period of time.

4.3.3 Charging Devices

The surface charge deposited on the PRF during charging depends on the dielectric properties and dark conductivity of the PRF film and the parameters and the design of the corona unit.[8] In previous experiment work, we determined that charging was the most critical parameter. Therefore, we evaluated several charging devices to determine which one best met our present needs.

4.3.3.1 The Scorotron

A scorotron, shown in Figure 4-33, consists of one or more corona wires and a control grid. The control grid is placed close to the film surface and held at a potential several hundred volts lower than the corona potential.[9] The film surface is charged to a level determined primarily by the control grid. The resulting surface potential is independent of film characteristics and is, therefore, uniform and relatively repeatable.

4.3.3.2 The Corotron

A shielded corotron, shown in Figure 4-34, consists of a single corona wire with a ground shield surrounding about 75 percent of its volume. Corotrons are smaller, simpler and provide more rapid charging than scorotrons. They are also more reliable. The ground shield increases the ion density and, therefore, the charging current.[10] It also prevents overcharging by reducing the amount of excess ions. The efficiency of a corotron depends on the ambient relative humidity; thus, charging repeatability is often a problem. One way to help ensure controllability and repeatability is to use a charge integrating circuit of the type shown in Figure 4-35.

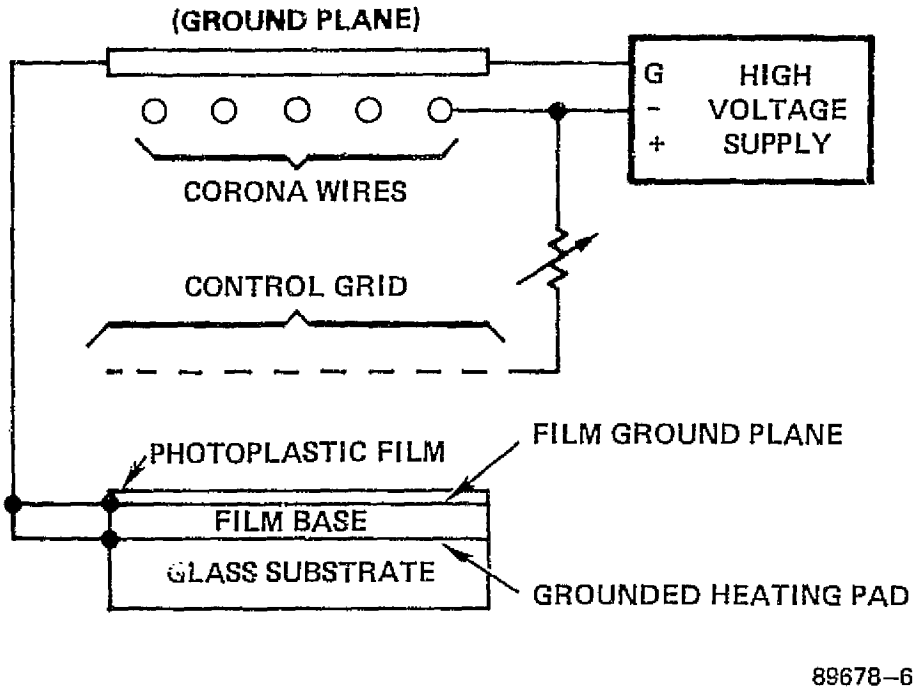

SCOROTRON CHARGING UNIT

FIGURE 4-33. SCHEMATIC DIAGRAM OF SCOROTRON CHARGING UNIT

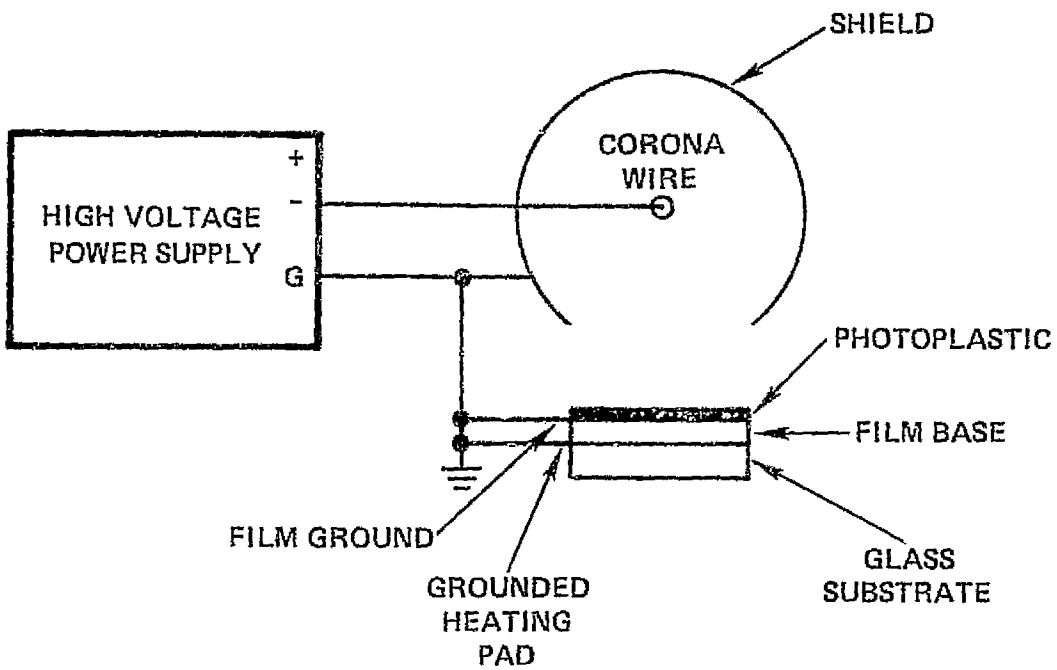

FIGURE 4-34. SCHEMATIC DIAGRAM OF A SHIELDED COROTRON CHARGING UNIT

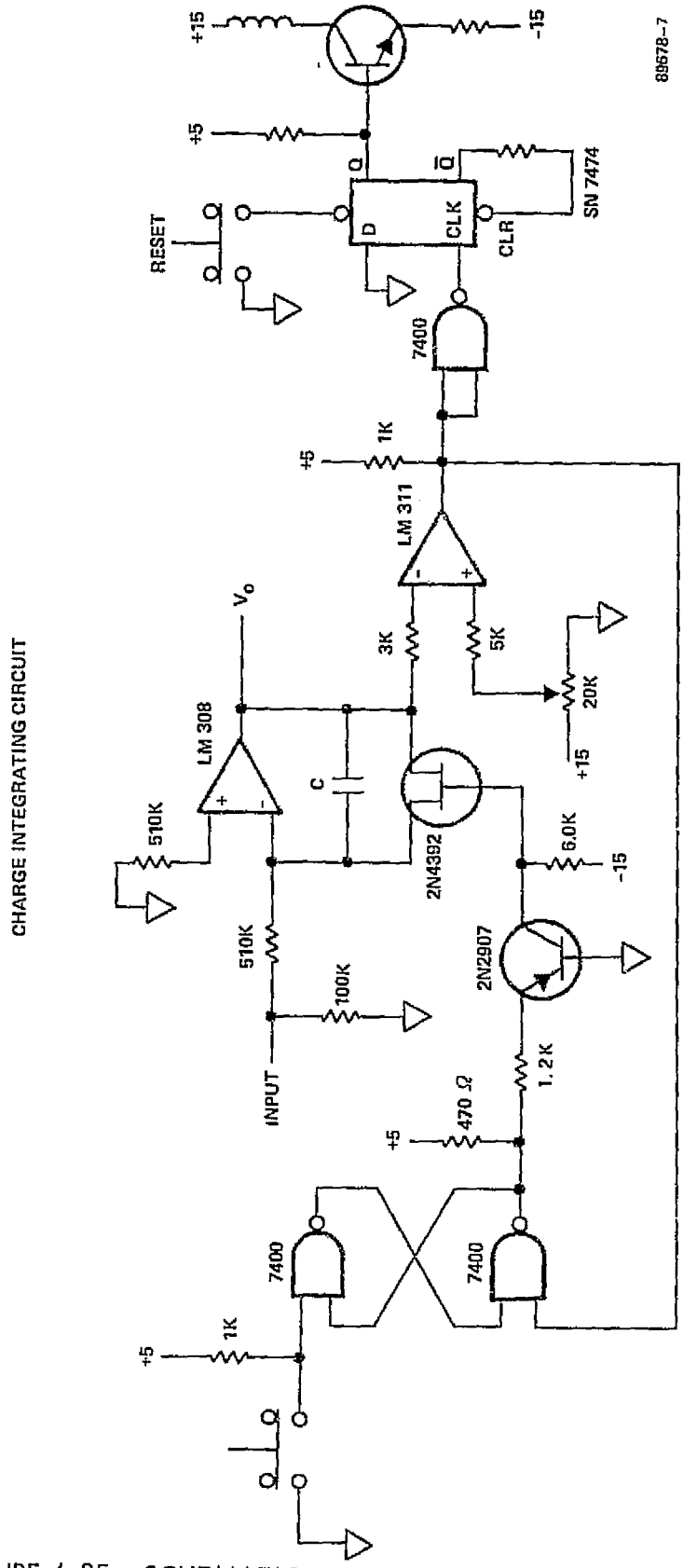

FIGURE 4-35. SCHEMATIC OF CHARGE INTEGRATING CIRCUIT

4.3.4 Charging Characteristics Investigation

Electrophotographic materials can be characterized by their electrical parameters as well as by their holographic response. The electrical sensitometry, which characterizes the electrostatic latent image, is independent of processing materials or techniques. It is equally relevant to the experimental characterization of both photoplastic and electrophotographic recording films.

4.3.4.1 Experimental Apparatus Procedure

A corotron unit with a single corona wire, positioned about 1 inch from the film surface, was used for all experiments. The rest position of the corona wand was below the path of the laser beam to allow convenient exposure. In use, the wand is moved to the center of the selected recording pad area and activated to charge the film surface. After charging is completed, the corona wand is returned to its rest position.

A schematic diagram of the experimental setup is shown in Figure 4-36. The corona charging unit and the probe of a Monroe electrostatic voltmeter are placed side-by-side. The film holder, on NESA® glass substrate with a 1 cm^2 heating pad, was mounted on a rail so that the film could be rapidly moved between the charging station and the readout station. As previously noted, the corona wand was positioned 1 inch from the film. The voltmeter probe was positioned 1/4 inch from the film. An unexpanded laser beam was incident on the readout station through the substrate support of the PRF. In this way, the charge decay that results from exposure could be monitored in real time. The beam intensity was controlled by an adjustable attenuator, whereas the exposure time was controlled by an electromechanical shutter. The output of the Monroe electrostatic voltmeter was coupled to an X-Y chart recorder. This allowed the change in surface voltage as a function of time to be plotted directly. Using this system, the surface potential of the film was monitored over the entire recording cycle.

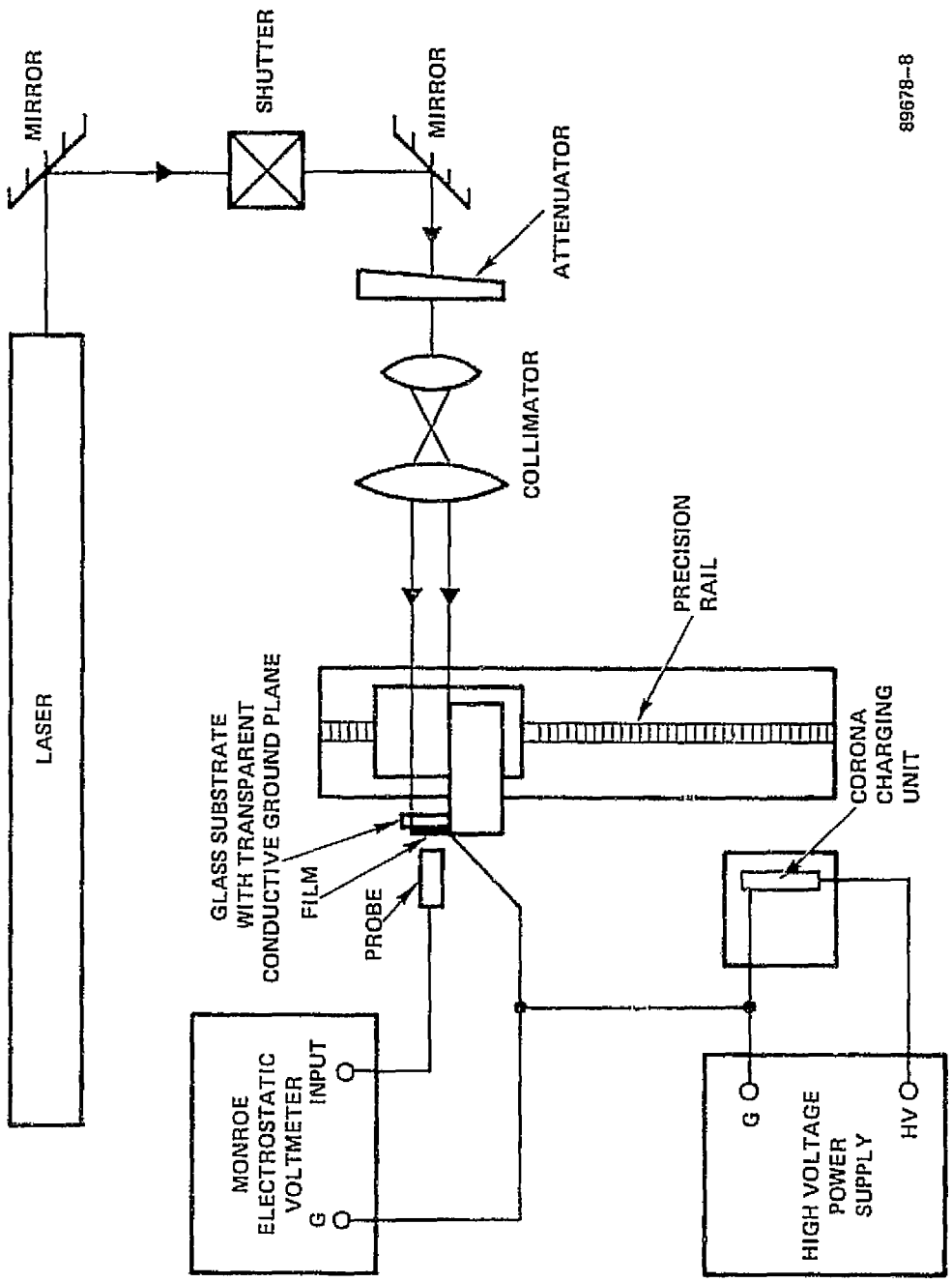

FIGURE 4-36. EXPERIMENTAL SETUP USED FOR CHARGING PHENOMENA MEASUREMENTS

Our procedure was first to charge the film in the dark. The charged film was then rapidly moved to the readout station. The time delay between the charging and readout operations was approximately 15 seconds. Each experiment was initiated with at least 5 seconds of dark decay before beginning either exposure or heating.

4.3.4.2 Results

In previous work with PVK/TNF type photoplastic recording films, we found that about 300 V of surface potential was needed to optimize holographic performance for a 2 μm thick device (both photoconductor and thermoplastic layers). The Scott Graphics TEP film photoconductor layer is 9 μm thick, which makes the entire device 10 μm thick. The electrostatic force is proportional to V/d, where V is the surface potential and d is the thickness of the photoconductor and thermoplastic layers. As d has increased by a factor of 5, the surface voltage V must also be increased by a corresponding amount to obtain optimized holographic performance.

The charging characteristics of the corotron were investigated first. The behavior of the TEP photoconductor without thermoplastic was studied; corona voltages of 10 kV and 7.5 kV, were used. The surface potential was measured as a function of charging time for each of the corona voltages. Figure 4-37 shows the results of these experiments. The optimum potential is reached in 1 second for a corona voltage of 10 kV and in about 4 seconds for a corona voltage of 7.5 kV. For subsequent tests, a corona voltage of 10 kV for a 1 second period was used for charging.

The uniformity of charge deposition using a single-wire corona unit was determined by charging a 1 cm^2 recording area with the corona wire positioned approximately 1 inch from the film surface. The resulting surface voltage profile was measured with the electrostatic voltmeter. Figure 4-38 shows a typical voltage profile; the surface potential falls off by about 6 percent at the edge of the recording area. This level of variation is not considered significant.

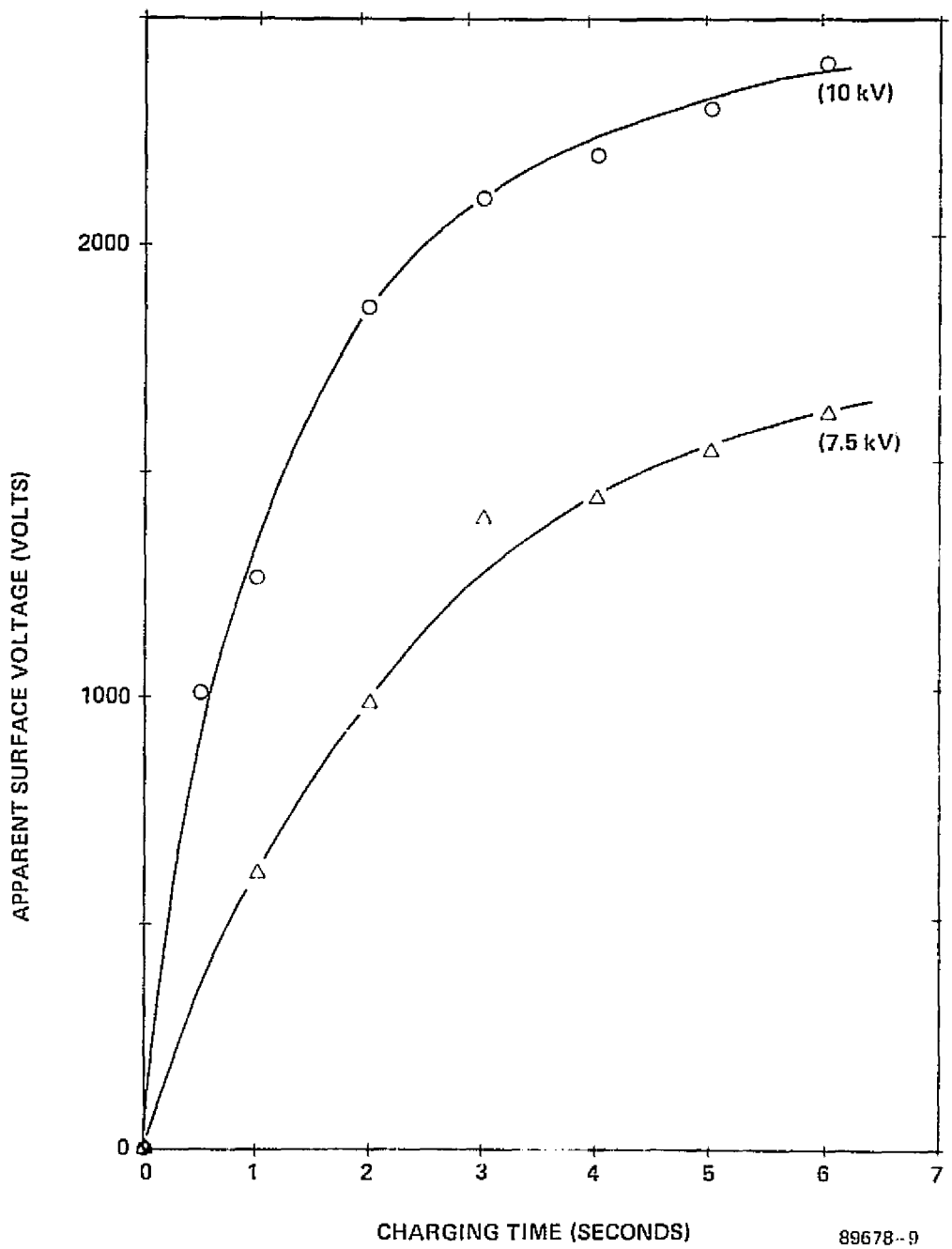

FIGURE 4-37. SURFACE POTENTIAL AS A FUNCTION OF CHARGING TIME WITH CORONA VOLTAGE AS A PARAMETER

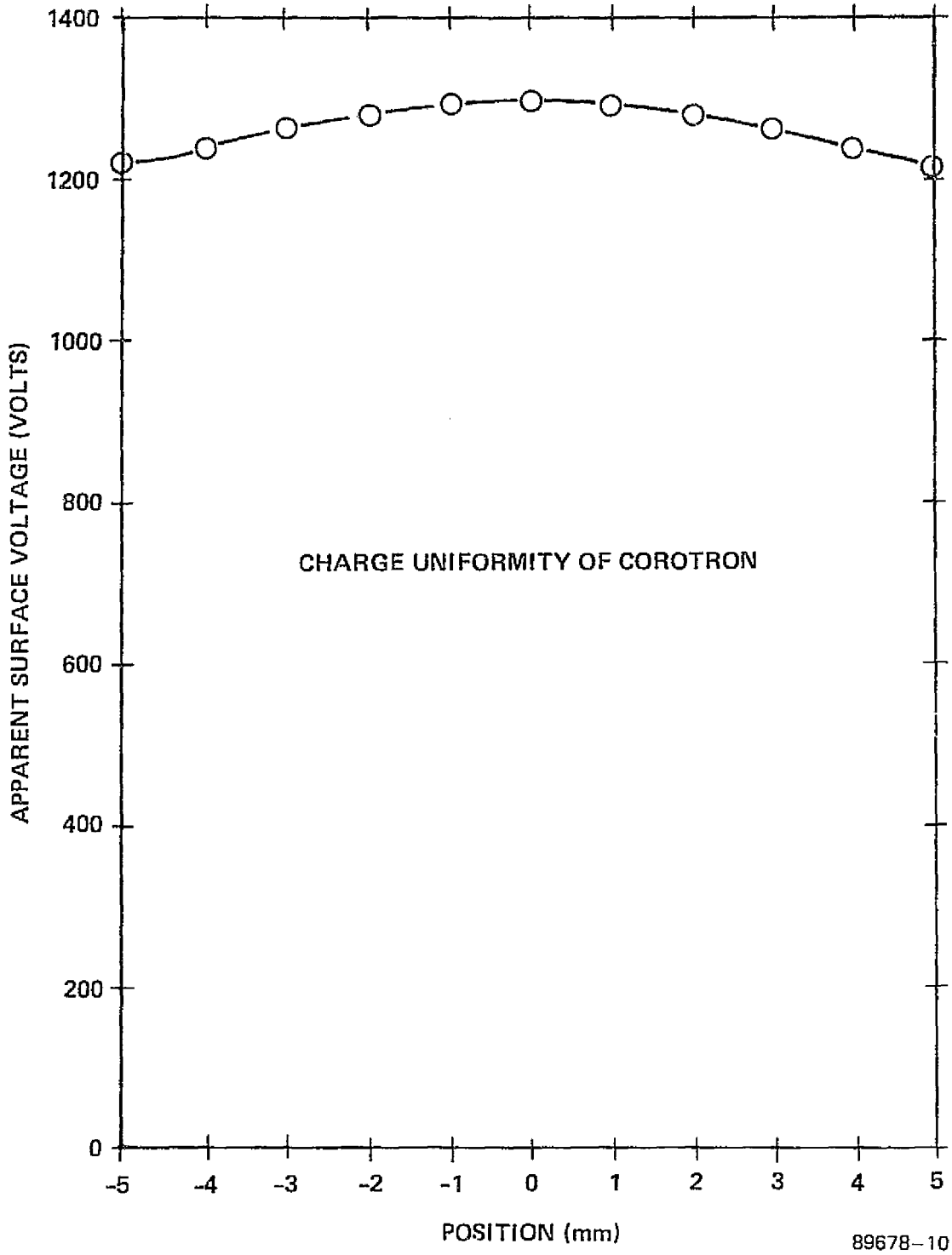

FIGURE 4-38. UNIFORMITY OF COROTRON CHARGING

We also considered the effect of various kinds of background illumination. All light sources, including the laser, were turned off. First, the film was charged and moved to the readout station. The dark decay of the surface voltage was then measured. Second, the laser was turned on and the effect of background plasma glow was measured. Third, blue safe lights (recommended by Scott Graphics) were turned on and their effect measured. Finally, the effect of the laser beam with a power density of 570 $\mu W/cm^2$ was measured. Figures 4-39 and 4-40 show the results for the Scott Graphics photoconductors tested. They are designated as TEP P5-003, having a peak spectral sensitivity at 590 nanometers, and TEP P4-005, having a peak spectral sensitivity at 633 nanometers. The plasma glow of the laser did not affect either photoconductor, whereas the blue safe lights contributed to charge decay with both samples. The decay caused by the laser beam is about 15 times faster than that of the blue safe lights. However, for repeatable results, the safe lights were always turned off during and after charging.

As Scott Graphics photoconductors continue to be conductive for some time after an exposure is completed, it was recommended that they not be exposed to ambient illumination for 24 hours prior to use. We examined the effects of pre-exposure by various light sources. We checked to determine whether exposure to the blue safe lights would also generate persistent conductivity. The results of this experiment are shown in Figure 4-41. Sample No. 1 was not pre-exposed to the safe lights, whereas Sample No. 2 was pre-exposed for 1 minute. Sample No. 3 was pre-exposed to white flourescent lights for 1 minute and Sample No. 4 was pre-exposed to 200 $\mu J/cm^2$ of helium-neon laser light. The blue safe lights do not appear to pre-expose the film, as is shown by the dark decay rate which is the same as that of the unexposed sample. Both white flourescent lights and laser light do pre-expose the film and cause persistent conductivity.

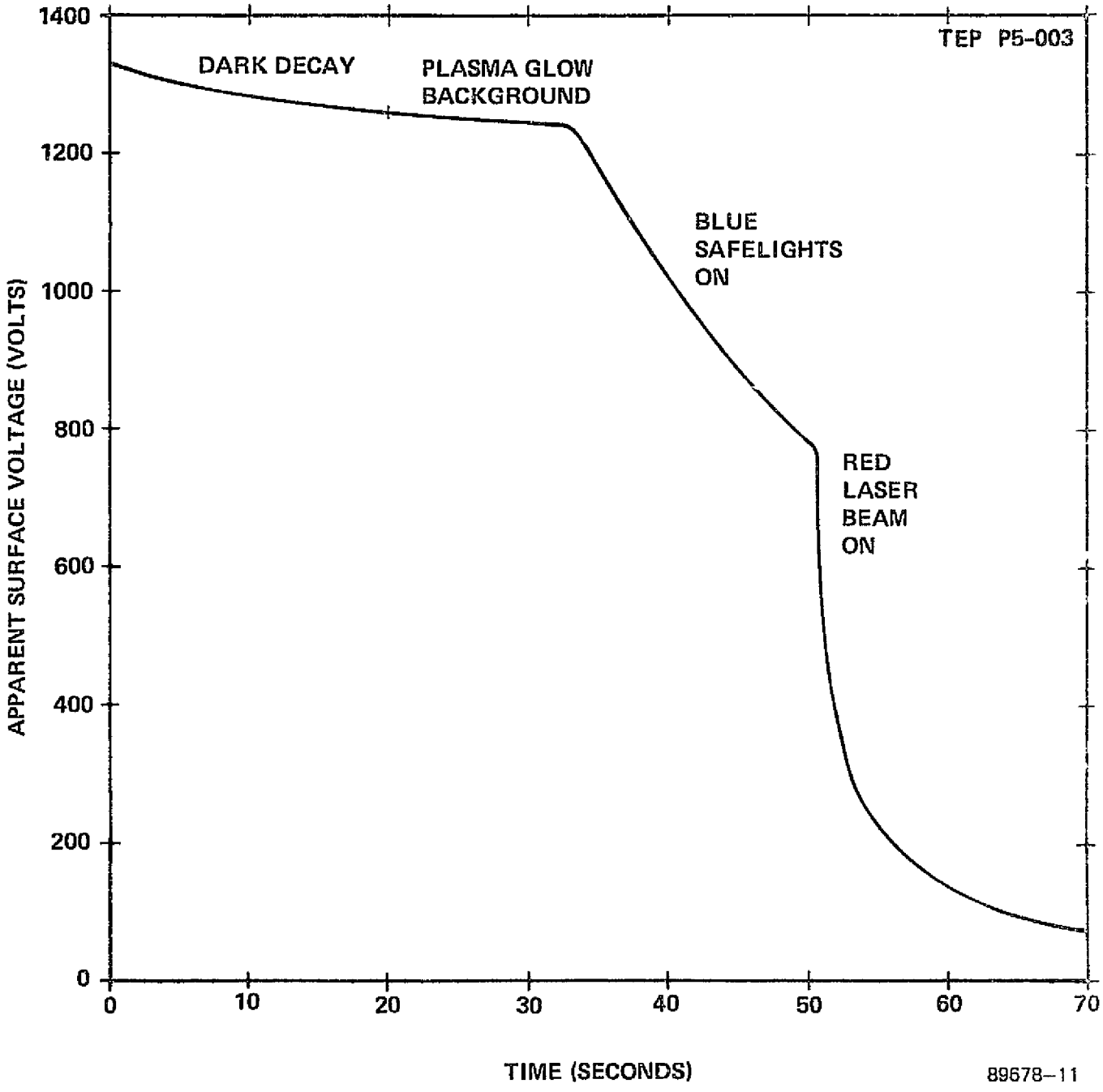

FIGURE 4-39. EFFECTS OF BACKGROUND ILLUMINATION ON TEP P5-003

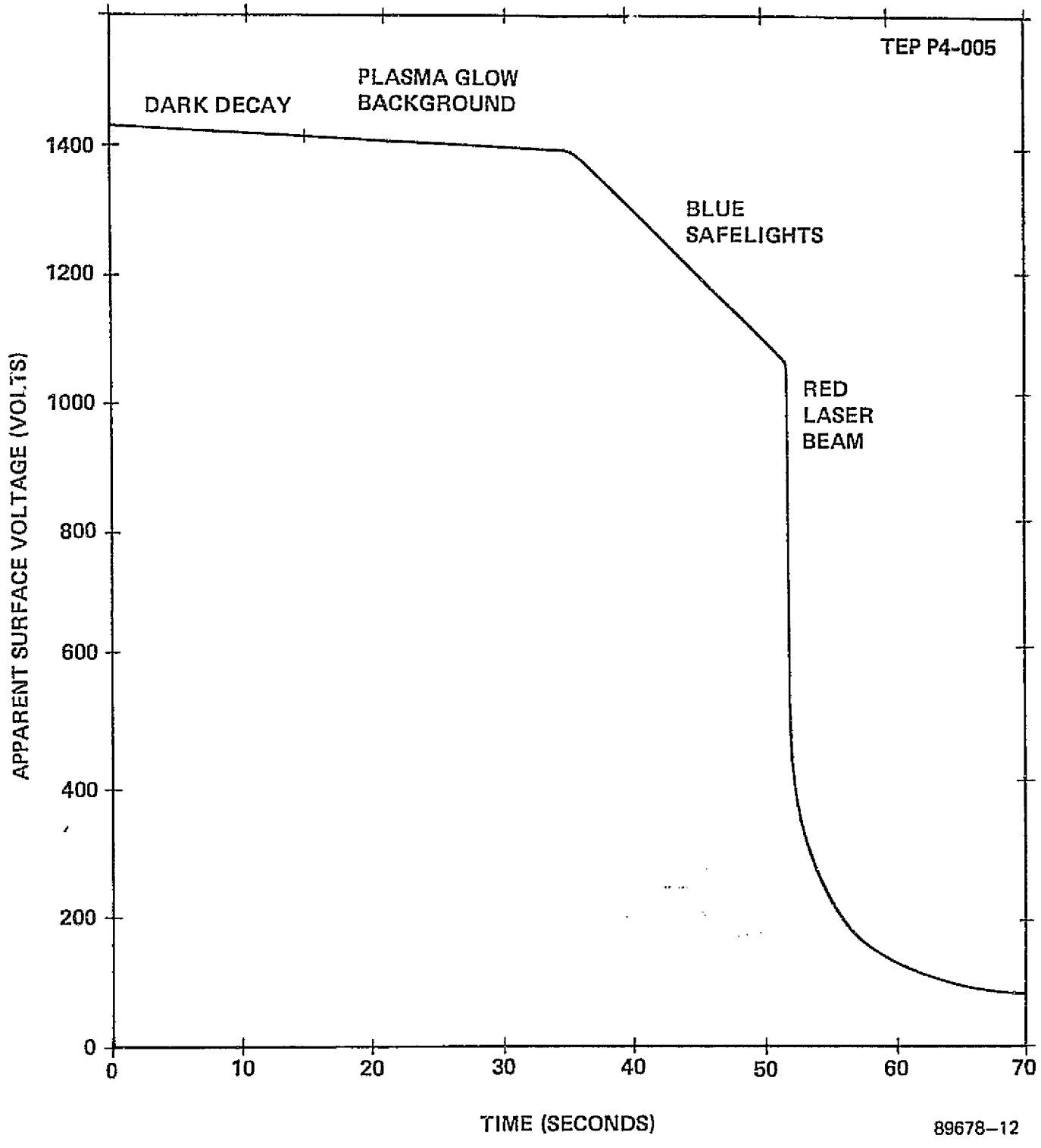

FIGURE 4-40. EFFECTS OF BACKGROUND ILLUMINATION ON TEP P4-005

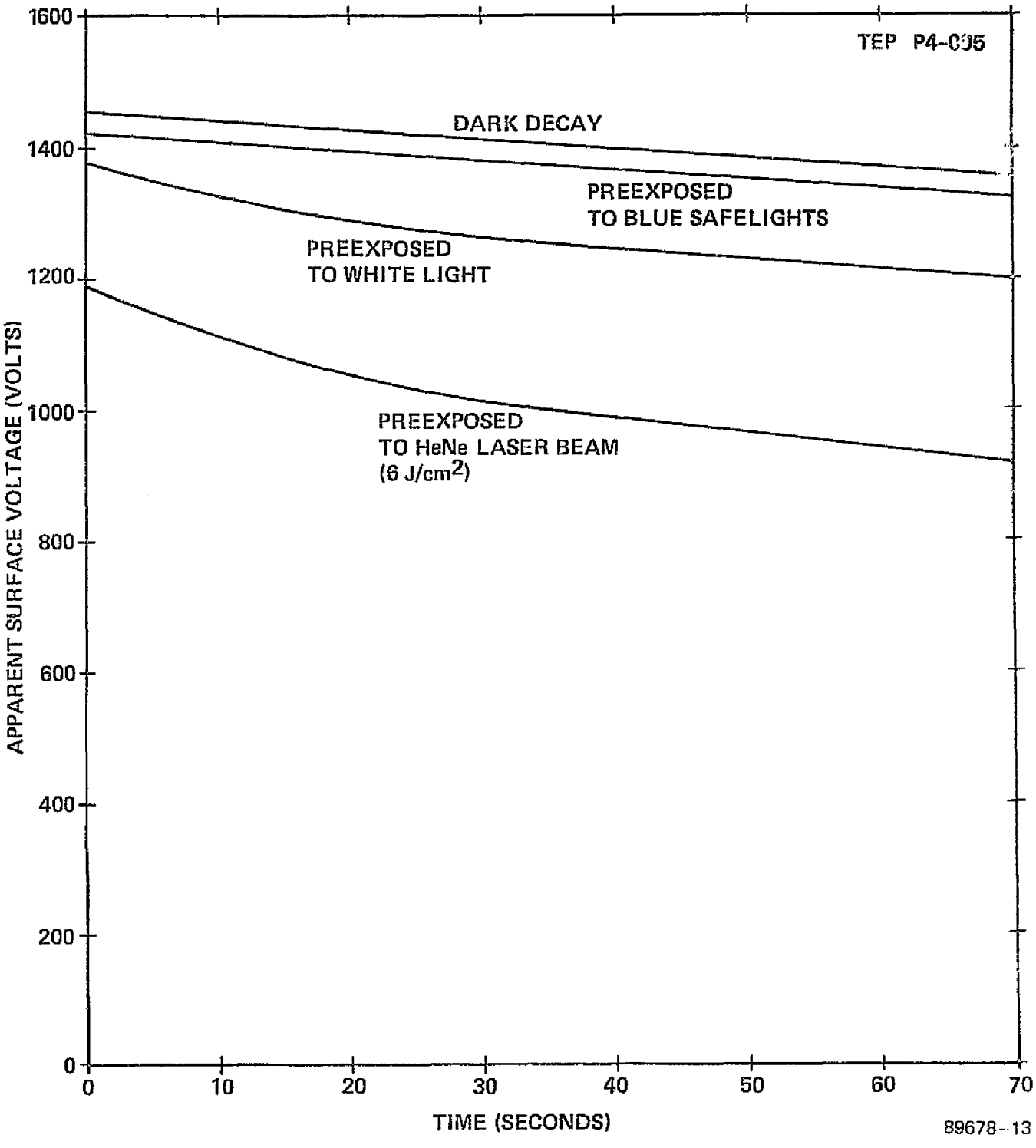

FIGURE 4-41. DARK DECAY OF TEP P4-005 PHOTOCONDUCTOR AFTER PREEXPOSURE

The change in surface voltage as a function of exposure was also measured. In Figure 4-42, the change in apparent surface voltage (ASV) as a function of exposure is plotted for TEP P5-003 with the initial surface voltage as a parameter. In Figure 4-43, similar data are plotted for the TEP P4-005 photoconductor. Clearly, the initial surface voltage has a significant influence. In general, for equivalent exposures, samples charged to a higher initial voltage exhibited a larger voltage decay. For the same exposure and initial surface potential, the voltage decay was larger for the TEP P4-005 photoconductor than for the TEP P5-003 photoconductor. This is expected because the TEP P4-005 photoconductor is more sensitive at 633 nm than the TEP P5-003 photoconductor is.

The effect of the entire write/read/erase cycle was measured for both films. Five recording cycles separated by 1 minute intervals were run. Figure 4-44 shows the first cycle for the TEP P4-005 photoconductor and Figures 4-45(a) and 4-45(b) show the second and fith cycles, respectively. The major change occurring in the second cycle is due to the phenomenon of persistent conductivity. The photoconductor had been exposed to the laser beam during the initial cycle, making the rate of dark decay higher during subsequent cycles. As a result, more of the deposited charge bled off in the time between charging and exposure. The higher level of dark decay remains approximately constant during later cycles.

The effect of the higher dark decay rate on hologram recording is to lower the fringe contrast on preexposed cycles for the same charge and exposure conditions as the first cycle. Lower fringe contrast results, of course, in lower diffraction efficiency. Therefore, to maintain diffraction efficiency (and SNR) approximately constant, different recording parameters are required for initial and pre-exposed cycles. One possible solution is to pre-expose the film prior to an exposure sequence. However, this is not a satisfactory solution, since the higher level of dark decay that results makes control of charging more difficult.

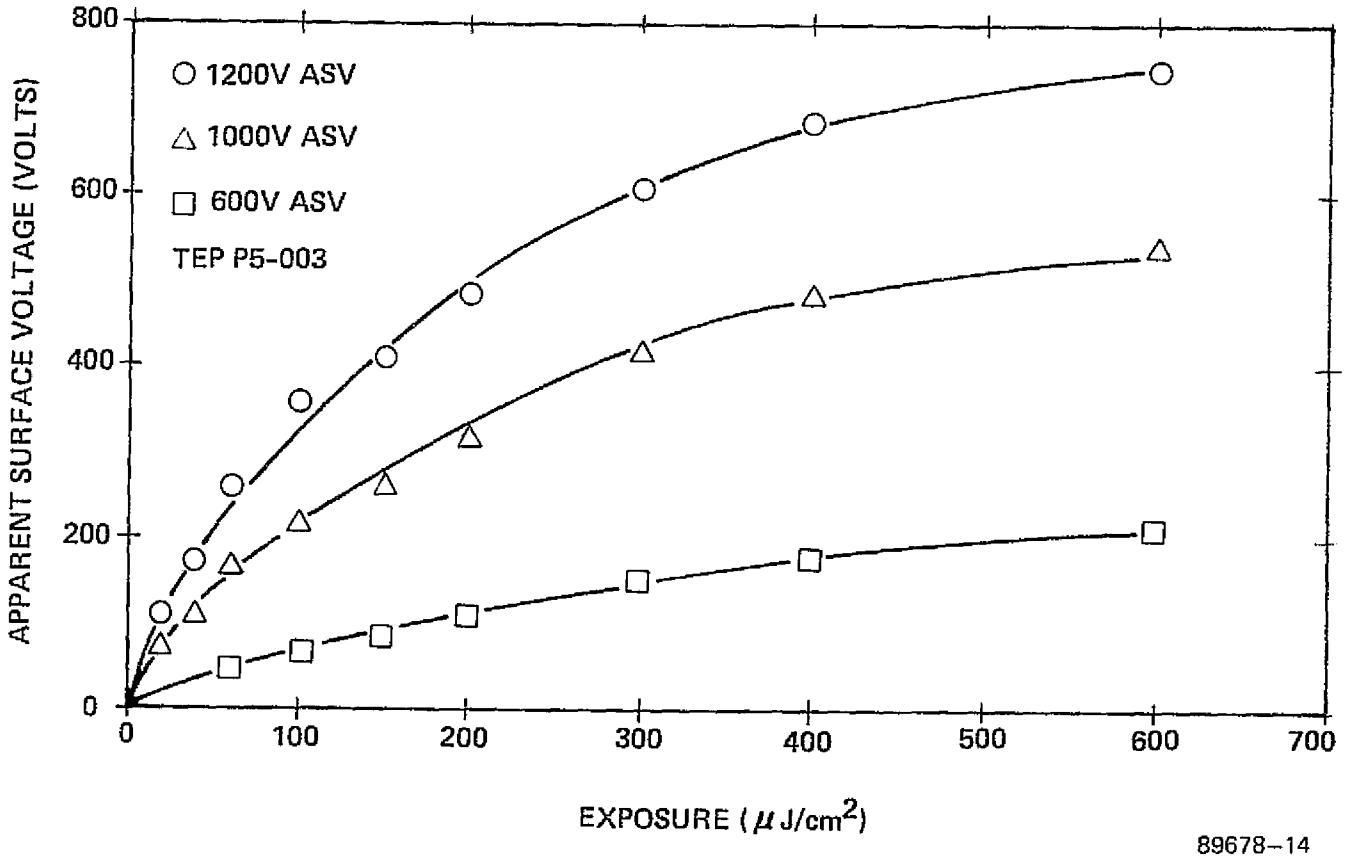

FIGURE 4-42. ΔASV AS A FUNCTION OF EXPOSURE FOR TEP P5-003

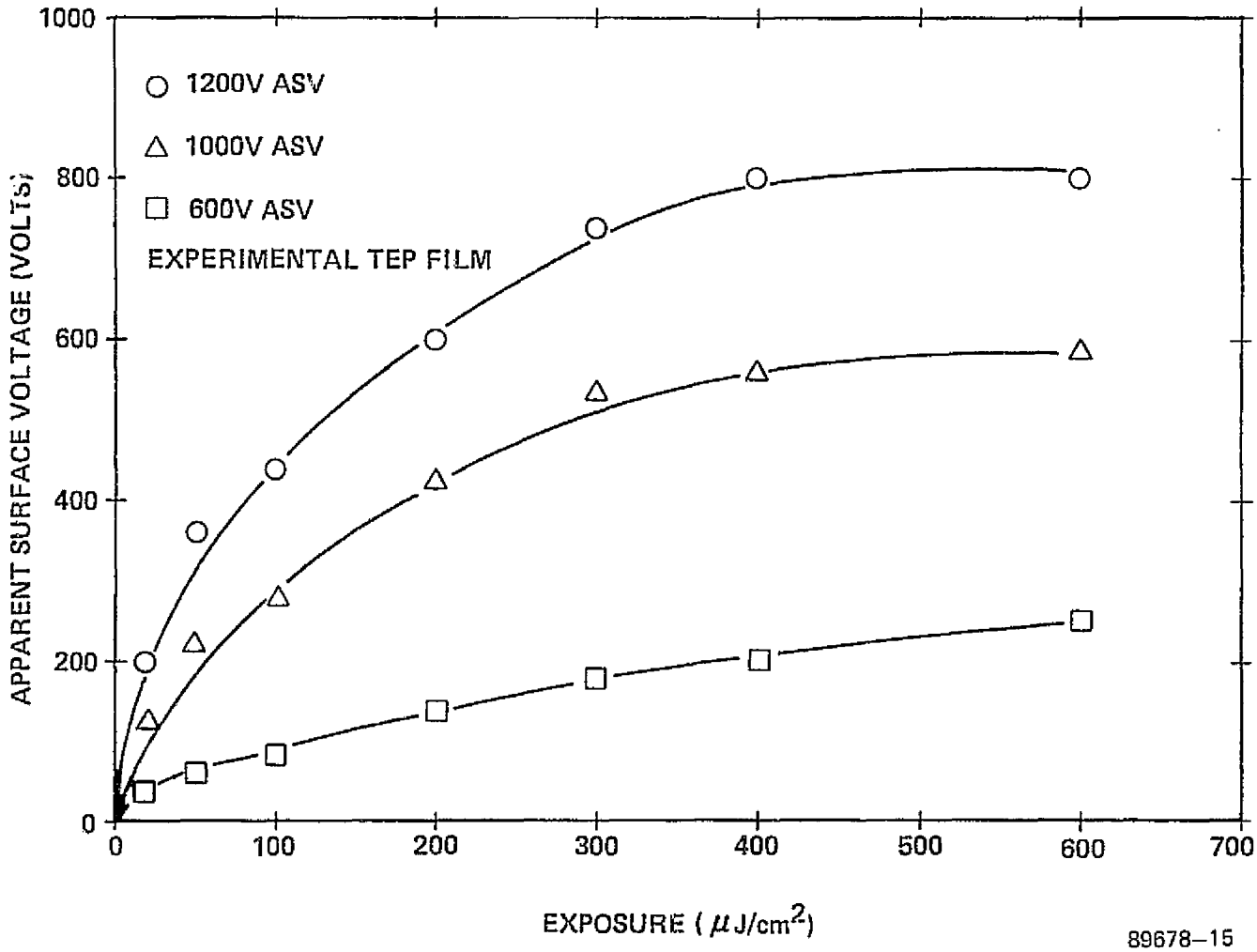

FIGURE 4-43. ΔASV AS A FUNCTION OF EXPOSURE FOR TEP P4-005

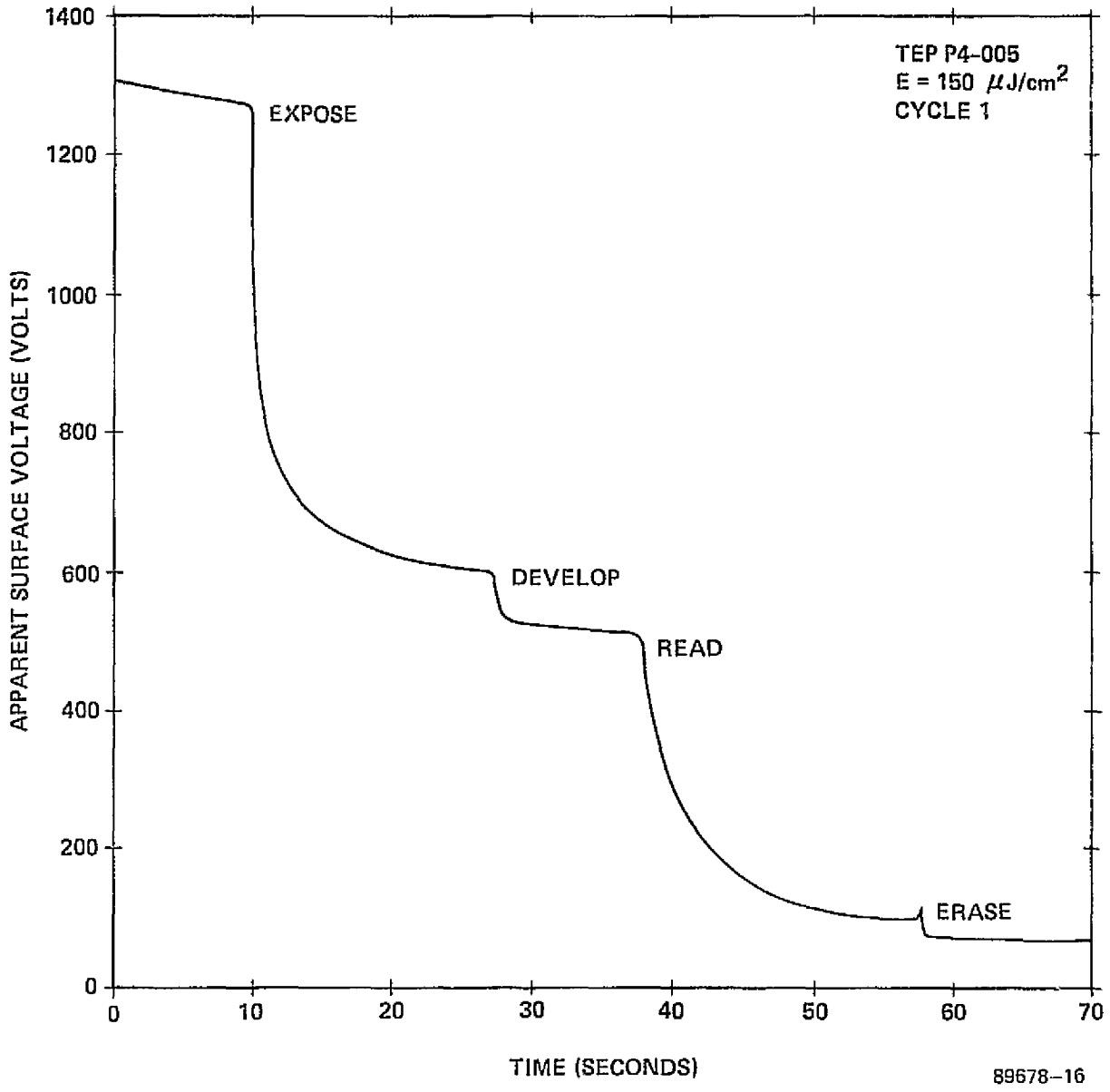

FIGURE 4-44 ASV AS A FUNCTION OF TIME
FOR TEP P4-005 (CYCLE 1)

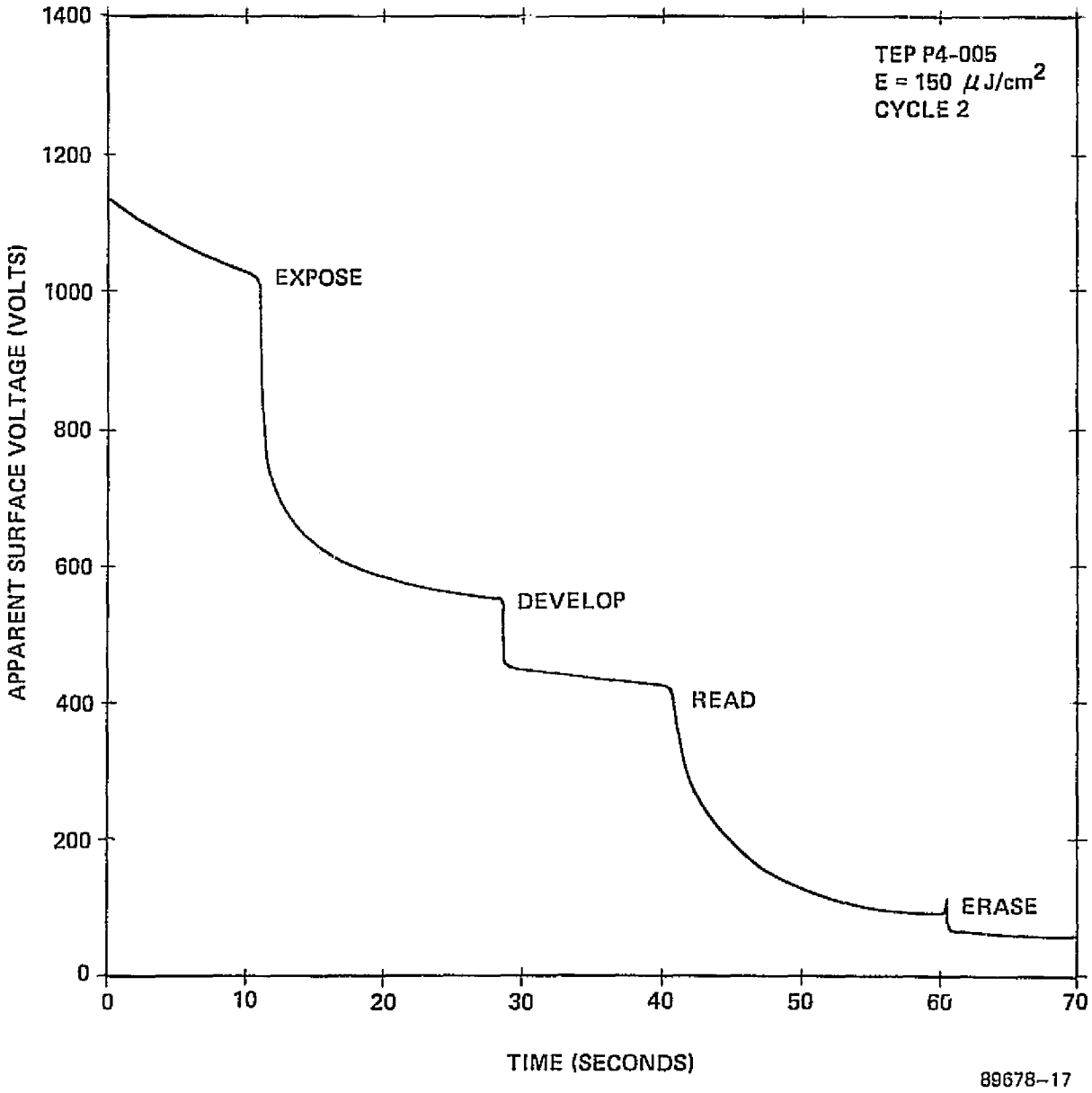

FIGURE 4-45a. ASV AS A FUNCTION OF TIME FOR TEP P4-005 (CYCLE 2)

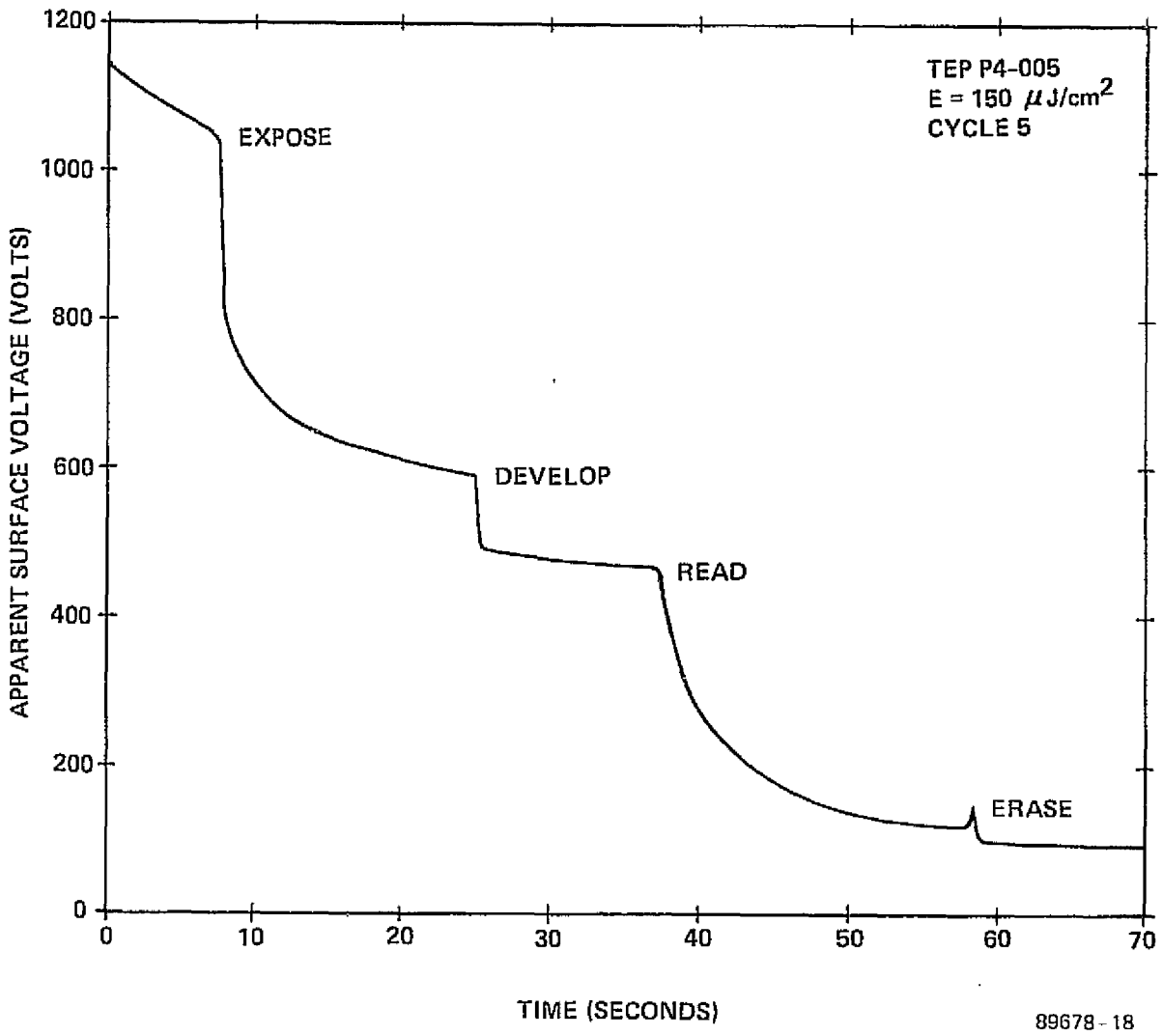

FIGURE 4-45b. ASV AS A FUNCTION OF TIME FOR TEP P4-005 (CYCLE 5)

Figure 4-46 shows an initial cycle on the TEP P5-003 photoconductor. For a given initial charge and exposure, the decay rate of surface voltage is less for the P5-003 photoconductor than the P4-005 sample. Subsequent cycles on the P4-005 photoconductor show the effects of persistent conductivity.

A TEP P4-005 photoconductor overcoated with thermoplastic was cycled through a complete write/read/erase process while the surface voltage was monitored; the exposure used was 200 $\mu J/cm^2$. Exposure to light caused less charge decay than the heating process. This indicates that the thermoplastic sandwich has a higher conductivity when heated than when exposed to light. At the end of a recording cycle, a residual potential of approximately 300 V remained on the film. This residual ASV makes it difficult to control the initial surface charge during subsequent cycles.

From early experimental work, we were aware of the holographic response of PVK/TNF type photoconductors. In order to compare the electrical response of PVK/TNF with that of m-phenylene diamine photoconductors, we coated a glass substrate with a 9 μm layer of PVK/TNF and monitored the surface voltage during a write/read/erase cycle. Figure 4-47 shows the result for a 100 $\mu J/cm^2$ exposure. Both the decay in the dark and decay rate during exposure are greater for the PVK/TNF photoconductor than for the m-phenylene diamine photoconductor. This is because the PVK/TNF OPC is more sensitive than the dye-sensitized m-phenylene diamine OPC. After development and erasure, the surface potential first increases and then slowly decays for the PVK/TNF samples. For the m-phenylene diamine materials, there is a slight increase and then a very rapid decay owing to heating. The effect of holographic performance is not known.

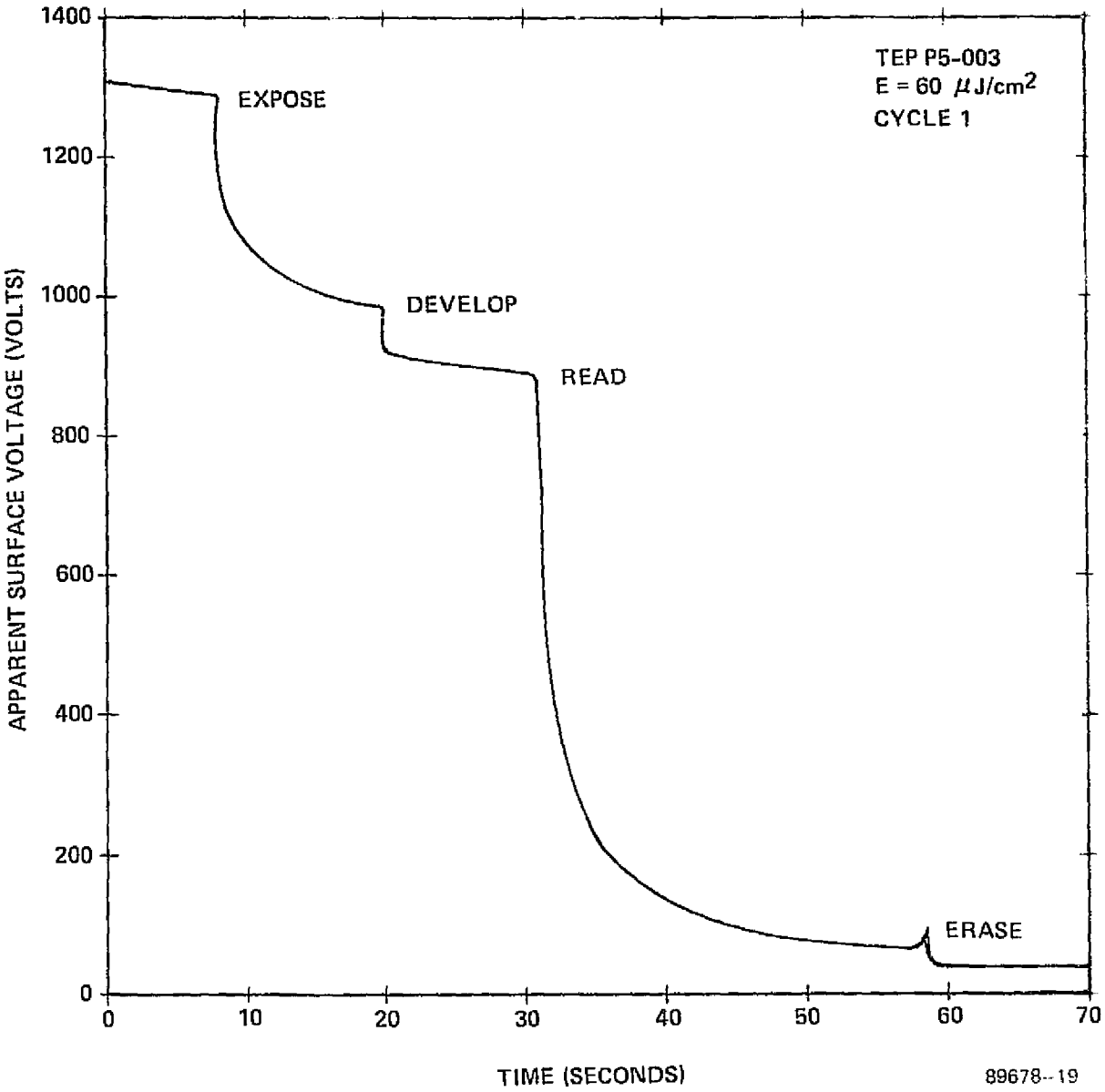

FIGURE 4-46. ASV AS A FUNCTION OF TIME FOR TEP P5-003 (CYCLE 1)

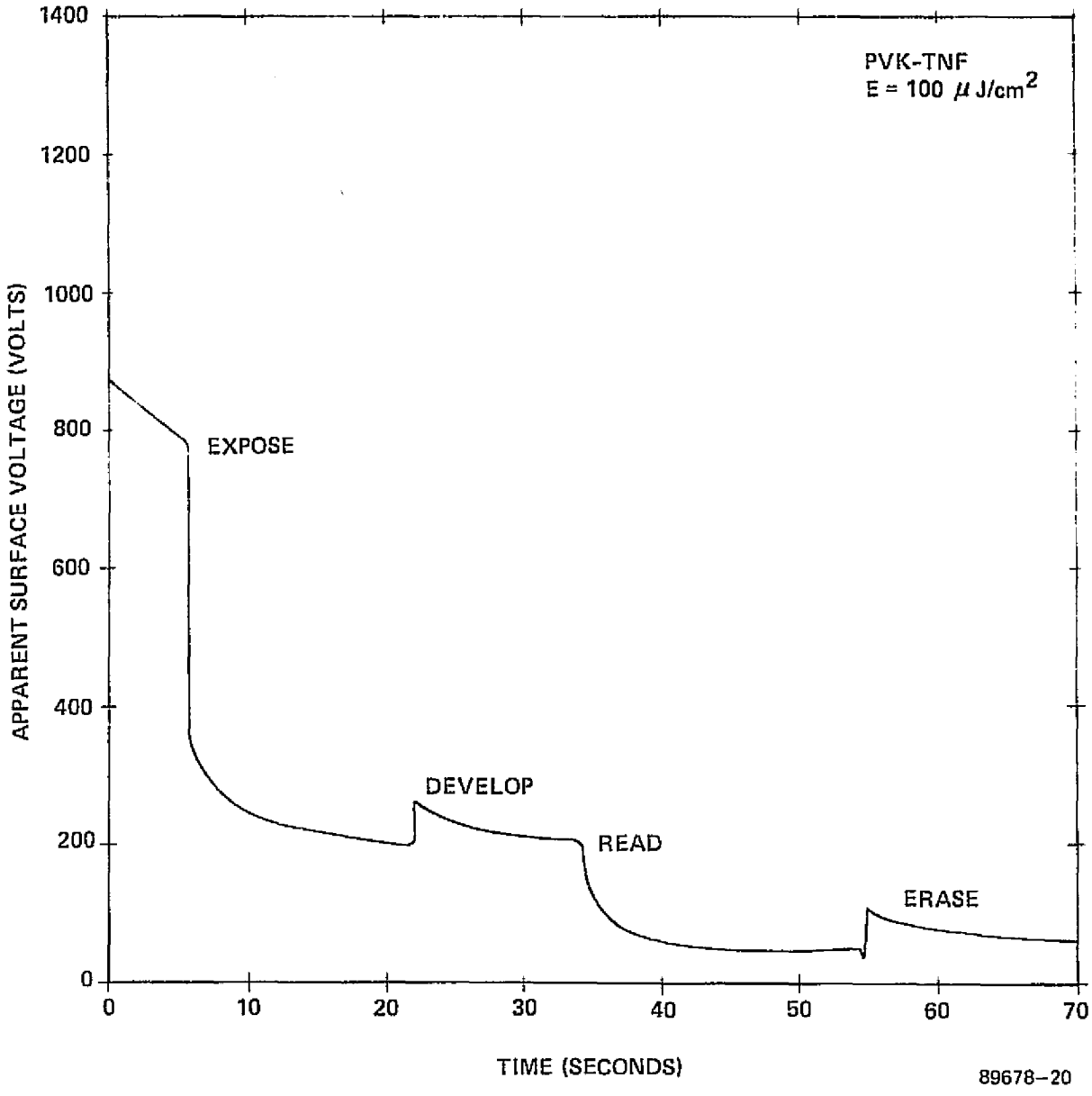

FIGURE 4-47. ASV AS A FUNCTION OF TIME FOR PVK/TNF (9 μm THICK LAYER)

4.3.4.3 Conclusions and Recommendations

The factors affecting charging and subsequent electrical interactions were found to be complex. However, they are basic to the understanding and controlling of data recording behavior of the recording material, and therefore merit consideration in future studies.

The efficiency and repeatability of the Corotron charging device was found to be dependent upon temperature and relative humidity; hence, some type of external control is needed to obtain repeatable charging. For m-phenylene diamine photoconductors, external charge control will work only for the initial recording cycle, because residual charge and persistent conductivity introduce random variations into the charging process.

The following observations are descriptive of physical conditions which appear to exist in the photoconductor after one write/read/erase cycle:

1. Exposure to a helium-neon laser beam generates many shallowly trapped carriers. Upon recharging, the electrostatic forces will re-excite some of the carriers into the conduction band, resulting in high dark decay. Under identical conditions, the surface voltage at the time of exposure will be less on the second cycle than on the first. It takes about 24 hours for the TEP photoconductor to return to an unexcited (equilibrium) state.

2. At the end of a recording cycle there will be some residual charge on the thermoplastic surface. As the thermoplastic has low conductivity, the residual charge can be neutralized only by reversal charging. However, the amount of residual charge varies in a random fashion; this makes the reversal charging step as difficult to control as the first charging step. Nonetheless, reverse charging before erasure is recommended because it reduces the magnitude of

the residual charge. In addition, the reverse charging process has been observed to increase the number of recording cycles obtained with a photoplastic recording film.

3. High intensity laser light, in conjunction with heat, tends to bleach the photosensitizing dye of the Scott Graphics PRF. After approximately 15 recording cycles, in which exposure and heat were used simultaneously, the dye was bleached out completely. After several record cycles, the exposure sensitivity decreases significantly. More record cycles are possible if light and heat are not simultaneously applied, but past experience with PRF indicates that this will result in an unacceptable increase in noise.

4.3.5 Film Base Study

Scott Graphics TEP films are constructed of a polyester film base coated with a transparent conductive layer and a dye-sensitized organic photoconductor. As the OPC is grainless, it contributes no scattering noise during recording or readout. Thus, the main source of scattering noise during the recording and readout processes is the film base. Scott Graphics supplied a number of film samples which had the same OPC coated on different polyester film bases. We found that the maximum signal-to-noise ratio obtained from holographic reconstructions with the different film bases ranged between 12 and 17 dB. To determine which was best suited for our needs, we made a general experimental comparison of the set of film bases available from Scott Graphics.

4.3.5.1 Experimental Setup

The parameter used to compare the film bases was the average signal to average noise power ratio (SNR) of the throughput image of a standard test pattern. The test pattern is a 1.5- by 3-cm ground glass target with a 0.5-cm by 3-cm opaque strip in the center. The test target was imaged through the selected film base by a

high quality lens. The S/N ratio of the throughput image was determined with a scanning photomultiplier, log amplifier and chart recorder.

4.3.5.2 Results

The results of this experiment are summarized in Table 4-1. The film base designated Type B is the standard Scott Graphics production base. The Type B film base had a throughput SNR that ranged from 14.6 to 18.6 dB. Newer film bases, such as Type F and Type 2D, generally provided a higher throughput signal-to-noise ratio and are better suited for holographic recording; they generated even less noise than NESA® glass substrates typically used for resistive heating. This is an interesting and unexpected result. The Type A film base was the original polyester film base used by Scott Graphics and was later replaced by Type B. The Type F film base is an experimental film base.

To determine the source of film base noise, we examined several film bases with a microscope using dark field illumination. Figures 4-48(a) and 4-48(b) show the front and back surfaces of a Type B base. The scattering centers in the Type B base are uniformly distributed spherical particles about 1 μm in diameter. Figures 4-49(a) and 4-49(b) show samples of the Type A base and the Type 2D base, respectively. The high quality 2D base is the obvious choice for photoplastic recording films for holographic recording applications.

4.3.5.3 Conclusions

Variations in quality of different batches of the same film base is a problem area for holographic recording. The photomicrographs of the vesicular defects illustrate a common problem with polyester film bases that do not meet the quality standards of film bases such as Kodak Estar® or Dupont Cronar®. As a result, it is difficult to state with certainty that one film base is superior to another on the basis of the testing of a single batch; the next batch may be very different. We note, however, that when careful preinspection was used, the overall quality of the film bases was quite high. A possible solution, then, is to statistically check samples of the film base prior to coating

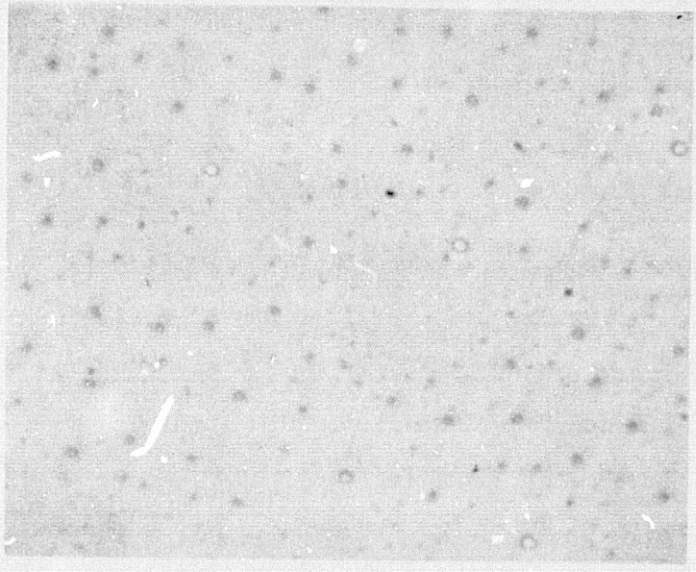

a. B BASE, FRONT SURFACE

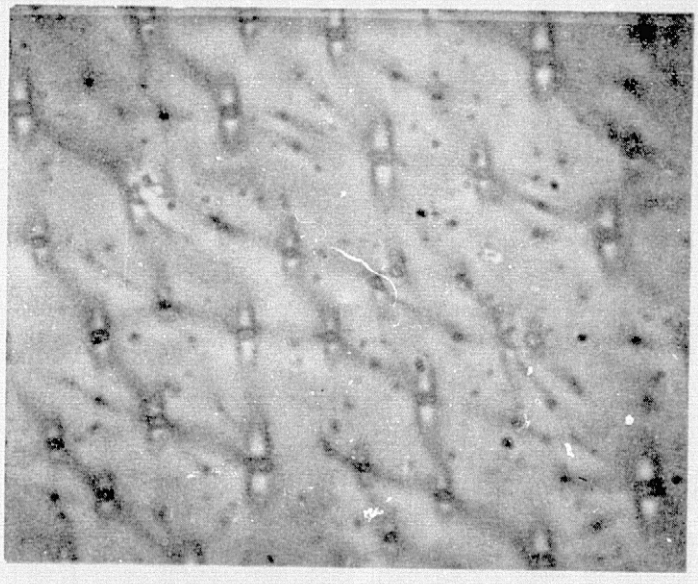

b. B BASE, BACK SURFACE 89678–2

FIGURE 4-48. PHOTOMICROGRAPHS OF SCOTT GRAPHICS B BASE

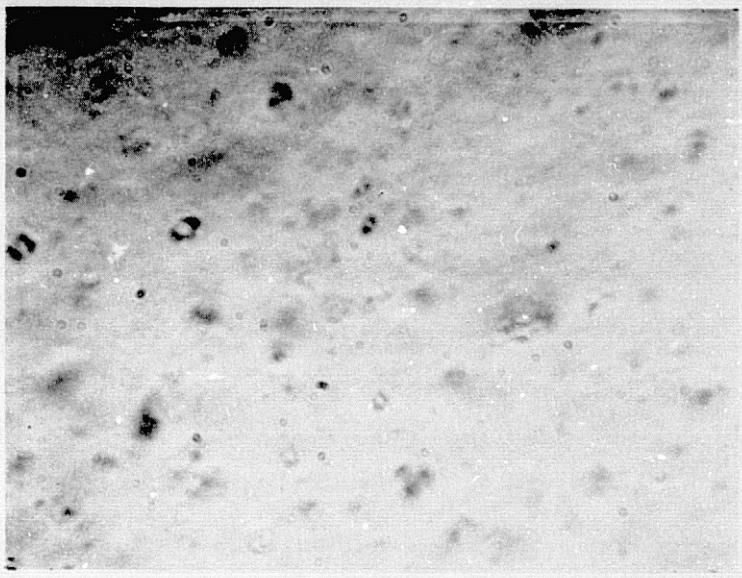

a. A BASE

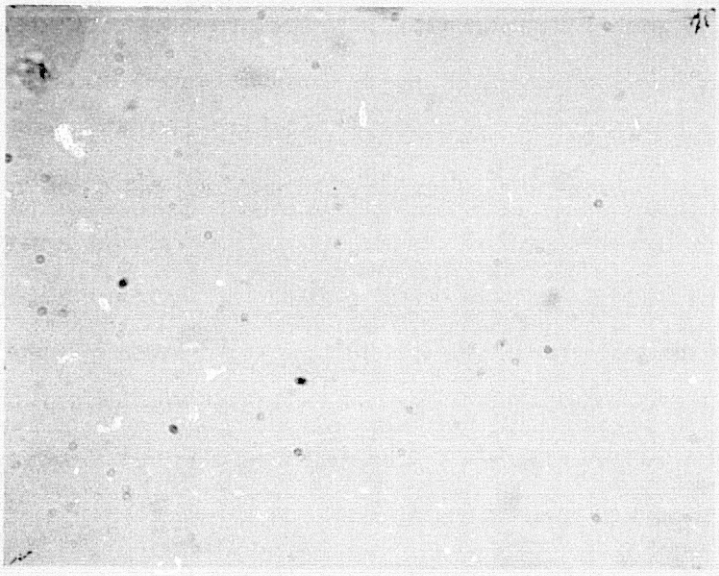

b. 2D BASE

89678–3

FIGURE 4-49. PHOTOMICROGRAPHS OF SCOTT GRAPHICS A AND 2D BASES

to ensure that a defect-free batch of polyester is being used. This assumes, of course, that the quality of polyester within one batch is relatively constant, an assumption that may not always be justified.

4.3.6 Holographic Properties

The holographic performance of the Scott Graphics photoplastic recording films was determined from diffraction efficiency and SNR measurements. The two TEP films, TEP P5-003 (peak sensitized at 590 nm) and TEP P4-005 (peak sensitized at 633 nm), overcoated with a 1 μm layer of Foral 105 thermoplastic were experimentally characterized. Parameters for this investigation were development energy, exposure level, and apparent surface voltage.

4.3.6.1 Experimental Apparatus

A schematic diagram of the experimental setup is shown in Figure 4-50; it is a modified Mach-Zehnder interferometer. A Spectra-Physics Model 125 helium-neon (λ = 632.8 nm) was the coherent light source for both recording and readout. Exposure time was controlled with an electromechanical shutter. The mirror M' and the combining beam splitters B_S' were fully adjustable. The Mach-Zehnder interferometer permitted accurate path length equalization (as inferred from fringe contrast) and the generation of spatial frequencies ν in the 0 to 800 cycle/mm range. The spatial frequency bandpass of the material is determined by the thickness of the thermoplastic layer. For 1 μm thick thermoplastic layers, the optimum spatial frequency response is in the range of 500 to 600 cycles/mm. A spatial frequency of 500 cycles/mm was chosen for the experimental investigation.

The photoplastic recording film was held by vacuum grooves against a 1 cm^2 resistive heating pad (75 ohm/square resistivity) for both development and erasure. A 200 ms heat pulse was used for development, and an 800 ms heat pulse was used for erasure. The film was charged with a single wire corotron positioned 1 inch from the film surface. The corotron shield, the film conductive layer, and the resistive heating

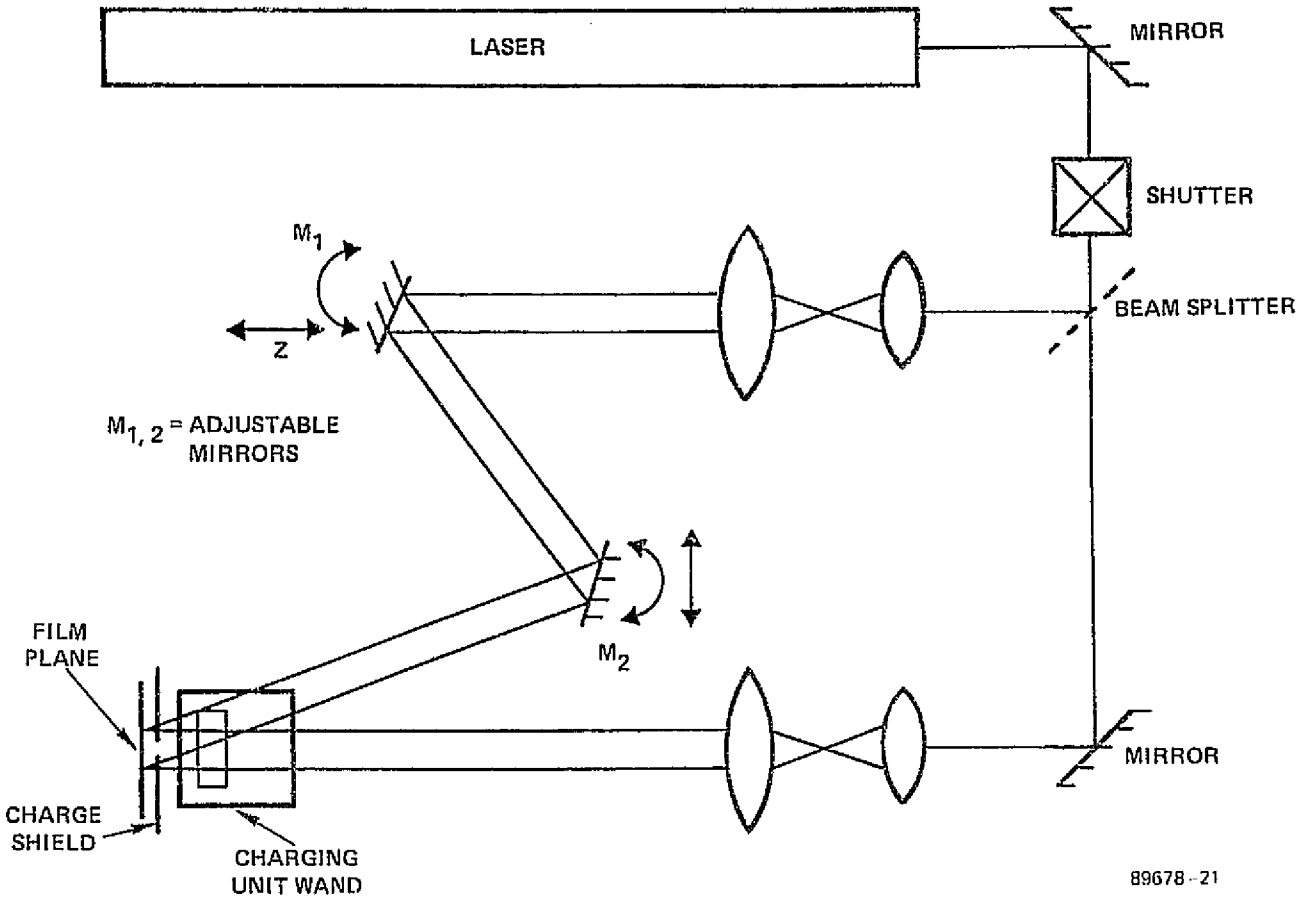

FIGURE 4-50. SCHEMATIC DIAGRAM OF MACH ZHENDER INTERFEROMETER

pad had a common ground. A plexiglas shield with a 4 cm^2 aperture isolated the unused area of the PRF during charging; hence, only that small area of the PRF which was to be recorded on was sensitized. The charge level was controlled by the corona voltage and the charging time. Charge monitoring was not implemented.

As previously noted, the performance of different TEP films were evaluated. The TEP P5-003 photoconductor coated on a 5-mil Type B polyester base is a standard Scott Graphics product which is used as the recording material in the A. B. Dick/Scott System 200 (an updatable microfiche/system). As such, its characteristics are well-known and quality control is relatively good. The TEP P4-005 photoconductor, coated on 4-mil Type 2D polyester base, is an experimental TEP film that has been sensitized for laser recording at 632.8 nm.

4.3.6.2 Diffraction Efficiency

We measured diffraction efficiency by recording and reconstructing plane wave grating holograms. Preliminary experiments indicated that diffraction efficiency remained close to its maximum value over a broad exposure range. Hence, to determine the effects of charging and development variations, an exposure was chosen for each material that approximately maximized diffraction efficiency. Recording parameters were a reference-to-signal beam ratio K = 1 (100 percent modulation) and a spatial frequency ν = 500 cycles/mm.

Figures 4-51 and 4-52 show diffraction efficiency as a function of development energy for the TEP P4-005 and P5-003 photoplastic recording films, respectively; initial surface potential was the parameter for this experiment. The TEP P4-005 photoplastic recording film has a stronger dependence on development energy than the TEP P5-003 photoplastic recording film. The TEP P4-005 also requires about 15 percent more development energy.

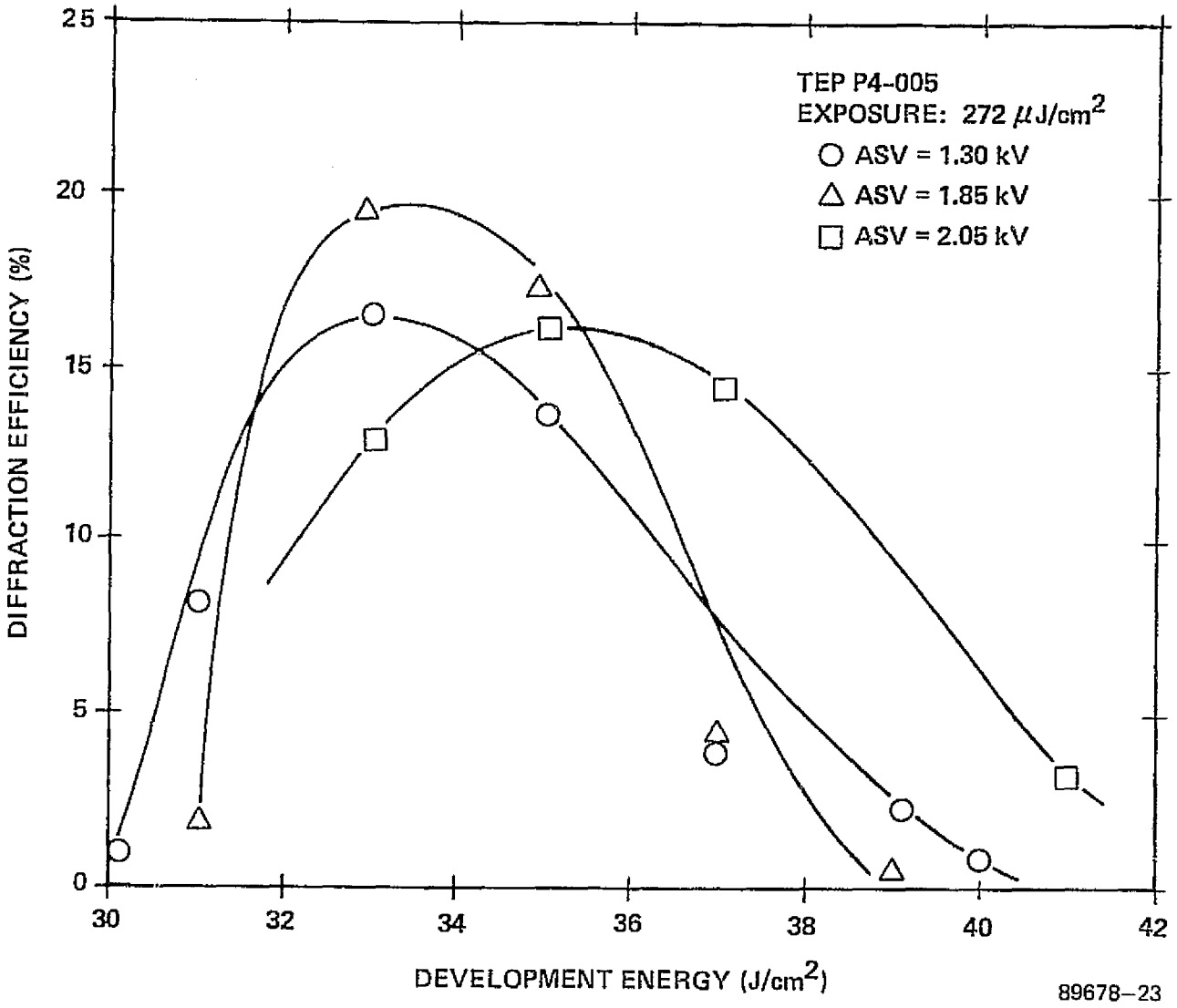

FIGURE 4-51. DIFFRACTION EFFICIENCY AS A FUNCTION OF DEVELOPMENT FOR TEP P4-005

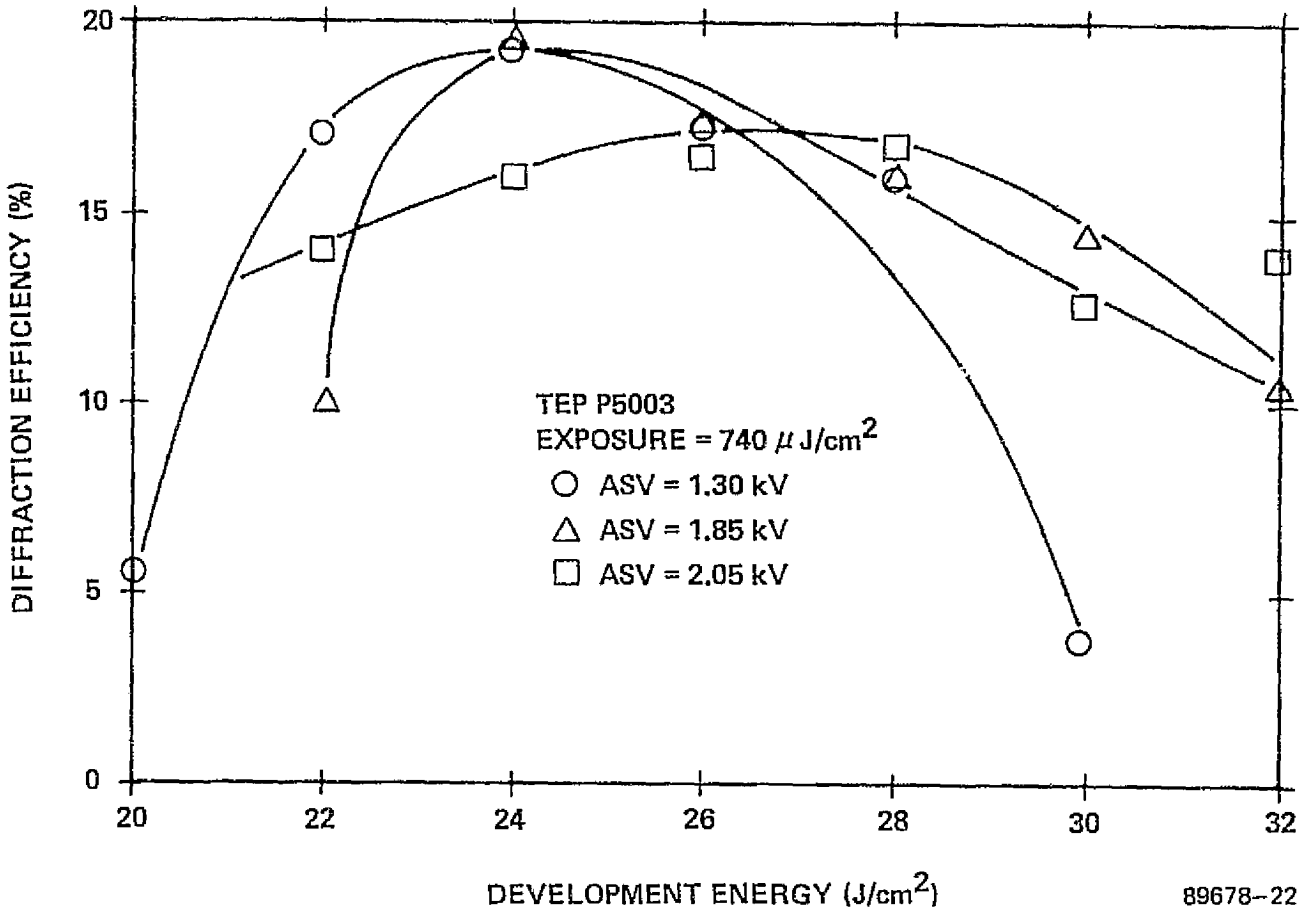

FIGURE 4-52. DIFFRACTION EFFICIENCY AS A FUNCTION OF DEVELOPMENT FOR TEP P5-003

The maximum diffraction efficiency obtained with both materials was 20 percent. The optimum apparent surface potential was 1.85 kV, whereas the optimum development energy was 33 J/cm^2 and 24 J/cm^2, for the P4-005 and P5-003 photoplastic recording films, respectively. For each surface potential, diffraction efficiency was measured as a function of exposure for optimized development. The results are shown in Figures 4-53 and 4-54. For each charge level there is a critical exposure value above which diffraction efficiency remains approximately constant. As the initial surface potential increased, the critical exposure decreased. For TEP P5-003, with an apparent surface potential of 1.85 kV and an optimum development energy of 24 J/cm^2, diffraction efficiency reached the 20 percent level. The critical exposure is about 400 μJ/cm^2. For TEP P4-005 with an apparent surface potential of 1.85 kV and the optimum development energy of 33 J/cm^2, diffraction efficiency reached 20 percent for an exposure of 150 μJ/cm^2.

For all remaining photoplastic recording film holographic experiments, an initial apparent surface potential of 1.85 kV was used, together with the development energies of 33 J/cm^2 and 24 J/cm^2 for the TEP P4-005 and TEP P5-003 photoplastic recording films, respectively.

4.3.7 Signal-to-Noise Ratio

Data storage performance was evaluated by recording Fresnel holograms of a ground glass diffuser with an opaque central region. The transmitting region of the input signal is equivalent to a wideband stochastic (white noise) source, whereas the opaque region provides an absolute reference for noise measurement. The information packing density was approximately 2.5 Mb/cm^2. The experimental procedure was as follows. First, we set the carrier frequency ν_c at 550 cycles/mm; (this is near the maximum spatial frequency response of the photoplastic layer). Next, for K = 12, holograms were recorded for a range of exposures E and processed with the previously determined development energies and charging voltages. Finally, we reconstructed the real image of each hologram and measured diffraction efficiency and SNR.

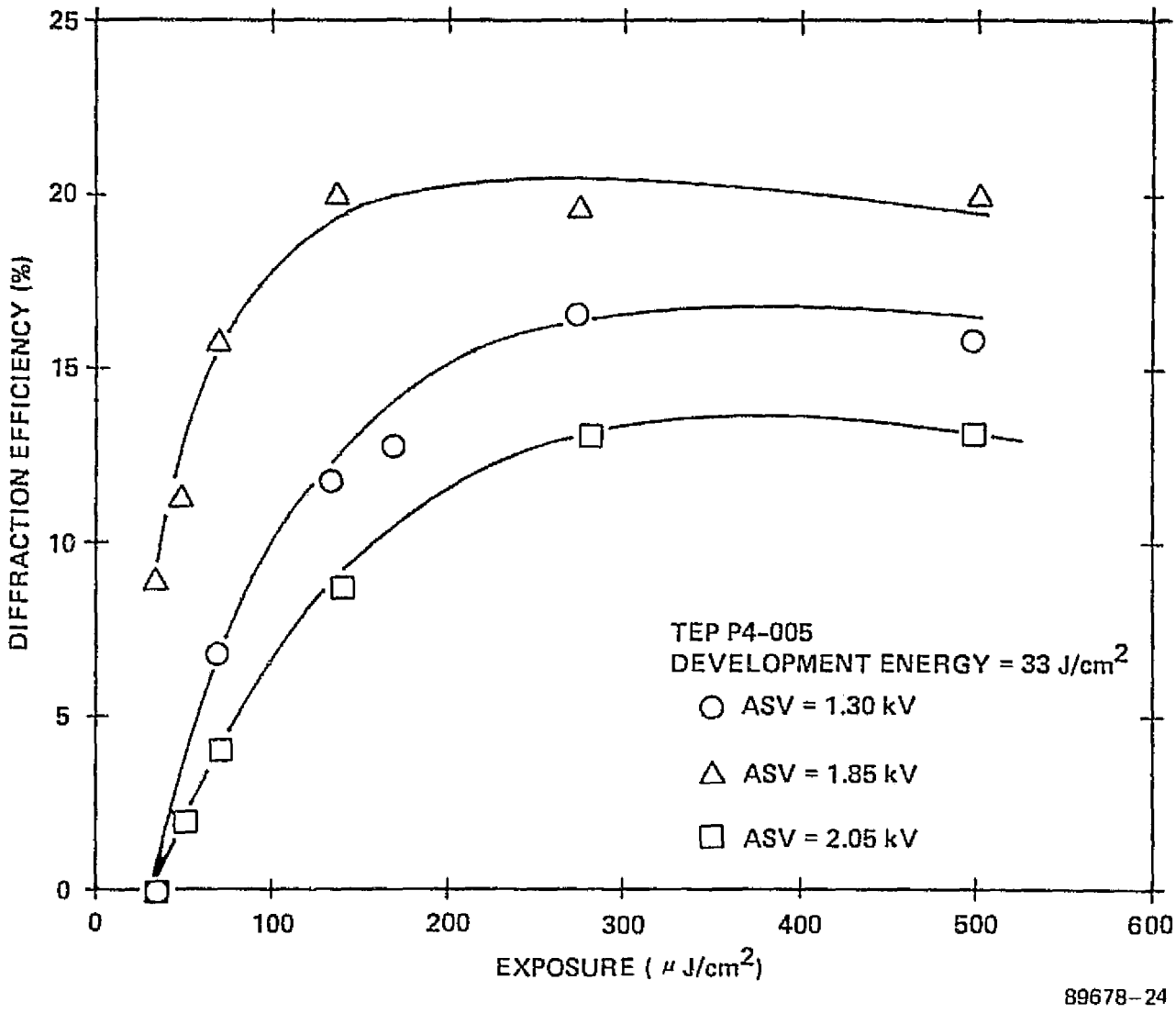

FIGURE 4-53. DIFFRACTION EFFICIENCY AS A FUNCTION OF EXPOSURE FOR TEP P4-005

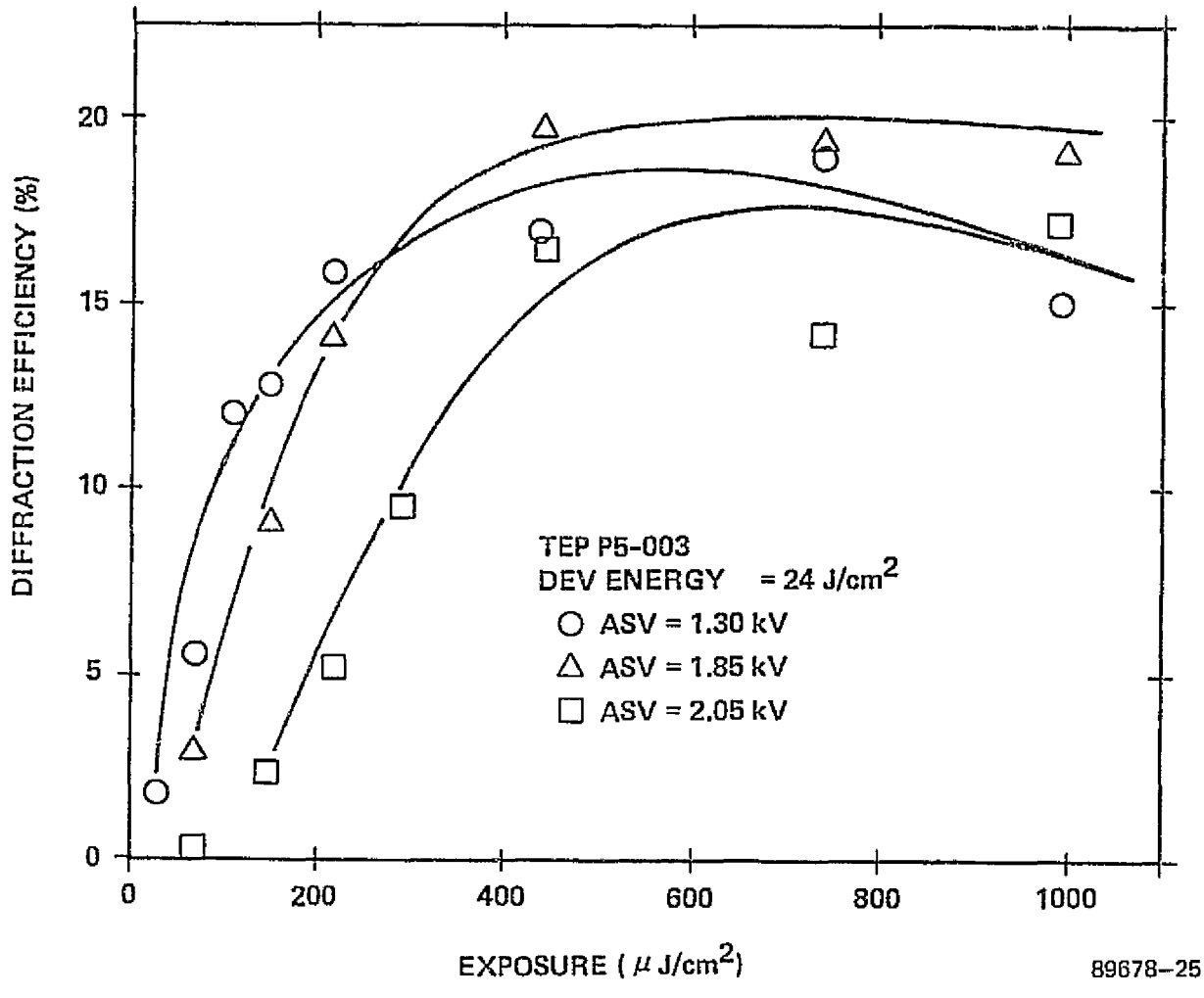

FIGURE 4-54. DIFFRACTION EFFICIENCY AS A FUNCTION OF EXPOSURE FOR TEP P5-003

TABLE 4-1. THROUGHPUT SNR FOR VARIOUS SCOTT GRAPHICS FILM BASES

Film Base	SNR (dB)
None	21.0
NESA Glass	18.2
P5-003 on B Base	18.6
P4-005 on B Base	14.6
P4-005 Photoconductor on a 2D Base	18.5
P4-005 on 2D Base	19.7
P5-003 on F Base	19.5
P5-003 Seconds on B Base	18.0
P5-003 Photoconductor on A Base	16.1

The results for TEP P5-003 are shown in Figure 4-55(a). The SNR maximum was 10 dB for an exposure of 400 $\mu J/cm^2$; the corresponding DE was 5 percent. For larger exposures, the SNR remained constant while diffraction efficiency increased. Optimum results were measured for an exposure of 1000 $\mu J/cm^2$, which yielded a SNR of 10 dB with a corresponding diffraction efficiency of 8.2 percent. The DE and SNR, as a function of exposure, for the TEP P4-005 are shown in Figure 4-55(b). The maximum SNR obtained was 15 dB for an exposure of 320 $\mu J/cm^2$; the corresponding diffraction efficiency was 11 percent. For higher exposures, the SNR decreased, while diffraction efficiency values saturated. The increase in SNR for the TEP P4-005 is apparently due to a higher quality film base. The TEP P4-005 was on the 2D film base, whereas the P5-003 PRF was coated on the B base. No decrease in reconstructed signal brightness occurred across the real image. This implies a fairly flat spatial frequency response over a ±90 cycles/mm bandpass centered on 550 cycles/mm. The bandpass depends, of course, on thermoplastic thickness.

4.3.8 Consistency of Performance

To examine consistency of performance of the photoplastic recording film, the diffraction efficiency of plane wave gratings was used as a control variable. We recorded 10 gratings with $K = 1$, $\nu = 550$ cycles/mm and exposures of 150 $\mu J/cm^2$ and 400 $\mu J/cm^2$ for the TEP P4-005 and TEP P5-003 PRF, respectively. The results of this experiment are summarized in Table 4-2. Neither film provided consistent readout performance. We attribute this behavior primarily to nonuniformities in the thermoplastic coating. This hypothesis is supported by the fact that the diffraction efficiency depends on the position of the hologram on the fiche. We observed that one side of the film typically had higher diffraction efficiencies than the other side since the coating thickness varies monotonically across the fiche surface, a significant difference in holographic performance can be expected. As these were experimentally coated films, this is not surprising.

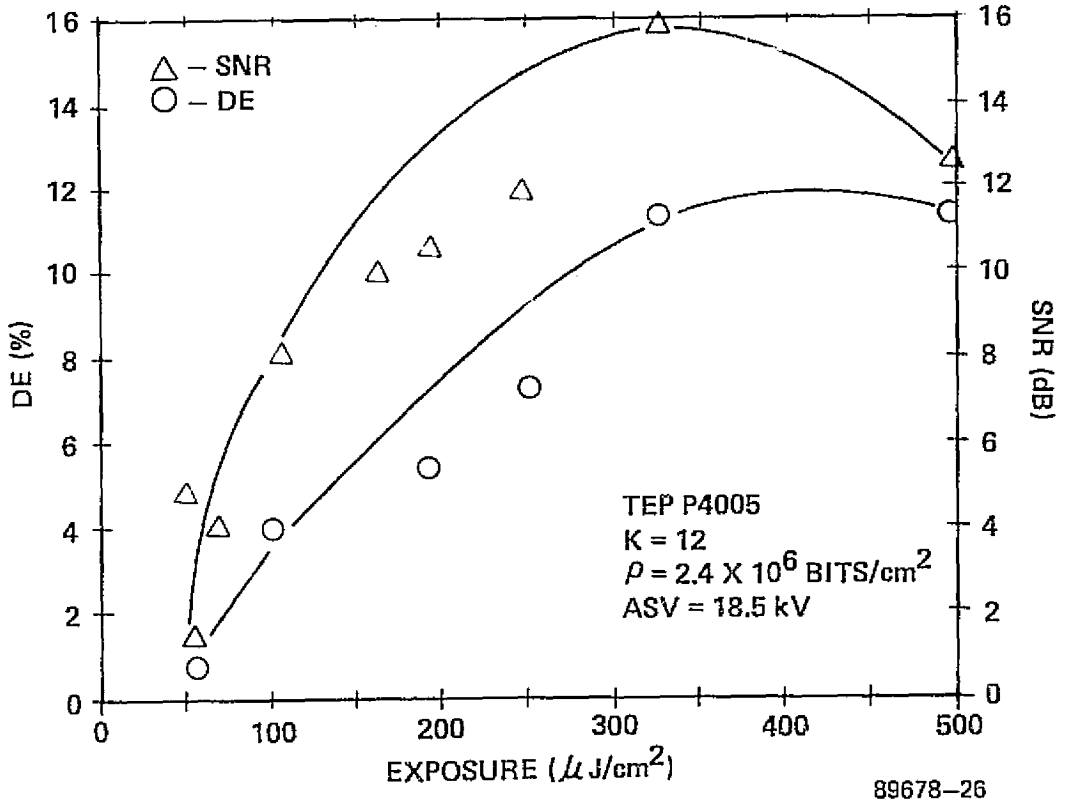

FIGURE 4-55a. DIFFRACTION EFFICIENCY AND SIGNAL-TO-NOISE RATIO AS A FUNCTION OF EXPOSURE FOR SCOTT GRAPHICS TEP PHOTOCONDUCTORS (P4-005)

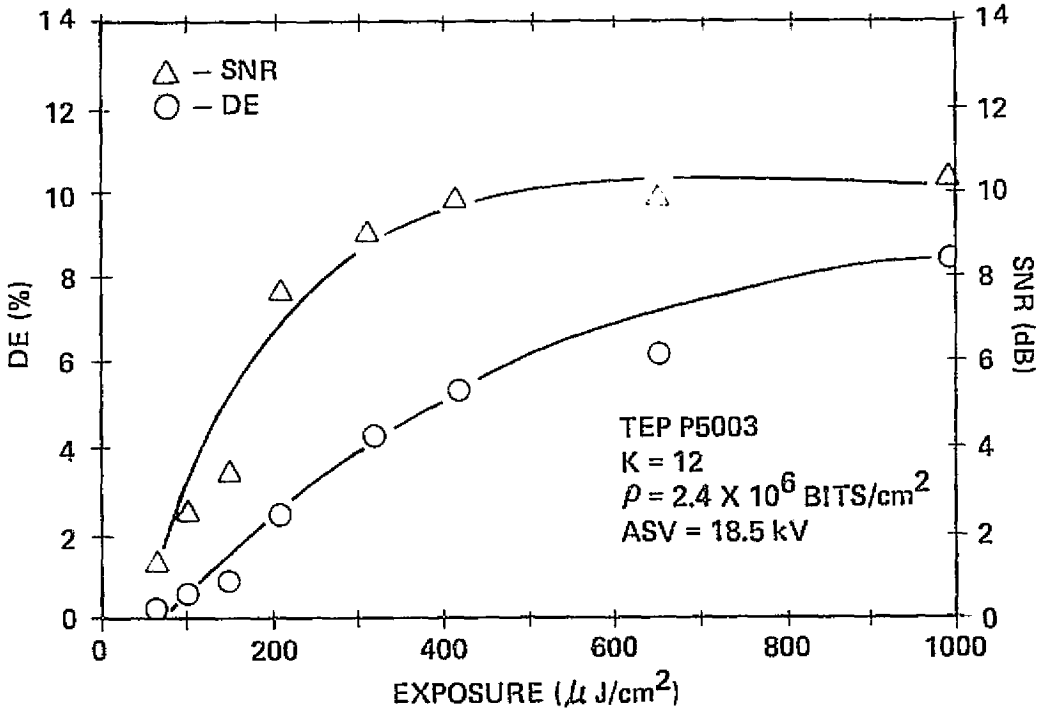

FIGURE 4-55b. DIFFRACTION EFFICIENCY AND SIGNAL-TO-NOISE RATIO AS A FUNCTION OF EXPOSURE FOR SCOTT GRAPHICS TEP PHOTOCONDUCTORS (P5-003)

TABLE 4-2. HOLOGRAPHIC PERFORMANCE CONSISTENCY OF SCOTT GRAPHICS PHOTOPLASTIC RECORDING FILMS

Exposure No.	DE (%) for P4-005 PRF ($E = 160\ \mu J/cm^2$)	DE (%) for P5-003 PRF ($E = 740\ \mu J/cm^2$)
1	15.6	16.7
2	13.2	16.3
3	12.4	13.8
4	8.0	9.5
5	8.0	16.7
6	11.6	17.5
7	10.0	15.0
8	12.9	11.8
9	13.8	10.8
10	15.2	17.1

4.3.9 A Blazing Anomaly

While reading out plane wave grating holograms, we obtained a rather unexpected result. When the signal was used for reconstruction rather than the reference beam, as much as 38 percent of the incident light was diffracted into one order. Diffraction efficiencies of this level exceed the theoretical maximum theoretical value for planar phase holograms, which is 33.9 percent. The diffraction efficiency of the hologram was observed to be orientation sensitive, suggesting that perhaps a blazed grating was being formed. In such a grating, the thermoplastic surface between grating lines forms an angle that causes the incident light to be refracted in the direction of the first order diffracted beam. The blazing effect is dependent on geometry. If the direction of the readout beam is reversed, the high efficiency is not observed. If the readout beam is incident parallel to, but from the opposite direction of the original strong diffracted order, high efficiency is again observed. Blazing is not typically observed for photoplastic recording materials, because it requires a shear force to generate the off-normal fringe angle. The thermoplastic cannot support such a shear force while it is fluid. Thus, the blazing must take place as the thermoplastic cools and is momentarily plastic. Blazing requires a relatively simple interference pattern. The interference of two plane waves forms such a pattern to make a holographic grating. However, since we are interested in recording complex data signals, the blazing effect does not normally occur. As a precaution, all holographic measurements were made using a geometry that inhibited the blazing effect.

4.3.10 Summary and Conclusions

Table 4-3 summarizes the results of our experimental activities with the Scott Graphics photoplastic recording films. For recording at 632.8 nm, the P4-005 PRF on Type 2D base performed better than the P5-003 PRF on the Type B base. We note that lower exposures are required for the P4-005 PRF. Similarly, the diffraction efficiency and SNR are higher for the P4-005 PRF than for the P5-003 PRF. The exposure requirement is a characteristic of the photoconductor, but SNR is determined in part by

TABLE 4-3. SUMMARY OF SCOTT GRAPHICS PRF PERFORMANCE

	Film	TEP P5-003	TEP P4-005
I	Gratings		
	DE_{max}	20%	20%
	Exposure	400 $\mu J/cm^2$	150 $\mu J/cm^2$
	ASV	~1850 V	~1850 V
	ν	500 ℓ/mm	500 ℓ/mm
II	Fresnel Holograms		
	SNR max	10.3 dB	16 dB
	DE at SNR max	8.4	9.3
	Exposure	540 $\mu J/cm^2$	324 $\mu J/cm^2$
	ASV	~1850 V	~1850 V
	K	12	12
	SNR of throughput	16 dB	19 dB
	ν_c	550 ℓ/mm	550 ℓ/mm
III	Construction		
	Base Transmission	36%	27%
	Type Base	B	2D
	Base Thickness	5 mil	4 mil

the film base. The primary disadvantage of the P4-005 PRF is base transmission. Since the photoconductor has a maximum sensitivity at 632.8 nm, it is highly absorptive at that wavelength during readout.

A main disadvantage common to both photoplastic recording films is the inconsistent performance. The lack of performance consistency is due to nonrepeatable charging and nonuniform thermoplastic thickness. These problem areas can be minimized through stricter manufacturing techniques and quality control. The two effects are interrelated which prevent the relative magnitude of each component from being identified. The coating problem can be solved by better manufacturing quality control. Further research work, however, is needed in the area of charge control.

4.4 REFERENCES

1. Urbach, J. C. and R. W. Meier, "Thermoplastic Xerographic Holography," Applied Optics 5, April 1966, pp. 666-667.

2. Lin, L. H. and M. L. Beauchamp, "Write-Read-Erase in Situ Optical Memory Using Thermoplastic Holograms," Applied Optics 9, September 1970, pp. 2088-2092.

3. Aftergut, S., R. F. Kopczewki and J. F. Burgess, "Reflective Photoplastic Film," Photo. Sci. & Eng. 15, Nov-Dec 1971, pp. 495-500.

4. Colburn, W. S. and E. N. Tompkins, "Improved Thermoplastic Devices for Holographic Recording," Applied Optics 13, December 1974, pp. 2934-2941.

5. Lo, D. S., L. H. Johnson and R. W. Honebrink, "Thermoplastic Recording," Annual SPIE Meeting, August 1976, San Diego CA.

6. Schaffert, R. M., Electrophotography, 2nd Ed., Focal Press, New York (1975), pp. 630-31.

7. Zech, R. G., L. M. Ralston, and M. W. Shareck, "Holographic Recording Materials," Final Technical Report, Contract F30607-74-C-0030, Rome Air Development Center, July 1974, pp. 81-104.

8. Schaffert, R. M., "High Electrostatic Contrast in Electrophotography," Photo. Sci. & Eng. 15 (2) 148, March-April 1971, pp. 148-157.

9. Dessauer, J. H. and H. E. Clark, Xerography And Related Processes, Focal Press, New York (1965), p. 206.

10. Schaffert, R. M., op cit, p. 237.

APPENDIX 4A

BACKGROUND ON KALLE PHOTOPLASTIC RECORDING PLAN

APPENDIX 4A

BACKGROUND ON KALLE PHOTOPLASTIC RECORDING FILM

Dr. R. G. Zech, Recording Materials Project Engineer, visited Kalle AG in Wiesbaden, West Germany to discuss Kalle's photoplastic recording film capabilities. On 23 September 1974, he met with Dr. Roland Moraw and Mr. Gunther Schadlich at the main Kalle facility in Biebrich. The objectives of the visit were: (1) to determine Kalle's capability for producing large quantities of high quality photoplastic recording film, (2) to observe first hand Kalle's methods of manufacturing and quality control and (3) to discuss technical aspects of the use and processing of photoplastic recording films for holographic data storage.

To initiate the technical discussion Dr. Moraw outlined the development of the Kalle PRF. He indicated that Kalle has concentrated on ungrounded PRF, but is also working on a system that uses an internal conductive plane. In anticipation of expected questions, Dr. Moraw noted that the PRF has limited cyclability since it was not designed for this purpose. Important points were that the polyester base loses planarity (tends to curl) after about 100 cycles and that a material intended for a large number of read/write/erase cycles must be made with great precision, whereas a single use material can have lower overall quality. Kalle apparently reserves highest quality fabrication for PRF on conductive glass substrates. Dr. Moraw indicated, however, that there is some possibility of obtaining 500 read/write cycles, but that there are many problems to be solved.

A number of questions aimed at gauging Kalle's overall capability and dedication in the photoplastic recording film area were prepared in advance. The major part of the discussions focussed on these questions. The questions are listed together with a summary of Kalle AG responses.

I. GENERAL QUESTIONS

Question 1: What are the overall manufacturing capabilities of Kalle in in the area of light-sensitive materials?

Answer 1: Kalle is primarily a plastics company with both raw material and finished product capabilities in all plastics except polycarbonates. Kalle is also a manufacturer of graphic arts and reprographic materials (diazo papers, printing plates, etc.). Kalle is a division of Hoechst, AG with 8,000 employees in Biebrich and a very large production facility (2 to 3 entire city blocks by casual estimate). It was suggested that Kalle is somewhat similar to, but smaller than, DuPont.

Question 2: Can Kalle produce other photoplastic systems than the PVK/TNF system? Is Kalle interested in producing other photoplastic systems?

Answer 2: Kalle can produce (and is aware of) other PRF systems. They do not, however, at this time have an interest in manufacturing other types of PRF. Dr. Morow stated that research and development costs cannot be justified unless a definite application requiring a large volume of film is identified.

Question 3: Other than Harris Corporation, who is expected to be Kalle's major customers?

Answer 3: Kalle did not care to disclose the name or application of end-users who are expected to be major consumers of PRF. However, in a general way, Dr. Moraw indicated that holographic nondestructive testing was a primary application, together with optical data storage.

II. SPECIFIC QUESTIONS

Question 1: What is the general composition of Kalle's photoplastic film? Why was this system chosen?

Answer 1: The Kalle photoplastic film consists of a 50 μm (±1 μm) optical quality polyester film base overcoated with a 0.9 μm photoconductor layer and a 0.6 μm topcoat of thermoplastic. PVK is the photoconductor and TNF is the sensitizer. Spectral response is flat and DE >30 percent was obtained for gratings recorded on a PRF optimized for ν = 500 ℓ/mm. Under commercial development is a photoplastic film coated on a 50 mm x 50 mm conductive glass substrate (Aurel® glass manufactured by Deutsche Baezers GmbH, Geisenheim/Rhein; about 20 Ω/□ resistivity, but relatively easy to damage). Kalle chose to develop a photoplastic system based on PVK because they have a general competence in this area; in, fact one of Kalle's commerical products is a PVK belt used in copying machines.

Question 2: What is your film base material? Who makes it? What is its commercial name?

Answer 2: Kalle uses an optical grade polyester of their own manufacture as a film base. The commercial name of the polyester is Hostophan® .

Question 3: Why doesn't Kalle's PRF have an internal ground plane? Can the present film be modified to include a ground plane?

Answer 3: The Kalle PRF does not have a conductive coating (internal ground plane). Cost is the major reason cited. Kalle does not have the capability at present for making conductive coatings on polyester. This effort would require a new R&D program.

Question 4: Can the thickness of the thermoplastic layer be varied? What are coating tolerances?

Answer 4: The thickness of the thermoplastic layer can be changed enough to vary the spatial frequency response peak from 50 ℓ/mm to 1000 ℓ/mm. No specific tolerances were available. However, Dr. Moraw noted that the ν_m ~800 to 900 ℓ/mm the shift in peak frequency was about 50 to 100 ℓ/mm.

Question 5: What is near and long term image stability?

Answer 5: Information stability is estimated to be many years at room temperature. However, elevated temperatures cause degradation, as expected. For example, Dr. Moraw found the DE decreased by 50 percent in 60 minutes at 40°C (development temperature is ~65°C).

Question 6: How many times can the PRF be cycled? What limits cycling? Are certain photoplastic systems less sensitive to cycling degradation?

Answer 6: The present Kalle photoplastic film can be cycled only about 10 times. Degrading factors include warpage of the film base, plasticizer volitalization, material transport between layers and charge buildup between the PVK and film base layer. The near term prognosis for a greater number of cycles is not good without further basic R&D.

Question 7: How critical are: a) charging voltage (or E-field) and b) development temperature?

Answer 7: Both charging and heating are very critical. Charge level is determined empirically by charging until frost is just observable (after heat development) and then reducing the charging voltage a small amount. Kalle has developed electronics for producing a thermoplastic layer temperature of 70°C ±1/2°C with excellent repeatability. Heat development time is 0.1 second.

Question 8: What is the rate of charge decay?

Answer 8: Charge decay in the Kalle photoplastic is slow because there is no internal ground plane. Dr. Morow said that their research suggests that no significant charge decay occurs for at least several minutes.

Question 9: For what applications did Kalle develop processing equipment? What are the specifications of this equipment? Can we lease?

Answer 9: Kalle has developed a holographic camera. That is, a conventional off-axis holographic interferometer together with apparatus for charging, heating and transporting the photoplastic recording film. The camera costs about DM 17,000 (~$6,800) and does not include the precision temperature controller. Specifications for the camera are not yet available. The camera is intended mainly for holographic nondestructive testing applications, although gratings or data mask holograms can easily be recorded.

We observed the camera in operation. The PRF is spooled and positioned mechanically. A fresh film sample is charged by a corona device consisting of 4 equally spaced spikes. Electrostatic force holds the film in place against a 50 x 50 mm^2 piece of Aurel® glass. After exposure, the film is heated to develop. A small centrifugal fan behind the Aurel® glass is used to cool the substrate after development. Gratings recorded while we observed, had a diffraction efficiency of about 15 percent and 5 percent, respectively. The reconstructed wave was not uniform; the nonuniformity was attributed to a defect in the conductive coating of the Aurel® glass. The overall time to produce a hologram was on the order of 10 seconds.

Question 10: How many square meters per day of photoplastic film can Kalle manufacture?

Answer 10: Currently, the Kalle photoplastic film is coated on an experimental coater. This limits both quantity and the quality of the film. A kilometer of film per month seems to be the near term limit. However, production coaters are available that could produce this quantity on a daily basis. Format is not a problem. Although 35 mm is the common size, the master roll is wide enough to allow for microfiche formats. The best QC and price would be obtained for large volumes.

Question 11: Is Kalle interested in doing fundamental R&D on photoplastic systems? Would Kalle consider coating photoplastic systems supplied by Harris Corporation?

Answer 11: Kalle did not respond positively about doing sponsored R&D on photoplastic systems.

Question 12: What is Kalle's price structure for small and large quantities of photoplastic film?

Answer 12: Kalle's price structure for small volumes was stated as DM12 ($4.80) per meter of 35 mm film, or $12.75 per square foot. Price structure for large volumes was not available, but can be obtained on demand.

III. SUMMARY

It appears that Kalle AG is an excellent source of photoplastic recording films. Although it is unlikely that PRF will ever represent a significant part of Kalle's sales, we were assured that the Kalle PRF would always be available on a special order basis. The cost of the film is, of course, rather high and it is not clear if it is fully systems qualified. Recyclability is the formost problem area relative to the NASA optical mass memory application; for single recording applications this is immaterial. The effect on performance of the absence of an internal ground plane in the film construction is a more important consideration.

APPENDIX 4B

THEORY OF THERMOPLASTIC DEFORMATIONS

APPENDIX 4B

THEORY OF THERMOPLASTIC DEFORMATIONS

This appendix presents a theoretical description of thermoplastic deformations in an effort to describe the behavior of the deformation process with respect to the operational parameters of the photoplastic recording film. A previous theoretical study of thermoplastic deformation described the growth of a frost deformation for the case in which a charged, deforming thermoplastic film was deposited directly on a grounded conducting plane. The theory involved the solution of the equations of fluid flow under electrostatic forces. An attempt is made here to extend the theory to the more conventional photoplastic recording film and treat the generation of a deformation induced by a spatially modulated electrostatic charge. Our treatment will parallel and draw largely from the earlier theory but with certain departures required by the altered photoplastic film, especially with respect to the charge-induced deformations.

I. FLUID DYNAMICS

Figure 4-56 illustrates the photoplastic film we are considering. A thermoplastic film of thickness d_1 and dielectric constant ϵ_1 is bordered by air on the top and by a photoconducting film of thickness d_2 and dielectric constant ϵ_2 on the bottom. The lower surface of the photoconductor is in contact with a conducting ground plane. The top surface of the thermoplastic contains a positive average charge density σ_o. Illumination of the photoconductor by a sinusoidally varying irradiance results in a negative charge density σ_s $(1 + \alpha \cos Kx)$ at the interface of the thermoplastic and photoconductor. The top surface of the thermoplastic deforms such that $y_s = d_1$ $(1 + \eta \cos Kx)$. Since the model in which the top surface of the thermoplastic is an equipotential surface, agrees most closely with experiment[1] we will restrict our treatment to this case.

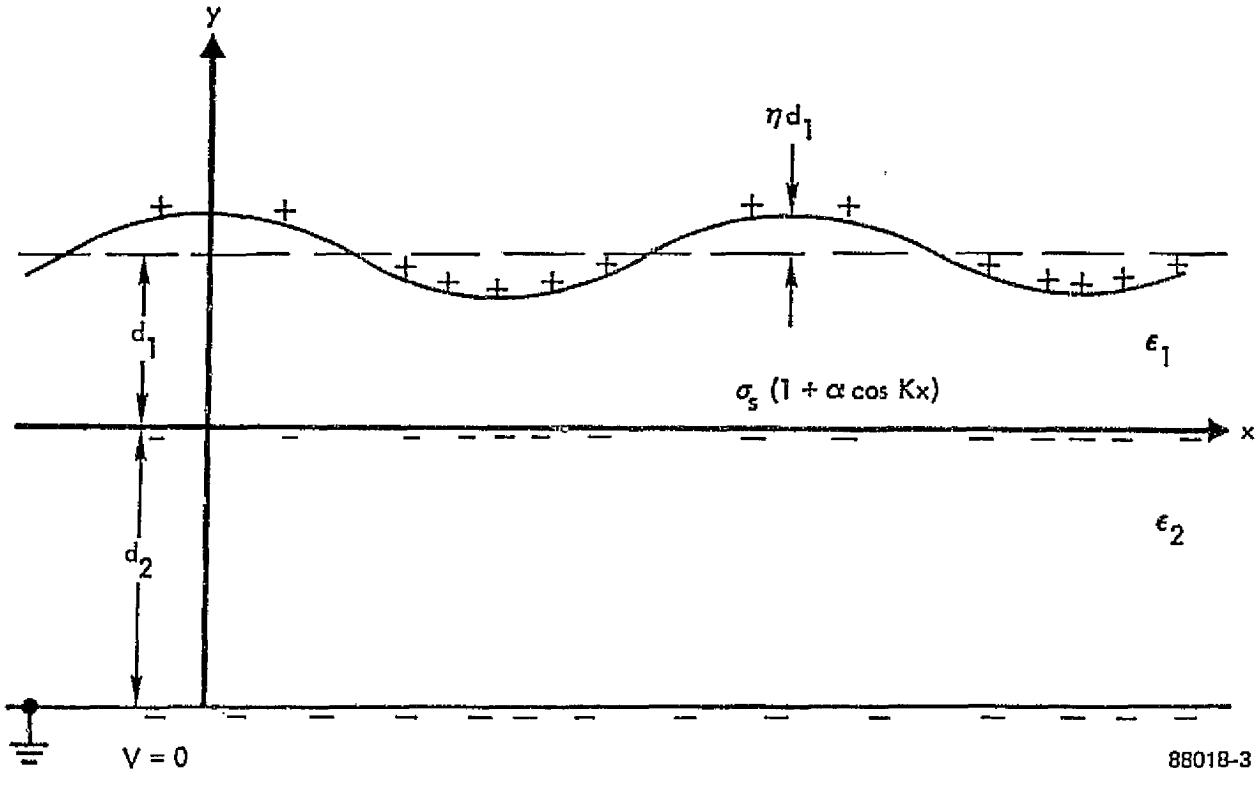

FIGURE 4-56. PHOTOPLASTIC FILM. THERMOPLASTIC SURFACE WITH AVERAGE CHARGE DENSITY σ_o HAS DEFORMATION AMPLITUDE ηd_1. BOTTOM SURFACE OF PHOTOCONDUCTOR IS A GROUNDED CONDUCTING PLANE.

We consider the thermoplastic an incompressible viscous fluid during development. The fluid velocity $\vec{V}(x,y,t)$ must satisfy the equation of continuity and the linearized Navier-Stokes equation

$$\nabla \cdot \vec{V} = 0$$

$$\frac{\partial \vec{V}}{\partial t} = \frac{\nabla p}{\rho} + \frac{\mu}{\rho} \nabla^2 \vec{V}, \tag{1}$$

where p is the pressure, ρ the density and μ the viscosity, subject to the condition at the thermoplastic-photoconductor interface, $V(x, y = 0, t) = 0$. Equation (1) reduces to:

$$\nabla^2 \Phi = 0$$

$$\nabla^2 \psi = \frac{\mu}{\rho} \frac{\partial \psi}{\partial t} \tag{2}$$

The velocity components are given in terms of Φ and ψ by:

$$V_x = \frac{\partial \Phi}{\partial x} + \frac{\partial \psi}{\partial y}$$

$$V_y = \frac{\partial \Phi}{\partial y} - \frac{\partial \psi}{\partial x} \quad .$$

The boundary conditions at the top surface are:

$$\frac{\partial y_s}{\partial t} = V_y \quad , \tag{3}$$

$$\frac{\partial V_x}{\partial y} + \frac{\partial V_y}{\partial x} = 0 \quad , \tag{4}$$

$$p - 2\mu \frac{\partial V_y}{\partial y} = -T \frac{\partial^2 y_s}{\partial x^2} + p_e \quad , \tag{5}$$

where p_e is the surface pressure resulting from the electrostatic charges, and T is the surface tension coefficient. This and the potentials in the other two regions have been calculated to first order in η; the result for the thermoplastic is:

$$\phi_1(x, y, t) =$$

$$(\sigma_o + \sigma_s)\frac{d_2}{\epsilon_2} + \frac{\sigma_o}{\epsilon_1}\, y$$

$$+ \frac{\alpha\sigma_s \sin h\, Kd_2}{K} \quad \frac{\sin h\, K(d_1 - y)}{\epsilon_1 \sin h\, Kd_2 \cos h\, Kd_1 + \epsilon^2 \cos h\, Kd_2 \sin h\, Kd_1} \cos Kx$$

$$- \eta(t)\frac{\sigma_o d_1}{\epsilon_1} \quad \frac{\epsilon_1 \sin h\, Kd_2 \cos h\, Ky + \epsilon_2 \cos h\, Kd_2 \sin h\, Ky}{\epsilon_1 \sin h\, Kd_2 \cos h\, Kd_1 + \epsilon_2 \cos h\, Kd_2 \sin h\, Kd_1} \cos Kx$$

$$+ \eta(t)\frac{\alpha\sigma_s d_1}{2} \quad \frac{\sin h\, Kd_2}{\epsilon_1 \sin h\, Kd_2 \cos h\, Kd_1 + \epsilon_2 \cos h\, Kd_2 \sin h\, Kd_1}$$

$$\times \frac{\epsilon_1 \sin h\, 2Kd_2 \cos h\, 2Ky + \epsilon_2 \cos h\, 2Kd_2 \sin h\, 2Ky}{\epsilon_1 \sin h\, 2Kd_2 \cos h\, 2Kd_1 + \epsilon_2 \cos h\, 2Kd_2 \sin h\, 2Kd_1} \cos 2Kx$$

$(\partial\phi_1/\partial x)\, y_s$ has no terms of zero or first orders in η, so that the electrostatic pressure to first order in η is $\frac{1}{2}\,\epsilon_1 \left|\partial\phi_1/\partial y\right|^2 y_s$. It can be seen that the existence of a modulated charge distribution with spatial frequency K at the thermoplastic-photoconductor interface results in a term with spatial frequency 2K in the potential in the thermoplastic. Such a term does not exist when there is no interfacial charge modulation, as when initially nonzero surface deformations grow into a frost pattern. This term results in a surface pressure component of frequency 2K, and hence a deformation which we have not included in our treatment. Consequently, it is evident that the response of photoplastic film exhibits a nonlinearity (even for small deformations) totally unrelated to the photoresponse of the photoconductor, the nonlinearity of the deformation response of the thermoplastic, and the intrinsic nonlinearity of thin phase holograms. This nonlinearity must be included in any study of nonlinearity noise in photoplastic film. For our present purposes we will assume that the nonlinear

deformations are negligible and retain only the constant and fundamental terms in the electrostatic pressure. To first order in η we have:

$$p_e = p_o(t) + \eta f(K) \cos Kx + g(K) \cos Kx \quad , \tag{6}$$

where

$$p_o(t) = \frac{\sigma_o^2}{2\epsilon_1} - \frac{\alpha^2 \sigma_s^2 \epsilon_1 \sinh^2 Kd_2}{2(\epsilon_1 \sinh Kd_2 \cosh Kd_1 + \epsilon_2 \cosh Kd_2 \sinh Kd_1)}$$

$$+\eta(t) \frac{\alpha\sigma_s \sigma_o Kd_1}{2} \frac{\sinh Kd_2 (\epsilon_1 \sinh Kd_2 \sinh Kd_1 + \epsilon_2 \cosh Kd_2 \cosh Kd_1)}{\epsilon_1 \sinh Kd_2 \cosh Kd_1 + \epsilon_2 \cosh Kd_2 \sinh Kd_1} \quad ,$$

$$f(K) = -\frac{\sigma_o^2 Kd_1}{\epsilon_1} q_1(K) - \frac{(\alpha\sigma_s)^2 Kd_1}{\epsilon_1} q_2(K) \quad ,$$

$$g(K) = -\alpha\sigma_s \sigma_o \frac{\sinh Kd_2}{\epsilon_1 \sinh Kd_2 \cosh Kd_1 + \epsilon_2 \cosh Kd_2 \sinh Kd_1} \quad .$$

For brevity of notation we have used:

$$q_1(K) = \frac{\epsilon_1 \sinh Kd_2 \sinh Kd_1 + \epsilon_2 \cosh Kd_2 \cosh Kd_1}{\epsilon_1 \sinh Kd_2 \cosh Kd_1 + \epsilon_2 \cosh Kd_2 \sinh Kd_1} \quad ,$$

$$q_2(K) = \frac{\epsilon_1^2}{2} \frac{\sinh^2 Kd_2}{(\epsilon_1 \sinh Kd_2 \cosh Kd_1 + \epsilon_2 \cosh Kd_2 \sinh Kd_1)^2}$$

$$\times \frac{\epsilon_1 \sinh 2Kd_2 \sinh 2Kd_1 + \epsilon_2 \cosh 2Kd_2 \cosh 2Kd_1}{\epsilon_1 \sinh 2Kd_2 \cosh 2Kd_1 + \epsilon_2 \cosh 2Kd_2 \sinh 2Kd_1} \quad .$$

The fluid velocity potential Φ must satisfy Laplace's equation and the stated boundary conditions. Since an arbitrary function of t can be added to the

velocity potential function to satisfy the boundary conditions and still satisfy Laplace's equation, we define Φ such that Bernoulli's equation is:

$$p = -\rho \frac{\partial \Phi}{\partial t} + p_o(t) \quad . \tag{7}$$

Inserting Equation (6) and Equation (7) into Equation (5) the surface pressure boundary condition becomes:

$$-\rho \frac{\partial \Phi}{\partial t} - 2\mu \frac{\partial V_y}{\partial y} = -T \frac{\partial^2 y_s}{\partial x^2} + \eta f(K) \cos Kx + g(K) \cos Kx \quad . \tag{8}$$

Integrating Equation (3),

$$y_s = y_{so} + \int_o^t V_y(x, y_s, t')\, dt'$$

$$= d_1 + \eta_o d_1 \cos Kx + \int_o^t V_y(x, y_s, t)\, dt' \quad . \tag{9}$$

The solution of Equation (2) results in a vertical velocity component which can be written in the form:

$$V_y(x, y_s, t) = e^{\omega t}\, \omega \gamma(K)\, d_1 \cos Kx \quad . \tag{10}$$

Inserting Equation (10) and Equation (9) into Equation (8) we obtain the two relations:

$$-\rho \frac{\partial \Phi}{\partial t} - 2\mu \frac{\partial V_y}{\partial y} = \left[T + \frac{f(K)}{K^2 d_1}\right] K^2 d_1\, \gamma(K)\, e^{\omega t} \cos Kx \tag{11}$$

and

$$\left[\eta_o - \gamma(K)\right]\left[T + \frac{f(K)}{K^2 d_1}\right] + \frac{g(K)}{K^2 d_1} = 0 \quad . \tag{12}$$

Equation (11) is in the form obtained earlier[1] in which the factor in brackets is regarded as an effective surface tension coefficient. The solution of Equation (2) satisfying the boundary condition at $y = 0$ and those of Equation (4) and Equation (11) leads to an evaluation of the deformation growth rate ω as a function of K and the physical parameters. Two cases of particular interest are the frost deformation resulting from initially small, but nonzero, surface deformations and the generation of a single deformation by the presence of an induced, spatially modulated charge density at the thermoplastic-photoconductor interface. For the discussion of these cases we will define the following quantities:

$$\omega_o = \frac{T}{2\mu d_1} \qquad V_1 = \frac{\sigma_o d_1}{\epsilon_1}$$

$$V_o = \sqrt{\frac{d_1 T}{\epsilon_1}} \qquad V_\alpha = \frac{\alpha \sigma_s d_1}{\epsilon_1} \quad .$$

The frost deformation corresponds to the condition $\alpha = 0$, and therefore $g(K) = 0$, and $\gamma = \eta_o$ by Equation (12). We have:

$$\eta = \eta_o e^{\omega t} \tag{13}$$

with

$$\frac{\omega}{\omega_o} = \left\{\left(\frac{V_1}{V_o}\right)^2 q_1(K) - Kd_1\right\}\left\{\frac{\frac{1}{2}\sinh 2Kd_1 - Kd_1}{\cosh^2 Kd_1 + K^2 d_1^2}\right\} \quad . \tag{14}$$

Equation (14) reduces to that of Budd[1] when $d_2 \longrightarrow 0$. It should be noted that the growth rate given by Equation (14) is independent of σ_s. One could therefore expect the formation of frost to be unrelated to the level of uniform exposure of the photoconductor, assuming no additional charge is added to the thermoplastic surface.

Next we consider the growth of a charge-induced deformation from an initially smooth surface, in which case $\eta_o = 0$ and:

$$\gamma(K) = \frac{g(K)}{[K^2 T + f(K)]} \quad .$$

We obtain the result for a signal deformation

$$\eta = \gamma(K)\,[e^{\omega t} - 1] \quad , \tag{15}$$

where

$$\frac{\omega}{\omega_o} = \left\{\left(\frac{V_1}{V_o}\right)^2 q_1(K) + \left(\frac{V_\alpha}{V_o}\right)^2 q_2(K) - Kd_1\right\} \left\{\frac{1/2 \sinh 2Kd_1 - Kd_1}{\cosh^2 2Kd_1 + K^2 d_1^{\,2}}\right\} \quad ,$$

and

$$\gamma(K) = \frac{V_\alpha V_1}{V_o^{\,2}} \; \frac{\epsilon_1 \sinh Kd_2 \left[\left(\frac{V_1}{V_o}\right)^2 q_1(K) + \left(\frac{V_\alpha}{V_o}\right)^2 q_2(K) - Kd_1\right]^{-1}}{(\epsilon_1 \sinh Kd_2 \cosh Kd_1 + \epsilon_2 \cosh Kd_2 \sinh Kd_1)\, Kd_1} \tag{17}$$

The induced deformation is seen to be proportional to the amplitude of modulated charge at the interface. A characteristic of both the frost deformation and the signal deformation is that the growth rate and the spatial frequency response of the deformation are approximately independent of d_2 for $Kd_2 \gg 1$, provided a variation in d_2 is accompanied by an adjustment of the charging voltage (thermoplastic surface to ground) to maintain V_1 at a constant level. From this one might expect, then, that the holographic characteristics of photoplastic would not be appreciably affected by moving the ground plane away from the photoconductor, perhaps even detached entirely from the photoplastic film.

II. EXAMPLES

We can observe some of the properties of a frost and signal deformation by looking at a particular choice of parameters. Let us take $\epsilon_1 = \epsilon_2$, $Kd_2 >> 1$ and $V_\alpha^2 << V_1^2$. The growth rates for frost and signal deformations are then equal and given by

$$\omega = \omega_o \left\{ \left(\frac{V_1}{V_o} \right)^2 - Kd_1 \right\} \left\{ \frac{1/2 \sinh^2 Kd_1 - Kd_1}{\cosh^2 Kd_1 + K^2 d_1^2} \right\} .$$

For a signal deformation

$$\gamma(K) = \left(\frac{V_\alpha}{V_o} \right) \left(\frac{V_1}{V_o} \right) \frac{e^{-Kd_1}}{Kd_1 \left[\left(\frac{V_1}{V_o} \right)^2 - Kd_1 \right]}$$

Figures 4-57, 4-58 and 4-59 show the normalized d formations for these voltages in the low voltage range. The value $K_T = \frac{1}{d_1} \left(\frac{V_1}{V_o} \right)^2$ has a particular significance for a surface deformation. This is the maximum spatial frequency for a frost deformation with positive growth rate. For $K>K_T$ the frost deformation decreases to zero from its initial value. Growing signal deformations, however, do exist above this frequency, but approach ans asymptotic limit shown by the dashed curves in the figure. For $K<<K_T$ signal deformations increase without limit (within our present approximation) as in the case of a frost deformation. Several observations can be made from the figures with regard to the charging voltage (proportional to V_1). One would expect the development time to decrease for a given magnitude of deformation as the surface charge increases; for the voltages considered, $V_1/V_o = 0.5$, 1 and 2 the development times for approximately the same peak signal deformation are $t = 75/\omega_o$, $10/\omega_o$ and $2.5/\omega_o$, respectively. For higher voltages the deformation curves peak more sharply and at progressively higher spatial frequencies, but K_T rapidly becomes more remote from the spatial frequency at the peak. Finally, it is observed that the magnitude of a frost deformation increases rapidly with respect to a

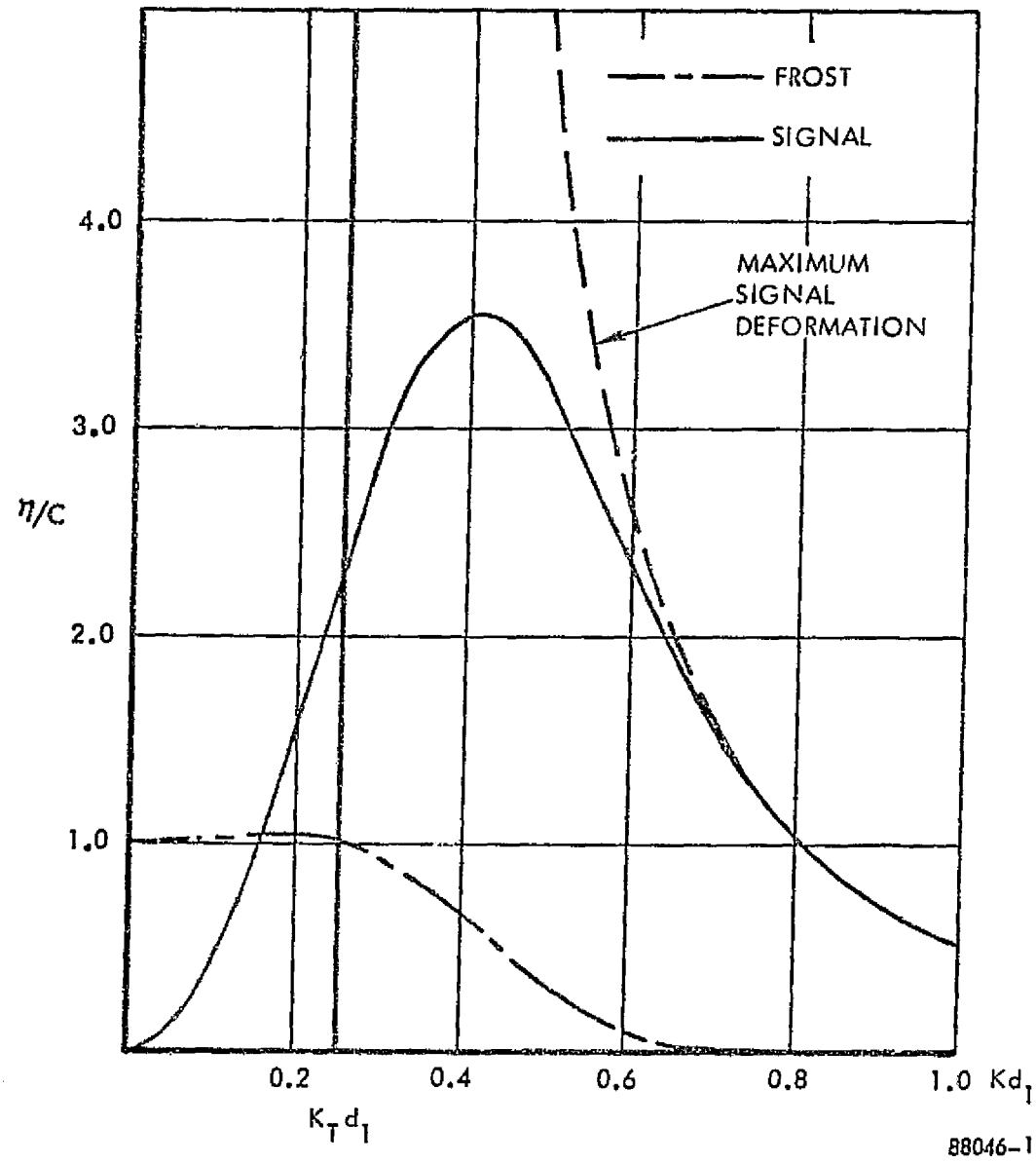

FIGURE 4-57. FROST AND SIGNAL DEFORMATION VERSUS Kd_1. $V_1/V_o = 0.5$, $\omega_o t = 75$. $c = \eta_o$ FOR FROST AND $c = V_\alpha/2V_o$ FOR SIGNAL

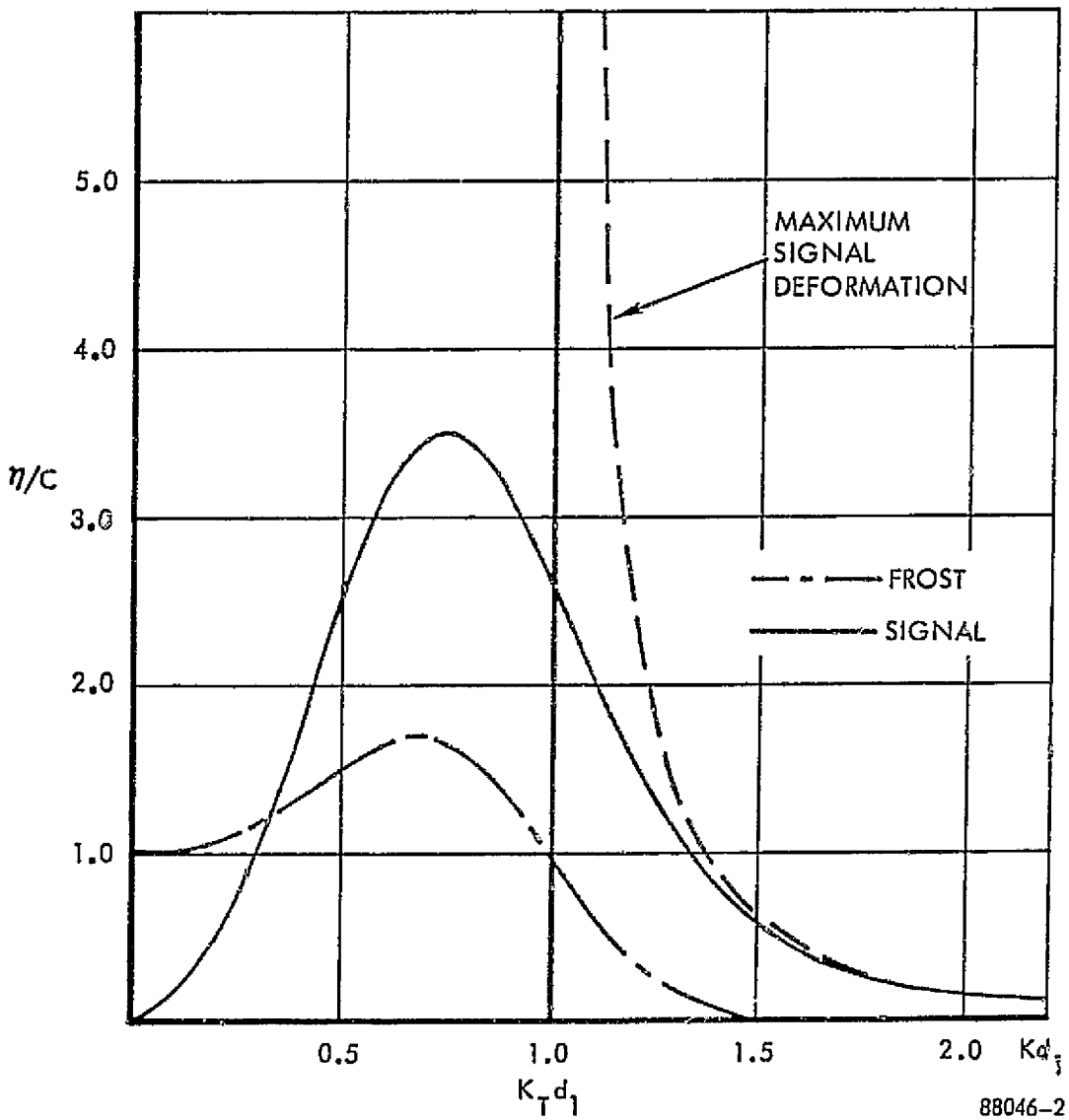

FIGURE 4-58. FROST AND SIGNAL DEFORMATION VERSUS Kd_1. $V_1/V_o = 1$, $\omega_o t = 10$. $c = \eta_o$ FOR FROST AND $c = V_\alpha/2V_o$ FOR SIGNAL

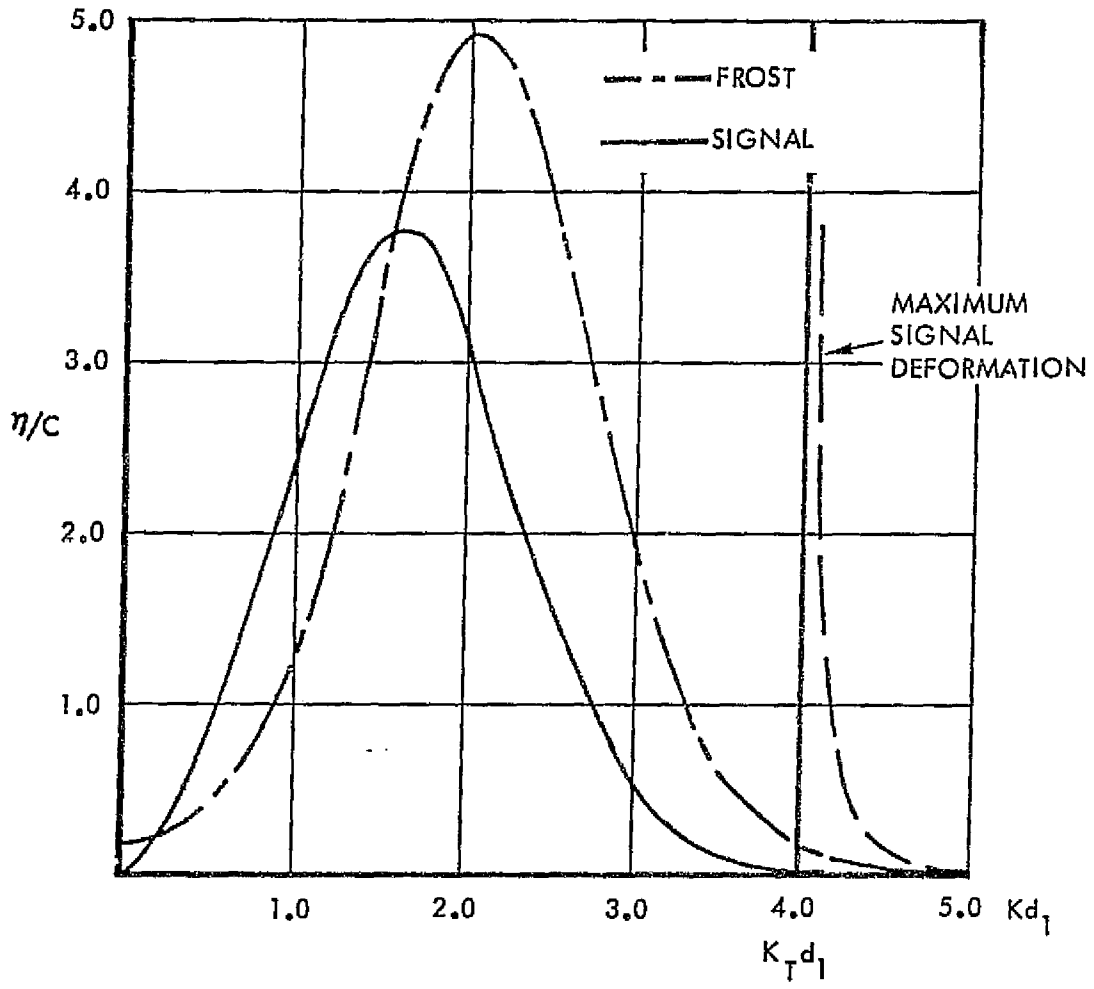

FIGURE 4-59. FROST AND SIGNAL DEFORMATION VERSUS Kd_1. $V_1/V_o = 2$, $\omega_o t = 2.5$. $c = 5\eta_o$ FOR FROST AND $c = V_\alpha/2V_o$ FOR SIGNAL

signal deformation as the voltage increases. This latter property can be simply described quantitatively for large voltages. At large voltages $\gamma(K)$ becomes small for $K \ll K_T$, which η is appreciable, and it is assumed for a frost deformation that $\eta_o \ll 1$. For a significant signal or frost deformation, then, $\omega(K)t$ must be large. The result is that η is sharply peaked for both signal and frost about the same value K_P, which has been shown[1] to be

$$K_P = \frac{1}{d_1} \ell n \left(\frac{V_1}{V_o}\right) .$$

Thus, when $V_1/V_o \gg 1$ we have

$$\left(\frac{\eta \text{ signal}}{\eta \text{ frost}}\right) \text{ peak} = \frac{1}{\eta_o} \frac{V_\alpha V_1}{V_o^2} \frac{e^{-K_P d_1}}{K_P d_1 \left[\left(\frac{V_1}{V_o}\right)^2 - K_P d_1\right]}$$

$$= \frac{\alpha(\sigma_s/\sigma_o)}{\eta_o \left(\frac{V_1}{V_o}\right)^2 \ell n \left(\frac{V_1}{V_o}\right)} .$$

Thus, one would expect that lower voltages would be more favorable for signal generation when frost is to be minimized, although development times are appreciably longer.

III. DISCUSSION

Using values[2] $T = 36$ dynes/cm, $\epsilon_1 = 2.5$ and $d_1 = 0.5\mu$ we find $V_o \approx 30$ volts. The charging voltage V_c is the potential difference between the thermoplastic surface and the ground plane; if $d_2 = 5d_1$ and $\epsilon_1 = \epsilon_2$ then $V_1 \approx V_c d_1/(d_1 + d_2) = V_c/6$ before recharging. Typically V_c is 90-180 volts, so that V_1/V_o is 1/2 -1 before a recharge. After exposure and recharging of the surface to V_c, V_1 will be approximately

$$V_1 = \frac{d_1}{d_1 + d_2}\left[1 + \frac{\sigma_s}{\sigma_o}\,\frac{d_1}{d_1 + d_2}\right] V_c \quad ,$$

where σ_s/σ_o is the fraction of charge density transferred from the ground plane to the dielectric interface. The recharging procedure increases V_1/V_o, then, by a factor of at most 2, and consequently has the effect of increasing the rate of growth of a signal or a frost deformation, move the peak response to higher spatial frequencies and produce a narrower bandwidth. In practice, V_1/V_o appears to be somewhat higher than the present estimate; this may be due to uncertainty of the physical constants used.

Note that if $d_2 \gg d_1$ the ratio $(V_1/V_o)^2$ is proportional to d_1. For a given photoconductor thickness and charging voltage V_c, a decrease in d_1 rapidly becomes more favorable for a signal deformation than for a frost deformation. This is consistent with previous observations of thermoplastic deformations.[3,4]

IV. SUMMARY

We have attempted to describe the response of a thermoplastic-photoconductor recording material both for a signal resulting from a photoinduced electrostatic interfacial charge distribution and for a self-propagating frost deformation. The analysis extends a previous theory of thermoplastic deformation for an equipotential thermoplastic surface to the multiple layer photoplastic and includes the process of signal generation. The theory reveals a nonlinearity in the electrostatic surface pressure, an insensitivity of frost formation to uniform photoconductor illumination, and an insensitivity to ground plane location. Signal deformations are found to grow to some asymptotic value for spatial frequencies above the maximum frequency for frost deformation growth. Low voltages are seen to favor signal deformations with respect to frost deformations, but require long development times.

V. FURTHER COMMENTS

Several aspects of thermoplastic deformations must be mentioned which have not received here the attention that their importance demands.

First, it must be emphasized that the ratio ($\eta_{signal}/\eta_{frost}$) peak cannot be interpreted as the signal to frost noise ratio. We have assumed in our treatment, and all other known theoretical studies, that a single deformation is present. In practice, of course, there are many deformation components, and these interact with one another, as evidenced by the fact that the growth of frost is inhibited by the existence of the signal. In view of the importance of this phenomenon for data storage applications, it would seem that a better understanding of this is essential.

Also important for the same reason is the behavior of frost noise with signal irradiance variations over a hologram area. The dependence of the signal-to-noise ratio on irradiance variations has been recognized more generally with regard to optical storage; the effects would appear to be especially profound in the case of photoplastics.

The thermoplastic fluid flows during development because of the decrease in viscosity associated with elevated temperatures. The fact that the temperature is not constant during the process should not affect the spectral characteristic of the deformation because the form of the response function is independent of the value of the viscosity, if it is uniform, and affects only the rate of the process. On the other hand, a temperature gradient through the thermoplastic, which certainly exists, should modify the spatial frequency response; one might approximately describe the effect by defining an effective thermoplastic thickness related to the magnitude of the temperature gradient. The precise character of the temperature gradient effects is rather uncertain and merits further consideration.

APPENDIX 4B

REFERENCES

1. Budd, F., "Dynamical Theory of Thermoplastic Deformation," J. Appl. Phys. 36, 1613 (1965).

2. Cressman, P. J., "New Type of Thermoplastic Deformation," J. Appl. Phys. 34, 2327 (1963).

3. Claus, C. J. and R. W. Gundlach, "Imaging by Plastic Deformation," in Xerography and Related Processes, edited by J. H. Dessauer and H. E. Clark (New York: The Focal Press, 1965).

4. Credelle, T. L. and F. W. Spong, "Thermoplastic Media for Holographic Recording," RCA Review, 33, 206 (1969).

APPENDIX 4C

VENDOR SURVEY REPORT

WRITE/READ/ERASE RECORDING MATERIAL FOR 10^{12} BIT NASA OPTICAL MASS MEMORY

APPENDIX 4C
VENDOR SURVEY REPORT

I. OBJECTIVE

To determine the feasibility of developing a light-sensitive recording material in the near term that is write/read/erasable, system-qualified for currently envisioned space-borne optical memories, and available as a custom product with storage performance uniformity and batch-to-batch consistency.

II. RECORDING MATERIAL SPECIFICATIONS

As outlined in Table 4C-1

III. VENDOR PROFILES

1. Company

Multi-State Devices, Ltd.
1330 Trans Canada Highway S.
Dorval 740
Quebec, Canada
(514) 279-4567

Contact

Dr. H. Keith Eastwood
Manager, Material Research

Material

Vanadium Oxide(s)

TABLE 4C-1

WRITE/READ/ERASABLE RECORDING MATERIAL SPECIFICATIONS

NASA 10^{12} BIT OPTICAL MASS MEMORY; HOLOGRAPHIC FICHE-ORIENTED SYSTEM

- Type: planar phase or amplitude with gray scale capability.
- Exposure Sensitivity: $< 100\mu J/cm^2$ to achieve SNR and DE goals.
- Spectral Response: broadband; centered on a major laser wavelength, e.g., 632.8, 514.5, or 488.0 nm (visible) or 1.06 μm (IR).
- Frequency Response: low pass with cutoff spatial frequency greater than 1000 ℓ/mm or broadband (center frequency of at least 800 ℓ/mm and bandpass of at least 400 ℓ/mm).
- Holographic Performance: SNR goal of at least 20 dB/bit at a packing density of 10^6 bits/cm^2; DE at SNR goal of at least 1%.
- Photographic Performance (absorption media): $D_{max} \geq 2$, $D_{min} \leq 0.15$ and $\gamma \geq 1$.
- Write/Erase Capability: minimum of 10^3 complete cycles with less than 10% degradation of holographic and photographic properties. Recycle time of less than 1 second. Preferred erasure mode is optical.
- Wiener Noise, $\Phi_n(\nu)$: less than $10^{-8} mm^2$ for spatial frequencies ν greater than 200 ℓ/mm (all stochastic scattering processes, due either to base or to light-sensitive layer).
- Reciprocity Failure: negligible or compensatable for exposure times in the 10^{-8} to 10^{-5} second range.
- Performance Consistency: random samples should show less than 5% rms variation in holographic and photographic performance.
- Film Base: highest grade, best optical quality polyester; equivalent to or better than Estar or Cronar. Thickness variations $< \lambda/10$ per mm for a thickness of 7 mils.
- Processing: none preferred; dry, on-line with light or heat the only alternative.
- Shelf Life: minimum of one year at 20°C and 50% RH.
- Archival Life: at least one year at 20°C and 50% RH.
- Production Status: available on special order basis in variable quantities and with full quality assurance.
- Updating Capability Without Full Erasure: desirable, but optional.
- Image Permanence: no image degradation for repeated or extended readout.
- Environmental Characteristics: data storage properties are to be unaffected by temperatures in the 10 to 30°C range and relatively humidity in the 25 to 75% range.
- Format: available and usable in die-cut standard microfiche format (105 mm x 148 mm).

Summary

- VO_2 is the most useful vanadium oxide; others are V_2O_3 (transition at -165° C) and V_2O_5 (no transition).
- Thin films of vanadium oxide are coated on quartz or sapphire substrates by reactive sputtering. Typical VO_2 film thickness in the 500 Å to 1 μm range. A substrate thickness of 6 mils with a 1.5 inch diameter is typical for sapphire. Substrates up to 10 inches in diameter are available. Sapphire is the preferred substrate.
- Vanadium oxides are considered crystalline transition metal oxides: they are semiconductors at low temperatures and semimetals above their transition temperature.
- It is probably not possible to coat VO_2 on polyester because of the high deposition temperature. The reactive sputtering coating process requires a temperature of 400° C. This temperature will destroy all known optical grades of polyester.
- Laser spot recording experiments provide the following data:

  Laser: CW YAG, $\lambda = 1.06$ μm

  Shutter: A/O modulator

  Bias Temperature: 65° C

  Type: VO_2 on sapphire (600 Å film thickness)

  Data: 5 μm diameter spots

  Exposure Time Range: 10-50 nanoseconds

  Power at Film Plane: 3-10 mW

Irradiance Range (average): $1.5\text{-}5 \times 10^7$ mW/cm^2

Exposure Range (average): 150 μJ/cm^2 - 2.5 mJ/cm^2

NOTE

All exposures in this range wrote spots without damaging the VO_2 film or substrate and were erasable.

Recycling: Indefinitely on sapphire substrate, but a limited number of times on quartz. At least 20 full cycles optically without degradation. More than 3×10^8 cycles electronically. Can recycle small areas in less than 1 second.

Contrast: Greater than 100:1 at 1.06 μm, but less than 3:1 at 633 nm.

Color: Yellow-brown with a peak transmittance of ~8 percent at 1.06 μm.

Readout Mode: Transmission (high contrast) or reflection (low contrast).

Gray Scale Capability: Yes, by cycling on different minor hysteris loops.

Resolution: At least 750 ℓ/mm.

Erasure: requires cooling to about 40° C; can be done with stream of cooling fluid (liquid or gas); easy to do for large areas, very difficult to control on a bit by bit or microhologram basis; thermoelectric cooling not tried.

- VO_2 coated on sapphire substrate can be purchased on special order basis; a 2-inch diameter by 6-mil thick piece is recommended for initial experimental work.

- VO_2 has definite optical memory potential; digital recording has already been demonstrated; holographic recording is feasible. Further R/D is needed to increase peak transmittance, narrow hysteresis curve, and improve contrast at visible wavelengths, e.g., 633 nm.

2. Company

Scott Graphics, Inc.
Subsidiary of Scott Paper Company
Holyoke, MA 01040
(413) 536-7800

Contact

Dr. Johan F. Dirks
Manager, Engineering Research Laboratories

Material

Photoplastic Recording Film (PRF)
Phenylene-diamine photoconductor/dye sensitizing system

Summary

- Scott Graphics has developed and manufactures several electrophotographic recording materials. They have an extensive research base in electrophotography, and a corresponding production capability.
- Scott Graphics has developed and markets the System 200 Updatable Record Processor that stores microimages on a transparent electrophotographic film (TEP film).
- The basic TEP film construction can be directly modified by the addition of thermoplastic top coat to form a photoplastic recording film (PRF).

- A preliminary experimental characterization of PRF based on the TEP film package is in progress. Experimental results to date are encouraging; exposure sensitivity is 150 - 300 $\mu J/cm^2$ at 633 nm and SNR = 22 dB with a DE = 10 percent (insertion loss of 75 percent) has been obtained for a packing density of 10^6 $bits/cm^2$.
- There are no fundamental problems with the Scott Graphic PRF/Concept. However, improvements in exposure sensitivity and film base quality are required. Overall, this system is an attractive candidate. Scott Graphics has the capability to produce this type of recording material in volume.

3. Company

Horizons Incorporated
Division of Horizons Research Incorporated
23000 Mercantile Road
Cleveland, OH 44122
(216) 464-2424

Contact(s)

Mr. Harry L. Fichter, Technical Marketing
Dr. Gene Wainer, Ch. of Board/Director of Research

Material

Photoplastic Recording Film (PRF)
Poly-N-vinyl Carbazole/2,4,7 Trinitrofluoronone (PVK/TNF)

Summary

- Horizons is a very broadbased research/development/production group with a strong recording materials orientation. Their main products are a high-resolution, dry-working dye film and a PVK based photoresist. They have over 500 patents, many of which cover PVK-related chemical photosystems.
- Horizons has the capability for coating transparent metallic layers on polyester.
- Horizons has the personnel and background for procuring, testing and coating PVK/TNF and thermoplastic compositions.
- Horizons has the personnel and facilities for bringing to product status a PVK/TNF photoplastic recording film.
- There is considerable recording materials potential at Horizons in the area of dye films, photoresists, and electrostatic imaging. Of particular interest is an "ion spitter," a concept which presently is used for an on-line UPC bar recorder. Related to this is an electrostatic recorder concept capable of high megabit/second rates which is called "contrography."
- Horizons has the overall capabilities for the development to production status of PVK/TNF photoplastic films in fiche or tape form that would be keyed to the needs of the NASA Optical Mass Memory Program.

4. Company

Honeywell Corporate Research Center
10701 Lyndale Ave. S.
Bloomington, MN 55340
(612) 887-4434

Contact(s)

Dr. D. Chen

Dr. T. C. Lee, Staff Scientists

Material

PVK/TNF Photoplastic Recording Film

Summary

- Honeywell has a demonstrated capability in the area of PVK/TNF photoplastic recording film.
- An impressive 16 mm polyester tape with a transparent metallic ground plane and PVK/TNF photosystem has been developed.
- The Honeywell PVK/TNF photoplastic recording film is capable of recording efficient holograms with acceptable SNR with an exposure of about 20 $\mu J/cm^2$.
- Honeywell's R/D efforts are internally funded. They have not given consideration to producing large quantities of the PRF. They stated that not all problems are solved, and that scaling up from experimental to production level would probably not be a trivial problem. They may be interested in the future in large quantity production of PRF on a special order basis.
- Honeywell's accomplishments in developing a photoplastic tape are impressive. This work is obviously directed toward a holographic data storage system. It is not known if Honeywell is willing to modify the emphasis of their current R/D work to satisfy NASA's needs.

5. Company

Sperry-Univac
Univac Park
P. O. Box 3525
St. Paul, MN 55165
(612) 456-2998

Contact

Dr. Alan D. Kaske, Engineering Manager
Applied Physics Laboratories

Material

PVK/TNF Photoplastic Recording Film (PRF)

Summary

- Sperry-Univac is working in several optical memory related areas. These include recording materials, page composers and beam deflectors.
- Sperry-Univac has been working on PVK/TNF type photoplastic recording film for about two years. They showed holographic reconstructions with excellent DE and SNR. Their most important contribution is in the area of reuse; a conventional PVK/TNF system has been cycled up to 50,000 times with only about 50 percent degradation of holographic parameters.
- Sperry-Univac has not addressed the problems associated with coating a PVK/TNF photosystem and thermoplastic on a flexible substrate. Although no fundamental change in the PRF is required, fabrication is more difficult.
- Sperry-Univac has demonstrated a high level of competence with PVK/TNF recording materials. The overall level of effort is not, however, substantial. No production capability was evident.

6. Company

Stanford Research Institute
Menlo Park, CA 94025
(415) 326-6200

Contact

Mr. Matt Lehmann
Research Associate

Material

Photodichroic NaF

Summary

- Principal recording material emphasis is on photodichroic media such as NaF doped with Li by ion implantation.
- Li-doped NaF is fully reusable and does not require a cryogenic environment.
- This material can be used for either holographic or digital recording. However, known performance levels are not impressive.
- Photodichroics are still very much in a preliminary research and development stage. They are judged not suitable for the NASA Holographic Optical Mass Memory.

IV. OVERALL SUMMARY

1. Photoplastic recording film, particularly the PVK/TNF type, is the only light-sensitive material that could in the near term meet all systems and operational requirements; this is the concensus of all groups surveyed. No other known recording materials even approximately satisfy present specifications or offer the hope of doing so in the near future.

2. The problem areas of major importance relative to most photoplastic recording films are: a) lack of availability of a polyester film base of high optical quality, b) no demonstrated quality control approach that insures repeatable performance from batch to batch, c) no implementation of closed-loop corona charging and heat development and erasure subsystems to assure consistency of performance, and d) uncertainty about the effects of recycling fatigue on holographic performance over the first 1,000 cycles.

3. Kalle AG has a PVK/TNF photoplastic film which is already sold as a custom product. QC is excellent and they manufacture their own high quality polyester substrate (called Hostophan®). The main problem is the lack of a transparent internal ground plane. This is by their choice, and does not represent a limitation in their current applications. Another problem is the type of thermoplastic used, but again this could be modified to suit our requirements. Overall, a development effort with Kalle is a possible alternative. However, their status as a foreign supplier merits special consideration.

4. The most qualified American vendor with respect to near term production capability is Scott Graphics. Their M-phenylene diamine/dye sensitized photoplastic recording film could have production status in one year.

5. Horizons Incorporated has the best overall technical depth in light-sensitive systems. They could provide a production capability for PVK/TNF photoplastic recording film.

6. Honeywell and Sperry-Univac unequivocally demonstrated that high-quality holographic storage and 1,000 or more cycles are feasible for photoplastic recording film. The PVK/TNF photoplastic system on 16 mm tape seen at Honeywell approaches complete systems qualification.

This quality and performance level probably can be duplicated for large quantities of fiche (or tape) by research-oriented vendors such as Horizons Incorporated within two years. Scott Graphics may be limited to development of their particular photoplastic system because of legal considerations. Horizons Incorporated's patent position in N-vinyl carbazole may permit them to avoid this complication.

7. An overall conclusion is that a systems-qualified photoplastic recording medium could be available in two years with a directed production development effort. No fundamental problems are known to exist at this time. Best qualified American vendors are Scott Graphics and Horizons Incorporated. Kalle AG merits consideration on the basis of presently available capabilities. Honeywell has the best proven PVK/TNF film technology.

V. RECOMMENDATION

Choose as the baseline recording material a photoplastic recording film, preferably one using a PVK/TNF photosystem, with special emphasis on:

a) Critical components: polyester film base, transparent ground plane, photoconductor, photosensitizing dyer, and thermoplastic top layer.

and

b) Critical subsystems: current-controlled corona discharge unit; precision heating units for development and erasure; and transport and handling mechanisms.